

EFFICIENT HISTORY MATCHING AND OPTIMIZATION OF
UNCONVENTIONAL RESERVOIRS USING THE FAST MARCHING METHOD

A Dissertation

by

ATSUSHI IINO

Submitted to the Office of Graduate and Professional Studies of
Texas A&M University
in partial fulfillment of the requirements for the degree of

DOCTOR OF PHILOSOPHY

Chair of Committee,	Akhil Datta-Gupta
Co-Chair of Committee,	Michael J. King
Committee Members,	Nobuo Morita
	Yalchin Efendiev
Head of Department,	Jeff Spath

December 2018

Major Subject: Petroleum Engineering

Copyright 2018 Atsushi Iino

ABSTRACT

For reliable performance assessment of unconventional reservoirs, we need to model the complex hydraulic fracture network that interacts with pre-existing/ induced fractures and reservoir rock, as well as the underlying physics such as gas desorption, Knudsen diffusion, phase behavior in nano-scale pores and stress-dependent fracture conductivity. Numerical simulation is a robust and versatile tool to incorporate relevant physics but the substantial computational time required can often be a bottleneck for the practical application.

Recently, a rapid simulation approach based on the Fast Marching Method (FMM) has been proposed. The high frequency asymptotic solution of the diffusivity equation leads to the Eikonal equation, which can be efficiently solved by the FMM for the Diffusive Time-of-Flight (DTOF) that governs the pressure ‘front’ propagation. The key concept of the FMM-based simulation is to utilize the DTOF as a 1-D spatial coordinate embedding reservoir heterogeneity to transform an original 3-D reservoir model into an equivalent 1-D model, leading to orders-of-magnitude faster computation compared to the normal finite difference simulation.

In this study, we first developed and validated the FMM-based blackoil simulation for multi-phase flow in unconventional reservoirs. We also present the field history matching example of Eagle Ford Shale to demonstrate the efficacy and utility of history matching workflow coupled with the FMM-based simulator, which assists in the

uncertainty assessment of reservoir and fracture properties as well as the production forecast.

Second, we further extended the FMM-based simulation to the multi-component compositional simulation. We propose a robust optimization workflow for the gas injection EOR in unconventional reservoirs. Use of the rapid FMM-based simulation enables a large number of Huff-n-Puff simulations with a field-scale reservoir model in a practical timeframe, which also provides us with comprehensive understanding on how each operational parameter influences the displacement and recovery processes.

Third, we adopted the FMM-based approach to multi-well simulations and optimization of the infill well spacing. The FMM-based simulation was extended to a multi-well scenario under the bottomhole pressure constraints. The computational efficiency of our approach enables extensive simulation runs to determine the point of diminishing return for additional well placement to obtain the optimal well spacing.

Lastly, we further extended the FMM-based multi-well simulation to the scenario of constant rate production where the drainage volume partition associated with each well dynamically changes over time. We proposed and validated new methodologies to appropriately model such dynamic partition changes.

DEDICATION

To my family: Yuka and Mikiko

ACKNOWLEDGEMENTS

I would like to thank my committee chair, Dr. Akhil Datta-Gupta, co-chair, Dr. Michael J. King, and my committee members, Dr. Nobuo Morita and Dr. Yalchin Efendiev, for their guidance and support throughout the course of this research.

I would also like to express my sincere gratitude to Dr. Norio Arihara for his advising during my B.E. and M.E. programs at Waseda University in Japan and for his recommendation for the graduate study at Texas A&M University.

I also appreciate INPEX Corporation for their financial support and encouragement during the graduate study.

Thanks also go to my friends and colleagues and the department faculty and staff for making my time at Texas A&M University a great experience.

Finally, thanks to my parent, my wife and my daughter for their patience and love.

CONTRIBUTORS AND FUNDING SOURCES

Contributors

This work was supported by a dissertation committee consisting of Professor Akhil Datta-Gupta (advisor), Michael J. King and Nobuo Morita of the Department of Petroleum Engineering and Professor Yalchin Efendiev of the Department of Mathematics.

The Eikonal solvers used for this dissertation were developed by Jixiang Huang and Chen Li. The basic formulations for the FMM-based multi-phase and multi-component simulation were originally proposed by Yusuke Fujita. The data analyzed for Chapter II was provided by Anadarko Petroleum Corporation and the history matching was collaborated with Aditya Vyas. The fracture propagation simulation in Chapter IV was carried out by Tsubasa Onishi.

All other work conducted for the dissertation was completed by the student independently.

Funding Sources

Graduate study was supported by a fellowship from INPEX Corporation where the student has been working since April 2007.

TABLE OF CONTENTS

	Page
ABSTRACT	ii
DEDICATION	iv
ACKNOWLEDGEMENTS	v
CONTRIBUTORS AND FUNDING SOURCES	vi
TABLE OF CONTENTS	vii
LIST OF FIGURES	xi
LIST OF TABLES	xxi
CHAPTER I INTRODUCTION AND LITERATURE REVIEW	1
1.1 Introduction	1
1.2 Literature Review	4
1.2.1 Asymptotic Approach and Diffusive Time-of-Flight	4
1.2.2 Solution of Eikonal Equation: Fast Marching Method	7
1.2.3 Reservoir Simulation using Diffusive Time-of-Flight as 1-D Spatial Coordinate	8
1.3 Dissertation Outline	11
CHAPTER II EFFICIENT MODELING AND HISTORY MATCHING OF SHALE OIL RESERVOIRS USING THE FAST MARCHING METHOD	13
2.1 Chapter Summary	13
2.2 Background	14
2.3 Mathematical Formulation	17
2.3.1 Asymptotic Pressure Solution for Multi-phase System	17
2.3.2 Eikonal Equation for Multi-phase System	19
2.3.3 Coordinate Transformation from 3-D to 1-D along the DTOF	21
2.3.4 Dual-porosity Formulation	24
2.4 Implementation	27
2.4.1 Simulation Workflow	27
2.4.2 Discretization	29
2.4.3 Well Model	32

2.4.4 Calculation of V_p and $w(\tau)$ Function	33
2.4.5 Averaging Reservoir Properties	38
2.5 Validation	41
2.5.1 Single-phase Case—Homogeneous Reservoir	42
2.5.2 Multi-phase Case—Homogeneous Reservoir	48
2.5.3 Computation Time	52
2.5.4 Multi-phase Case—Unconventional Reservoirs	55
2.6 Comparison between Cell-center FMM and 27pt-stencil FMM	62
2.6.1 Accuracy, Stability and Convergence	62
2.6.2 CPU Time	65
2.6.3 Case Example That Requires 27pt-stencil FMM	66
2.7 Field Application: History Matching	69
2.7.1 Production Data	70
2.7.2 Base Case Model	71
2.7.3 Benchmarking with Commercial FD Simulator	74
2.7.4 Uncertain Parameters	76
2.7.5 Sensitivity Analysis	78
2.7.6 First Stage History Matching	79
2.7.7 Second Stage History Matching	84
2.7.8 Production Forecast	92
2.8 Limitations	94
2.8.1 Gas Liberation Case	94
2.8.2 Waterflooding Case	103
2.9 Conclusions	113

CHAPTER III OPTIMIZING CO₂ AND FIELD GAS INJECTION EOR IN UNCONVENTIONAL RESERVOIRS USING THE FAST MARCHING METHOD

115

3.1 Chapter Summary	115
3.2 Background	117
3.3 Mathematical Formulation	120
3.3.1 Dual-porosity Compositional Formulation	120
3.3.2 Phase Equilibrium Calculation	121
3.3.3 Phase Density, Compressibility and Viscosity	124
3.4 Validation using 3-D Homogeneous Case	125
3.4.1 Model Setting	126
3.4.2 CPU Time	127
3.5 Validation using CO ₂ Huff-n-Puff Example in Unconventional Reservoir	129
3.5.1 Model Setting	129
3.5.2 Base Case Simulation	133
3.5.3 CPU Time	136
3.5.4 Sensitivity Analysis	137
3.6 Field Scale Application	139

3.6.1 Model Setting	140
3.6.2 Fluid Composition and Phase Behavior	142
3.6.3 Primary Depletion	143
3.6.4 Huff-n-Puff: Base Case Simulation.....	144
3.6.5 Huff-n-Puff: Sensitivity Analysis.....	147
3.6.6 Optimizing Huff-n-Puff.....	147
3.7 Conclusions	152
 CHAPTER IV RAPID FIELD-SCALE WELL SPACING OPTIMIZATION IN TIGHT AND SHALE OIL RESERVOIRS USING THE FAST MARCHING METHOD	 154
4.1 Chapter Summary.....	154
4.2 Background	155
4.3 Methodology	157
4.3.1 Mathematical Formulation	157
4.3.2 Drainage Volume Partition.....	158
4.3.3 Simulation Workflow	159
4.4 Validation	161
4.4.1 Case Setting	161
4.4.2 Depletion by Parent Well Production.....	163
4.4.3 Performances after Infill Well Placement	164
4.4.4 CPU Time.....	168
4.5 Field-scale Application	168
4.5.1 Generating Fracture Geometry	169
4.5.2 Optimal Well Spacing	173
4.6 Conclusions	176
 CHAPTER V EXTENTION OF FMM-BASED MULTI-WELL SIMULATION TO CONSTANT RATE PRODUCTION SCENARIO	 178
5.1 Chapter Summary.....	178
5.2 Background	179
5.3 Methodology and Validation.....	182
5.3.1 FMM-based Flux Partition	183
5.3.2 FMM-based Flux Partition with Dynamic Update.....	188
5.3.3 Inter-partition Transmissibility.....	192
5.4 Extreme Rate Contrast	202
5.5 Application to Million-cell Model with Fractured Wells.....	203
5.5.1 Model Setting	204
5.5.2 Comparison of Simulation Results.....	205
5.6 Summary	209
 CHAPTER VI CONCLUSIONS AND RECOMMENDATIONS	 212

6.1 Conclusions	212
6.2 Recommendations and Future Work.....	215
NOMENCLATURE.....	217
REFERENCES.....	222
APPENDIX A COUPLING FMM-BASED SIMULATION WITH EXISTING RESERVOIR SIMULATOR	234
APPENDIX B FMM-BASED SIMULATION FOR RESERVOIRS WITH MULTIPLE ROCK TYPES ACROSS DTOF CONTOURS	237
APPENDIX C MAP-BACK 1-D SOLUTIONS ONTO ORIGINAL GRID BASED ON MASS CONSERVATION	249
APPENDIX D CALCULATING INTER-PARTITION TRANSMISSIBILITY: STEP-BY-STEP ILLUSTRATION	260

LIST OF FIGURES

	Page
Figure 1.1 Examples of ‘phase’ function or DTOF for vertical well in homogeneous reservoirs (left), horizontal well in heterogeneous reservoirs (middle) and multi-stage fractured well in heterogeneous reservoirs (right) (reprinted with permission from Iino and Datta-Gupta, 2018)	6
Figure 1.2 Analogy between radial coordinate in homogenous reservoir and DTOF as spatial coordinate (Zhang et al., 2016).....	9
Figure 2.1 Initial water saturation, diffusivity and DTOFs (modified from Fujita (2014)) (a) Initial water saturation, (b) water diffusivity, (c) oil diffusivity, (d) two-phase diffusivity, (e) water-phase DTOF, (f) oil-phase DTOF and (g) two-phase DTOF (reprinted with permission from Iino et al., 2017a).....	21
Figure 2.2 Illustration of Dual-porosity and Single-permeability system (reprinted with permission from Iino et al., 2017a).....	24
Figure 2.3 Flow chart of multi-phase 1-D simulation based on the FMM (reprinted with permission from Iino et al., 2017a).....	28
Figure 2.4 Schematics of the 1-D DTOF grid blocks. Subscripts i and $i+1/2$ denote the cell-center and cell-interface, respectively	31
Figure 2.5 Illustration of moving linear regression to evaluate variance of $w(\tau)$ function	35
Figure 2.6 $w(\tau)$ with different span size (top) and bias-variance trade-off for optimum span size selection (bottom). The number of 1-D grid blocks is 200. Black line in top three plots denotes the $w(\tau)$ function that is analytically calculated	36
Figure 2.7 Special treatment for well cells for pore volume calculation from 27pt-stencil FMM solution	37
Figure 2.8 Schematics of dual-porosity system	39
Figure 2.9 Illustration of calculating average fracture/ matrix transmissibility coefficient in 1-D DTOF domain	41
Figure 2.10 Log-log diagnostic plot for three validation cases	44

Figure 2.11 $w(\tau)$ function (line: analytical, symbol: numerical) for different numbers of 1-D grid blocks	46
Figure 2.12 Bottomhole pressure for constant rate drawdown (10 stb/day) for different numbers of 1-D grid blocks	47
Figure 2.13 RMS of $w(\tau)$ function for different numbers of 1-D grid blocks from cell-center FMM and smoothing.....	48
Figure 2.14 Relative permeability for 3-D homogeneous and multi-phase example.....	50
Figure 2.15 PVT data for 3-D homogeneous and multi-phase example	50
Figure 2.16 Calculated DTOF, drainage volume and $w(\tau)$ function for 3-D homogeneous and multi-phase example (reprinted with permission from Iino et al., 2017a)	51
Figure 2.17 Comparison between FMM (solid lines) and FDSim (symbols) for 3-D homogeneous and multi-phase example (reprinted with permission from Iino et al., 2017a).....	52
Figure 2.18 Comparison of CPU time (bottom) between commercial FDSim and FMM-based simulation and speed-up factor (top). Number of 1-D grid blocks and number of time steps are fixed to be 200 and 128, respectively (reprinted with permission from Iino et al., 2017a)	53
Figure 2.19 Comparison of CPU time of FMM-based simulation for different number of 1-D grid blocks.....	54
Figure 2.20 Comparison of CPU time between 3-D simulation and 1-D simulation in terms of simulation cell counts	55
Figure 2.21 Configuration of hydraulic fractures for 3D synthetic example (reprinted with permission from Iino et al., 2017a).....	57
Figure 2.22 Reservoir properties and initial water saturation for the fracture in unconventional reservoir example (reprinted with permission from Iino et al., 2017a)	58
Figure 2.23 Rock compaction curves for fracture in unconventional reservoir example (reprinted with permission from Iino et al., 2017a)	58
Figure 2.24 Relative permeability for 3-D homogeneous and multi-phase example.....	59

Figure 2.25 Calculated DTOF (left), drainage pore volume and $w(\tau)$ function (right) for unconventional reservoir example (reprinted with permission from Iino et al., 2017a).....	60
Figure 2.26 DTOF maps corresponding to each flow regime (a) through (f) in Figure 2.25 (reprinted with permission from Iino et al., 2017a)	60
Figure 2.27 Comparisons of simulation results between the FMM and commercial FD simulator for unconventional reservoir example (reprinted with permission from Iino et al., 2017a).....	61
Figure 2.28 $w(\tau)$ function from 27pt-stencil FMM.....	63
Figure 2.29 Bottomhole pressure for constant rate drawdown of 10 stb/day from FMM-based simulation with $w(\tau)$ function using 27pt-stencil FMM (2-D homogeneous reservoir)	63
Figure 2.30 Comparison of RMS of $w(\tau)$ function between 27pt-stencil FMM (blue triangle) and cell-center FMM with smoothing (red circle)	64
Figure 2.31 CPU time comparison for solving Eikonal equation between cell-center FMM (red) and 27pt-stencil FMM (blue).....	65
Figure 2.32 Single hydraulic fracture model in 2-D homogeneous reservoir and DTOF	66
Figure 2.33 Comparison of $w(\tau)$ functions from cell-center DTOF with smoothing (red) and 27pt-stencil FMM (blue) in 2-D homogeneous reservoir completed by single fracture	67
Figure 2.34 Bottomhole pressure for constant rate drawdown of 1 stb/ from cell-center DTOF with smoothing (red) and 27pt-stencil FMM (blue) in 2-D homogeneous reservoir completed by single fracture	68
Figure 2.35 Pore volume and $w(\tau)$ function from cell-center and 27pt-stencil FMM.....	69
Figure 2.36 Production data of 10-stage hydraulically fractured well in a shale oil reservoir: wellhead pressure and oil, gas and water rates (Top) and GOR and water cut (bottom) (reprinted with permission from Iino et al., 2017a)	70
Figure 2.37 Definition of regions for base case model (reprinted with permission from Iino et al., 2017a).....	71

Figure 2.38 Reservoir properties of the base case model for fracture (reprinted with permission from Iino et al., 2017a).....	72
Figure 2.39 Rock compaction curves for field application (reprinted with permission from Iino et al., 2017a).....	73
Figure 2.40 PVT data for field application	73
Figure 2.41 Relative permeability of matrix for field application	73
Figure 2.42 Calculated DTOF (left), drainage pore volume and $w(\tau)$ function (right) for unconventional reservoir example (reprinted with permission from Iino et al., 2017a).....	74
Figure 2.43 Comparison between FMM and commercial FD simulator for base case simulation. Blue solid line: FMM, red dashed line: FDSim, symbols: observed data (reprinted with permission from Iino et al., 2017a)	75
Figure 2.44 Setup of geometric parameters (left) and groups (right) for sensitivity study and history matching (reprinted with permission from Iino et al., 2017a)	77
Figure 2.45 Rock compaction table used for sensitivity study. Greater table number represents more severe transmissibility reduction (reprinted with permission from Iino et al., 2017a).....	78
Figure 2.46 Sensitivity analysis for history matching example (first stage)	79
Figure 2.47 Objective function versus generation number (first stage)	80
Figure 2.48 Parameter ranges of initial generation, top 30% realizations of firs stage.....	81
Figure 2.49 Comparisons between observed data and simulated cumulative production (first stage).....	83
Figure 2.50 Sensitivity analysis for history matching example (second stage)	84
Figure 2.51 Objective function versus generation number (first and second stages)	85
Figure 2.52 Comparisons between observed data and simulated well performances (second stage).....	86
Figure 2.53 Parameter distribution after second stage history matching	88

Figure 2.54 Distributions of parameter combinations before and after history matching	92
Figure 2.55 Production forecast using multiple history matched models	93
Figure 2.56 Uncertainty assessment of production forecast.....	93
Figure 2.57 Permeability distribution with three different level of heterogeneity.....	95
Figure 2.58 Gas-oil relative permeability for gas liberation case	96
Figure 2.59 Total mobility, total compressibility and diffusivity change as per pressure depletion and gas saturation increase	97
Figure 2.60 Comparisons of pressure and saturation at 5 days between FDSim and FMM-based simulation for gas liberation case	99
Figure 2.61 Comparisons of pressure and saturation at 100 days between FDSim and FMM-based simulation for gas liberation case	100
Figure 2.62 Workflow of FMM-based simulation incorporating DTOF update	101
Figure 2.63 Cross-plots of pressure (blue) and gas saturation (red) at 5 days between FDSim and FMM-based simulation with and without DTOF updates for gas liberation case	102
Figure 2.64 Cross-plots of pressure (blue) and gas saturation (red) at 100 days between FDSim and FMM-based simulation with and without DTOF updates for gas liberation case	103
Figure 2.65 Relative permeability for waterflooding case	104
Figure 2.66 Total compressibility, total mobility and diffusivity change versus water saturation for waterflooding case	105
Figure 2.67 Comparison of pressure (line) and saturation contours (color) at 5 days between FMM-based simulation and FDSim for waterflooding case	107
Figure 2.68 Cross-plots of grid block pressure and saturation at 5 days between FMM-based simulation (vertical axis) and FDSim (horizontal axis) for waterflooding case	108

Figure 2.69 Comparison of pressure (line) and saturation contours (color) at 100 days between FMM-based simulation and FDSim for waterflooding case	109
Figure 2.70 Cross plots of grid block pressure and saturation at 100 days between FMM-based simulation and FDSim for waterflooding case	110
Figure 2.71 Comparisons of pressures and saturations at 100 days between different frequencies of DTOF update for waterflooding case ($V_{dp} = 0.9$ & $M = 1$)	112
Figure 3.1 Comparisons between FMM-based (lines) and FDSim (symbols) for homogeneous case (reprinted with permission from Iino et al., 2017b)	127
Figure 3.2 CPU Time comparison (bottom) and speed-up factor (top) between FMM-based and FD simulations. Number of 1-D grid blocks and number of time steps are fixed to be 200 and 128, respectively (reprinted with permission from Iino et al., 2017b)	128
Figure 3.3 Comparison of speed-up factors between blackoil and compositional simulations	129
Figure 3.4 Geometry of multi-stage hydraulic fractures for CO2 Huff-n-Puff case (reprinted with permission from Iino and Datta-Gupta, 2018)	130
Figure 3.5 Geometry of multi-stage hydraulic fractures for CO2 Huff-n-Puff case (reprinted with permission from Iino and Datta-Gupta, 2018)	131
Figure 3.6 Relative permeability and rock compaction tables for CO2 Huff-n-Puff case (reprinted with permission from Iino and Datta-Gupta, 2018)	132
Figure 3.7 Comparison of FMM-based simulation with FDSim in primary depletion before Huff-n-Puff (reprinted with permission from Iino and Datta-Gupta, 2018)	133
Figure 3.8 Simulated well performance during CO2 Huff-n-Puff (line: FMM-based simulation, symbol: FDSim) (reprinted with permission from Iino and Datta-Gupta, 2018)	135
Figure 3.9 Breakdown of CPU time of FMM-based simulation for 1000day primary depletion plus 1000day CO2 Huff-n-Puff (reprinted with permission from Iino and Datta-Gupta, 2018)	137

Figure 3.10 Sensitivity of operational parameters for Huff-n-Puff on incremental recovery (reprinted with permission from Iino and Datta-Gupta, 2018)	138
Figure 3.11 Comparisons between FMM-based simulation and FDSim: incremental oil and CPU time for fifty combinations of operational parameters for Huff-n-Puff (reprinted with permission from Iino and Datta-Gupta, 2018)	139
Figure 3.12 Fracture properties and computed DTOF for field-scale example of Huff-n-Puff optimization (reprinted with permission from Iino and Datta-Gupta, 2018)	141
Figure 3.13 Slimtube and swelling test simulation (reprinted with permission from Iino and Datta-Gupta, 2018)	143
Figure 3.14 Simulated well performances for primary depletion for field-scale example of Huff-n-Puff optimization (reprinted with permission from Iino and Datta-Gupta, 2018).....	144
Figure 3.15 Simulated BHP and cumulative oil responses with base case parameters for field scale example of Huff-n-Puff optimization (reprinted with permission from Iino and Datta-Gupta, 2018).....	146
Figure 3.16 Footprint of injected gas at each cycle (Base case)	146
Figure 3.17 Sensitivity analysis on incremental recovery for field-scale example of Huff-n-Puff optimization (reprinted with permission from Iino and Datta-Gupta, 2018)	147
Figure 3.18 Incremental oil recovery vs. generation number during the optimization using Genetic Algorithm (reprinted with permission from Iino and Datta-Gupta, 2018)	148
Figure 3.19 Box plots of parameters before/ after Huff-n-Puff optimization (reprinted with permission from Iino and Datta-Gupta, 2018).....	149
Figure 3.20 Box plots of simulated incremental recovery, V.R.R. and solvent usage before/ after optimization	150
Figure 3.21 Footprint of injected gas at final cycle (worst, base and best cases).....	151
Figure 3.22 Average pressure during Huff-n-Puff (worst, base and best cases).....	151

Figure 4.1 Comparison of well drainage partition. Circles in the permeability field on the left represent the producers (Huang, 2017)	159
Figure 4.2 An illustration of drainage volume partition and 1-D simulation. Circles in the permeability field on the left represent the producers (reprinted with permission from Iino et al., 2018).....	160
Figure 4.3 Permeability of matrix and hydraulic fractures for infill validation case (reprinted with permission from Iino et al., 2018).....	162
Figure 4.4 Relative permeability for infill validation case (reprinted with permission from Iino et al., 2018)	163
Figure 4.5 Cumulative oil and gas production of parent well– comparison between FMM-based simulation (line) and FDSim (symbol) (reprinted with permission from Iino et al., 2018).....	164
Figure 4.6 Pressure profile after 1 year production by parent well– comparison between FMM-based simulation and FDSim (reprinted with permission from Iino et al., 2018)	164
Figure 4.7 Child well locations and drainage volume partition on the middle layer based on the ‘equal-tau’ for difference well spacing (reprinted with permission from Iino et al., 2018)	166
Figure 4.8 Comparison of cumulative oil production between FMM-based simulation and finite difference simulation (reprinted with permission from Iino et al., 2018)	167
Figure 4.9 Pressure profile after 1 year since the infill well was placed: FMM-based simulation (upper row) and FDSim (lower row) (reprinted with permission from Iino et al., 2018).....	167
Figure 4.10 Complex fracture modeling workflow for infill development (reprinted with permission from Iino et al., 2018).....	169
Figure 4.11 Permeability of field-scale example for reservoir simulation with different infill well spacing (top view of middle layer) (reprinted with permission from Iino et al., 2018)	173
Figure 4.12 Cumulative oil production and incremental recovery for field-scale example (reprinted with permission from Iino et al., 2018)	174

Figure 4.13 Pressure maps of the middle layer: (a) just before the child well placement at 1 year and (b)-(e) at the end of simulation at 2 years (reprinted with permission from Iino et al., 2018).....	175
Figure 5.1 Dynamic change in pressure (top) and drainage volume partition based on streamlines (bottom) by depletion from three wells controlled by constant rates of 25, 50 and 100 stb/day.....	181
Figure 5.2 Comparisons of simulated bottomhole pressures between FDSim (symbol) and FMM-based simulation (line) for three wells producing at different constant rates.....	182
Figure 5.3 Drainage volume partition at each time step from FMM-based flux calculation (top) and FDSim (bottom). Production rate = 25, 50 and 100 stb/day.....	186
Figure 5.4 Comparison of simulated bottomhole pressure between FDSim (symbol) and FMM-based simulation (line) using flux-based drainage volume partition at different time steps	188
Figure 5.5 Flowchart of FMM-based multi-well simulation using flux-based drainage volume partition with dynamic update	190
Figure 5.6 Comparison of bottomhole pressure between FDSim (symbol) and FMM-based simulation (line) with dynamic update of drainage volume. Drainage volume partition was updated with different frequency denoted by black diamonds	191
Figure 5.7 Percentage of drainage volume associated with each well from FMM-based flux partition.....	192
Figure 5.8 FMM-based multi-well simulation workflow incorporating inter-partition transmissibility	194
Figure 5.9 Illustration of DTOF-contour where inter-partition transmissibility is computed.....	195
Figure 5.10 Workflow to calculate inter-partition transmissibility using the FMM.....	197
Figure 5.11 Inter-partition transmissibility for 2-D homogeneous example with three wells. Different numbers of DTOF-contours are examined.....	198

Figure 5.12 Example of grid block set-up for FMM-based simulation incorporating inter-partition transmissibility	199
Figure 5.13 Comparison of bottomhole pressure between FDSim (symbol) and FMM-based simulation using inter-partition transmissibility (line).....	201
Figure 5.14 Comparisons of log-log diagnostic plot (symbol: FDSim, dashed line: FMM with equal-tau, solid line: FMM with inter-partition transmissibility)	201
Figure 5.15 Comparison of simulated BHP between FDSim (symbol) and FMM-based simulation (line) with four different methods. Production rate = 10, 10 and 100 stb/day	203
Figure 5.16 Geometry of hydraulic fractures for four fractured wells case	204
Figure 5.17 Relative permeability and rock compaction for four fractured wells case	205
Figure 5.18 Comparison of BHP responses for four fractured wells case	206
Figure 5.19 Equal-tau and flux-based partition for four fractured wells case.....	207
Figure 5.20 Inter-partition transmissibility for four fractured wells case. Different numbers of DTOF-contours are examined.....	208

LIST OF TABLES

	Page
Table 2.1 Constant for transmissibility calculation.....	30
Table 2.2 Averaging method for reservoir properties for FMM-based simulation	38
Table 2.3 Single-phase validation cases.....	42
Table 2.4 Simulation input for 3-D homogeneous and multi-phase example (reprinted with permission from Iino et al., 2017a).....	49
Table 2.5 Simulation input for unconventional reservoir example (reprinted with permission from Iino et al., 2017a).....	57
Table 2.6 Parameter uncertainties for sensitivity and history matching (reprinted with permission from Iino et al., 2017a).....	77
Table 2.7 Input data for gas liberation case	95
Table 3.1 Initial composition for 3-D homogeneous compositional case (reprinted with permission from Iino et al., 2017b).....	126
Table 3.2 Reservoir properties and initial condition for CO ₂ Huff-n-Puff case (reprinted with permission from Iino and Datta-Gupta, 2018).....	130
Table 3.3 Initial composition and molecular weight for CO ₂ Huff-n-Puff case (reprinted with permission from Iino and Datta-Gupta, 2018).....	132
Table 3.4 Computational efficiency of FMM-based compositional simulation for CO ₂ Huff-n-Puff simulation	136
Table 3.5 Ranges of operational parameters of Huff-n-Puff for 1,000 days (reprinted with permission from Iino and Datta-Gupta, 2018).....	138
Table 3.6 Reservoir and hydraulic fracture properties for field-scale example of Huff-n-Puff optimization (reprinted with permission from Iino and Datta-Gupta, 2018)	141
Table 3.7 Composition of reservoir fluid and solvent for field-scale example of Huff-n-Puff optimization (reprinted with permission from Iino and Datta-Gupta, 2018)	142

Table 3.8 Parameter ranges, objective function and simulation setting for Huff-n-Puff optimization (reprinted with permission from Iino and Datta-Gupta, 2018)	145
Table 4.1 Reservoir, fluid and rock property for infill validation case (reprinted with permission from Iino et al., 2018).....	162
Table 4.2 Simulation setting for additional depletion by parent and child wells (reprinted with permission from Iino et al., 2018)	165
Table 4.3 Comparison of grid block number and CPU time between FDSim and FMM-based simulation	168
Table 4.4 Pumping schedule for fracturing simulation (reprinted with permission from Iino et al., 2018)	170
Table 4.5 Statistical parameters used to generate discrete natural fractures (reprinted with permission from Iino et al., 2018).....	170
Table 4.6 Reservoir, fluid and rock properties for field-scale application of infill spacing optimization (reprinted with permission from Iino et al., 2018)	172
Table 4.7 Comparison of grid block number and CPU time between FDSim and FMM for field-scale application	176
Table 5.1 Input data for four fractured wells case.....	205

CHAPTER I

INTRODUCTION AND LITERATURE REVIEW*

1.1 Introduction

Unconventional reservoirs contribute to a significant share of the energy supply in the US and are predicted to keep increasing their production in the next 25 years (EIA 2016). The economical exploitation from such ultra-low permeability formations has been achieved by the technology breakthrough of extended-reach horizontal drilling and multi-stage hydraulic fracturing (Alexander et al. 2011; King 2010), leading to the complex fracture network that interacts with pre-existing/ induced fractures and reservoir rock. Furthermore, the fluid transport modelling used in conventional reservoirs has been found often inadequate for unconventional reservoirs due to the complicated underlying physics such as gas desorption, Knudsen diffusion, phase behavior in nano-scale pores and stress-dependent fracture conductivity (Najabaei et al. 2013; Cho et al. 2013; Wang et al., 2015). Thus, the robust performance assessment of the unconventional reservoirs remains a

* Material adapted with permission from “Efficient Modeling and History Matching of Shale Oil Reservoirs Using the Fast Marching Method: Field Application and Validation” by Iino et al. 2017a: Paper SPE-185719-MS Presented at the SPE Western Regional Meeting held in Bakersfield, California, USA, 23-27 April 2017. Copyright 2017 Society of Petroleum Engineers. Further reproduction is prohibited without permission.

* Material adapted with permission from “Optimizing CO₂ and Field Gas Injection EOR in Unconventional Reservoirs Using the Fast Marching Method” by Iino and Datta-Gupta 2018: Paper SPE-190304-MS Presented at SPE IOR Conference held in Tulsa, Oklahoma, USA, 14-18 April 2018. Copyright 2018, Society of Petroleum Engineers. Further reproduction is prohibited without permission.

technical challenge as it requires an integrated modelling of a hydraulic fracture network, reservoir heterogeneity and relevant physics.

For performance assessment and prediction of unconventional reservoirs, empirical and analytical techniques have been widely used including decline curve analysis (Arps, 1945; Fetkovich 1980; Ilk et al. 2008; Valko 2009; Duong 2011) and pressure or rate transient analysis (Clarkson and Qanbari, 2015; Tabatabaie and Pooladi-Darvish, 2016). However, such techniques are based on the absence or simplification of underlying physics such as reservoir heterogeneity, complex fracture geometry and multi-phase and compositional effects, which may often lead to an unreliable or erroneous prediction. Numerical simulation is a robust and versatile tool to evaluate the performance of multi-stage hydraulically fractured wells in unconventional reservoirs (Wang et al., 2015). The advantage over the empirical and analytical approaches is the capability to incorporate the complex underlying physics (Du et al., 2009; Cipolla et al., 2010a, 2010b and 2011; Novlesky et al., 2011; Diaz de Souza et al., 2012; Kam et al., 2015). The challenge is the substantial computational time required that can often be a bottleneck for the practical application of the numerical simulation especially when high resolution models are involved to accurately describe the hydraulic fracture geometry and flow in the vicinity of the hydraulic fractures under multi-phase and compositional effects.

Thus, there is an increasing need for a novel approach that offers high computational efficiency as well as the flexibility to incorporate the relevant physics. Recently, the Fast Marching Method (FMM)-based simulation has been proposed, which is a bridge between the two approaches discussed above: the analytical approach and full

3-D numerical simulation (Datta-Gupta et al., 2011; Xie et al., 2015a and 2015b; Zhang et al., 2016). The FMM-based simulation is based on a high frequency asymptotic solution of the diffusivity equation in heterogeneous and fractured reservoirs. The high frequency solution leads to the Eikonal equation which is solved for a ‘Diffusive Time-of-Flight’ (DTOF) that governs the propagation of the ‘pressure front’ in the reservoir (Vasco et al., 2000; Kulkarni et al., 2001). The FMM is an efficient and robust algorithm to solve the Eikonal equation for the DTOF in a matter of seconds or minutes for million-scale high resolution models (Sethian, 1996). The key concept of the FMM-based simulation is to utilize the DTOF as a 1-D spatial coordinate which embeds geological heterogeneity in original 3-D space, leading to a rapid 1-D flow simulation that is equivalent to a 3-D flow simulation (Zhang et al., 2016).

In this research, we develop a rapid and robust FMM-based simulator for multi-phase and compositional flow in unconventional reservoirs. Most recently, an increasing interest has emerged in technologies and strategies to improve the recovery from unconventional reservoirs including gas injection EOR and infill well placement (Schmidt and Sekar, 2014; Jacobs, 2015a and 2015b; Todd and Evans, 2016; Alfarge 2017a; Rassenfos, 2017; Ranjan, 2015; Marongiu-Porcu et al., 2015; Miller et al., 2016; Rafiee and Grover, 2017; Lindsay et al., 2018). We also propose and validate efficient workflow using the FMM-based simulation not only for history matching but also for optimization of gas injection EOR and infill well spacing in unconventional reservoirs.

1.2 Literature Review

In the following sections, we review literatures on the asymptotic approach, the Fast Marching Method and the FMM-based reservoir simulation.

1.2.1 Asymptotic Approach and Diffusive Time-of-Flight

In petroleum engineering, diffusion, multi-phase displacement and solute transport problems are common physical processes of interest to describe reservoir and fluid dynamics. At a first glance, it appears that there is little in common with wave-like propagation such as seismology and geometrical optics; however, analogies between such physical processes and wave propagation have been extensively explored to date.

Several works in literature explicitly transform diffusion equations into wave equations. Wilson (1983) presented a transformation of inverse problem in pressure transient into an inverse scattering problem. Pierce (1986) developed a mathematical formulations for inverting coefficients in the diffusivity equation (e.g. porosity and permeability), which can be considered as a transformation to the corresponding wave problem. He concluded based on the stability analysis that the inversion might be unstable for noisy data. Kuchuk and Habashy (1992) developed analytical solutions for pressure in laterally composite reservoirs by transforming the diffusion equation into the 1-D Helmholtz equation that is solved with reflection-transmission method. Oliver (1994) showed that the wave transform proposed by Bragg and Dettman (1968) resulted in simplified solutions to the problem of pressure transient testing in linear composite

reservoirs. The identified challenge was instability in the inverse wave transformation of measured pressure data into wave-like signals.

More importantly, the asymptotic approach, which has been widely used in other fields such as electromagnetic and seismology (Kline and Kay, 1965; Cerveny et al., 1978), has also proven to be a powerful and versatile tool for modeling fluid flow in porous media. One typical form of asymptotic solutions for the diffusion problem can be written as follows (Virieux et al, 1994; Vasco et al., 2000):

$$P(\mathbf{x}, \omega) = e^{-\sqrt{-i\omega}\tau(\mathbf{x})} \sum_{n=0}^{\infty} \frac{A_n(\mathbf{x})}{(\sqrt{-i\omega})^n}, \quad (1.1)$$

where P : pressure in frequency domain, ω : frequency, A_n : amplitude terms associated with the various orders of $(-i\omega)^{-1/2}$ and $\tau(\mathbf{x})$: phase function which was named ‘Diffusive Time-of-Flight’ (DTOF) by Kulkarni et al. (2001). The asymptotic solution consists of the summation of infinite numbers of $A_n(\mathbf{x})/(\sqrt{-i\omega})^n$, however, it is known that only the first few terms have physical importance. The high frequency limit that represents the rapidly varying component in pressure leads to the Eikonal equation that governs the ‘phase’ function of the propagating wave (Vasco et al., 2000):

$$\nabla \tau(\mathbf{x}) = \frac{1}{\sqrt{\alpha(\mathbf{x})}}, \quad (1.2)$$

where α is diffusivity. Obviously, the R.H.S. of Eq. (1.2) physically indicates the slowness of the propagating pressure wave. Thus, depending on the physical processes that we describe and on the definition of the asymptotic solution (1.1), it may take different forms. For pressure diffusion, Eq. (1.2) is a generalized form of ‘radius of investigation’ proposed

by Lee (1982) to the heterogeneous reservoirs and arbitrary well completions as illustrated in **Figure 1.1** (Datta-Gupta et al., 2011; Iino and Datta-Gupta, 2018).

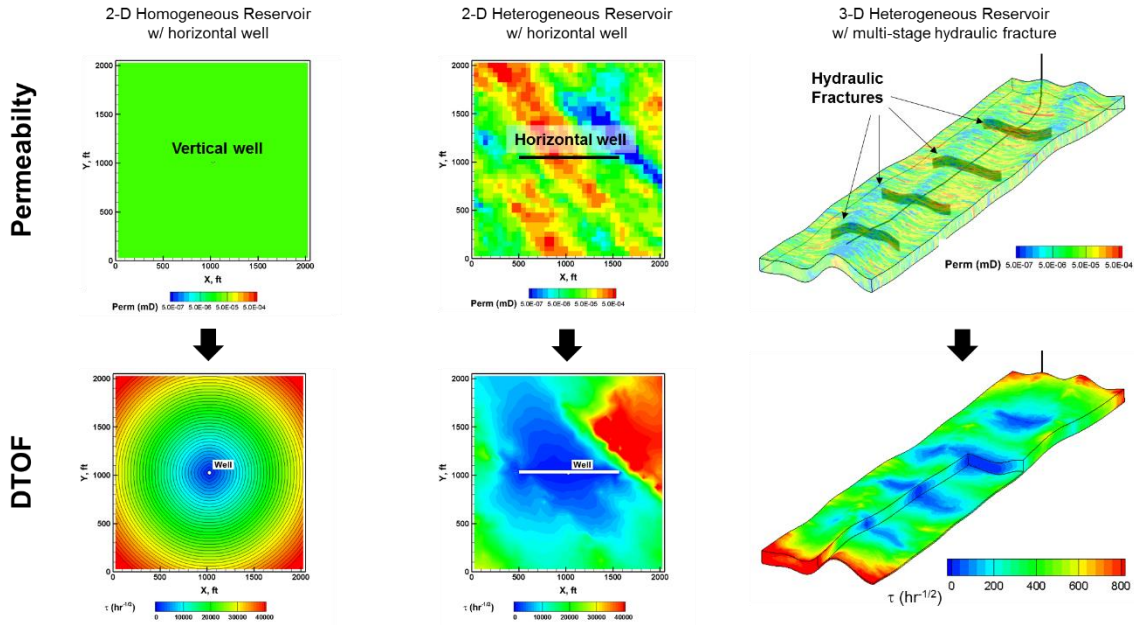


Figure 1.1 Examples of ‘phase’ function or DTOF for vertical well in homogeneous reservoirs (left), horizontal well in heterogeneous reservoirs (middle) and multi-stage fractured well in heterogeneous reservoirs (right) (reprinted with permission from Iino and Datta-Gupta, 2018)

The early applications of the asymptotic solutions to modeling fluid flow in porous media were often developed in conjunction with the method of characteristics, which involves ray tracing. Smith (1981) modeled contaminant convection and dispersion for the high Peclet-number laminar flow along the ray paths for transmission and reflection of concentration. Chapman et al. (1999) analyzed heat convection and diffusion with the existence of linear or circular obstacles using ray paths. Vasco and Datta-Gupta (1999)

proposed an efficient inversion approach that analytically computes tracer concentration sensitivity with respect to porosity, permeability and pressure gradient along ray paths. This inversion approach has been further extended to diffusion and two-phase displacement problems (Vasco et al., 2000; Vasco and Datta-Gupta, 2001; Vasco and Finsterle, 2004; Vasco 2008; Vasco 2009; Vasco 2011; Vasco and Datta-Gupta, 2016). It has also been proven that convective streamlines can be alternatively utilized for the sensitivity computation instead of ray trajectories (Kulkarni et al., 2001; He et al., 2004).

1.2.2 Solution of Eikonal Equation: Fast Marching Method

As stated in the previous section, one of the major solution techniques of the Eikonal equation for phase function is the method of characteristics that involves ray tracing (Courant and Hilbert, 1953; Cervený et al., 1978; Um and Thurber, 1987). However, Vidale (1988) pointed out that there have been several difficulties recognized in the ray tracing approach: (1) non-unique ray paths that connect two points of interest if slowness strongly varies in space, (2) expensive computational costs to trace a large number of ray paths and (3) potential failure to find global minimum travel time in shadow zone.

An alternative approach is a front tracking based on the finite difference approximation where no explicit ray trajectories are constructed. Vidale (1988 and 1990) proposed a finite difference scheme, which sequentially solves the local Eikonal equation for the phase function as tracking the wave front propagating outwards from sources. It successfully provided orders of magnitude faster computation compared to ray tracing,

however, the instability issue arose. Following his work, much effort has been devoted to improve the stability of the finite difference scheme (Van Trier and Symes, 1991; Schneider 1995).

To tackle these challenges, a fast, accurate and unconditionally stable algorithm to solve 3-D Eikonal equation named ‘Fast Marching Method’ (FMM) was proposed (Sethian, 1996; Sethian, 1999; Sethian and Popovici, 1999). Analogous to the Dijkstra’s method (Dijkstra, 1959), the FMM is a one-pass algorithm but tracks a curvature or surface of the wave front rather than tracking only the single shortest path. The phase function will be solved from sources in an orderly one-pass fashion from smaller values of phase to larger values, leading to significant computational efficiency. The gradient of phase function in Eq. (1.2) is approximated by the entropy-satisfying upwind finite difference, and the accuracy of the solution depends on the number of stencils to be used for gradient calculations (Hassouna and Frag, 2007). To date, applicability of the FMM has been widely extended to the anisotropic slowness, multiple arrivals, corner point grids and unstructured grids, etc. (Sethian, 2002; Zhang et al., 2013; Yang et al., 2017a and 2017b).

1.2.3 Reservoir Simulation using Diffusive Time-of-Flight as 1-D Spatial Coordinate

As stated above, the application of asymptotic solutions and phase function to reservoir modeling and characterization had been mainly studied in conjunction with either ray paths or convective streamlines. In the last decade, a novel approach of reservoir simulation and characterization using the FMM and resulting DTOF has been developed and proposed. Analogous to the streamline simulation (Datta-Gupta and King, 2007) but

without any necessity of explicit trajectories, the key idea is to utilize the DTOF as the 1-D spatial coordinate embedding the reservoir heterogeneity to transform the 3-D problem into the equivalent 1-D problem. The approach is visually intuitive, in-between analytical and numerical methods, and computationally efficient.

Datta-Gupta et al. (2011) presented a drainage volume propagation from the multi-stage fractured well in heterogeneous unconventional reservoirs using the DTOF obtained from the FMM. Xie et al. (2015a and 2015b) developed an approximated pressure solution along the 1-D DTOF coordinate. Their approach consists of two decoupled steps: (1) computing the DTOF for entire reservoir domain by the FMM and generate correlation between drainage pore volume and physical time and (2) calculating pressures by the geometric approximation along the DTOF. Zhang et al. (2016) proposed a novel approach of rapid numerical simulation using the DTOF contours as 1-D grid blocks. **Figure 1.2** illustrates the analogy between the radial coordinate in homogeneous reservoirs and the DTOF as a spatial coordinate in heterogeneous reservoirs.

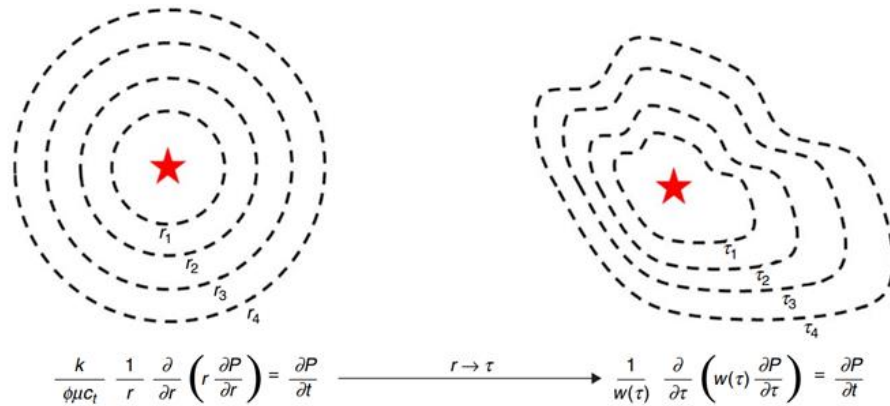


Figure 1.2 Analogy between radial coordinate in homogenous reservoir and DTOF as spatial coordinate (Zhang et al., 2016)

For homogeneous reservoirs (Figure 1.2 left), pressure will propagate radially from the well (denoted by red star) and the radial diffusivity equation can be formulated as follows:

$$\frac{k}{\phi\mu c_i} \frac{1}{2\pi r} \frac{\partial}{\partial r} \left(2\pi r \frac{\partial p}{\partial r} \right) = \frac{\partial p}{\partial t}, \quad (1.3)$$

where viscosity and compressibility are assumed to be constant. On the other hand for heterogeneous reservoirs (Figure 1.2 left), the DTOF contours can be regarded as a ‘twisted’ radial coordinate and the diffusion equation can be formulated along the DTOF (Zhang et al., 2016):

$$\frac{1}{w(\tau)} \frac{\partial}{\partial \tau} \left(w(\tau) \frac{\partial p}{\partial \tau} \right) = \frac{\partial p}{\partial t}, \quad (1.4)$$

King et al. (2016) and Wang (2018) discussed validity to use the DTOF as a 1-D spatial coordinate for pressure calculation. In Eq. (1.4), $w(\tau)$ is defined as the derivative of drainage pore volume with respect to the DTOF:

$$w(\tau) = \frac{dV_p(\tau)}{d\tau}. \quad (1.5)$$

Comparing Eq. (1.4) with Eq. (1.3) indicates that $w(\tau)$ function physically represents a surface area of propagating pressure front. In this research, we focus on $w(\tau)$ function generated from the DTOF solutions using geological/ reservoir models. However, it can also be obtained by inverting the production data, which provides insight and interpretation on the hydraulic fracture properties and flow regime identification (Yang et al., 2015 and 2016; Xue et al, 2016).

Fujita et al. (2016) further extended the DTOF-based 1-D simulation to incorporate the complex flow physics in nano-porous shale gas such as gas adsorption, Knudsen diffusion and triple-continua system. Cui et al. (2016) and Zhang and Zhu (2017) applied the FMM-based approach for flow and temperature modeling of the multi-stage hydraulically fractured well. Yang et al. (2017a and 2017b) presented a DTOF-based 1-D simulation for unstructured grids that are typically involved to describe the complicated hydraulic fracture geometry in unconventional reservoirs. Extension to the multi-phase and multi-component flow was proposed by Fujita (2014).

1.3 Dissertation Outline

This research mainly focuses on development and validation of efficient workflow for history matching and optimization for unconventional reservoirs using the FMM-based simulation. The rest of this dissertation is organized by the following three major chapters and conclusions. The specific objectives of each chapter are outlined as follows:

In Chapter II, we develop and validate the FMM-based blackoil simulation for the multi-phase flow in unconventional reservoirs. We also present the field history matching example of Eagle Ford Shale to demonstrate the efficacy and utility of history matching workflow coupled with the FMM-based simulator, leading to better understanding on uncertainties in estimations of reservoir and fracture properties as well as production forecast.

In Chapter III, we further extend the FMM-based simulation to the multi-component compositional simulation. We propose a robust optimization workflow for gas

injection EOR in unconventional reservoirs. Use of the rapid FMM-based simulation enables a large number of Huff-n-Puff simulations with a field-scale reservoir model in a practical timeframe, which also provides us with comprehensive understanding on how each operational parameter influence the displacement and recovery processes.

In Chapter IV, we extend the FMM-based simulation to multiple well scenario under the bottomhole pressure constraints, aiming at the optimization of infill well spacing using the high resolution reservoir model. The computational efficiency of our approach enables extensive simulation runs to determine the point of diminishing return for additional well placement to obtain the optimal well spacing. We demonstrate that the FMM-based simulation can be incorporated with integrated workflow of infill well modeling in conjunction with simulations of the fracture propagation.

In Chapter V, we further extend the FMM-based multi-well simulation to the scenario of constant rate production where the drainage volume partition associated with each well dynamically changes over time. We propose and validate new methodologies to appropriately model such dynamic partition changes.

CHAPTER II

EFFICIENT MODELING AND HISTORY MATCHING OF SHALE OIL RESERVOIRS USING THE FAST MARCHING METHOD[†]

2.1 Chapter Summary

In this chapter, we develop and demonstrate a novel Fast Marching Method (FMM)-based multi-phase simulation for a rapid field-scale modeling of unconventional reservoirs.

Modeling of unconventional reservoirs requires accurate characterization of complex flow mechanisms in multi-continua because of the interactions between reservoir rocks, microfractures and hydraulic fractures. It is also essential to account for the complicated geometry of well completion, the reservoir heterogeneity and multi-phase flow effects. Currently, such multi-phase numerical simulation for multi-continua reservoirs needs substantial computational time that hinders efficient history matching and uncertainty analysis. In this chapter, we propose an efficient approach for field scale application and performance assessment of shale reservoirs using rapid multi-phase simulation with the FMM.

The key idea of the reservoir simulation using the FMM is to recast the 3-D flow equation into 1-D equation along the ‘diffusive time of flight’ (DTOF) coordinate, which

[†] Material adapted with permission from “Efficient Modeling and History Matching of Shale Oil Reservoirs Using the Fast Marching Method: Field Application and Validation” by Iino et al. 2017a: Paper SPE-185719-MS Presented at the SPE Western Regional Meeting held in Bakersfield, California, USA, 23-27 April 2017. Copyright 2017 Society of Petroleum Engineers. Further reproduction is prohibited without permission.

embeds the 3-D spatial heterogeneity. The DTOF is a representation of the travel time of pressure propagation in the reservoir. The pressure propagation is governed by the Eikonal equation which can be solved efficiently using the FMM. The 1-D formulation leads to orders of magnitude faster computation than the 3-D finite difference simulation. The use of FMM-based simulation also enables systematic history matching and uncertainty analysis using population-based techniques that require substantial simulation runs.

We first validate the accuracy and computational efficiency of the FMM-based multi-phase simulation using synthetic reservoir models and comparison with a commercial finite-difference simulator. Next, we apply our proposed approach to a field example in Texas for a multi-stage hydraulically fractured horizontal well. The 3-D heterogeneous reservoir model was built and history matched for oil, gas and water production using the Genetic Algorithm with the FMM-based flow simulation. Multiple history-matched models were obtained to examine uncertainties in the production forecast associated with respect to the properties related to hydraulic fractures, microfractures and the matrix.

2.2 Background

Unconventional reservoirs contribute to a significant share of the energy supply in the US and are predicted to keep increasing their production in the next 25 years (EIA 2016). The economical exploitation from such ultra-low permeability formations has been achieved by the technology breakthrough of extended-reach horizontal drilling and multi-stage hydraulic fracturing (Alexander et al. 2011; King 2010), leading to the complex

fracture network that interacts with pre-existing/ induced fractures and reservoir rock. Furthermore, the fluid transport modelling used in conventional reservoirs has been found often inadequate for unconventional reservoirs due to the complicated underlying physics such as gas desorption, Knudsen diffusion, phase behavior in nano-scale pores and stress-dependent fracture conductivity (Najabaei et al. 2013; Cho et al. 2013; Wang 2015). Thus, robust performance assessment of the unconventional reservoirs remains a technical challenge as it requires an integrated modelling of a hydraulic fracture network, reservoir heterogeneity and relevant physics.

In the current industrial practice, various empirical and analytical techniques have been widely used to predict oil and gas production from unconventional reservoirs because of their simplicity. The commonly used approach among empirical methods is decline curve analysis. On the basis of the well-known Arps' decline curve model, many researchers have developed empirical formulations to fit the time-rate history observed in unconventional reservoirs (Arps, 1945; Fetkovich 1980; Duong 2011; Valko 2009; Ilk et al. 2008). However, the reliability of the decline curve analysis depends on the quantity and quality of the available production data and may result in erroneous prediction of future performance due to the absence of underlying physical theory. On the other hand, analytical methods such as pressure transient analysis (PTA) and rate transient analysis (RTA) are based on the physical theory described by the diffusivity equation. In these approaches, the parameters in the well and reservoir models will be calibrated such that the model replicates the observed rate/ pressure history. However, the conventional PTA and RTA assumes single phase, homogenous reservoir properties, simple geometries of

reservoir boundary and planar hydraulic fractures. Although recent studies have incorporated the multi-phase effects (Clarkson and Qanbari 2015; Tabatabaie and Pooladi-Darvish 2016), it still requires the assumption of homogeneous reservoir properties and simple planar geometry for the hydraulic fractures. In unconventional reservoirs, there is significant impact on the performance prediction due to the reservoir heterogeneity and complex geometry and network of multi-stage hydraulic fractures (Kam et al. 2015; Cipolla et al. 2010a; Cipolla et al. 2011).

Numerical simulation is also widely used to evaluate the performance of multi-stage hydraulically fractured wells in unconventional reservoirs (Wang et al. 2015). The advantage over the empirical and analytical approaches is the capability of incorporating complex underlying physics. Several recent studies have used reservoir simulation to model the geometry of hydraulic fractures, stress-dependent reservoir properties, reservoir heterogeneity and multi-phase effect (Cipolla et al. 2010b; Diaz de Souza et al. 2012; Novlesky et al. 2011; Du et al. 2009). However, the substantial computational time required is often a bottleneck for the practical application of the numerical simulation especially when high resolution models are involved to accurately describe the hydraulic fracture geometry, flow in the vicinity of the hydraulic fractures, reservoir heterogeneity and multiple continua. Thus, there is an increasing need for a novel approach that offers high computational efficiency as well as the flexibility to incorporate the relevant physics.

In this chapter, the FMM-based 1-D simulation was extended to the three-phase flow problems in unconventional reservoirs with reservoir heterogeneity and multi-stage hydraulically fractured well. First, we will briefly describe the background of the FMM

and the 1-D simulation along the DTOF. Then we develop the 1-D mathematical formulation that accounts for the multi-phase flow. Synthetic examples will be presented to illustrate the validity and the computational efficiency of our proposed approach by comparison with the commercial finite difference simulator (FDSim). Finally, the field application demonstrates the power and utility of our proposed approach for efficient modeling and history matching of a multi-stage hydraulically fractured horizontal well in a shale oil reservoir.

2.3 Mathematical Formulation

In the previous chapter, we reviewed the asymptotic approach that leads to the Eikonal equation for the single-phase system. As discussed by Fujita (2014), we can extend this approach to the multi-phase system.

2.3.1 Asymptotic Pressure Solution for Multi-phase System

In the absence of gravity, capillarity and permeability anisotropy, the general mass balance equation for phase- j can be written as:

$$\frac{\partial}{\partial t}(\phi \rho_j S_j) + \nabla \cdot (\rho_j \mathbf{u}_j) = 0, \quad (2.1)$$

where ϕ : porosity, ρ : density, S : saturation and u : Darcy velocity, respectively. The Darcy velocity is defined as a product of phase effective mobility and pressure gradient:

$$\mathbf{u}_j = -\frac{kk_{rj}}{\mu_j} \nabla p, \quad (2.2)$$

where k_r : relative permeability and μ : viscosity. By substituting Eq. (2.2) into Eq. (2.1), we obtain the mass balance equation with the following form:

$$\frac{\partial}{\partial t}(\phi \rho_j S_j) - \nabla(\rho_j k \lambda_j) \cdot \nabla p - (\rho_j k \lambda_j) \cdot \nabla^2 p = 0, \quad (2.3)$$

where λ_j is the phase mobility k_{rj}/μ_j . By introducing the compressibility c_r and c_j for rock and fluid, respectively, Eq. (2.3) can be further rearranged as:

$$\phi S_j (c_r + c_j) \frac{\partial p}{\partial t} + \phi \frac{\partial S_j}{\partial t} - \frac{1}{\rho_j} \nabla(\rho_j k \lambda_j) \cdot \nabla p - (k \lambda_j) \cdot \nabla^2 p = 0. \quad (2.4)$$

Summing up Eq. (2.4) for three phases yields:

$$\phi c_t \frac{\partial p}{\partial t} - \sum_j^{o,g,w} \left[\frac{1}{\rho_j} \nabla(k \rho_j \lambda_j) \right] \cdot \nabla p - k \lambda_t \cdot \nabla^2 p = 0. \quad (2.5)$$

By assuming that $(\nabla p)^2 \approx 0$, the product of $\nabla \rho$ and ∇p will vanishes. Eq. (2.5) can be further rearranged as:

$$\phi c_t \frac{\partial p}{\partial t} - \nabla(k \lambda_t) \cdot \nabla p - k \lambda_t \cdot \nabla^2 p = 0, \quad (2.6)$$

where λ_t is the total mobility that is a summation of mobility for three phases. Now we apply the Fourier transformation to Eq. (2.6) and express the pressure in the frequency domain:

$$\phi c_t (-i\omega) \tilde{p}(\mathbf{x}, \omega) - \nabla(k \lambda_t) \cdot \nabla \tilde{p}(\mathbf{x}, \omega) - k \lambda_t \cdot \nabla^2 \tilde{p}(\mathbf{x}, \omega) = 0, \quad (2.7)$$

where i , ω and \mathbf{x} represent the imaginary unit, frequency and spatial location, respectively.

With the same way for the single-phase case (Virieux et al, 1994; Vasco et al., 2000), the asymptotic solution for Eq. (2.7) is:

$$\tilde{p}(\mathbf{x}, \omega) = \exp\left[-\sqrt{-i\omega}\tau(\mathbf{x})\right] \times \sum_{n=0}^{\infty} \frac{A_n(\mathbf{x})}{\left(\sqrt{-i\omega}\right)^n}. \quad (2.8)$$

The infinite series solution (2.8) was inspired from the Bessel's solution for the radial diffusion problem. A_n are real functions relating to the amplitude of pressure wave, and τ is the phase function which we call the Diffusive Time-of-Flight (DTOF). Note that the DTOF has the dimension of square root of time. Substituting the asymptotic solution (2.8) into Eq. (2.7) yields:

$$\begin{aligned} & -(i\omega)\left[\lambda_t k \nabla \tau \cdot \nabla \tau - \phi c_t\right] \sum_{n=0}^{\infty} \frac{A_n}{\sqrt{-i\omega}^n} \\ & -(\sqrt{-i\omega}) \left[\nabla \cdot (\lambda_t k \nabla \tau) \sum_{n=0}^{\infty} \frac{A_n}{\sqrt{-i\omega}^n} + 2\lambda_t k \sum_{n=0}^{\infty} \frac{\nabla \tau \cdot \nabla A_n}{\sqrt{-i\omega}^n} \right] \\ & + \sum_{n=0}^{\infty} \frac{\nabla \cdot (\lambda_t k \nabla A_n)}{\sqrt{-i\omega}^n} = 0. \end{aligned} \quad (2.9)$$

2.3.2 Eikonal Equation for Multi-phase System

Let us focus on the pressure wave with a high frequency that contributes to the early and rapid variations of pressure disturbance. With the high frequency limit, only the terms of higher order of $i\omega$ has a significant physical meaning in Eq. (2.9). The terms with

the highest order of $i\omega$ can be found in the first term of Eq. (2.9) that corresponds to $n = 0$:

$$(i\omega)\left(\lambda_t k |\nabla \tau|^2 - \phi c_t\right) A_0 = 0. \quad (2.10)$$

Since A_0 is a non-zero real function, the gradient of the DTOF must satisfy the following condition:

$$|\nabla \tau|^2 = \frac{1}{\lambda_t k / \phi c_t}. \quad (2.11)$$

Thus, we come up with the Eikonal equation for multi-phase system:

$$|\nabla \tau| = \frac{1}{\sqrt{\alpha_{mp}}}, \quad (2.12)$$

where the multi-phase diffusivity has been defined as:

$$\alpha_{mp} \equiv \frac{k \lambda_t}{\phi c_t}. \quad (2.13)$$

The Eikonal equation for anisotropic permeability can be also derived following Zhang et. al (2016). With the same manner as the single-phase, the multi-phase Eikonal equation can be efficiently solved for the DTOF τ using the Fast Marching Method. **Figure 2.1** illustrates an example of diffusivity in a 2-D and two-phase reservoir with the homogeneous porosity and permeability and nonuniform initial water saturation. With the given distribution of water saturation as depicted in Figure 2.1a, the two-phase diffusivity was calculated as the summation of water and oil diffusivities (Figure 2.1b through Figure 2.1d). The corresponding DTOFs were also calculated using the water, oil and two-phase

diffusivities (Figure 2.1e through Figure 2.1g). Since the propagation of the pressure front in the multi-phase system is controlled by the total mobility, Figure 2.1e and Figure 2.1f are obviously not the appropriate solutions for multi-phase flow.

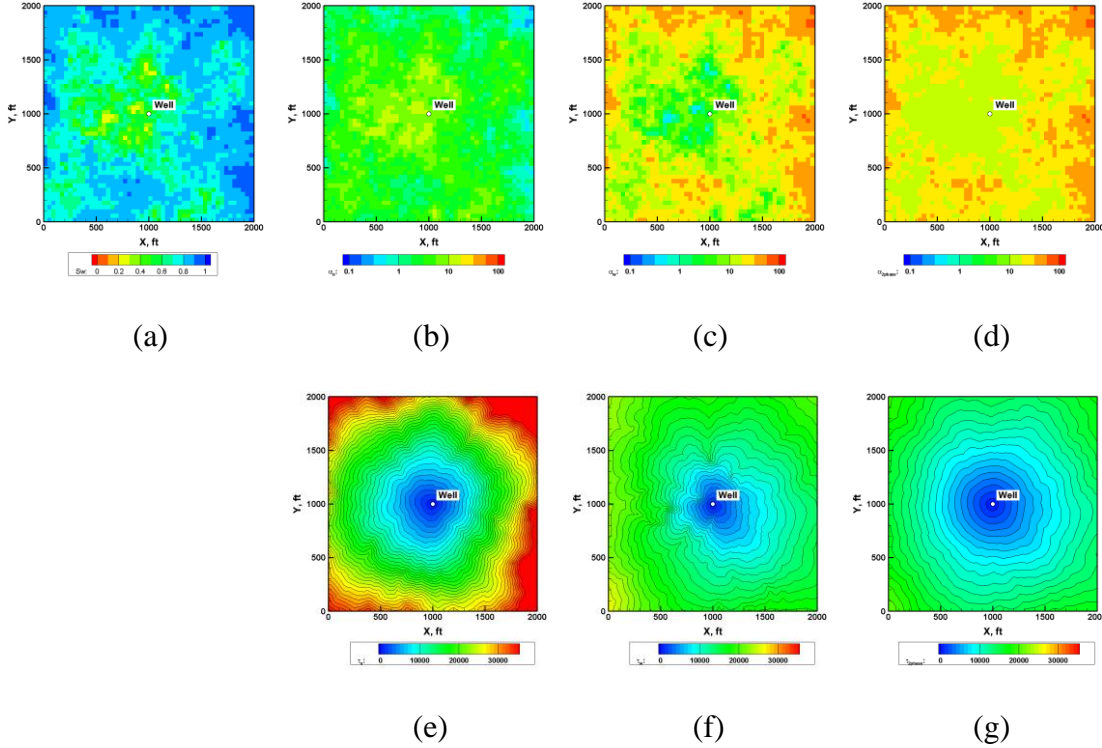


Figure 2.1 Initial water saturation, diffusivity and DTOFs (modified from Fujita (2014)) (a) Initial water saturation, (b) water diffusivity, (c) oil diffusivity, (d) two-phase diffusivity, (e) water-phase DTOF, (f) oil-phase DTOF and (g) two-phase DTOF (reprinted with permission from Iino et al., 2017a)

2.3.3 Coordinate Transformation from 3-D to 1-D along the DTOF

In order to decouple the 3-D flow equations for fracture into 1-D equations along the DTOF, we also assumed that pressure changes are aligned with the DTOF contour:

$$\nabla p \approx \frac{\partial p}{\partial \tau} \nabla \tau. \quad (2.14)$$

The Darcy velocity (2.2) can be rewritten as:

$$\mathbf{u}_j \approx - \left(\frac{kk_{rj}}{\mu_j} \right) \left(\frac{\partial p}{\partial \tau} \nabla \tau \right). \quad (2.15)$$

Suppose $d\Omega_\tau$ is the domain between two DTOF contours, we integrate Eq. (2.1) over this domain:

$$\int \frac{\partial}{\partial t} (\phi \rho_j S_j) d\Omega_\tau = \int \nabla \cdot (\rho_j \mathbf{u}_j) d\Omega_\tau = \oint (\rho_j \mathbf{u}_j) \cdot \mathbf{n} d\Gamma_\tau, \quad (2.16)$$

where $d\Gamma_\tau$ is the surface area of $d\Omega_\tau$. The unit vector \mathbf{n} that is perpendicular to the DTOF can be represented by:

$$\mathbf{n} \equiv \frac{\nabla \tau}{|\nabla \tau|}. \quad (2.17)$$

Substituting Eqs. (2.15) and (2.17) into (2.16) yields:

$$\int \frac{\partial}{\partial t} (\phi \rho_j S_j) d\Omega_\tau = - \oint \left[\left(\rho_j \frac{kk_{rj}}{\mu_j} \right) \frac{\partial p}{\partial \tau} \nabla \tau \right] \cdot \frac{\nabla \tau}{|\nabla \tau|} d\Gamma_\tau. \quad (2.18)$$

Rearranging the Eikonal equation, permeability can be expressed by

$$k = \frac{\phi c_t}{\lambda_t} \frac{1}{|\nabla \tau|^2}. \quad (2.19)$$

Remember the surface area Γ_τ can be approximated by the derivative of Ω_τ with respect to the infinitesimal distance s :

$$\Gamma_t \approx \frac{d\Omega_t}{ds} = \frac{d\tau}{ds} \frac{d\Omega_t}{d\tau} = |\nabla \tau| \frac{d}{d\tau} \left(\frac{V_p}{\phi} \right)_{ref} = \frac{|\nabla \tau|}{\phi_{ref}} w(\tau), \quad (2.20)$$

With Eqs. (2.19) and (2.20), the R.H.S. of Eq. (2.18) becomes:

$$\begin{aligned} -\oint \left[\left(\rho_j \frac{kk_{rj}}{\mu_j} \right) \frac{\partial p}{\partial \tau} \nabla \tau \right] \cdot \frac{\nabla \tau}{|\nabla \tau|} d\Gamma_\tau &\approx -\oint w(\tau) \left(\frac{c_t}{\lambda_t} \right)_{ref} \left[\left(\rho_j \frac{kk_{rj}}{\mu_j} \right) \frac{\partial p}{\partial \tau} \right] \cdot \frac{d(\nabla \tau)}{|\nabla \tau|} \\ &= -\Delta \tau \frac{\partial}{\partial \tau} \left[w(\tau) \left(\frac{c_t}{\lambda_t} \right)_{ref} \left(\rho_j \frac{k_{rj}}{\mu_j} \right) \frac{\partial p}{\partial \tau} \right], \end{aligned} \quad (2.21)$$

where subscript *ref* denotes the reference condition in which the DTOF was generated. On the other hand, the volume integration on L.H.S. in Eq. (2.18) can be rewritten as follows by assuming that every properties can be considered constant within the infinitesimal domain of Ω_τ :

$$\int \frac{\partial}{\partial t} (\phi \rho_j S_j) d\Omega_\tau = \int d\Omega_\tau \frac{\partial}{\partial t} (\phi \rho_j S_j) = \Delta V_{p,ref} \frac{\partial}{\partial t} \left(\frac{\phi}{\phi_{ref}} \rho_j S_j \right), \quad (2.22)$$

where the integration $\int d\Omega_\tau$ gives the bulk volume that is equivalent to the pore volume divided by porosity. Equating the transfer term (2.21) with the accumulation term (2.22) yields the following form of mass conservation:

$$\frac{\partial}{\partial t} (\phi \rho_j S_j) = -\frac{\phi_{ref}}{w(\tau)} \frac{\partial}{\partial \tau} \left[w(\tau) \left(\frac{c_t}{\lambda_t} \right)_{ref} \left(\rho_j \frac{k_{rj}}{\mu_j} \right) \frac{\partial p}{\partial \tau} \right]. \quad (2.23)$$

Finally, the coordinate transformation for flux term can be obtained by equating Eqs. (2.1) and (2.23):

$$\nabla \cdot (\rho_j \mathbf{u}_j) \equiv -\frac{\phi_{ref}}{w(\tau)} \frac{\partial}{\partial \tau} \left[w(\tau) \left(\frac{c_t}{\lambda_t} \right)_{ref} \left(\rho_j \frac{k_{rj}}{\mu_j} \frac{\partial p}{\partial \tau} \right) \right]. \quad (2.24)$$

By introducing the formation volume factor B , Eq. (2.24) can be rewritten as:

$$\nabla \cdot \left(\mathbf{k} \frac{k_{rj}}{B_j \mu_j} \nabla p \right) \equiv -\frac{\phi_{ref}}{w(\tau)} \frac{\partial}{\partial \tau} \left[w(\tau) \left(\frac{c_t}{\lambda_t} \right)_{ref} \frac{k_{rj}}{B_j \mu_j} \frac{\partial p}{\partial \tau} \right]. \quad (2.25)$$

2.3.4 Dual-porosity Formulation

For modelling the shale reservoirs with the complicated flow mechanisms between multi-continua, the dual-porosity model (Warren and Root 1963) was used in this study. As illustrated in **Figure 2.2**, the dual-porosity system consists of two porous media with distinct reservoir properties: fracture and matrix. The fracture has a higher conductivity and plays a role of main flow path for fluid flow. The matrix, on the other hand, plays a role of a storage or sink/ source term communicating with fracture but no convective flow in-between. Thus, we assumed that propagation of high-frequency pressure wave only depends on the fracture properties and the DTOF calculation is involved only in the fracture domain (Fujita et al., 2016).

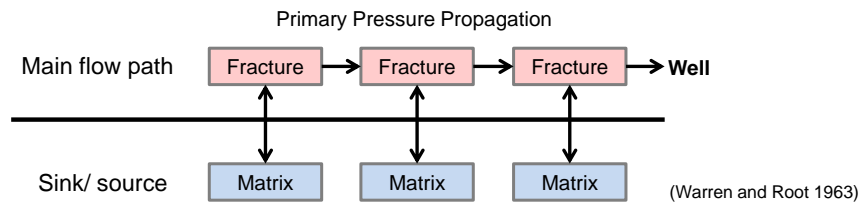


Figure 2.2 Illustration of Dual-porosity and Single-permeability system (reprinted with permission from Iino et al., 2017a)

In the absence of gravity and capillary forces, the mass balance equations in the fracture medium of the dual-porosity system are written as the following equations (Kazemi et al., 1976; Gilman and Kazemi, 1983):

$$\frac{\partial}{\partial t} \left(\phi_f \frac{S_{wf}}{B_w} \right) = \nabla \cdot \left(\mathbf{k}_f \frac{k_{rwf}}{B_w \mu_w} \nabla p_f \right) + \frac{\tilde{q}_w}{B_w} - \frac{\Gamma_w}{B_w}, \quad (2.26)$$

$$\frac{\partial}{\partial t} \left(\phi_f \frac{S_{of}}{B_o} \right) = \nabla \cdot \left(\mathbf{k}_f \frac{k_{rof}}{B_o \mu_o} \nabla p_f \right) + \frac{\tilde{q}_o}{B_o} - \frac{\Gamma_o}{B_o}, \quad (2.27)$$

$$\begin{aligned} \frac{\partial}{\partial t} \left[\phi_f \left(\frac{S_{gf}}{B_g} + R_s \frac{S_{of}}{B_o} \right) \right] = \nabla \cdot \left[\mathbf{k} \left(\frac{k_{rgf}}{B_g \mu_g} + R_s \frac{k_{rof}}{B_o \mu_o} \right) \nabla p_f \right] \\ + \left(\frac{\tilde{q}_g}{B_g} + R_s \frac{\tilde{q}_o}{B_o} \right) - \left(\frac{\Gamma_g}{B_g} + R_s \frac{\Gamma_o}{B_o} \right), \end{aligned} \quad (2.28)$$

where B : formation volume factor, R_s : solution gas-oil-ratio, \tilde{q} : flow rate per unit bulk volume and subscript f denotes fracture. The fluid transfer term Γ_j between the fracture and matrix is given by the following:

$$\Gamma_j = \sigma k_m \left(\frac{k_{mj}}{\mu_j} \right) (p_f - p_m), \quad (2.29)$$

where σ is a shape factor dimensioned by square-inverse of length that represents the connectivity between the matrix block and the surrounding fracture network. The matrix only have fluid transfer with the fracture and there is no convective flow within the matrix:

$$\frac{\partial}{\partial t} \left(\phi_m \frac{S_{wm}}{B_w} \right) = \frac{\Gamma_w}{B_w}, \quad (2.30)$$

$$\frac{\partial}{\partial t} \left[\phi_m \left(\frac{S_{gm}}{B_g} + R_s \frac{S_{om}}{B_o} \right) \right] = \frac{\Gamma_g}{B_g} + R_s \frac{\Gamma_o}{B_o}, \quad (2.31)$$

$$\frac{\partial}{\partial t} \left[\phi_m \left(\frac{S_{gm}}{B_g} + R_s \frac{S_{om}}{B_o} \right) \right] = \frac{\Gamma_g}{B_g} + R_s \frac{\Gamma_o}{B_o}, \quad (2.32)$$

where subscript m denotes the matrix. Now let us apply the coordinate transform to fracture to formulate the 1-D equations along the DTOF. By assuming that both the pressure and saturation changes are aligned with the DTOF contours, we apply Eq. (2.25) to Eqs. (2.26) through (2.28) and obtain the following 1-D equations for fracture:

$$\frac{\partial}{\partial t} \left(\phi_f \frac{S_{wf}}{B_w} \right) = \frac{\phi_{f,ref}}{w(\tau)} \frac{\partial}{\partial \tau} \left(w(\tau) \left(\frac{c_t}{\lambda_t} \right) \frac{k_{rwf}}{B_w \mu_w} \frac{\partial p_f}{\partial \tau} \right) + \frac{\tilde{q}_w}{B_w} \delta(\tau_{wb}) - \frac{\Gamma_w}{B_w}, \quad (2.33)$$

$$\frac{\partial}{\partial t} \left(\phi_f \frac{S_{of}}{B_o} \right) = \frac{\phi_{f,ref}}{w(\tau)} \frac{\partial}{\partial \tau} \left(w(\tau) \left(\frac{c_t}{\lambda_t} \right)_{ref} \frac{k_{ro}}{B_o \mu_o} \frac{\partial p_f}{\partial \tau} \right) + \frac{\tilde{q}_o}{B_o} \delta(\tau_{wb}) - \frac{\Gamma_o}{B_o}, \quad (2.34)$$

$$\begin{aligned} \frac{\partial}{\partial t} \left[\phi_f \left(\frac{S_{gf}}{B_g} + R_s \frac{S_{of}}{B_o} \right) \right] &= \frac{\phi_{f,ref}}{w(\tau)} \frac{\partial}{\partial \tau} \left[w(\tau) \left(\frac{c_t}{\lambda_t} \right)_{ref} \left(\frac{k_{rgf}}{B_g \mu_g} + R_s \frac{k_{rof}}{B_o \mu_o} \right) \frac{\partial p_f}{\partial \tau} \right] \\ &+ \left(\frac{\tilde{q}_g}{B_g} + R_s \frac{\tilde{q}_o}{B_o} \right) \delta(\tau_{wb}) - \left(\frac{\Gamma_g}{B_g} + R_s \frac{\Gamma_o}{B_o} \right), \end{aligned} \quad (2.35)$$

where the Dirac delta $\delta(\tau_{wb})$ means that the sink/ source term only appears at the inner boundary of $\tau = \tau_{wb}$ in the well grid. The validity of the assumption that the pressure and saturation contours are aligned with the DTOF contours will be discussed later. In the

discretized domain along the DTOF coordinate, the sink/ source term can be rewritten in terms of the bottomhole pressure as:

$$q_j = WI \left(\frac{k_{rj}}{\mu_j} \right) (p_{f,1} - p_w). \quad (2.36)$$

Derivation of the well index WI defined in the τ -coordinate system will be presented later.

2.4 Implementation

In this section, we will describe how the mathematical formulations are discretized and implemented. The well model specific to the DTOF coordinate will be introduced. Calculation of V_p and $w(\tau)$, which is the critical part of our proposed FMM-based approach, will be presented and validated.

2.4.1 Simulation Workflow

The simulation approach consists of two decoupled steps: calculating the DTOF on the original multi-dimensional grid and 1-D simulation on the DTOF coordinate. The workflow is illustrated in **Figure 2.3**. First, the multi-phase diffusivity is calculated for every grid block. The Eikonal equation is then solved by the FMM for the DTOF, followed by the calculation of the drainage pore volume V_p as a function of the DTOF. Subsequently, the drainage pore volume is discretized on 1-D DTOF coordinate and the $w(\tau)$ function is calculated. The 1-D simulation will be finally performed using the pore volume, transmissibility and well index defined on the 1-D DTOF system. In **Appendix**

2.4.2 Discretization

In the FMM-based reservoir simulation, the discretized 1-D equations are solved for pressure and saturation with the fully implicit method. Let us present how we discretize the water mass balance equation of fracture for instance. We first multiply the bulk volume ΔV_b to Eq. (2.33):

$$\Delta V_b \frac{\partial}{\partial t} \left(\phi_f \frac{S_{wf}}{B_w} \right) = \Delta \tau \frac{\partial}{\partial \tau} \left(w(\tau) \left(\frac{c_t}{\lambda_t} \right) \frac{k_{rwf}}{B_w \mu_w} \frac{\partial p_f}{\partial \tau} \right) + q_{w,sc} \delta(\tau_{wb}) - \Delta V_b \frac{\Gamma_w}{B_w}, \quad (2.37)$$

where $w(\tau)$ in front of the partial derivative with respect to τ was approximated as $\Delta V_b \phi_{f,ref} / \Delta \tau$. The accumulation term on L.H.S. is discretized in time:

$$\Delta V_b \frac{\partial}{\partial t} \left(\phi_f \frac{S_{wf}}{B_w} \right) \approx \frac{1}{\Delta t} \left[\left(\Delta V_p \frac{S_{wf}}{B_w} \right)_i^{n+1} - \left(\Delta V_p \frac{S_{wf}}{B_w} \right)_i^n \right], \quad (2.38)$$

where subscript i and superscript n denote the grid block index on 1-D DTOF space and time step level, respectively. The transfer term on the R.H.S. can be discretized as:

$$\begin{aligned} & \Delta \tau \frac{\partial}{\partial \tau} \left(w(\tau) \left(\frac{c_t}{\lambda_t} \right)_{ref} \frac{k_{rwf}}{B_w \mu_w} \frac{\partial p_f}{\partial \tau} \right) \\ & \approx \frac{\Delta \tau_i}{\Delta \tau_i} \left[\left\{ w(\tau) \left(\frac{c_t}{\lambda_t} \right)_{ref} \frac{k_{rwf}}{B_w \mu_w} \frac{\partial p_f}{\partial \tau} \right\}_{i+1/2}^{n+1} - \left\{ w(\tau) \left(\frac{c_t}{\lambda_t} \right)_{ref} \frac{k_{rwf}}{B_w \mu_w} \frac{\partial p_f}{\partial \tau} \right\}_{i-1/2}^{n+1} \right] \\ & = \left[\frac{w(\tau)}{\Delta \tau_{i+1/2}} \left(\frac{c_t}{\lambda_t} \right)_{ref} \right]_{i+1/2} \left(\frac{k_{rwf}}{B_w \mu_w} \right)_{i+1/2}^{n+1} (p_{i+1}^{n+1} - p_i^{n+1}) \\ & \quad - \left[\frac{w(\tau)}{\Delta \tau_{i-1/2}} \left(\frac{c_t}{\lambda_t} \right)_{ref} \right]_{i-1/2} \left(\frac{k_{rwf}}{B_w \mu_w} \right)_{i-1/2}^{n+1} (p_i^{n+1} - p_{i-1}^{n+1}) \end{aligned} \quad (2.39)$$

Thus, the 1-D transmissibility T_{1D} can be defined as:

$$T_{1D,i\pm} \equiv C \left[\frac{w(\tau) \left(\frac{c_t}{\lambda_t} \right)_{ref}}{\Delta \tau} \right]_{i\pm 1/2}, \quad (2.40)$$

where C is a constant depending on the unit system (see **Table 2.1** for detail).

Table 2.1 Constant for transmissibility calculation

Parameter	Unit system-1	Unit system-2
DTOF τ	$\text{ft}\times(\text{mD}\times\text{psi}\times\text{cp}-1)^{0.5}$	$(\text{day})^{0.5}$
$w(\tau)$	$\text{cuft}\times\{\text{ft}\times(\text{mD}\times\text{psi}\times\text{cp}-1)^{-0.5}\}$	$\text{cuft}\times(\text{day})^{0.5}$
c_t	psi^{-1}	psi^{-1}
λ_t	cp^{-1}	cp^{-1}
T_{geo}	$\text{bbl}/\text{day}/\text{psi}\times\text{cp}$	$\text{bbl}/\text{day}/\text{psi}\times\text{cp}$
C	0.001127	0.1781

Discretization of sink/source and matrix-fracture transfer terms are:

$$\Delta V_b \frac{\Gamma_w}{B_w} \approx C_2 (\Delta V_b \sigma k_m)_i \left(\frac{k_{rw}}{\mu_w B_w} \right)_i^{n+1} (p_{f,i}^{n+1} - p_{m,i}^{n+1}), \quad (2.41)$$

$$q_{w,sc} = WI \left(\frac{k_{rw}}{B_w \mu_w} \right)_1^{n+1} (p_{f,1}^{n+1} - p_w^{n+1}). \quad (2.42)$$

where C_2 is 0.001127 for field unit when ΔV_b enters as ft^3 .

Schematics of the 1-D DTOF grid blocks in xy -plane is illustrated in **Figure 2.4**.

Pore volume and $w(\tau)$ function defined on the 1-D DTOF grid blocks are basically computed from the FMM solution as discussed later, however, they need to be analytically calculated for the first cell in the vicinity of well which has the most significant impact on

the simulated well performances. Within a well grid block, the distance r from the wellbore can be translated by $\tau\sqrt{\alpha}$ and $\tau\sqrt[4]{\alpha_x\alpha_y}$ for the isotropic and anisotropic systems, respectively. Thus, the first cell should be defined within the well grid such that pore volume and $w(\tau)$ can be analytically calculated with the following formulations:

$$\Delta V_{p1} = \pi \tau_{3/2}^2 \sqrt{\alpha_{x,\text{wellgrid}} \alpha_{y,\text{wellgrid}}} h \phi, \quad (2.43)$$

$$w(\tau_{3/2})_{\text{analytical}} = 2\pi h \phi \tau_{3/2} \sqrt{\alpha_{\text{x,wellgrid}} \alpha_{\text{y,wellgrid}}} . \quad (2.44)$$

where similar expression can be applied for cases of yz - and xz -plane.

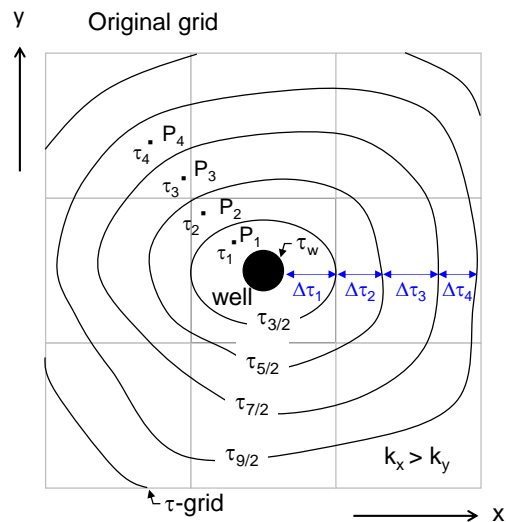


Figure 2.4 Schematics of the 1-D DTOF grid blocks. Subscripts i and $i+1/2$ denote the cell-center and cell-interface, respectively

2.4.3 Well Model

The well index WI specific to the coordinate system of the 1-D DTOF can be derived by the same way as the radial coordinate system. Let us consider the steady-state radial flow in isotropic system of which the line-source solution is approximated by:

$$p(r) = p(r_w) + \frac{qB\mu}{2\pi kh} \ln\left(\frac{r}{r_w}\right). \quad (2.45)$$

The average pressure between the wellbore (r_w) and the radius r is:

$$\bar{p} = \frac{\int_{r_w}^r p dV_p}{\int_{r_w}^r dV_p}. \quad (2.46)$$

By substituting Eq. (2.45) into Eq. (2.46) and carrying the integration out, we come up with the following equation:

$$\bar{p} = p_w + \frac{qB\mu}{2\pi kh} \left[\frac{r^2}{(r^2 - r_w^2)} \ln\left(\frac{r}{r_w}\right) - \frac{1}{2} \right]. \quad (2.47)$$

Since we define the first cell on the 1-D DTOF grid within the original well grid, the distance r can be replaced with the DTOF:

$$\tau = \frac{r}{\sqrt{\alpha}} \quad (r: \text{within isotropic well grid}). \quad (2.48)$$

The well index can be defined as:

$$WI = \frac{C_3 kh}{\frac{\tau_1^2}{(\tau_1^2 - \tau_w^2)} \ln\left(\frac{\tau_1}{\tau_w}\right) - \frac{1}{2}}. \quad (2.49)$$

where the constant C_3 is 0.007081 for field unit. For anisotropic permeability, we can simply replace the permeability with the geometric mean between two directions perpendicular to the well:

$$WI = \frac{C_3 \sqrt{k_x k_y} h}{\frac{\tau_1^2}{(\tau_1^2 - \tau_w^2)} \ln \left(\frac{\tau_1}{\tau_w} \right) - \frac{1}{2}}. \quad (2.50)$$

If the well is completed in multiple grid blocks in the original 3-D grid, the well index should be summed up for all the completions:

$$WI = \sum_l^{N_c} \frac{C_3 \sqrt{k_{x,l} k_{y,l}} h_l}{\frac{\tau_1^2}{(\tau_1^2 - \tau_{w,l}^2)} \ln \left(\frac{\tau_1}{\tau_{w,l}} \right) - \frac{1}{2}}. \quad (2.51)$$

where N_c is the number of completions and subscript l is the completion index. Note that τ_1 needs to be defined such that the first 1-D grid is defined within all the completion cells.

2.4.4 Calculation of V_p and $w(\tau)$ Function

According to the discretization scheme of the FMM, two different options will be used to calculate the pore volume V_p and $w(\tau)$ as a function of the DTOF.

The first option is based on the cell-center τ where the DTOF solutions are mapped onto the cell center of each grid block:

$$V_p(\tau) = \sum_{ijk}^N \Delta V_{p,ijk} \quad (\text{if } \tau_{ijk} \leq \tau). \quad (2.52)$$

Because the accumulation criteria for each grid block is simply based on the comparison between the cell-center τ_{ijk} and τ , this option results in a stair-wise $V_p(\tau)$, leading to the non-smooth $w(\tau)$ function that is calculated by the numerical derivative of $V_p(\tau)$. Thus, we use a smoothing technique that is typically used in the calculation of the welltest derivative (Horne, 1995):

$$w(\tau) \approx \frac{1}{\tau_i} \left[\frac{\ln(\tau_i / \tau_{i-j}) V_{p,i+j}}{\ln(\tau_{i+j} / \tau_i) \ln(\tau_{i+j} / \tau_{i-j})} + \frac{\ln(\tau_{i+j} \tau_{i-j} / \tau_i^2) V_{p,i}}{\ln(\tau_{i+j} / \tau_i) \ln(\tau_i / \tau_{i-j})} - \frac{\ln(\tau_{i+j} / \tau_i) V_{p,i-j}}{\ln(\tau_i / \tau_{i-j}) \ln(\tau_{i+j} / \tau_{i-j})} \right] \quad (2.53)$$

where the numerical derivative at point- i is calculated using the non-adjacent data located at $i-j$ and $i+j$. The span size j is determined by the optimum span selection that gives a trade-off between bias and variance. Although bias is typically evaluated by the deviation between the model estimate and observed (true) data, we do not have true values of $w(\tau)$ to be referred. Hence, we simply use the error in pore volume that is back-calculated from the smoothed $w(\tau)$ as a representation of bias:

$$\mathcal{E}_{PV} = \left| 1 - \frac{\sum_i^{N_\tau} w(\tau_i) \Delta \tau_i}{\sum_{ijk}^N \Delta V_{p,ijk}} \right|. \quad (2.54)$$

where N_τ is the number of 1-D DTOF grid blocks. On the other hand, variance is evaluated by the root-mean-squared (RMS) of sum with moving linear regression:

$$RMS = \frac{1}{N_\tau} \sum_1^{N_\tau} \sqrt{\frac{1}{n} \sum_i^n |w(\tau_i) - f(\tau_i)|^2}. \quad (2.55)$$

where n is the number of DTOF nodes and $f(\tau)$ is the linear regression within the moving window (**Figure 2.5**).

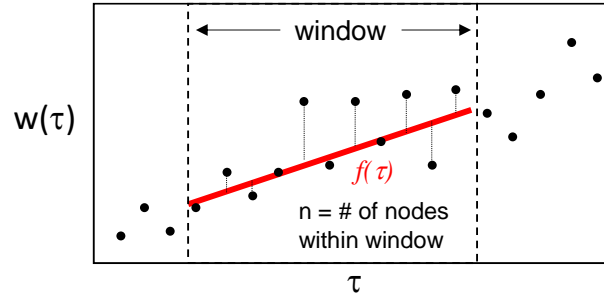
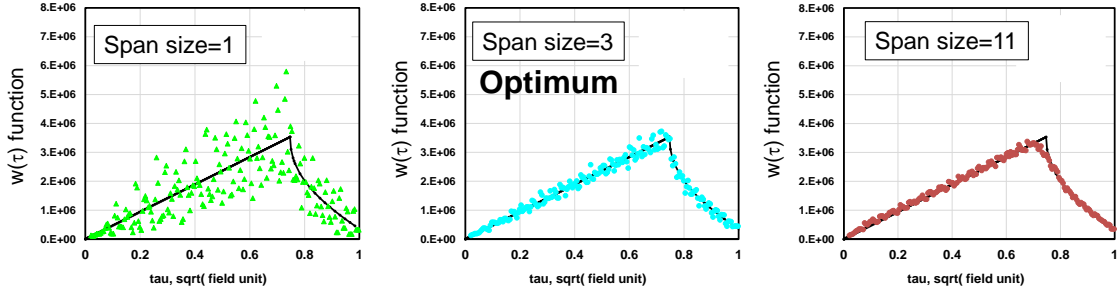
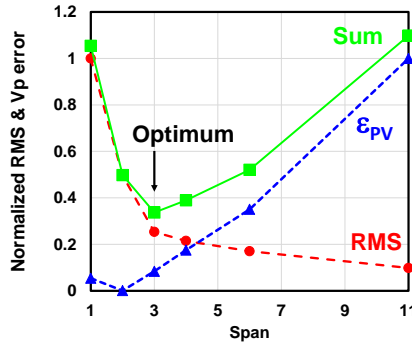


Figure 2.5 Illustration of moving linear regression to evaluate variance of $w(\tau)$ function

Figure 2.6 illustrates the $w(\tau)$ function with different span sizes and bias-variance trade-off calculated for 2-D homogeneous (41×41) model where the well is located at the center. The error in the pore volume and the RMS normalized by each maximum value clearly show the trade-off, indicating that the optimum span size is found at the span size of three (Figure 2.6d). The extreme span sizes of one and eleven show scattered and smeared $w(\tau)$ functions (Figure 2.6a and Figure 2.6c), respectively, whereas the optimum span size shows a good matching with the analytical calculation (black line) in Figure 2.6b.



(a) $w(\tau)$ (span size = 1) (b) $w(\tau)$ (span size=3) (c) $w(\tau)$ (span size=11)



(d) Bias-variance trade-off

Figure 2.6 $w(\tau)$ with different span size (top) and bias-variance trade-off for optimum span size selection (bottom). The number of 1-D grid blocks is 200. Black line in top three plots denotes the $w(\tau)$ function that is analytically calculated

The other option to calculate $w(\tau)$ function is based on the 27-pt stencil FMM (Li, 2018). In this approach, the DTOF is solved not only on the cell-center but also on vertices and midpoints of each segment of grid blocks, leading to the minimum and maximum DTOF values for each grid that represent the duration in which the pressure wave is

passing through. This enables us to calculate how much fraction of pore volumes of each grid block to be included in $V_p(\tau)$ by the interpolation based on τ -value:

$$V_p(\tau) = \sum_{ijk}^{N_c} \Delta V_{p0,ijk} \min\left(1, \frac{\tau^2}{\tau_1^2}\right) + \sum_{ijk}^N \Delta V_{p,ijk} \min\left[1, \max\left(0, \frac{\tau - \tau_{\min,ijk}}{\tau_{\max,ijk} - \tau_{\min,ijk}}\right)\right], \quad (2.56)$$

where N_c : number of completion cells, N : cell count of the original 3-D model, ΔV_{p0} : pore volume of the first τ grid block lying within each completion cell, ΔV_p : pore volume of each grid block. Note that special treatment will be made on completion cells as illustrated in **Figure 2.7**: the grid block is divided into the first τ -grid and the remaining part. In case that we calculate the pore volume for τ less than τ_1 , the quadratic interpolation will be used for the first τ -grid since the radial flow is expected. For the remaining part, the pore volume ΔV_p is redefined as the pore volume of the grid block minus that of the first τ -grid, and τ_{\min} is set to be τ_1 .

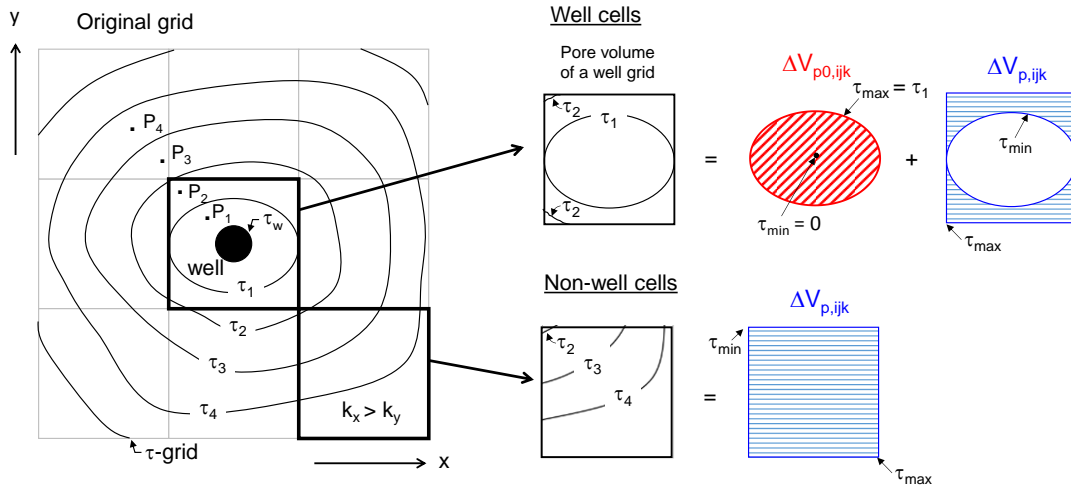


Figure 2.7 Special treatment for well cells for pore volume calculation from 27pt-stencil FMM solution

Thus, the obtained $V_p(\tau)$ is no longer a stair-wise function. The smooth $w(\tau)$ function can also be obtained from the following equation that does not involve any smoothing artifact:

$$w(\tau) = \sum_{ijk}^N \left[\frac{\Delta V_{p,ijk}}{\tau_{ijk,\max} - \tau_{ijk,\min}} (\text{if } \tau_{ijk,\min} < \tau < \tau_{ijk,\max}) \right]. \quad (2.57)$$

Comparison of V_p and $w(\tau)$ calculation between the cell-center and 27pt-setencil will be discussed later.

2.4.5 Averaging Reservoir Properties

In the FMM-based simulation, the pore volume and transmissibility in the 1-D DTOF domain are defined based on $V_p(\tau)$ and $w(\tau)$ functions as stated above. However, all the other properties such as rock types, matrix porosity and fracture/ matrix transmissibility coefficient $\Delta V_b \sigma k_m$ need to be averaged within the DTOF contour (**Table 2.2**).

Table 2.2 Averaging method for reservoir properties for FMM-based simulation

Reservoir properties	Averaging method
Matrix porosity	Volume-weighted average
Fracture/ matrix transmissibility coefficient	Volume-weighted geometric average
Rock type for relative permeability	Majority vote
Rock type for rock compaction	Majority vote
Initial water saturation	Pore volume-weighted average
Initial pressure	Pore volume-weighted average

Let us present an example of the fracture/ matrix transmissibility coefficient $\Delta V_b \sigma k_m$.

Suppose a group of matrix blocks of which size is $l_x \times l_y \times l_z$ lies in the bulk volume of $\Delta x \Delta y \Delta z$ (**Figure 2.8**).

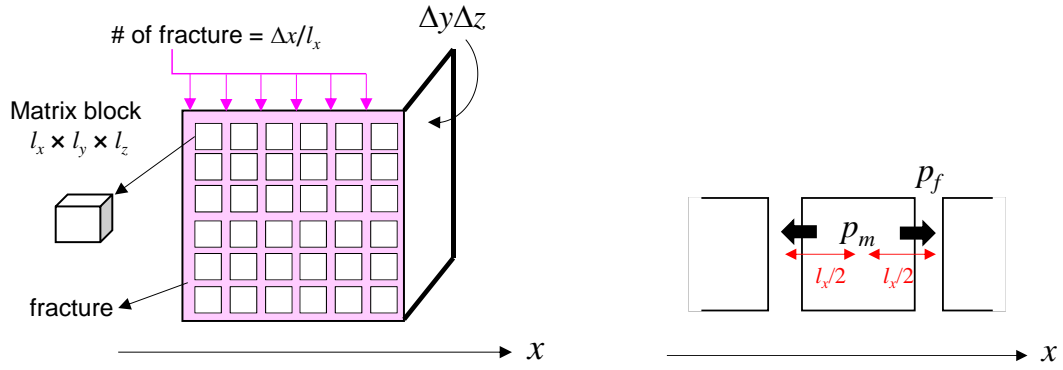


Figure 2.8 Schematics of dual-porosity system

The shape factor σ is defined as follows (Gilman and Kazemi 1983):

$$\sigma \equiv 4 \left(\frac{1}{l_x^2} + \frac{1}{l_y^2} + \frac{1}{l_z^2} \right). \quad (2.58)$$

The contact area A_x between fracture and matrix and transfer rate in x -direction are:

$$A_x = (\Delta y \Delta z) \times \frac{\Delta x}{l_x} = \frac{\Delta V_{bulk}}{l_x}, \quad (2.59)$$

$$q_{j,x} = -\lambda_j^{up} k_m A_x \frac{p_f - p_m}{(l_x/2)} \times 2, \quad (2.60)$$

where superscript up denotes the upstream continua. Substituting Eq. (2.59) into (2.60) and summing up the transfer rate in three directions yields:

$$q_j = -\lambda_j^{up} k_m \times \Delta V_{bulk} \times 4 \left(\frac{1}{l_x^2} + \frac{1}{l_y^2} + \frac{1}{l_z^2} \right) \times (p_f - p_m), \quad (2.61)$$

The total transfer rate of the grid blocks which lie in the same DTOF contour is:

$$q_j = - \sum_{ijk}^{\tau-contour} \left[\lambda_j^{up} k_m \Delta V_{bulk} \sigma (p_f - p_m) \right], \quad (2.62)$$

where ijk is the grid block index in the original 3-D grid system. Assuming the matrix pressure is uniform within each DTOF contour,

$$\begin{aligned} q_{j,i} &= - (p_{f,i} - p_{m,i}) \sum_{ijk}^{\tau-contour} \left[\lambda_j^{up} k_m \Delta V_{bulk} \sigma \right], \\ &\equiv - (p_{f,i} - p_{m,i}) \lambda_{j,i}^{up} \Delta V_{bulk,i} (\overline{k_m \sigma})_i \end{aligned} \quad (2.63)$$

where subscript i denotes the grid block index in 1-D DTOF system. Eq. (2.63) indicates that shape factor σ and matrix permeability k_m should be treated as a product in dual-porosity formulation and it should be averaged in each DTOF contour being weighted by bulk volume. In this study, we employed the geometric average:

$$\log(\overline{k_m \sigma})_i = \frac{\sum_{ijk}^{\tau-countor} \Delta V_{bulk,ijk,i} \log(k_m \sigma)_{ijk}}{\sum_i^{\tau-countor} \Delta V_{bulk,ijk,i}} .. \quad (2.64)$$

where $\Delta V_{bulk,ijk,i}$ denotes the portion of the bulk volume of grid block ijk that lies within the i -th DTOF contour. Thus, as well as the pore volume, we need to accumulate ΔV_{bulk}

and $\Delta V_{bulk} \log(k_m \sigma)$ as a function of the DTOF as illustrated in **Figure 2.9**. The other properties listed in Table 2.2 can be calculated with the similar manner.

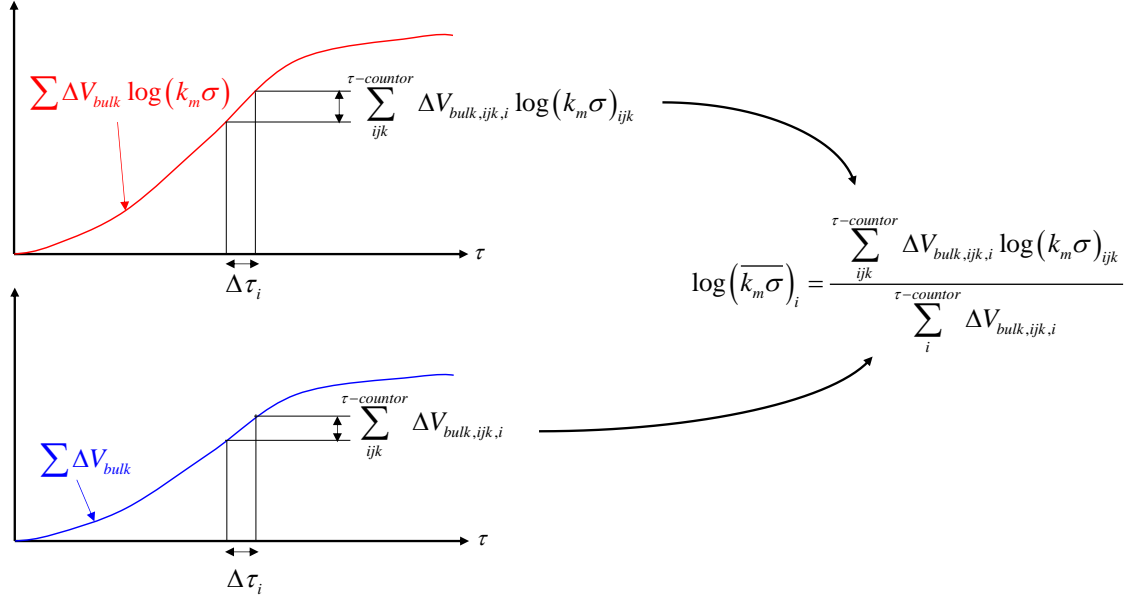


Figure 2.9 Illustration of calculating average fracture/ matrix transmissibility coefficient in 1-D DTOF domain

2.5 Validation

We validated the proposed FMM-based simulation using synthetic reservoir models. We start from the single-phase case to illustrate validity of our basic formulation and implementation without any multi-phase effects. Subsequently, we present multi-phase cases to show accuracy and computational efficiency of the FMM-based approach.

2.5.1 Single-phase Case—Homogeneous Reservoir

We first validate the FMM-based simulation approach using three cases in **Table 2.3**. Single-phase fluid was assumed with the viscosity and compressibility of 1 cp and 10^{-5} psi⁻¹, respectively. Rock compressibility was neglected and well radius was set to be 0.354 ft. For cases 1 and 2, the vertical wells were completed for the whole thickness at the center, whereas the horizontal well in case 3 was placed at the center with the lateral length of 754 ft. The storativity ratio ω and inter-porosity coefficient λ are defined as follows:

$$\omega = \frac{(\phi c_t)_f}{(\phi c_t)_f + (\phi c_t)_m}, \quad (2.65)$$

$$\lambda = r_w^2 \sigma \frac{k_m}{k_f}, \quad (2.66)$$

where reservoir parameters in Table 2.3 are equivalent to ω of 0.1 and λ of 2×10^{-5} , respectively.

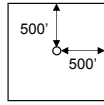
Table 2.3 Single-phase validation cases

Case	1. Single-porosity & Vertical well	2. Dual-porosity & Vertical well	3. Single-porosity & Horizontal well
Model size (ft ³)	500×500×20	500×500×20	3000×3000×50
Grid block numbers	501×501×1	501×501×1	501×501×21
Porosity	0.2	0.02 (Fracture) 0.18 (Matrix)	1 (Horizontal) 0.1 (Vertical)
Permeability (mD)	1	1 (Fracture) 0.001 (Matrix)	1
Shape factor (ft ⁻²)	-	0.15945	-

2.5.1.1 Comparison with analytical solutions

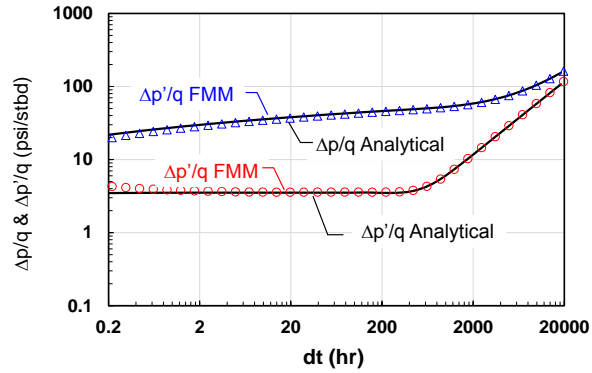
For validation cases here, analytical pressure solutions are available (Lee et al., 2003). **Figure 2.10** shows the comparisons of log-log diagnostic plots from FMM-based simulations and analytical solutions for constant rate drawdown test. For all the three cases, the number of 1-D grid blocks was set to be 400 with logarithmic gridding around the well and $w(\tau)$ function was calculated based on the cell-center DTOF and smoothing technique. The first two cases with a vertical well in the 2-D single-porosity (Case-1) and dual-porosity (Case-2) show excellent agreement between FMM-based simulations and analytical solutions (Figure 2.10a and Figure 2.10b). On the other hand in Case-3 with a horizontal well, matching is still reasonable but the minor deviation can be seen in the pressure derivative (Figure 2.10c). Deviation in the early time up to 2 hours is due to the wellbore storage-like effect by the pore volume of the well grid in the FMM-based simulation. Deviation in the mid-time (20-2000 hours) might be due to the boundary effect (Huang, 2017) since the distance between the well and vertical boundary is only 50 ft.

Single-porosity
& Vertical well



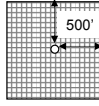
$$kh = 20 \text{ mD} \cdot \text{ft}$$

$$\phi = 0.1$$



(a) Vertical producer in 2-D homogeneous single-porosity model

Dual-porosity
& Vertical well

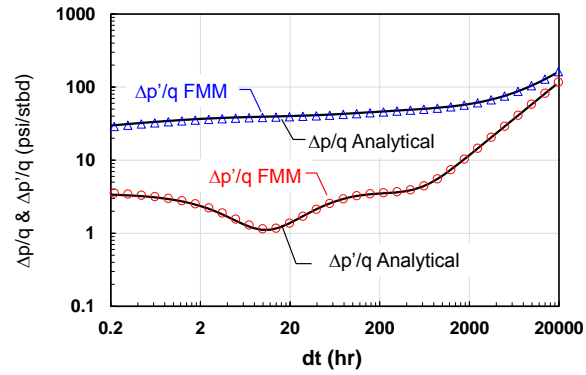


$$k_f h = 20 \text{ mD} \cdot \text{ft}$$

$$\phi = 0.02$$

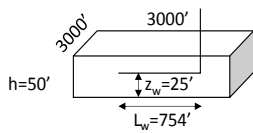
$$\omega = 0.1$$

$$\lambda = 2 \times 10^{-5} (=r_w^2 \sigma k_m / k_f)$$



(b) Vertical producer in 2-D homogeneous dual-porosity model

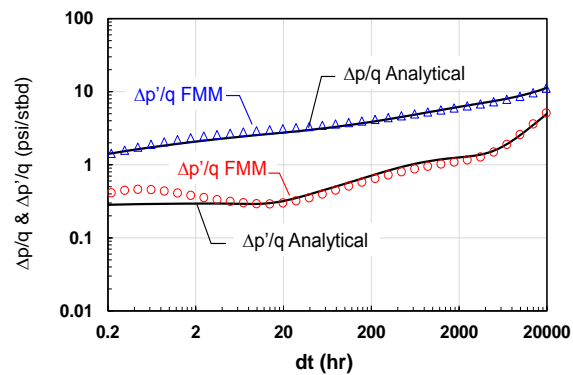
Single-porosity
& Horizontal well



$$k_f h = 20 \text{ mD} \cdot \text{ft}$$

$$\phi = 0.2$$

$$k_v / k_h = 0.1$$



(c) Horizontal producer in 3-D homogeneous single-porosity model

Figure 2.10 Log-log diagnostic plot for three validation cases

In the above examples, we discretized the 1-D DTOF coordinate into 400 grid blocks and confirmed good agreement with the analytical solutions. Next, we need to address (1) if solutions converge with respect to numbers of 1-D grid blocks and (2) how many 1-D grid blocks should be used to reasonably approximate the original 3-D simulation.

2.5.1.2 Convergence with respect to number of 1-D grid blocks

Accuracy and stability of the FMM-based simulation depend on those of $V_p(\tau)$ and $w(\tau)$ from the FMM solutions as we can see in the discretized 1-D formulations (2.38), (2.39) and (2.41). Especially, too small numbers of the 1-D grid blocks can cause erroneous $w(\tau)$ function if it is calculated by the cell-center τ and smoothing technique, leading to inaccurate simulation results. **Figure 2.11** illustrates the comparison of $w(\tau)$ functions between different numbers of the 1-D grid blocks (n_τ) where the 2-D homogeneous single-porosity model (Case-1) was used. For reference, the analytically calculated $w(\tau)$ function is also plotted with black solid lines. Obviously, $w(\tau)$ function with 40 grid blocks is underestimated compared to the analytical calculation (Figure 2.11a). However, once we increase the 1-D grid block number to 100, the calculated $w(\tau)$ gets closer to the analytical calculation but it is still underestimated in the near-well region. Further refinement with 400 and more grid blocks gives excellent matching with the analytical calculation as well as the convergence of $w(\tau)$ function as seen in Figure 2.11c through Figure 2.11e.

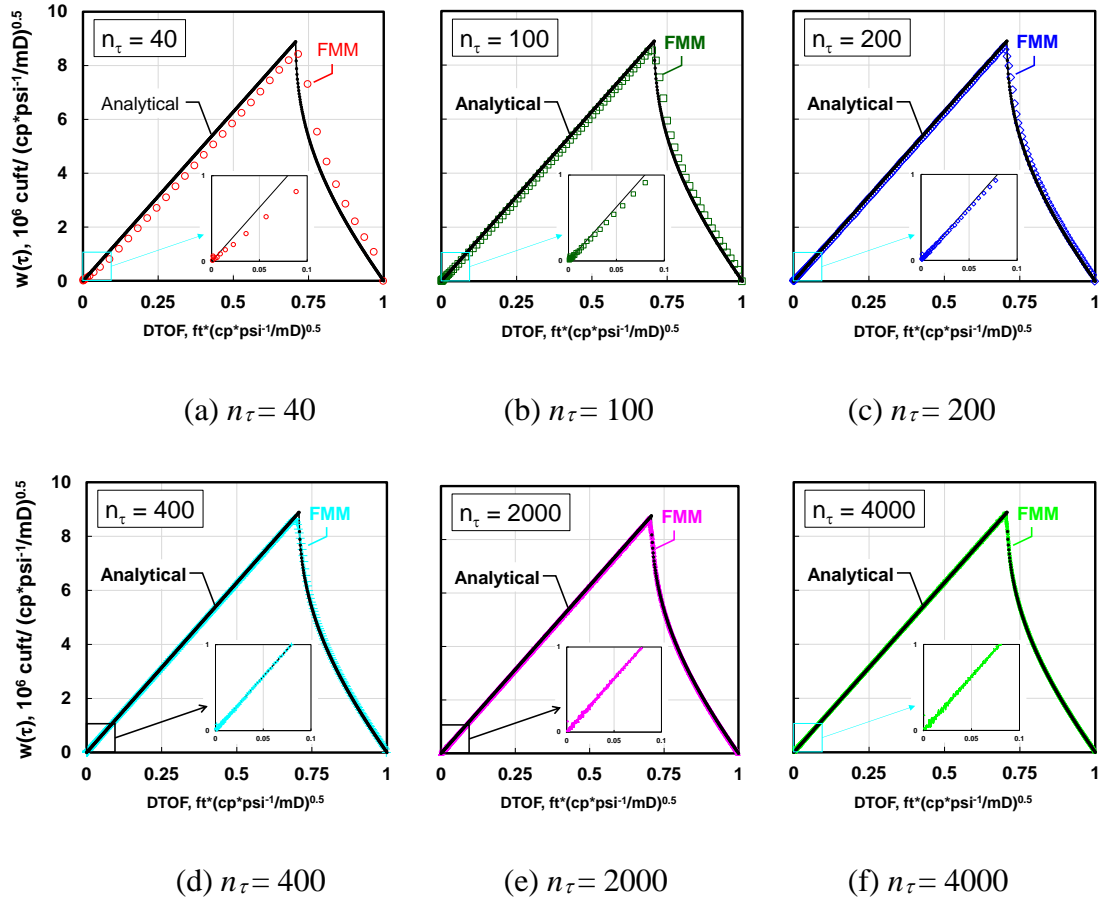


Figure 2.11 $w(\tau)$ function (line: analytical, symbol: numerical) for different numbers of 1-D grid blocks

Subsequently, we simulated a constant rate drawdown of 10 stb/day using the different numbers of the 1-D grid blocks using $w(\tau)$ functions in Figure 2.11. **Figure 2.12** shows comparisons of the bottomhole pressure between the FMM-based simulation and the analytical solution in the transient and pseudo-steady state period. As expected, the underestimated bottomhole pressure is seen in the FMM-based simulation with 40 and

100 grid blocks. For larger numbers of 1-D grid blocks, the solution converges to the analytical solution.

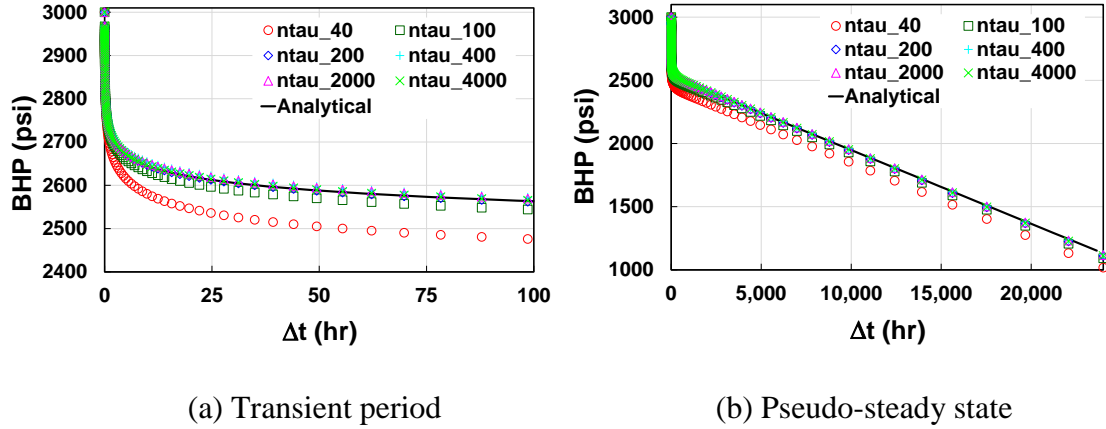


Figure 2.12 Bottomhole pressure for constant rate drawdown (10 stb/day) for different numbers of 1-D grid blocks

2.5.1.3 Validating Number of 1-D Grid Blocks

As we have seen the convergence of the 1-D simulation results with respect to numbers of 1-D grid blocks, there should be a point of diminishing improvement in simulation accuracy. We may utilize $w(\tau)$ function to evaluate the optimum number of 1-D grid blocks since the convergence of 1-D simulation results depends on that of $w(\tau)$ function.

Using the example of 2-D homogeneous single-porosity model (Case-1), we evaluated how $w(\tau)$ function converges with increasing number of 1-D grid blocks based on the RMS (**Figure 2.13**). The black circle shows the RMS where we used the $w(\tau)$

function with 4,000 grid blocks as a reference solution. It can be clearly observed that the solution starts converging around 200-400 grid blocks, which is consistent with the visual inspection of the plots in Figure 2.11. Alternatively, we could use the $w(\tau)$ function with the less number of 1-D grid blocks e.g. 40 grid blocks as a true solution (red triangle) to avoid unnecessary calculations of $w(\tau)$ function with fine grids. Thus, we can assess the desired number of 1-D grid blocks based on the $w(\tau)$ function without running 1-D simulations.

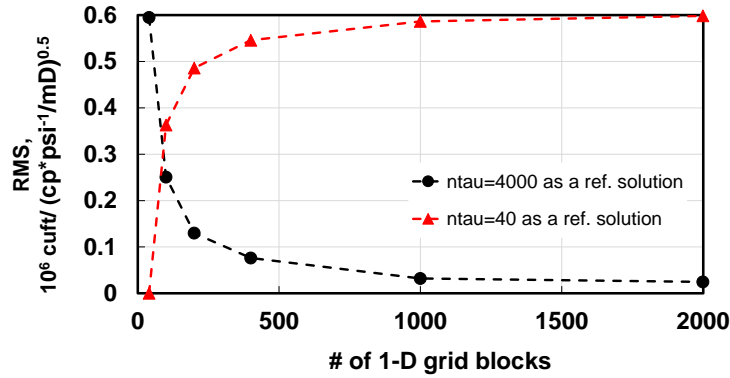


Figure 2.13 RMS of $w(\tau)$ function for different numbers of 1-D grid blocks from cell-center FMM and smoothing

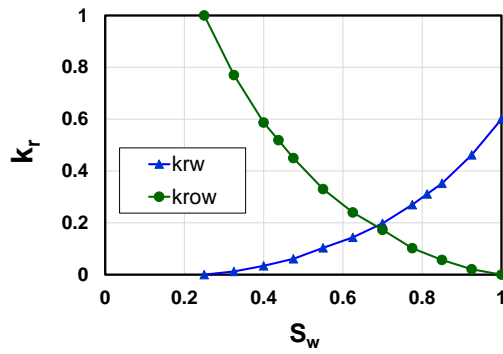
2.5.2 Multi-phase Case—Homogeneous Reservoir

In this subsection, we validate the FMM-based simulation for multi-phase flow using a homogeneous reservoir model. **Table 2.4** shows the reservoir properties, initial conditions for the fracture and matrix and well constraints. The model size was 4100' \times 4100' \times 50' dimensioned by 41 \times 41 \times 10 (16,810) grid blocks. The three-phase relative

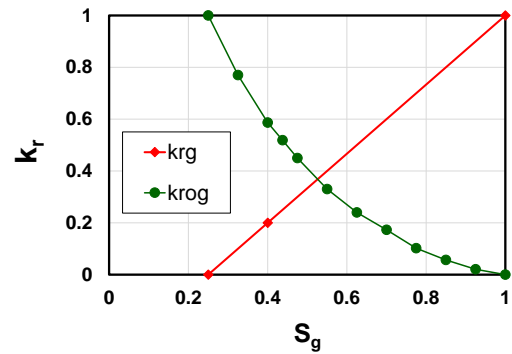
permeability is illustrated in **Figure 2.14**. The reservoir is undersaturated with the solution gas-oil-ratio (GOR) of 1,345 scf/stb at the initial pressure of 6,000 psi whereas the bubble point pressure is 2,860 psi. The blackoil table depicted in **Figure 2.15** was generated based on the Bakken fluid (Najabaei et al., 2013). The water compressibility and viscosity are 10^{-6} psi⁻¹ and 1 cp, respectively. The producer operating with the constant bottomhole pressure of 2,000 psi was placed at the center of the reservoir and completed vertically in all layers.

**Table 2.4 Simulation input for 3-D homogeneous and multi-phase example
(reprinted with permission from Iino et al., 2017a)**

Items		Fracture	Matrix
Reservoir Property	Porosity	0.01	0.10
	Permeability (mD)	2	10^{-4}
	k_v/k_h	0.1	-
	Shape factor (ft ²)	0.15 ft ²	-
	Rock compressibility (psi ⁻¹)	1.0×10^{-6}	1.0×10^{-6}
Initial Condition	Pressure (psi)	6000	6000
	Water saturation	0.0	0.40
	Solution GOR (scf/stb)	1345	1345
Well Constraints	Const. BHP (psi)	2000	-

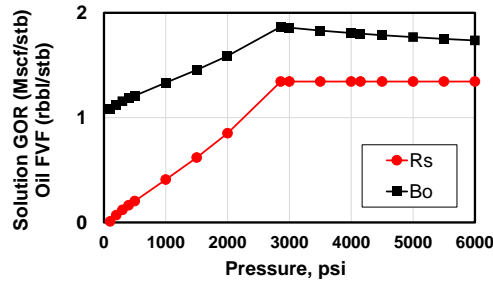


(a) Water-oil

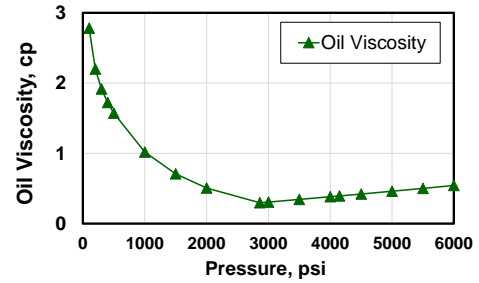


(b) Gas-oil

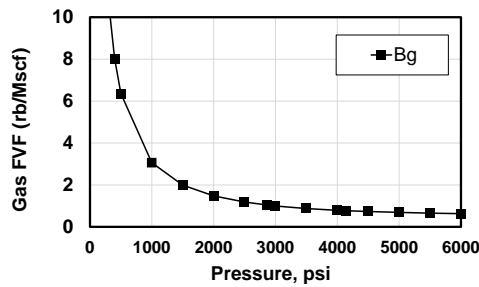
Figure 2.14 Relative permeability for 3-D homogeneous and multi-phase example



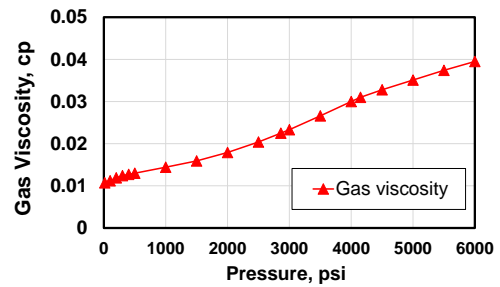
(a) Oil FVF and Solution GOR



(b) Oil viscosity



(c) Gas FVF



(d) Gas viscosity

Figure 2.15 PVT data for 3-D homogeneous and multi-phase example

The DTOF, V_p and $w(\tau)$ were computed as depicted in **Figure 2.16** where the number of 1-D grid was set to be 200. As the producer is completed in entire thickness, the pressure front expands laterally in the absence of gravity and capillarity. The $w(\tau)$ function shows a straight line until the DTOF of $28 \text{ hr}^{-1/2}$, followed by the decrease towards zero. Again, the $w(\tau)$ function physically implies the surface area of the pressure front and indicates flow regimes. The linear increase and subsequent decrease of the $w(\tau)$ function indicate the radial flow regime and the boundary effect, respectively.

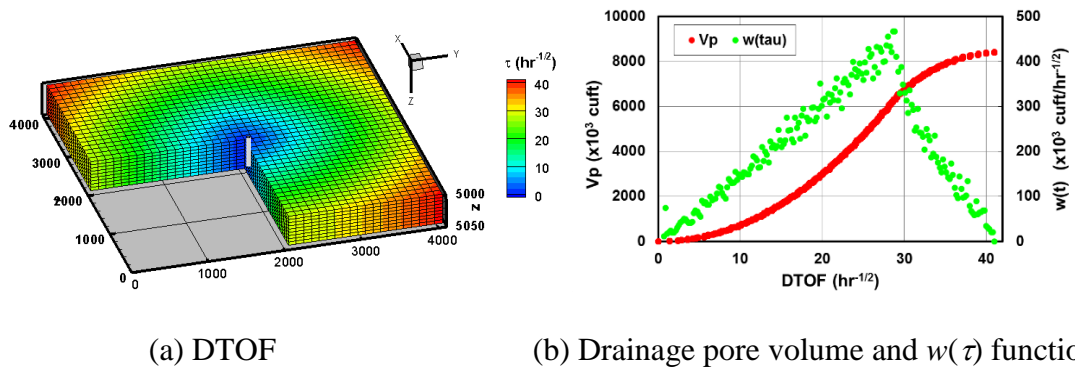


Figure 2.16 Calculated DTOF, drainage volume and $w(\tau)$ function for 3-D homogeneous and multi-phase example (reprinted with permission from Iino et al., 2017a)

Next, the 1-D simulation was performed on the DTOF coordinate. The oil rate, GOR and water rate simulated by the FMM-based approach are compared with a commercial FDSim in **Figure 2.17**. For all the three phases, the FMM-based simulation provides a close matching with the FDSim.

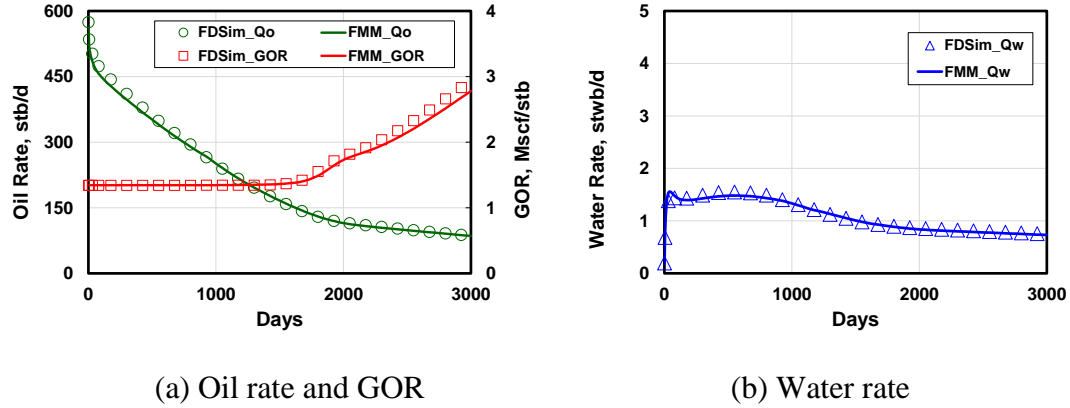


Figure 2.17 Comparison between FMM (solid lines) and FDSim (symbols) for 3-D homogeneous and multi-phase example (reprinted with permission from Iino et al., 2017a)

2.5.3 Computation Time

Computational efficiency of our proposed approach was also studied. **Figure 2.18** illustrates the CPU time comparison with the FDSim. The same dataset as the above multi-phase example was used except the number of grid blocks; the reservoir domain was further refined into $101 \times 101 \times 10$ (102,010) and $317 \times 317 \times 10$ (1,004,890). The number of 1-D grid was fixed to be 200 for all the cases, which was confirmed to be enough number based on the convergence check of $w(\tau)$ function. As the number of original grid blocks increases, more significant improvement in computation efficiency can be seen in our proposed approach that is based on the 1-D formulation. At least two orders of magnitude faster computation in the FMM-based simulation is expected in simulation with millions of grid cells, as compared to the FDSim.

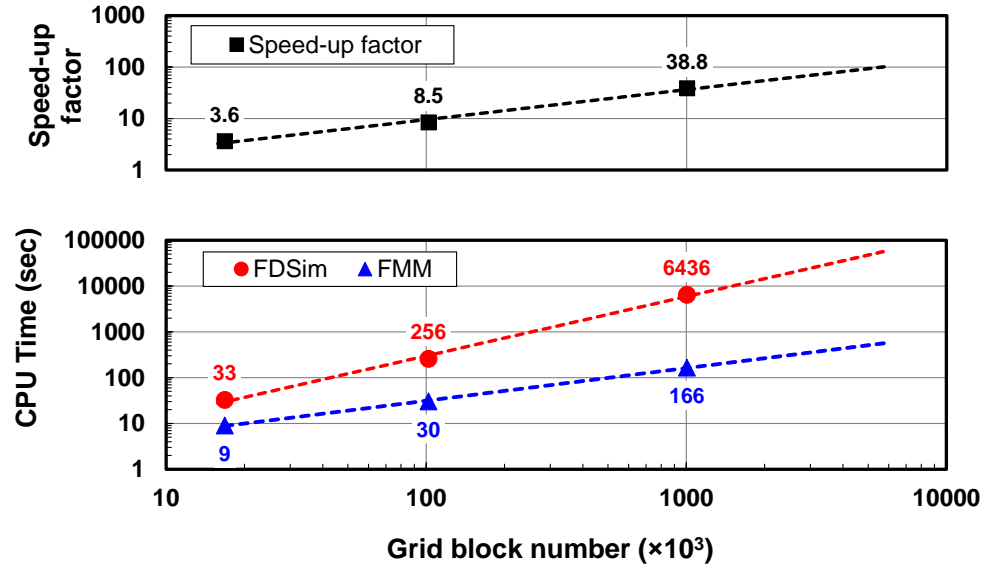
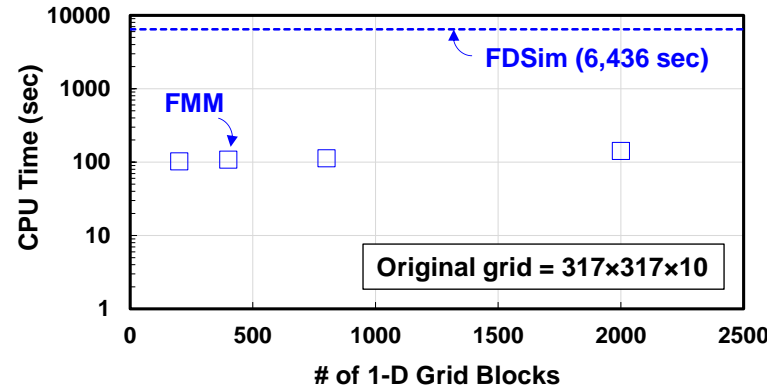


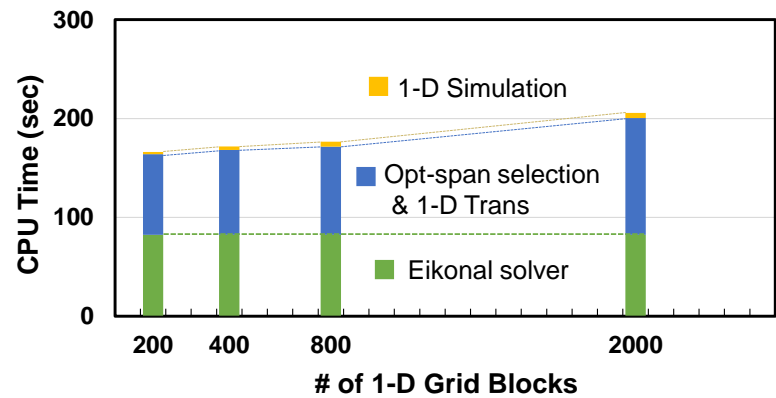
Figure 2.18 Comparison of CPU time (bottom) between commercial FDSim and FMM-based simulation and speed-up factor (top). Number of 1-D grid blocks and number of time steps are fixed to be 200 and 128, respectively (reprinted with permission from Iino et al., 2017a)

In the CPU time comparison in Figure 2.18, we fixed the number of 1-D grid blocks to be 200. We also studied CPU times for different numbers of 1-D grid blocks using the case of one million cells ($317 \times 317 \times 10$) as illustrated in **Figure 2.19a**. It indicates that the number of 1-D grid blocks does not significantly impact on CPU time performance in relative sense compared to the CPU time of the FDSim. **Figure 2.19b** shows the breakdown of CPU time for the FMM-based simulation. Solving the Eikonal equation for the DTOF only depends on the cell counts of original grid and has nothing to do with the number of 1-D grid blocks. The 1-D simulation requires only a small portion of the total

CPU time in this case. Although CPU time for the optimum span selection increases for the larger number of 1-D grid blocks, the impact is not significant.



(a) FDSim vs. FMM-based simulation for each number of 1-D grid blocks



(b) Breakdown of CPU time

Figure 2.19 Comparison of CPU time of FMM-based simulation for different number of 1-D grid blocks

There should be two different contributions to the speed up resulting from transforming the 3-D to 1-D problem: (1) reduction in cell counts for the flow simulation and (2) structural change in the Jacobian matrix by transforming the 3-D to 1-D equation. In order to distinguish the above two contributions, we compare the CPU time versus simulation cell counts between the 3-D and 1-D simulations (**Figure 2.20**). Note that CPU time in the 1-D simulation here only includes the 1-D flow simulation and neither include the Eikonal solver nor the 1-D transmissibility computation. We can observe the same trend between the 1-D and 3-D simulations, which indicates that structural change in Jacobian matrix has no or little impact on the computation time saving in the FMM-based simulation.

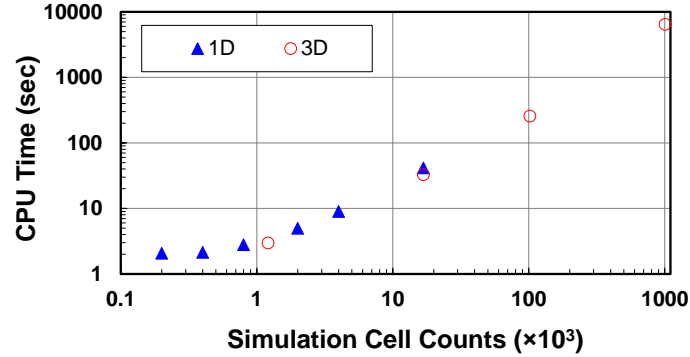


Figure 2.20 Comparison of CPU time between 3-D simulation and 1-D simulation in terms of simulation cell counts

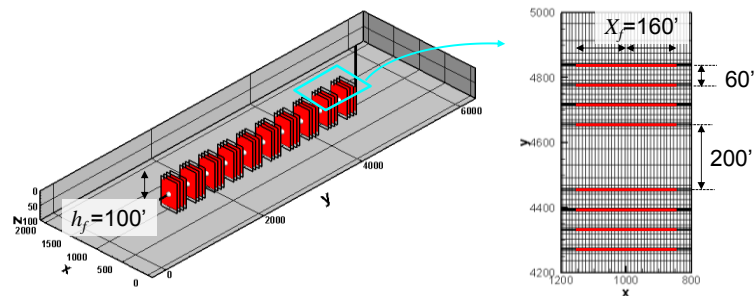
2.5.4 Multi-phase Case—Unconventional Reservoirs

Next, we present a 3-D synthetic example that includes reservoir heterogeneity and a multi-stage hydraulically fractured well.

A tartan grid was used with $200 \times 394 \times 5$ (0.394 million) grid blocks where the grid sizes are uniform in x - and z -directions ($\Delta x = 10'$ and $\Delta z = 20'$) and logarithmically resolved near the hydraulic fractures in y -direction (**Figure 2.21**). A horizontal well was completed with 40 transverse hydraulic fractures where the cluster and stage spacing were 60' and 200', respectively. The individual hydraulic fracture was represented by the grid blocks with the dimension of $320' \times 1' \times 100'$. Accounting for the fracture width of 1' that is much larger than reality, the effective properties rather than intrinsic properties were assigned for hydraulic fractures as summarized in **Table 2.5**. The matrix was assumed to be homogeneous. The heterogeneous properties for natural fractures are illustrated in **Figure 2.22**. In the simulation of shale reservoirs, the initial water saturation accounting for the completion fluids can be a key variable for the history matching (Diaz de Souza, 2012). In this example, the initial water saturations of 0.9 and 0.8 were assigned for hydraulic and natural fractures around the wellbore, respectively. The transmissibility reduction in the hydraulic and natural fractures due to the compaction was modeled as a function of pore pressure as depicted in **Figure 2.23** (Wang, 2017). The relative permeability used here is illustrated in **Figure 2.24**. The reservoir was initially undersaturated at the pressure of 4,000 psi and the bubble point pressure of 2861 psi where the same PVT data was used in the previous example (Figure 2.15). The horizontal well was operated at the constant bottomhole pressure of 2,000 psi, neglecting the pressure loss in the wellbore.

Table 2.5 Simulation input for unconventional reservoir example (reprinted with permission from Iino et al., 2017a)

	Hydraulic Fracture	Matrix	Fracture
Porosity	0.076	0.076	Figure 2.22a
Permeability (mD)	10.0	1×10^{-6}	Figure 2.22b, c
k_v/k_h	0.1	0.1	Figure 2.22b, c
Rock compressibility (psi^{-1})	1.0×10^{-6}	1.0×10^{-6}	1.0×10^{-6}
Shape factor	-	-	Figure 2.22d
Initial water saturation	0.8	0.4	Figure 2.22e
Initial pressure (psi)		4000	
Solution GOR (scf/stb)		1345	
Well constraints	Const. BHP of 2000 psi		



(a) 3-D view

(b) Top view of two stages

Figure 2.21 Configuration of hydraulic fractures for 3D synthetic example (reprinted with permission from Iino et al., 2017a)

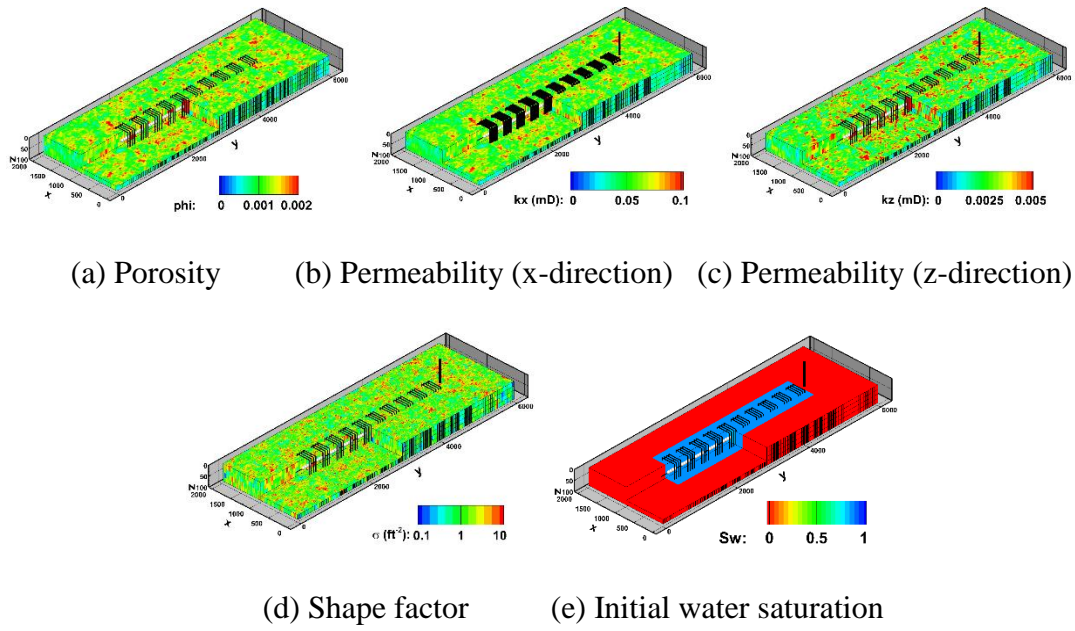


Figure 2.22 Reservoir properties and initial water saturation for the fracture in unconventional reservoir example (reprinted with permission from Iino et al., 2017a)

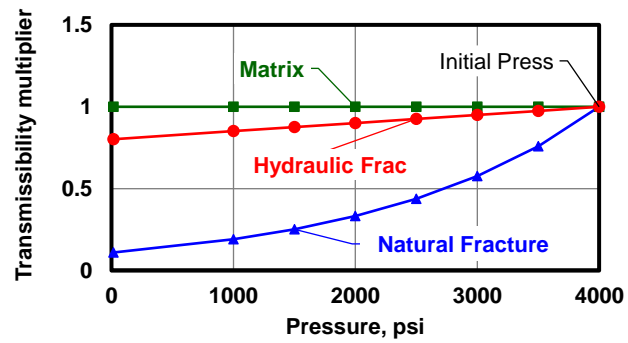


Figure 2.23 Rock compaction curves for fracture in unconventional reservoir example (reprinted with permission from Iino et al., 2017a)

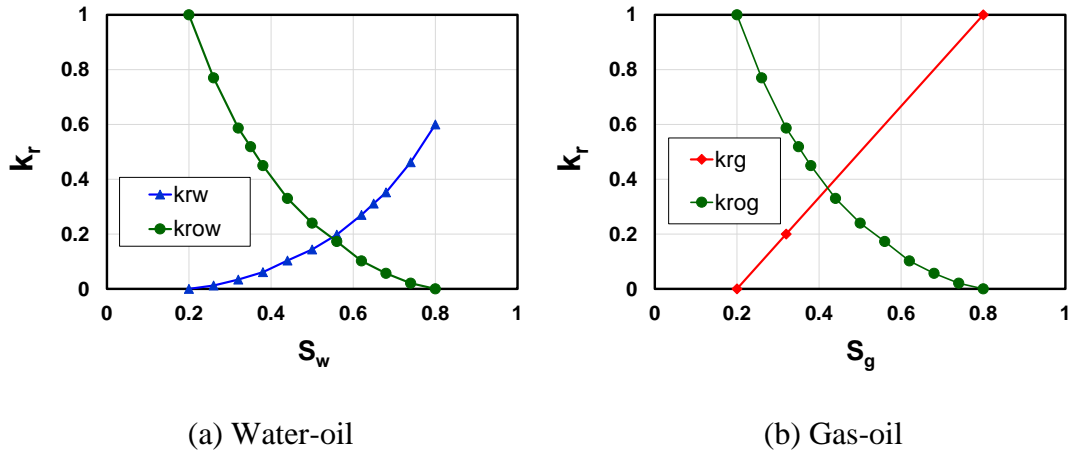


Figure 2.24 Relative permeability for 3-D homogeneous and multi-phase example

The DTOF, drainage pore volume and $w(\tau)$ function in the fracture system were computed as shown in **Figure 2.25**. Again, we can readily identify the expected flow regimes using $w(\tau)$ function and the DTOF map. In this example, six (6) distinct flow regimes were identified as captioned (a) through (g) in Figure 2.25 and the corresponding DTOF maps were depicted in **Figure 2.26**. Because of the small contrast of diffusivities between the hydraulic and natural fractures, no clear indication can be found for linear flow around each hydraulic fracture. Instead, the sharp increase (a) in the beginning indicates the radial flow in vertical direction, followed by the boundary effect represented by the steep decrease at (b). After the interference between stages seen at (c), the formation linear flow in x-direction starts as indicated in the flow regime (d). When the pressure propagation felt the boundaries in x-direction, subsequent linear flow (e) in y-direction would start. Finally, the complete pseudo-steady state (f) will be established that leads to $w(\tau)$ function towards zero.

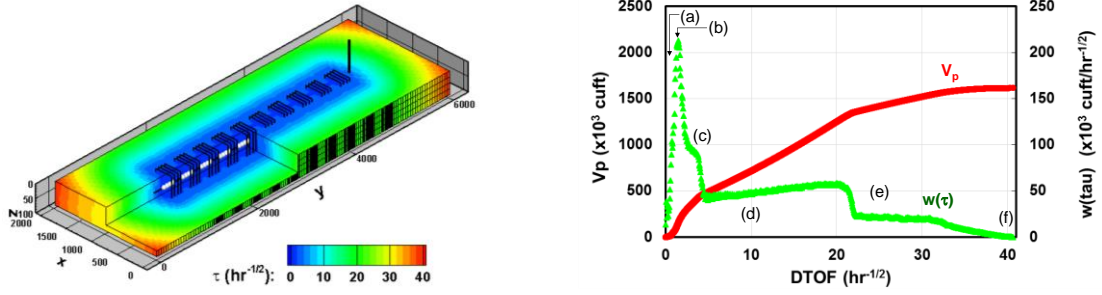


Figure 2.25 Calculated DTOF (left), drainage pore volume and $w(\tau)$ function (right) for unconventional reservoir example (reprinted with permission from Iino et al., 2017a)

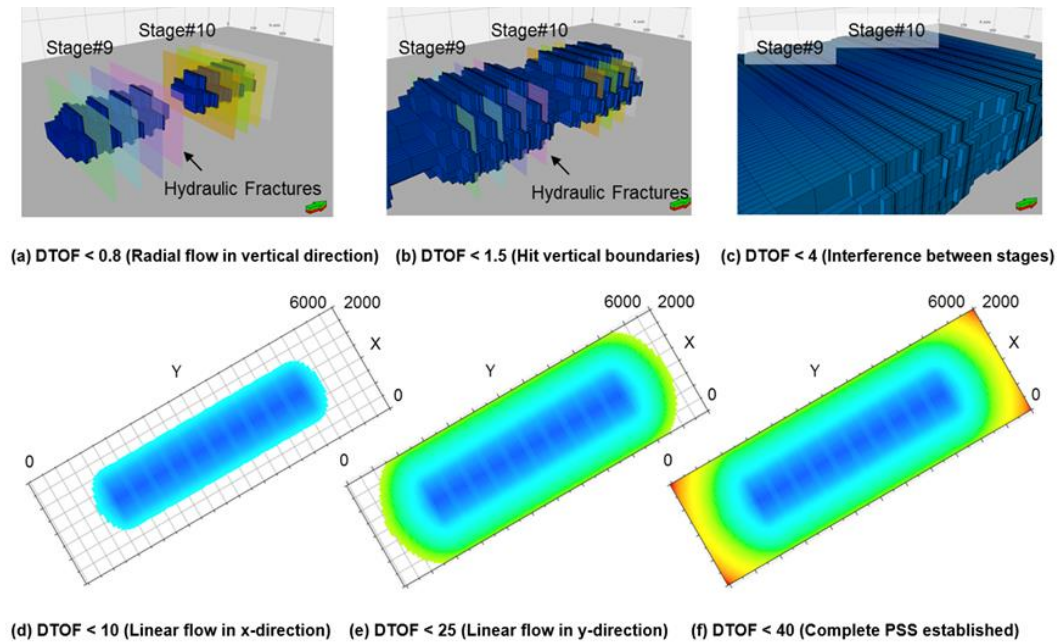
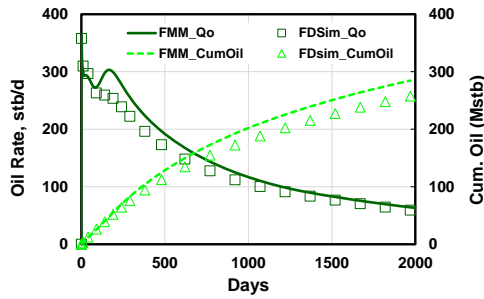


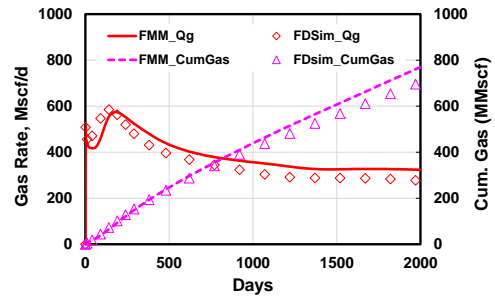
Figure 2.26 DTOF maps corresponding to each flow regime (a) through (f) in Figure 2.25 (reprinted with permission from Iino et al., 2017a)

The 1-D simulation was conducted using the DTOF as a spatial coordinate and the results were compared with the commercial FDSim. **Figure 2.27** shows the simulated well

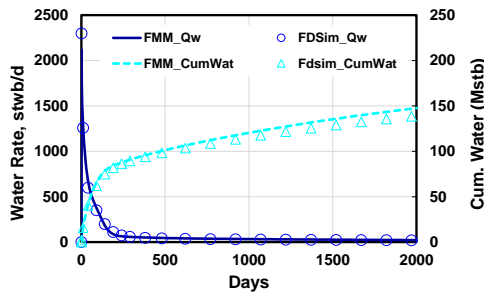
performance. It can be confirmed that the FMM-based simulation gives consistent results with the FDSim for all three phase productions. Initially, high water production rate was seen due to the high water saturation in and around the hydraulic fractures, followed by the stable rate that comes from the matrix (Figure 2.27c and Figure 2.27d). GOR keeps increasing as the bottomhole pressure (2,000 psi) is less than the bubble point pressure of 2,830 psi. The run time by the FDSim was 1,150 seconds while the FMM only needed 134 seconds, which offered an order of magnitude faster computation. Thus, our proposed approach is capable of efficient simulation with the high resolution heterogeneous models and multi-phase effects.



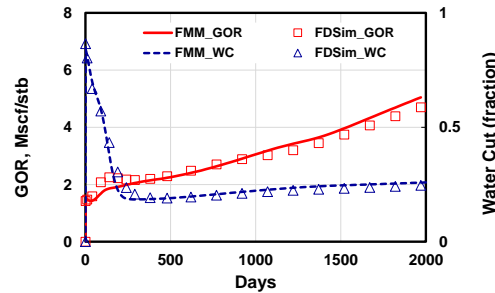
(a) Oil rate and cumulative oil



(b) Gas rate and cumulative gas



(c) Water rate and cumulative water



(d) GOR and water cut

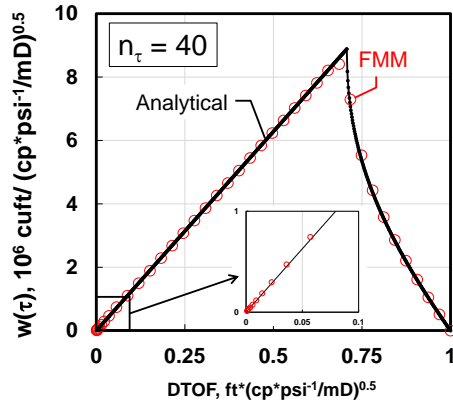
Figure 2.27 Comparisons of simulation results between the FMM and commercial FD simulator for unconventional reservoir example (reprinted with permission from Iino et al., 2017a)

2.6 Comparison between Cell-center FMM and 27pt-stencil FMM

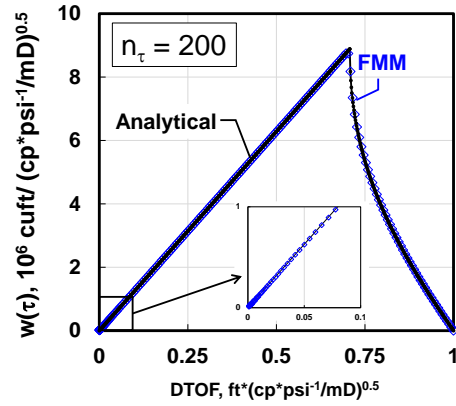
Thus far, we have used the cell-center FMM in conjunction with the smoothing technique to calculate $w(\tau)$ function in the validation cases above. As presented in 2.4.4, Chen (2018) proposed an improved calculation of $w(\tau)$ based on the 27pt-stencil FMM. In this section, we compare the two methods and discuss pros/ cons of each method.

2.6.1 Accuracy, Stability and Convergence

Using the single-phase example in 2.5.1 (Case-1), we calculated $w(\tau)$ function by Eq. (2.57) with the 27pt-stencil FMM as shown in **Figure 2.28** where two different numbers of 1-D grid blocks of 40 and 100 were tested. Comparing with the $w(\tau)$ function from the cell-center τ and the smoothing technique (Figure 2.11), excellent matching with the analytical calculation can be confirmed even for the small number of 1-D grid blocks ($n_\tau = 40$). The resulting bottomhole pressure for the constant rate drawdown of 10 stb/day also shows good agreement with the analytical solution (**Figure 2.29**).

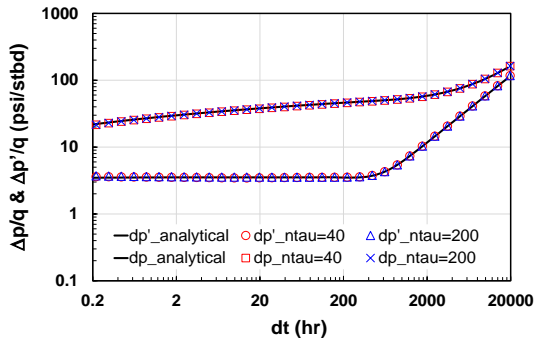


(a) 40 grid blocks

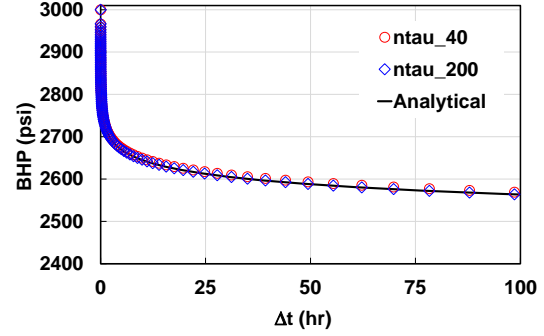


(b) 200 grid blocks

Figure 2.28 $w(\tau)$ function from 27pt-stencil FMM



(a) Log-log diagnostic plot

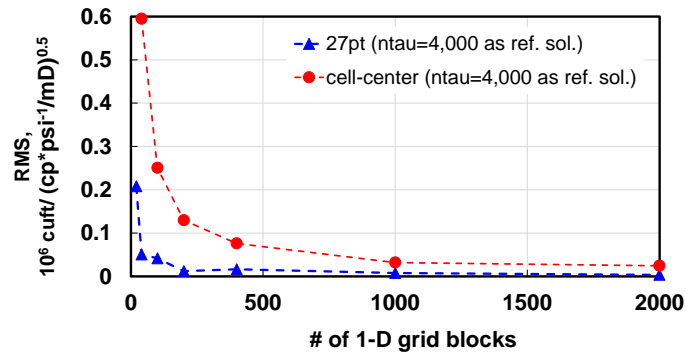


(b) Linear plot (transient plot)

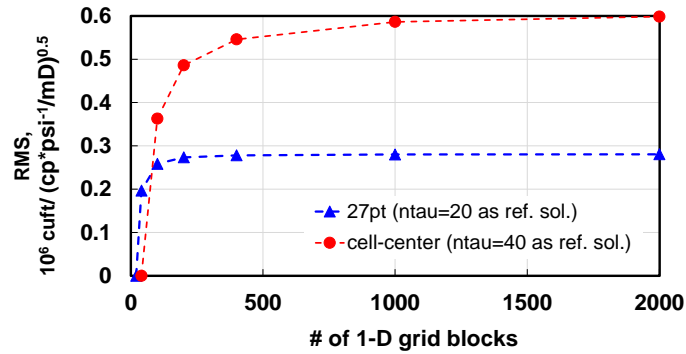
Figure 2.29 Bottomhole pressure for constant rate drawdown of 10 stb/day from FMM-based simulation with $w(\tau)$ function using 27pt-stencil FMM (2-D homogeneous reservoir)

We also calculated the RMS of $w(\tau)$ function for different numbers of 1-D grid blocks using $w(\tau)$ functions with (a) 4,000 grid blocks or (b) 20 grid blocks as a reference solution (**Figure 2.30**). As the number of 1-D grid blocks increases, $w(\tau)$ function from

the 27pt-stencil FMM (blue triangle) converges quickly, indicating that 40-100 grid blocks are sufficient numbers for the 1-D simulation. For comparison, the RMS of $w(\tau)$ function from the cell-center FMM and the smoothing technique is also depicted (red circle), which requires 200-400 grid blocks for $w(\tau)$ function to converge and yields larger errors compared to the 27pt-stencil FMM. Thus, the 27pt-stencil FMM can provide more stable and accurate $w(\tau)$ function than the cell-center FMM.



(a) $w(\tau)$ with 4,000 grid blocks as a reference solution



(b) $w(\tau)$ with 20 or 40 grid blocks as a reference solution

Figure 2.30 Comparison of RMS of $w(\tau)$ function between 27pt-stencil FMM (blue triangle) and cell-center FMM with smoothing (red circle)

2.6.2 CPU Time

As discussed above, $w(\tau)$ function from the 27pt-stencil FMM is more robust in terms of accuracy and convergence compared to the one from the cell-center FMM and the smoothing technique. However, the challenge of the 27pt-stencil FMM is expensive computational costs because the number of solution nodes of the DTOF, which is $(2*N_x+1) \times (2*N_y+1) \times (2*N_z+1)$ in the 27pt-stencil FMM, is larger than that of the cell-center FMM ($N_x \times N_y \times N_z$). **Figure 2.31** shows the comparison of CPU time for solving the Eikonal equation by the two methods. For high resolution models with millions of grid blocks, the 27pt-stencil FMM requires more computation time by 1-2 orders of magnitude compared to the cell-center FMM. Further details have been studied by Chen (2018). Thus, it is practically recommended to use the cell-center FMM in such cases that we validated in section 2.5.

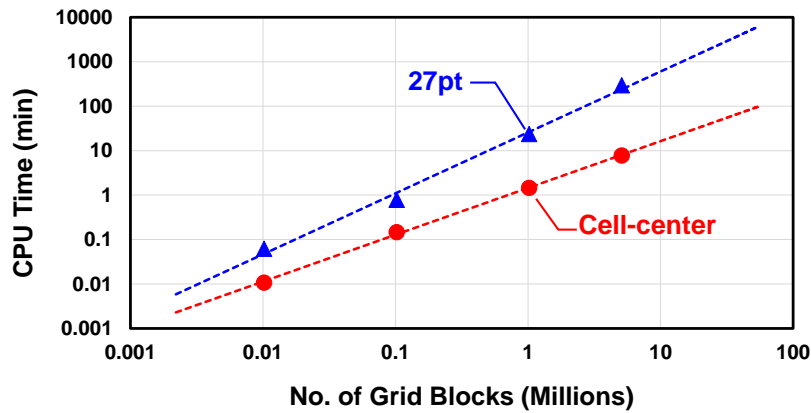


Figure 2.31 CPU time comparison for solving Eikonal equation between cell-center FMM (red) and 27pt-stencil FMM (blue)

2.6.3 Case Example That Requires 27pt-stencil FMM

One of the cases where the 27pt-stencil FMM works better than the cell-center FMM is a fractured well with the extreme contrast in permeability between fractures and formation. To illustrate this, we set up a 2-D homogeneous single-porosity model completed by a single hydraulic fracture as illustrated in **Figure 2.32**. The reservoir domain of 2,970'×3,000'×100' was gridded by 101×101×1 cells. The grid block width of hydraulic fracture cells was set to be 2' and logarithmic gridding was used in the direction perpendicular to the fracture plane. Single-phase fluid was assumed with the constant viscosity of 1 cp and the total compressibility of $1 \times 10^{-5} \text{ psi}^{-1}$. There is an 8-order of magnitude difference in permeability between hydraulic fracture (1000 mD) and formation (50 nD).

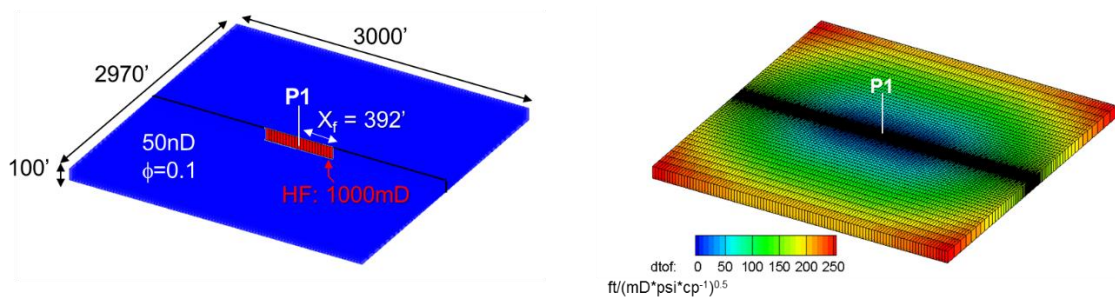


Figure 2.32 Single hydraulic fracture model in 2-D homogeneous reservoir and DTOF

We compared $w(\tau)$ functions from the two methods in **Figure 2.33** where significant difference can be seen in the DTF between 0.01-0.1, which corresponds to the interface between the hydraulic fracture and formation. $w(\tau)$ function from the 27pt-stencil FMM (blue triangle) well captures a linear flow regime characterized by a flat line that continues until the DTOF of 10. On the other hand, $w(\tau)$ function from the cell-center τ and the smoothing technique shows much less values around the fracture/ formation interface, which plays a role of transmissibility barrier that should not exist. We also carried out the FMM-based simulations using both $w(\tau)$ functions and compared the results with the FDSim (**Figure 2.34**). As expected, the FMM-based simulation with $w(\tau)$ function from the cell-center τ and the smoothing shows steep depletion and deviates from the FDSim (black solid line), whereas simulation with the 27pt-stencil FMM (blue triangle) gives excellent agreement with the FDSim.

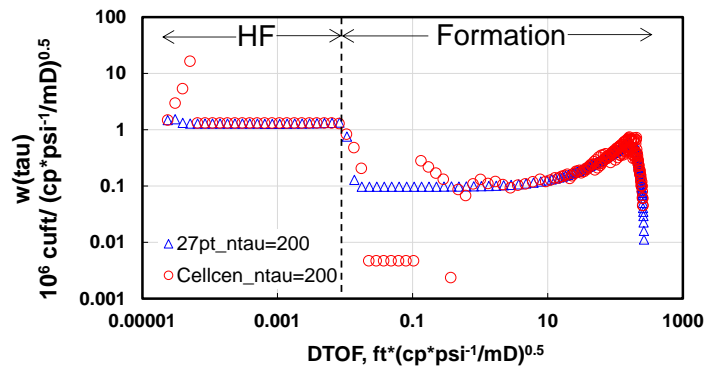


Figure 2.33 Comparison of $w(\tau)$ functions from cell-center DTOF with smoothing (red) and 27pt-stencil FMM (blue) in 2-D homogeneous reservoir completed by single fracture

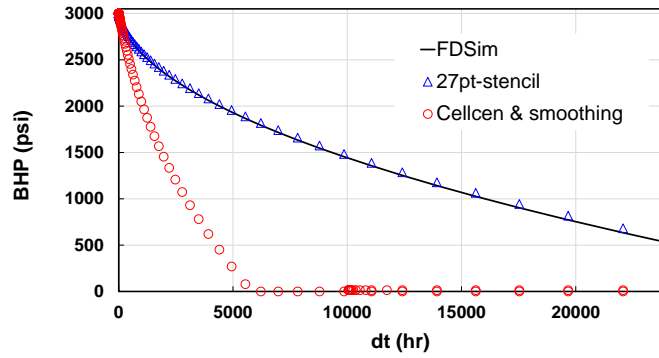
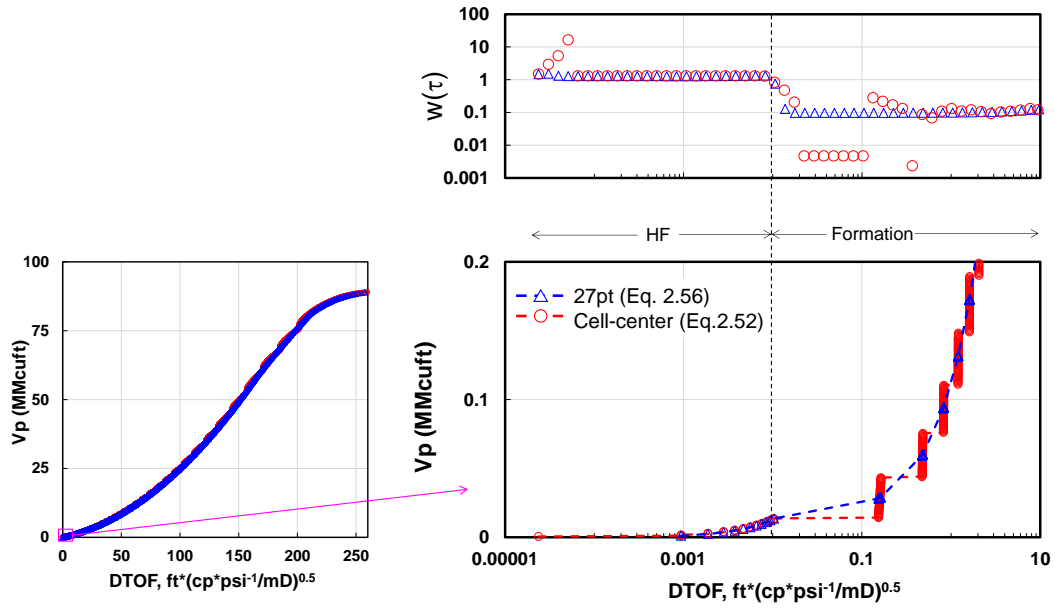


Figure 2.34 Bottomhole pressure for constant rate drawdown of 1 stb/ from cell-center DTOF with smoothing (red) and 27pt-stencil FMM (blue) in 2-D homogeneous reservoir completed by single fracture

The reason of this performance difference between the two methods is simply because of how the pore volume is accumulated as a function of the DTOF. $V_p(\tau)$ becomes a stair-wise function by Eq. (2.52) when the cell-center FMM is used, whereas smooth $V_p(\tau)$ can be obtained by Eq. (2.56) with the 27pt-stencil FMM. **Figure 2.35** illustrates comparison of $V_p(\tau)$ obtained from the two methods. Because of the lack of data in fracture/ formation interface ($0.01 < \tau < 0.1$), the cell-center FMM with smoothing fails to capture the slope of $V_p(\tau)$ function, leading to underestimated $w(\tau)$ function. On the other hand, the 27pt-stencil FMM can yield smooth transition from fracture to formation by the use of interpolation utilizing the maximum and minimum DTOF in each cell. This issue in the cell-center FMM can be potentially mitigated by the adaptive selection of optimum span size or calculating $V_p(\tau)$ and $w(\tau)$ functions individually for the fracture and formation.



(a) $V_p(\tau)$ for whole reservoir domain

(b) $w(\tau)$ (top) and $V_p(\tau)$ (bottom) around well

Figure 2.35 Pore volume and $w(\tau)$ function from cell-center and 27pt-stencil FMM

2.7 Field Application: History Matching

Next, we studied the application of our proposed method to the field example of the shale oil reservoir in Texas where the matrix permeability ranges between micro- and nano-Darcy. We modelled the reservoir section of the single horizontal well with 10-stage hydraulic fractures. The simulation model was then history-matched and used for the production forecast.

2.7.1 Production Data

The three-phase production and the wellhead pressure data are available for 380 days as illustrated in **Figure 2.36**. The well opened at 1,300 bbl/d liquid rate and declined to 100 bbl/d during the observation period. High water cut during the early production was due to the recovery of completion fluid. The production GOR stayed constant of 2.1 Mscf/stb for the first three months and then kept on increasing. This indicates that the reservoir was initially undersaturated and the liberation of solution gas started due to pressure depletion.

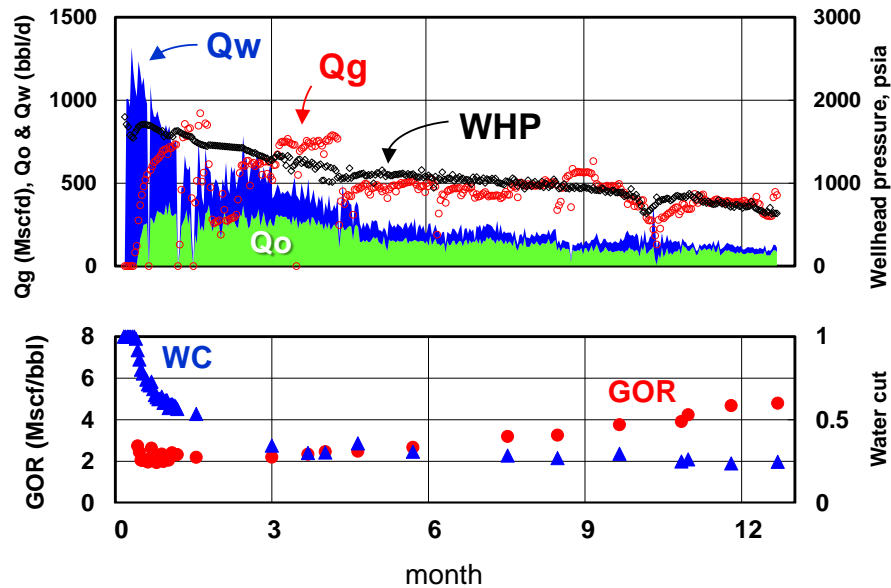


Figure 2.36 Production data of 10-stage hydraulically fractured well in a shale oil reservoir: wellhead pressure and oil, gas and water rates (Top) and GOR and water cut (bottom) (reprinted with permission from Iino et al., 2017a)

2.7.2 Base Case Model

The base case model was provided by the operating company. The modelled reservoir section is dimensioned 7,100'×2,500'×180' and resolved into 71×25×13 (23,075) grid blocks. The reservoir is undersaturated at the initial pressure of 3,953 psi against the bubble point pressure of 2,930 psi with the solution GOR of 2,100 scf/stb. A dual-porosity model is assumed. Three distinct regions were defined for the fracture as illustrated in **Figure 2.37**: hydraulic fractures, Stimulated Reservoir Volume (SRV) and non-SRV. Stages of the transverse hydraulic fractures are represented by the simulation grid blocks highlighted by red color.

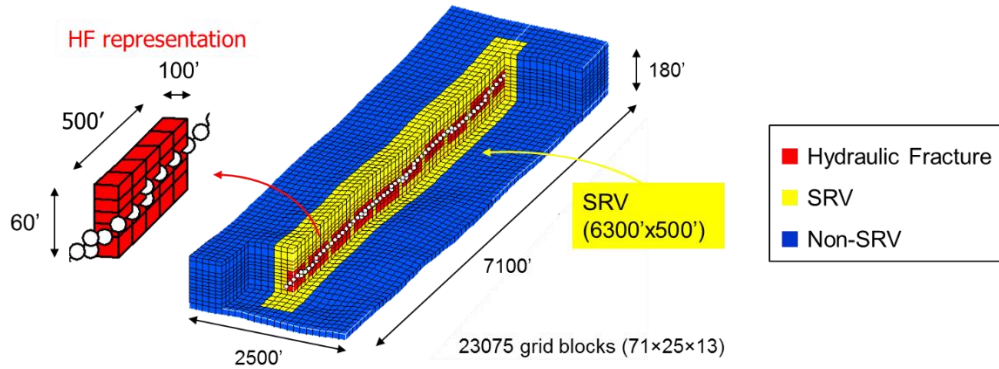


Figure 2.37 Definition of regions for base case model (reprinted with permission from Iino et al., 2017a)

Matrix properties were derived from core and log interpretations. For the purpose of the study, average matrix reservoir properties have been used: porosity, permeability and initial water saturation were 0.08, 2.7×10^{-5} mD and 0.41, respectively. The reservoir

heterogeneity was accounted for the fracture as per the regions defined above and shown in **Figure 2.38**. Due to the lack of data such as micro-seismic that indicates the SRV extent and production logging data to characterize the contribution to the production from individual hydraulic fractures, the base case values for the fracture and dimensions of hydraulic fractures and SRV were determined by the operator's prior experiences and to be calibrated in the history matching presented later. The reduction in pore volume and permeability due to the compaction was modelled as functions of pressure (**Figure 2.39**) and to be tuned as well during history matching. The PVT data is shown in **Figure 2.40**. The relative permeability of straight lines with no connect saturations is used for fracture, whereas **Figure 2.41** is used for matrix.

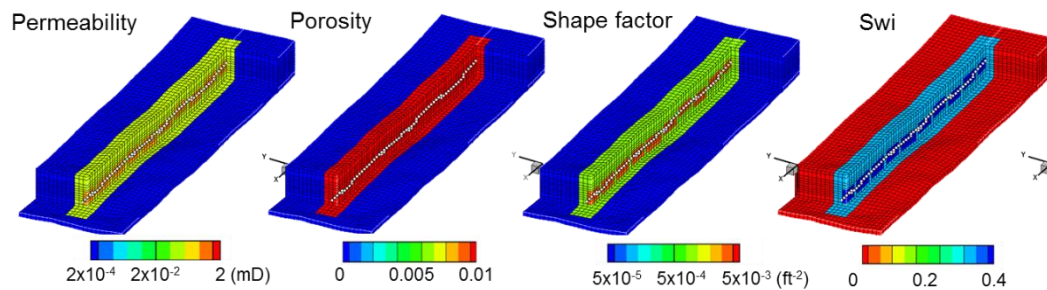
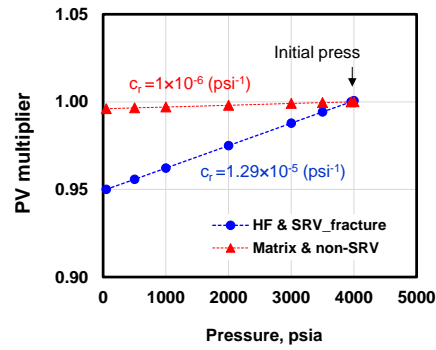
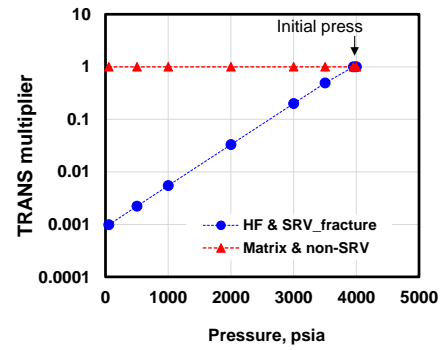


Figure 2.38 Reservoir properties of the base case model for fracture (reprinted with permission from Iino et al., 2017a)

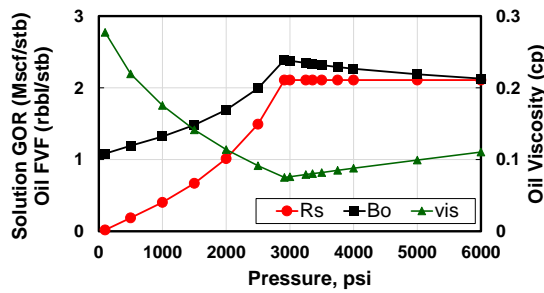


(a) Pore volume multiplier

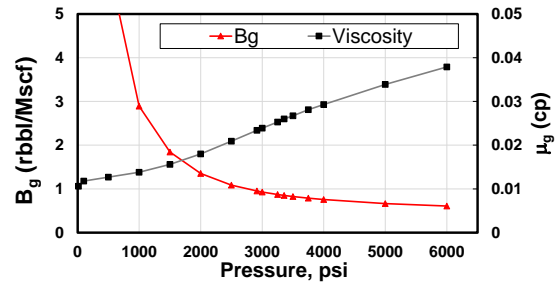


(b) Transmissibility multiplier

Figure 2.39 Rock compaction curves for field application (reprinted with permission from Iino et al., 2017a)

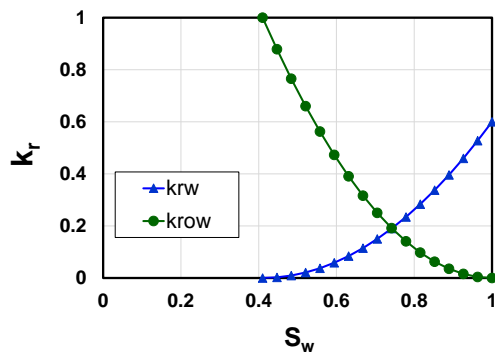


(a) Oil (saturated line only)

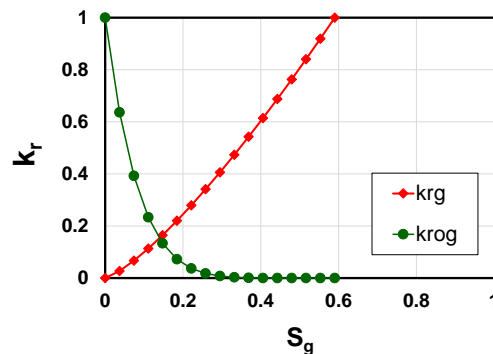


(b) Gas

Figure 2.40 PVT data for field application



(a) Water-oil



(b) Gas-oil

Figure 2.41 Relative permeability of matrix for field application

2.7.3 Benchmarking with Commercial FD Simulator

The base case simulation using our proposed approach was conducted for the history period of 380 days under the wellhead pressure constraint. The DTOF, V_p and $w(\tau)$ functions for the base case model are illustrated in **Figure 2.42**. Again, the DTOF is calculated only for the fracture in the dual-porosity model. From the DTOF map and $w(\tau)$ function, we can readily identify the four distinct flow regimes that imply the hydraulic fracture, SRV and Non-SRV. The Non-SRV region gives no significant contribution to the fracture drainage volume.

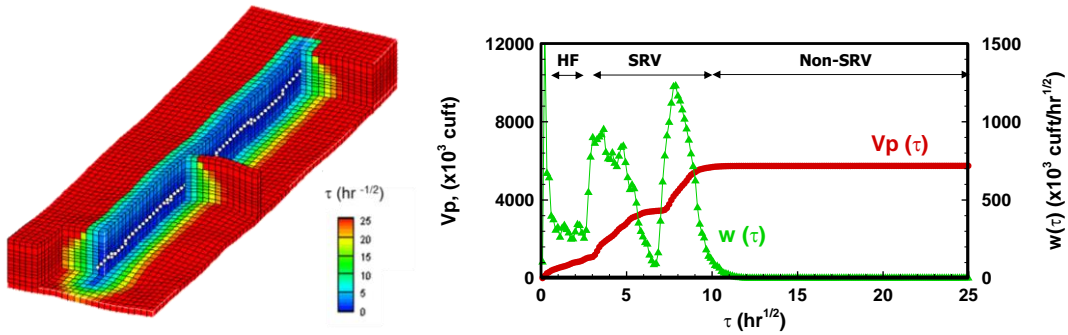
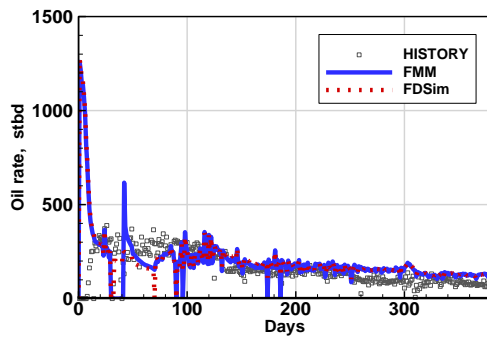


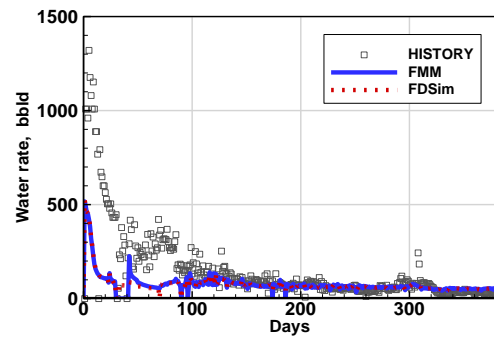
Figure 2.42 Calculated DTOF (left), drainage pore volume and $w(\tau)$ function (right) for unconventional reservoir example (reprinted with permission from Iino et al., 2017a)

Figure 2.43 shows the well performance simulated by our proposed approach and a commercial FDSim. For all the three phase production, the FMM-based simulation provides equivalent results with the FDSim. In Figure 2.43, simulation results are also

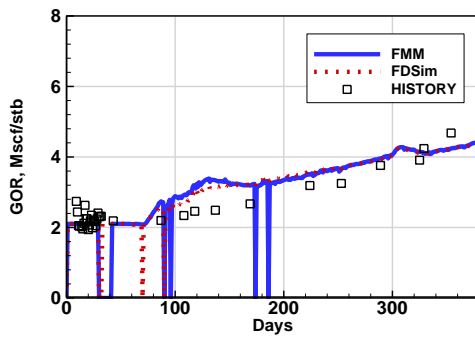
compared to the observed data where initial oil and water rate and the oil decline after 250 days from the simulation deviates. In the history matching presented later, the FMM-based approach was used for the forward simulation and the model parameters were calibrated to replicate the historical data. The FMM offered a three times faster computation compared to the FDSim.



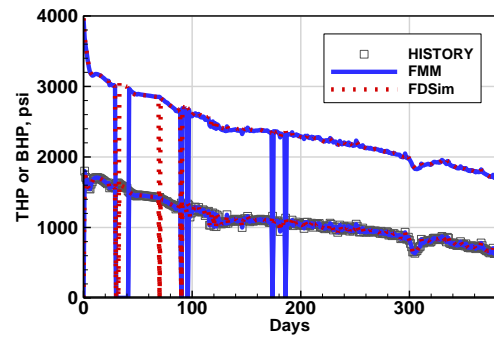
(a) Oil rate



(b) Water rate



(c) GOR



(d) Tubing head and bottomhole pressure

Figure 2.43 Comparison between FMM and commercial FD simulator for base case simulation. Blue solid line: FMM, red dashed line: FDSim, symbols: observed data (reprinted with permission from Iino et al., 2017a)

2.7.4 Uncertain Parameters

Due to the limited data availability, the significant uncertainty lies in the fracture properties and dimensions of hydraulic fractures and SRV. **Table 2.6** lists the uncertain parameters with the base values and ranges used for the sensitivity study. The terminologies for the dimensions of hydraulic fractures and SRV were defined as illustrated in **Figure 2.44**. For the sensitivity and history matching purpose, the 10-stage hydraulic fractures and SRVs were divided into three groups that have uniform properties. The sensitivity of the rock compaction was investigated by providing different rock tables as illustrated in **Figure 2.45**.

Table 2.6 Parameter uncertainties for sensitivity and history matching (reprinted with permission from Iino et al., 2017a)

Regions	Uncertain parameters	Base	Low	High
Hydraulic Fracture	Porosity (HF_poro1, HF_poro2, HF_poro3)	0.01	0.005	0.04
	Permeability (HF_perm1, HF_perm2, HF_perm3), mD	0.20	0.55	3.0
	Water saturation (HF_S _{wi})	0.4	0.2	0.95
	Shape factor (HF_sigma1, HF_sigma2, HF_sigma3), ft ⁻²	5×10 ⁻³	5×10 ⁻⁴	0.5
	Compaction table (HF_comp)	2	2	12
	Fracture half length (HF_Xf1, HF_Xf2, HF_Xf3), ft	50	50	150
	Fracture height (HF_h1, HF_h2, HF_h3), ft	60	40	100
SRV	Porosity (SRV_poro1, SRV_poro2, SRV_poro3)	0.01	0.005	0.02
	Permeability (SRV_perm1, SRV_perm2, SRV_perm3), mD	0.1	0.01	0.2
	Water saturation (SRV_ S _{wi} 1, SRV_ S _{wi} 2, SRV_ S _{wi} 3)	0.175	0.35	0.7
	Compaction table (SRV_comp)	2	2	12
	Shape factor (SRV_sigma1, SRV_sigma2, SRV_sigma3), ft ⁻²	1.25×10 ⁻³	1.25×10 ⁻⁴	0.125
	SRV_Width (SRV_W1, SRV_W2, SRV_W3), ft	500	300	900
Matrix	Porosity (Mat_poro)	0.08	0.059	0.094
	Permeability (Mat_perm), mD	2.7×10 ⁻⁵	2.3×10 ⁻⁷	1.3×10 ⁻⁴
	Water saturation (Mat_S _{wi})	0.41	0.3	0.77
	Connate water saturation (Mat_S _{wc})	0.7*S _{wi}	0.5*S _{wi}	1.0*S _{wi}

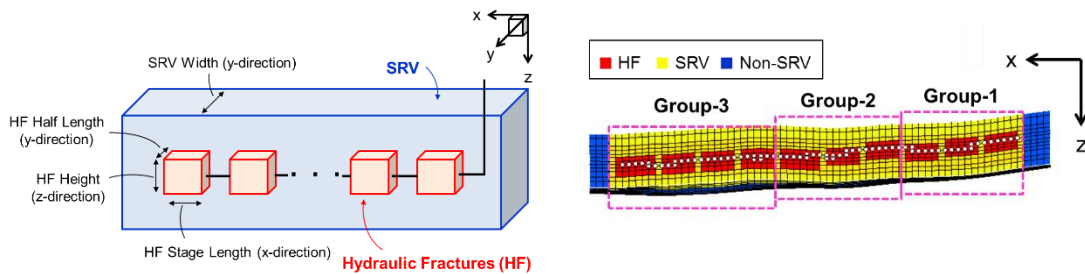


Figure 2.44 Setup of geometric parameters (left) and groups (right) for sensitivity study and history matching (reprinted with permission from Iino et al., 2017a)

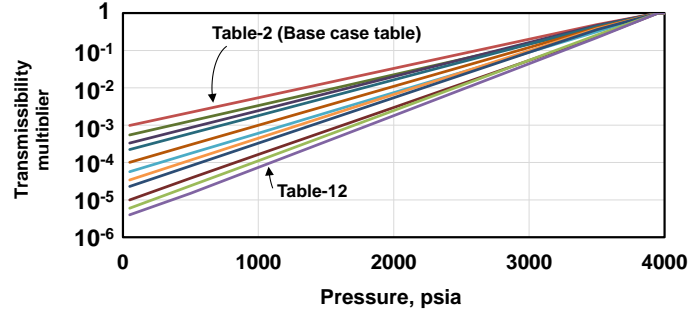


Figure 2.45 Rock compaction table used for sensitivity study. Greater table number represents more severe transmissibility reduction (reprinted with permission from Iino et al., 2017a)

2.7.5 Sensitivity Analysis

For the sensitivity study, the objective function was defined as the summation of misfits in the cumulative production for each of the three phases as:

$$f(\mathbf{m}) = \ln|\Delta\text{Cum_oil}| + \ln|\Delta\text{Cum_water}| + \ln|\Delta\text{Cum_gas}|, \quad (2.67)$$

where \mathbf{m} is a set of reservoir parameters and Δ represents the misfit of the model estimates from the observed data:

$$|\Delta y| \equiv \sqrt{\frac{1}{N_t} \sum_i^{N_t} |y_i^{\text{sim}} - y_i^{\text{obs}}|^2}. \quad (2.68)$$

where N_t is the number of time steps at which the observed data is available and subscript i is the time step level. **Figure 2.46** shows a tornado diagram of the objective function with respect to the parameters listed in Table 2.6. For hydraulic fractures, water saturation, shape factor and porosity have significant impact on the objective function. The half-

length of hydraulic fractures is also influencing while the height and stage lengths are less sensitive. For SRV, the most impacting parameter is the shape factor but all the other parameters except compaction have significant impact as well. The matrix porosity is less sensitive as even the low case has enough volume within the history period, while the matrix permeability is a heavy hitter that directly relates to the pressure support from the matrix to the fracture.

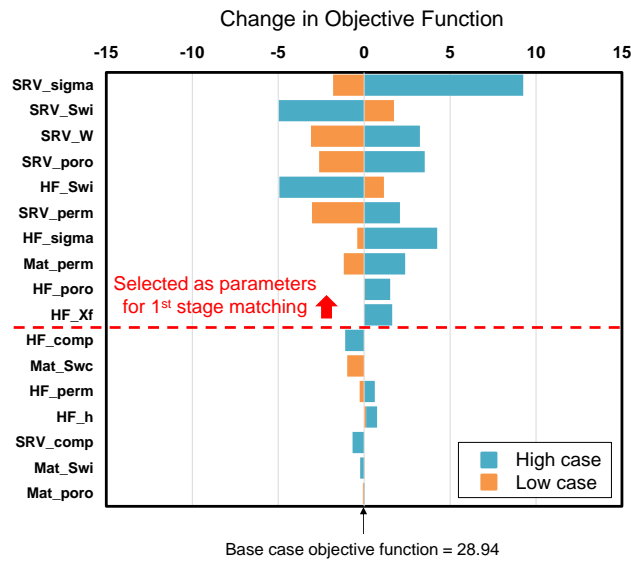


Figure 2.46 Sensitivity analysis for history matching example (first stage)

2.7.6 First Stage History Matching

The history matching was conducted by minimizing the objective function defined by Eq. (2.67). Due to a large number of parameters listed in Table 2.6, we used the two-stage genetic algorithm which starts with the limited number of parameters in the first

stage and then introduces the additional parameters in the subsequent stage (Cheng et al., 2008). Population size per generation was set to be 200.

The first stage history matching was conducted with tuning parameters selected based on the sensitivity analysis as noted by the red line in Figure 2.46. **Figure 2.47** shows the objective function versus generation number where the reduction in objective function almost stabilized by tenth generation.

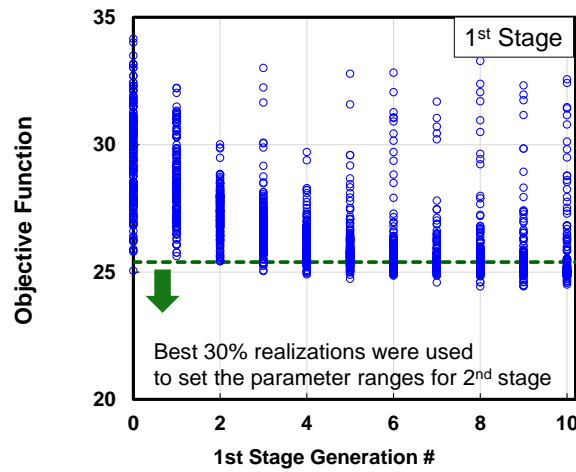
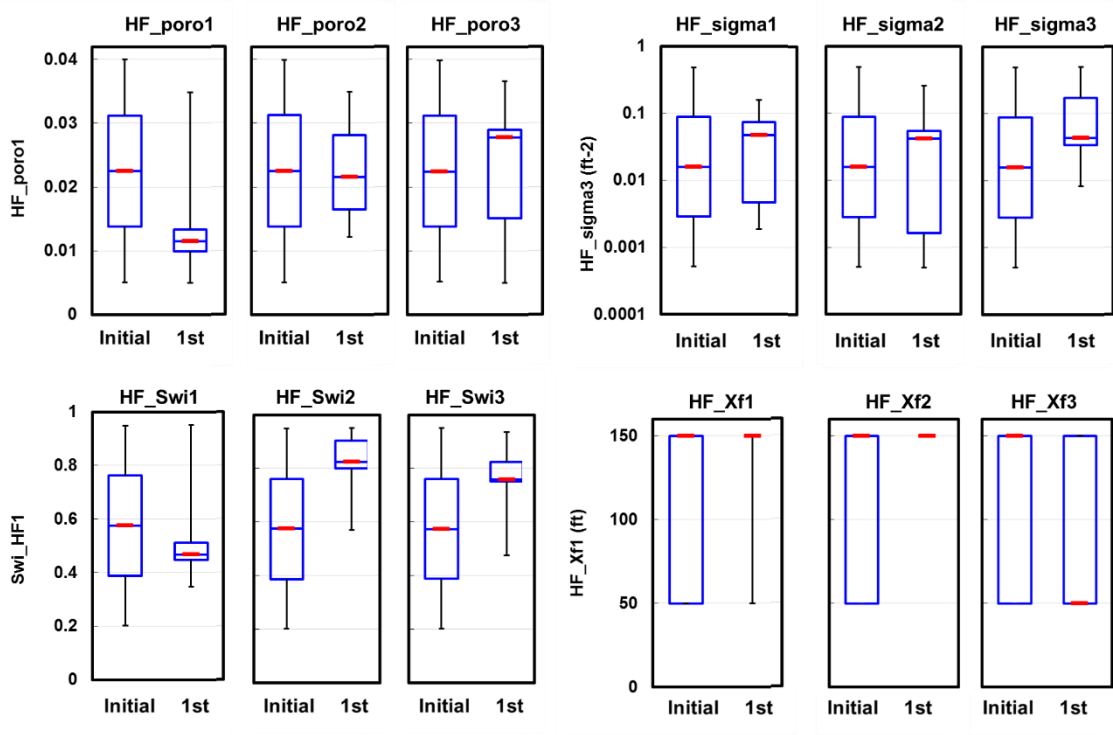


Figure 2.47 Objective function versus generation number (first stage)

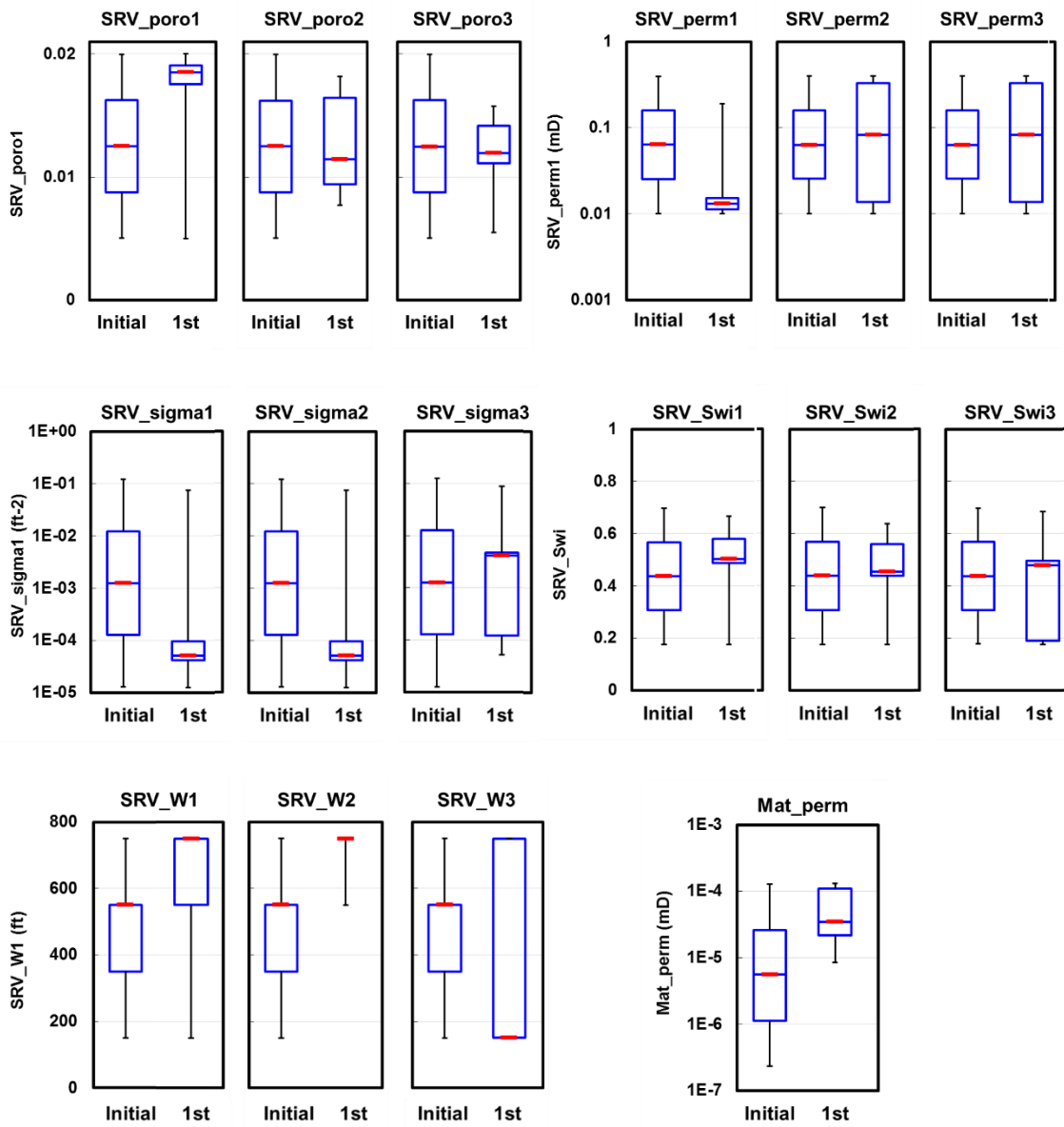
Among all the population in the first stage, we selected the top 30% realizations (621 realizations) based on the objective function to define the parameter ranges for the second stage matching. **Figure 2.48** illustrates the parameter distribution before and after the first stage, which shows that the parameter ranges were significantly narrowed down for several parameters such as water saturation of hydraulic fractures, matrix permeability,

SRV porosity and shape factor. On the other hand, the half-length of hydraulic fractures for groups 1 and 2 collapsed to a single value. One of the reasons is that the half-length can take only two discrete values (50 or 150 ft) as the hydraulic fractures are represented by the simulation grid blocks with different properties from SRV. The other reason is that the flow characteristics is influenced by fracture surface area defined as $\sqrt{k_{SRV} X_f}$, rather than individual half lengths. Therefore, the SRV permeability that has distributions in Figure 2.48 can partially play a role of the fracture half-length.



(a) Hydraulic fracture property

Figure 2.48 Parameter ranges of initial generation, top 30% realizations of first stage



(b) SRV and matrix property

Figure 2.48 Parameter ranges of initial generation, top 30% realizations of first stage (cont'd)

Comparisons between the observed production data and the simulation results are illustrated in **Figure 2.49**. The top 30% realizations capture overall trend of the observed data but indicate overshoot in the mid to late time of the matching period (200– 300 days). Thus, the second stage matching was performed to further improve the matching quality.

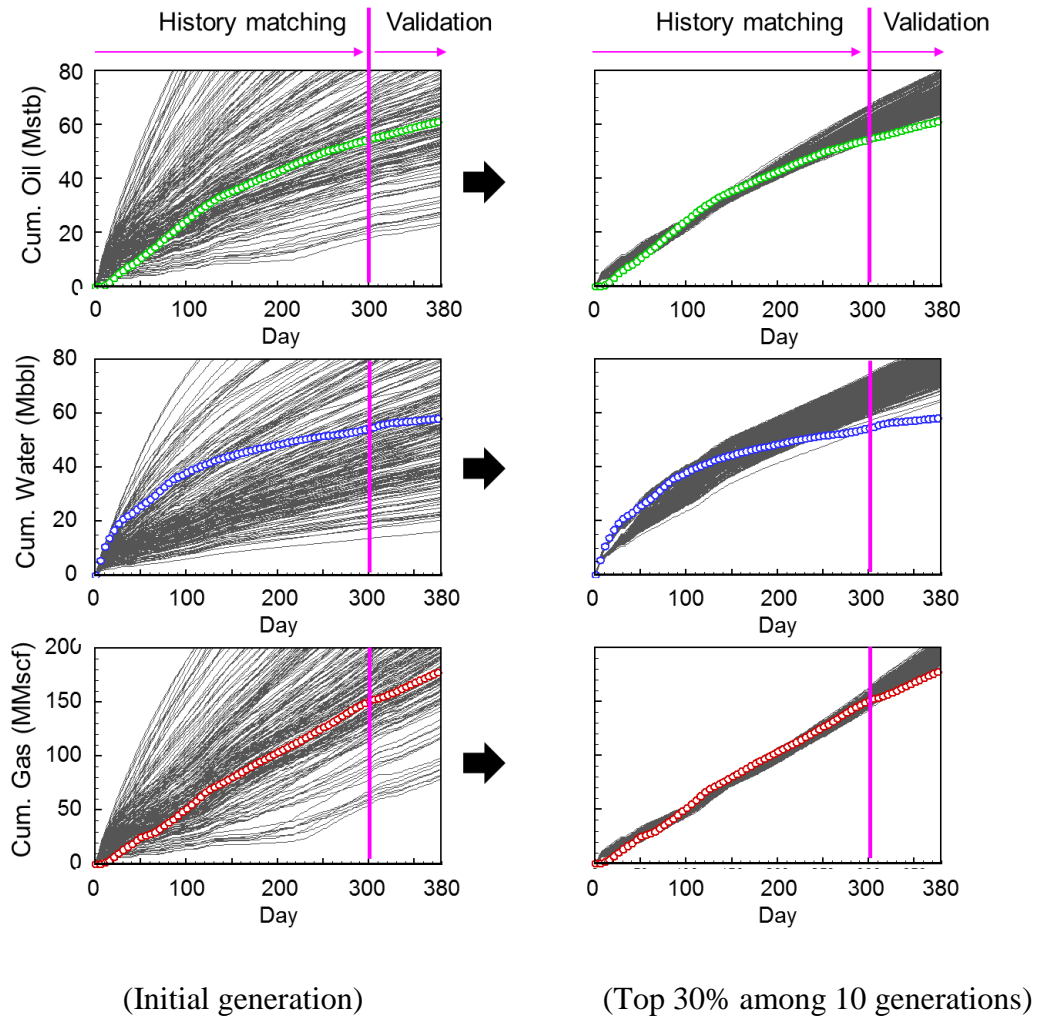


Figure 2.49 Comparisons between observed data and simulated cumulative production (first stage)

2.7.7 Second Stage History Matching

We performed the sensitivity analysis again with the updated parameter ranges. The tornado chart **Figure 2.50** shows more uniform sensitivity compared to that of the first stage (Figure 2.1) as we have already reduced the ranges of parameters used in the first stage. The second stage history matching involved all the parameters.

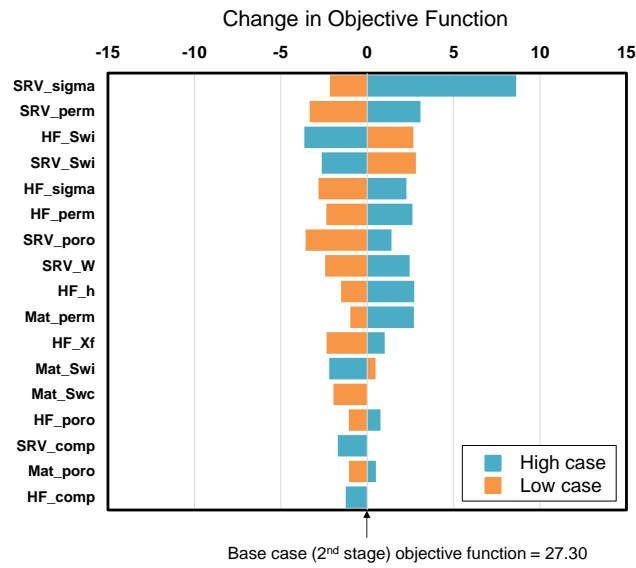


Figure 2.50 Sensitivity analysis for history matching example (second stage)

Figure 2.51 illustrates the objective function versus generation number in first and second stages. Obviously, the objective function in the second stage converged to the smaller value than the first stage. We selected 607 models that corresponds to the top 30% realizations among all the models in the second stage as history matched models.

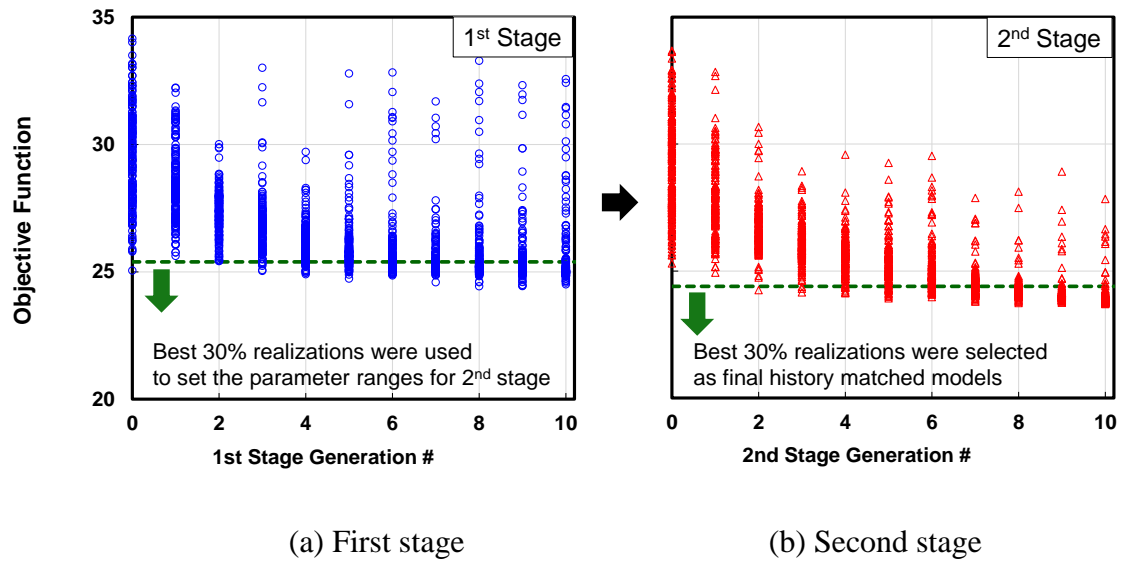


Figure 2.51 Objective function versus generation number (first and second stages)

The well performances simulated with the selected 607 models were compared with the observed data as illustrated in **Figure 2.52**. The selected models showed a good agreement with the three-phase production data with some variations not only in the history matching period but also in the validation period.

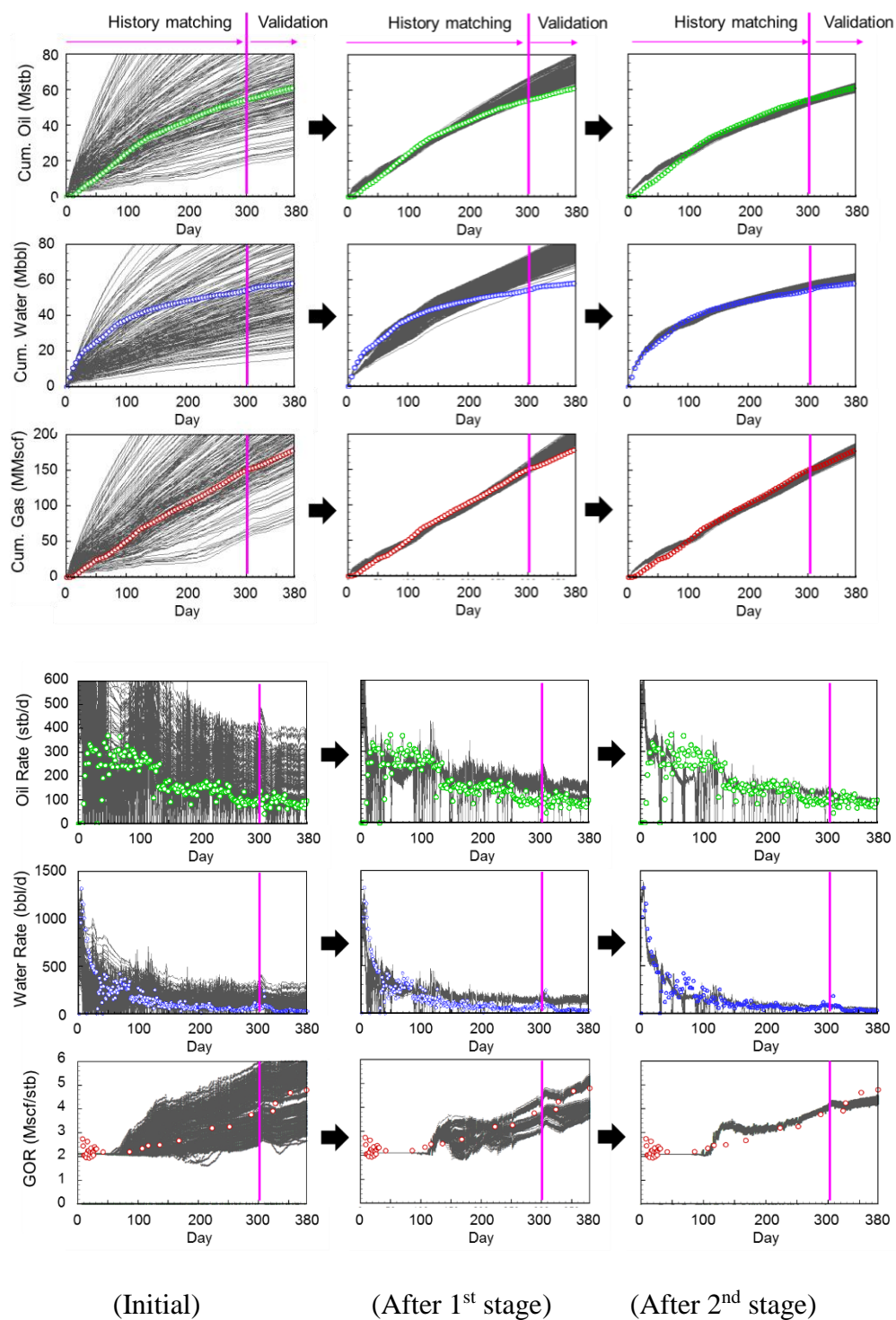
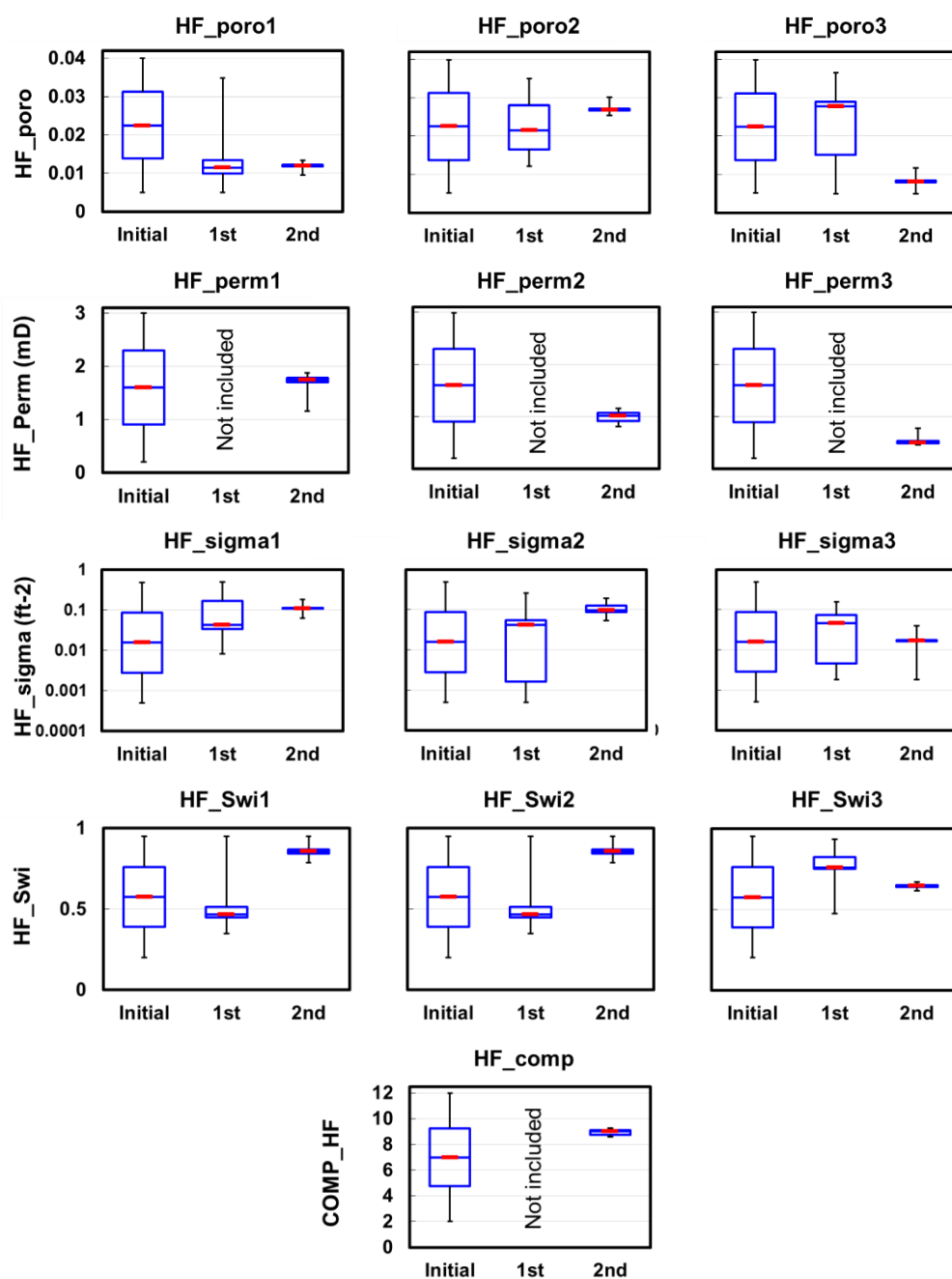


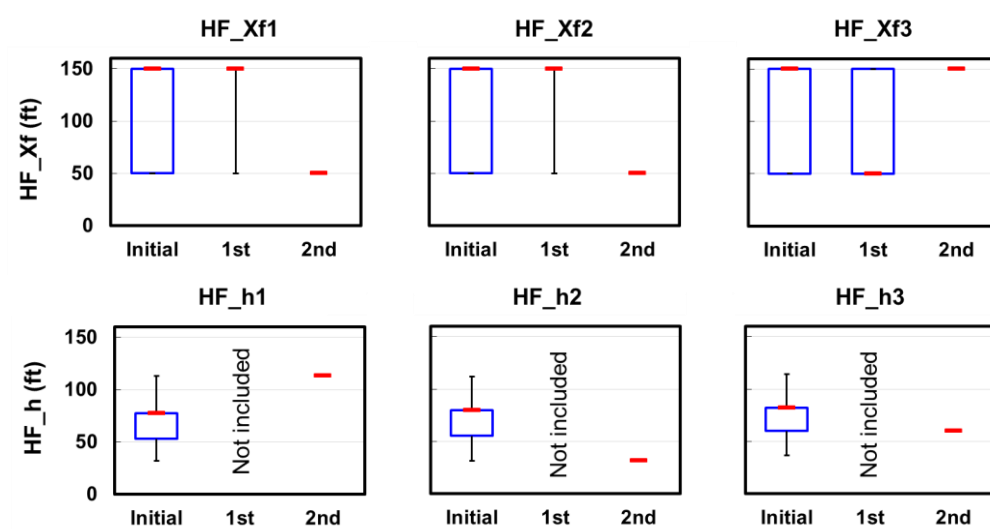
Figure 2.52 Comparisons between observed data and simulated well performances (second stage)

The model parameters are summarized in **Figure 2.53**. Although we narrowed down the ranges of parameters, model parameters were not perfectly constrained due to the non-uniqueness as expected. More physically, it is worth to see the combinations of parameters rather than individual parameters. **Figure 2.54** illustrates the cumulative distributions of fracture surface area and fracture/ matrix transmissibility for each group. Different distributions can be observed among different groups, which confirms that all the hydraulic fracture stages and SRV regions may not equally contribute to the production. However, it should be noted that we cannot distinguish the properties and dimensions between groups in this example because of the lack of data to characterize the individual groups of hydraulic fractures and SRV. The better quantitative characterization would be enabled by acquiring and utilizing microseismic and production logging data.



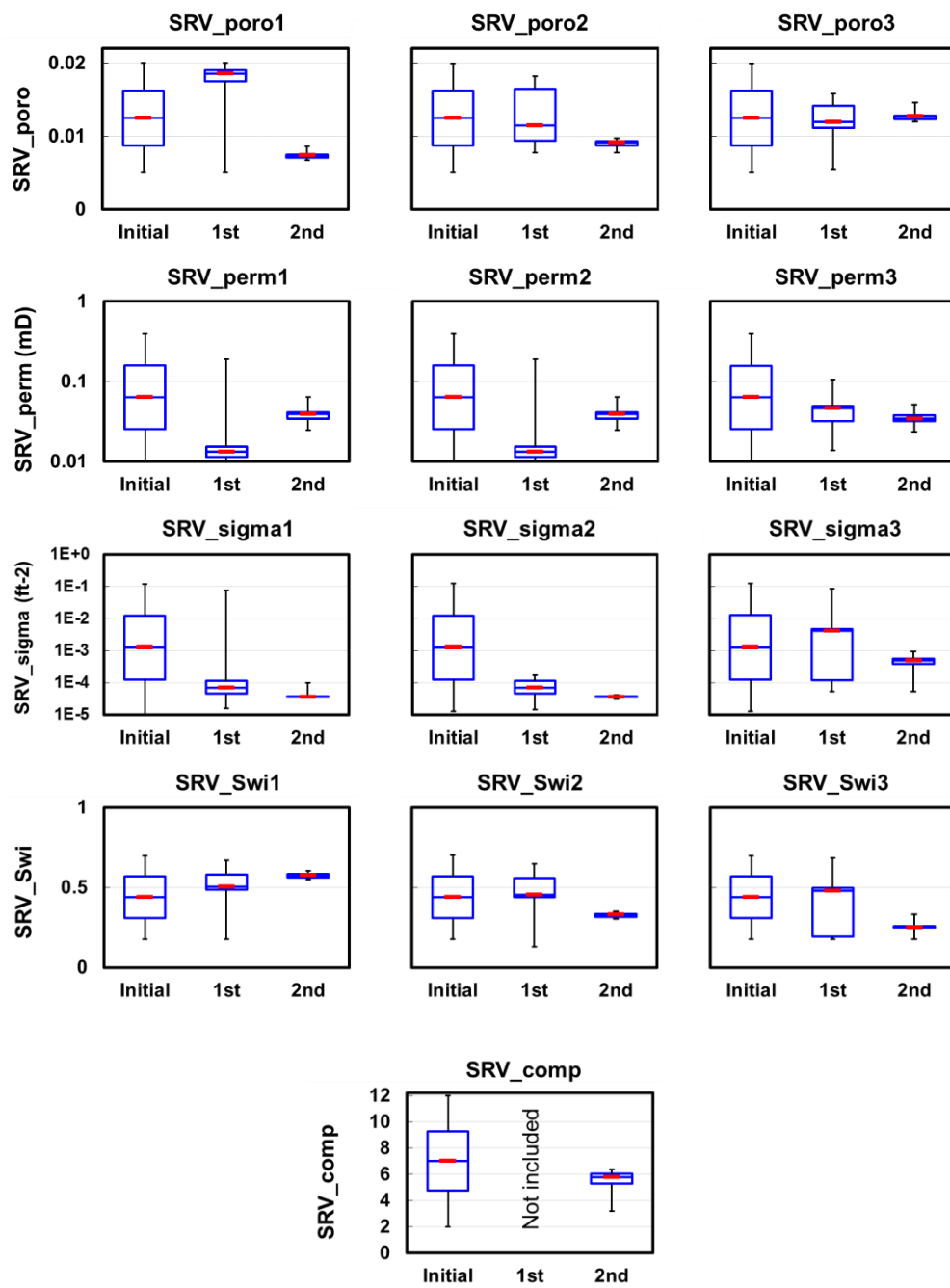
(a) Hydraulic fracture property

Figure 2.53 Parameter distribution after second stage history matching



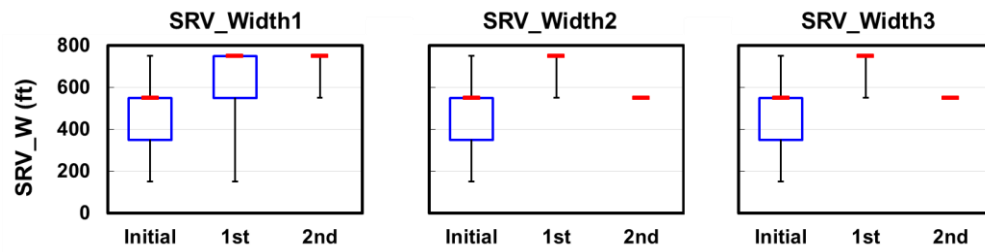
(b) Hydraulic fracture geometry

Figure 2.53 Parameter distribution after second stage history matching (cont'd)

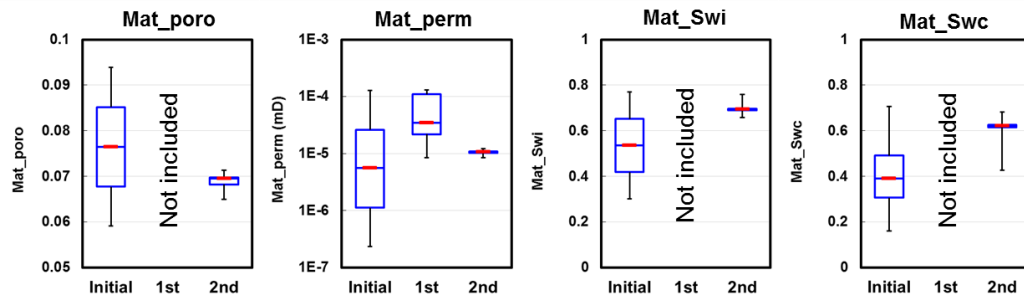


(c) SRV property

Figure 2.53 Parameter distribution after second stage history matching (cont'd)



(d) SRV geometry



(e) Matrix property

Figure 2.53 Parameter distribution after second stage history matching (cont'd)

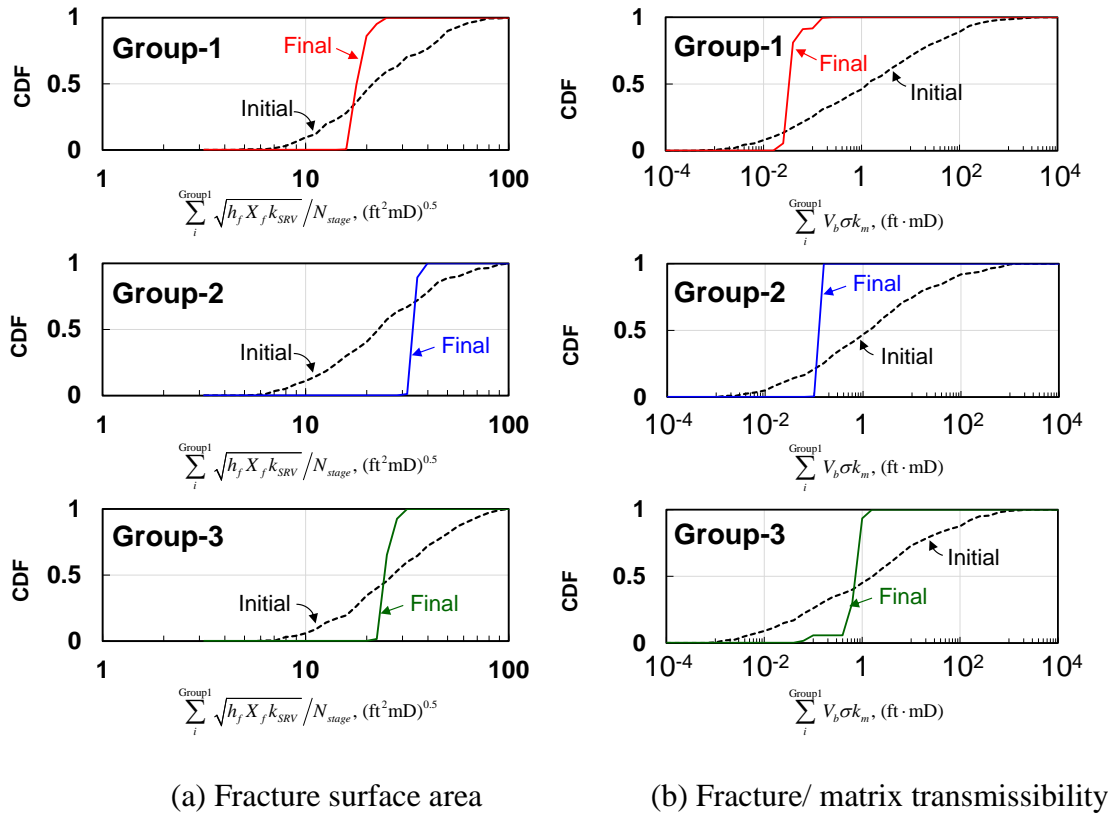


Figure 2.54 Distributions of parameter combinations before and after history matching

2.7.8 Production Forecast

The production forecast was conducted for another 1620 days using the selected 607 models. The forecast run was constrained with the last bottomhole pressure. **Figure 2.55** shows the predicted cumulative production of three phases and the GOR. For all three phases, variations can be seen between the selected models, leading to the range of uncertainty in the remaining recovery. Finally, the CDF of the expected incremental recovery are also shown for oil and gas in **Figure 2.56**. Unlike the empirical or analytical methods, our proposed approach involves a prediction not only for oil but also for gas and

water that might influence the effective productivity and the vertical flow. Thus, the proposed workflow assists the robust and systematic uncertainty analysis that honors the underlying physics and the available production history.

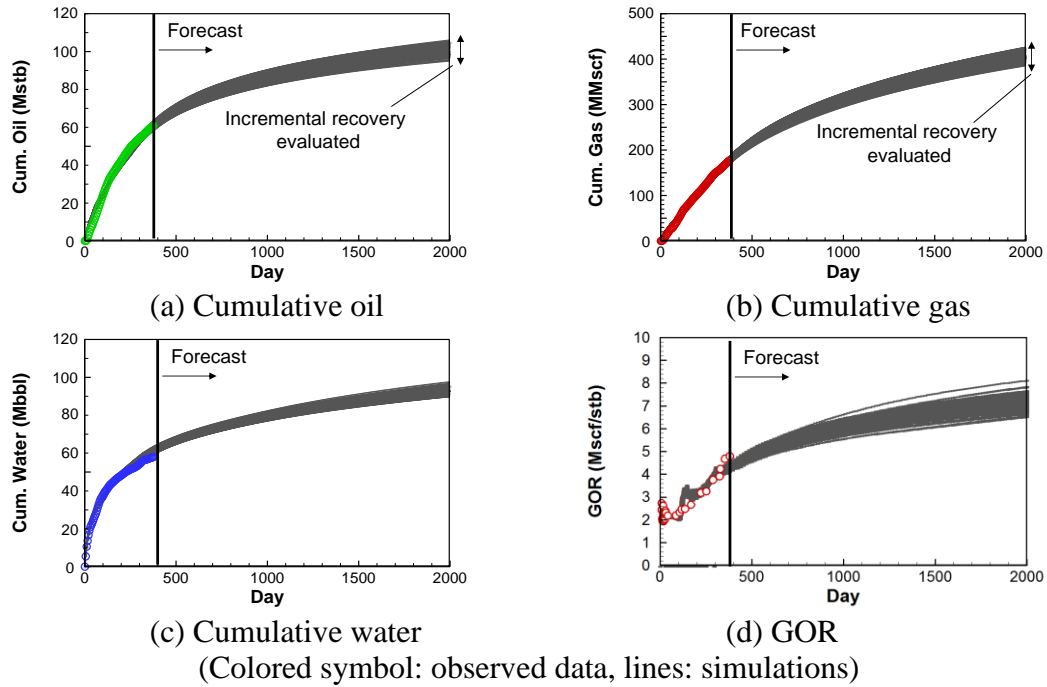


Figure 2.55 Production forecast using multiple history matched models

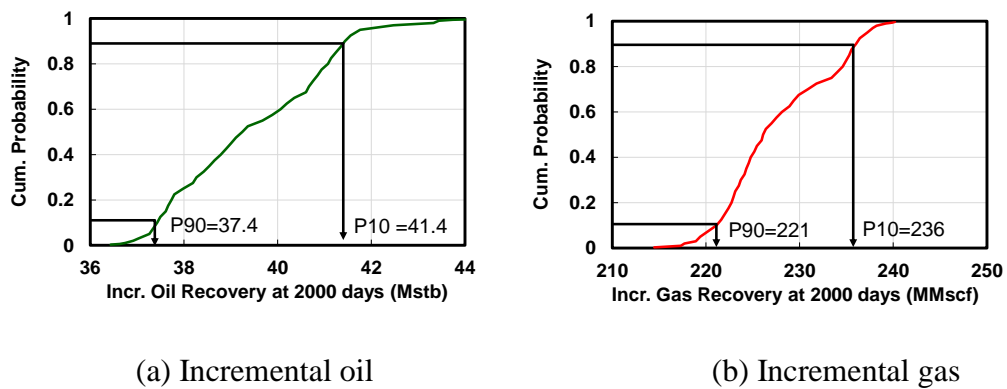


Figure 2.56 Uncertainty assessment of production forecast

2.8 Limitations

For the single-phase flow, King et al. (2016) and Wang (2018) validated the use of the DTOF contours as a spatial coordinate for pressure changes. The FMM-based multi-phase simulation proposed in this study has an additional assumption that the saturation change is aligned with the DTOF contours as well. In this section, we will validate this assumption and discuss limitations. In order to illustrate different physical processes, the following two cases were tested: (1) gas liberation and (2) waterflooding. Other special cases involving multiple rock types with extremely different relative permeability or compaction are discussed in **Appendix-B**.

2.8.1 Gas Liberation Case

Since the gas liberation is a pressure-dependent process, it is expected that the DTOF contours can be used as a spatial coordinate to describe the saturation change as well as the pressure change. In this section, we will validate the FMM-based multi-phase simulation for the gas liberation scenario.

2.8.1.1 Case Setting

We set up a 2-D reservoir model as summarized in **Table 2.7**. Three different levels of heterogeneity were tested as illustrated in **Figure 2.57** with the Dykstra Parson's coefficients of 0.3, 0.6 and 0.9, respectively. The same PVT data as Figure 2.15 was used. The bubble point pressure was set to be 2,860 psi against the initial pressure of 3,000 psi.

A vertical producer was placed at the center and operated with the constant BHP of 1,000 psi, leading to immediate gas liberation around the well.

Table 2.7 Input data for gas liberation case

Item	Value
Model size (ft ³)	11,000'×11,000'×10'
Grid block dimension	101×101×1 (10,201)
Mean Permeability (mD)	1
Dykstra Person's coeff	0.3, 0.6, 0.9
Porosity	0.046
Initial water saturation (immobile)	0.30
Rock compressibility (psi ⁻¹)	1.0×10 ⁻⁶
Water compressibility (psi ⁻¹)	1.0×10 ⁻⁶
Initial solution gas-oil ratio (Mscf/stb)	1.34
Bubble point pressure (psi)	2,860
Initial pressure (psi)	3,000
Well bottomhole pressure (psi)	1,000

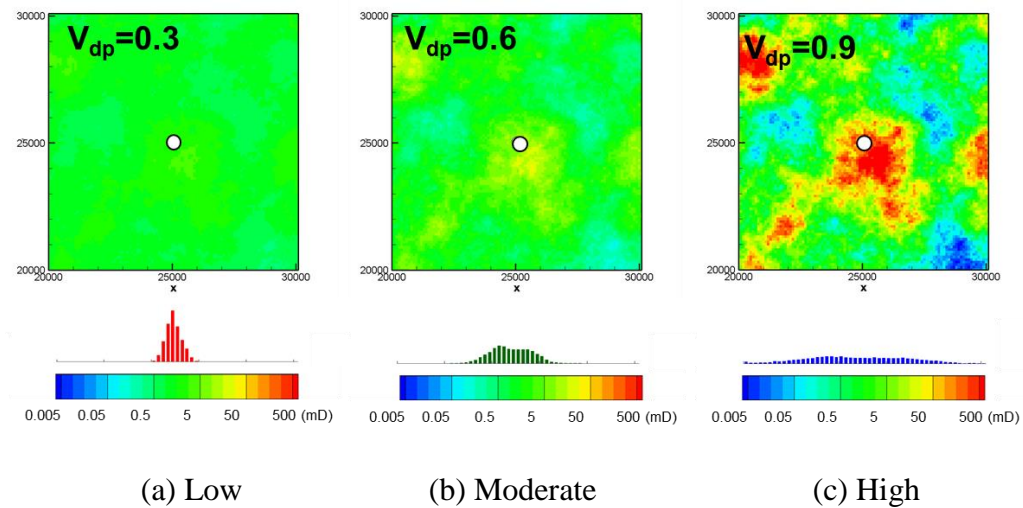


Figure 2.57 Permeability distribution with three different level of heterogeneity

Figure 2.58 shows the gas-oil relative permeability used in this example. Once the gas liberation begins, increases in the total mobility and total compressibility are expected. However, in terms of changes in diffusivity $k\lambda_t/\phi c_t$, increases in the total mobility and compressibility compensate each other. **Figure 2.59a** and **b** illustrate the total mobility and total compressibility according to the depletion of pressure and increase of gas saturation. In this particular example, increases in the total compressibility has the larger magnitude than the total mobility increase, leading to decreases in the diffusivity for less pressure as shown in **Figure 2.59c**.

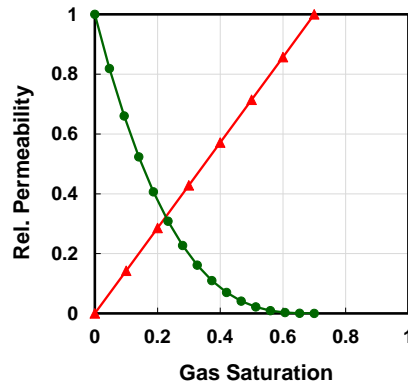
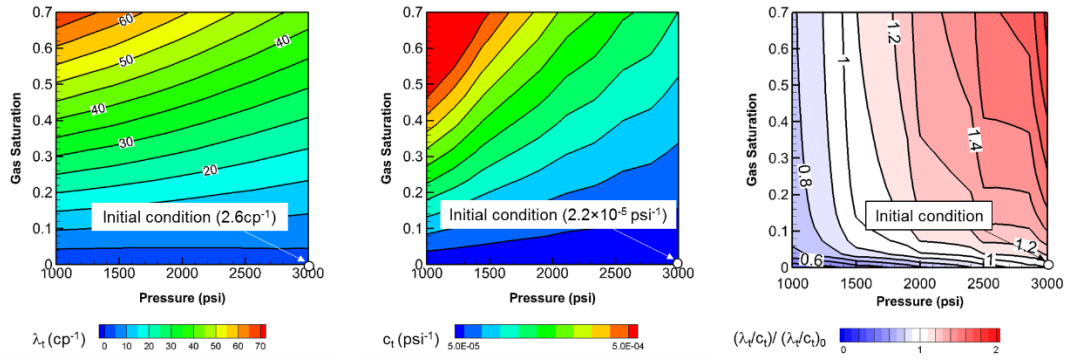


Figure 2.58 Gas-oil relative permeability for gas liberation case



(a) Total mobility (b) Total compressibility (c) Diffusivity change

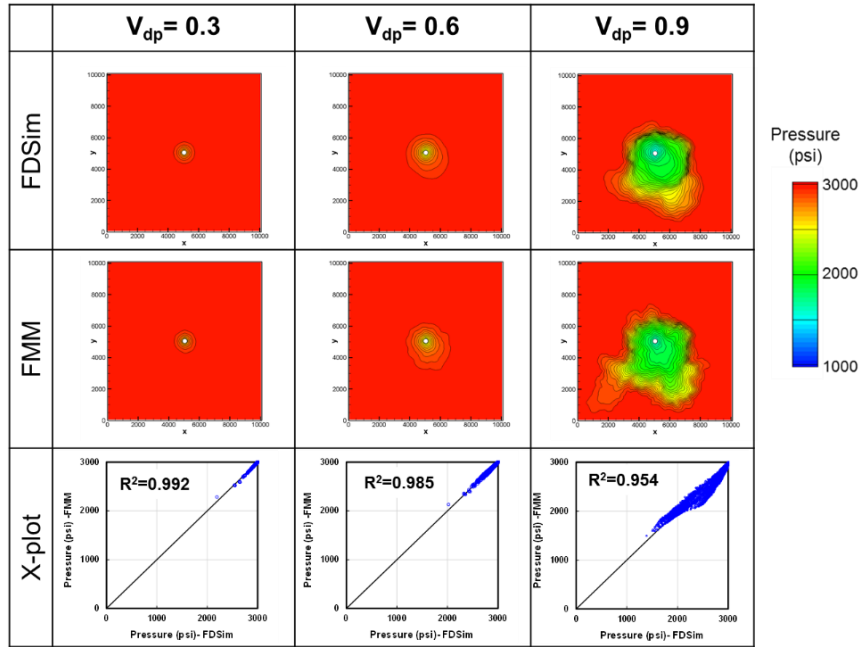
Figure 2.59 Total mobility, total compressibility and diffusivity change as per pressure depletion and gas saturation increase

2.8.1.2 Comparisons of Pressure and Saturation

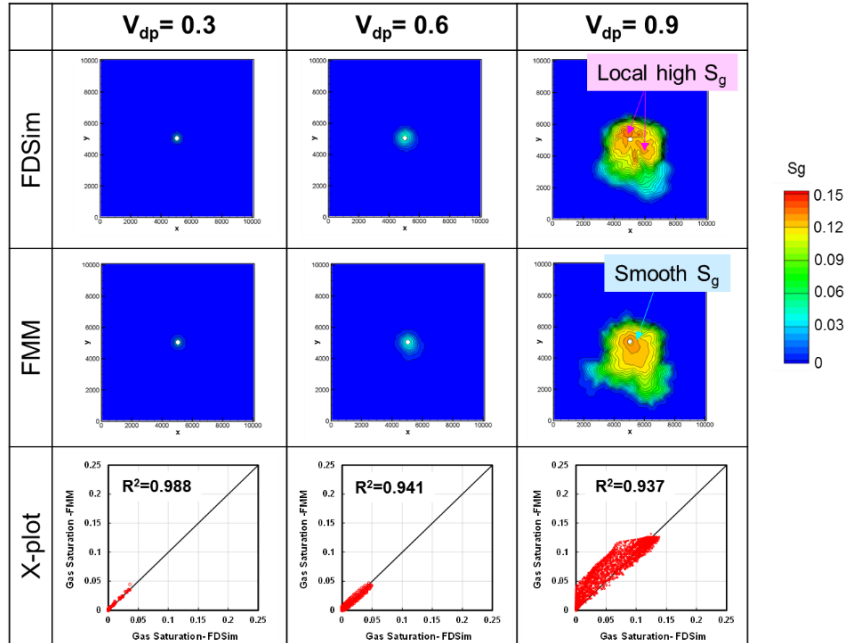
We run both the FDSim and FMM-based simulation for 100 days to obtain grid block pressures and saturations in order to see if the FMM-based simulation captures the trend of the FDSim. **Figure 2.60** compares pressure and gas saturations at 5 days where no significant boundary effect has appeared. The cross-plots in Figure 2.60 show grid block pressures or gas saturations from the FMM-based simulation in the vertical axis and those from the FDSim in the horizontal axis. The cross-plots of both pressures and saturations show wider spread for higher heterogeneity, indicating that the FMM-based simulation gets less accurate with increasing heterogeneity. This is because the Eikonal equation was derived based on the assumption of the smoothly varying media and the reflection should be accounted for if there exists high permeability contrasts in the reservoir (King et al., 2016). Furthermore, if we compare the cross-plots between pressures and gas saturations, the wider spread i.e. less R^2 -values can be observed in that

of the gas saturation. This is because the saturation change can be more affected by the underlying heterogeneity than the pressure change that is a diffusive process. The gas saturation contour from the FDSim shows local high saturations for the high heterogeneity case (top-right in Figure 2.60b) whereas the FMM-based simulation yields the smooth saturation (middle-right in Figure 2.60b). Thus, the assumption that pressure and saturation changes are aligned with DTOF contours becomes less valid for the higher heterogeneity, however, the FMM-based simulation captures the overall trend of the FDSim even for the high heterogeneity case ($V_{dp} = 0.9$).

Next, we compare the pressure and saturation at 100 days where significant boundary effects have appeared in the high heterogeneity case with V_{dp} of 0.9 (**Figure 2.61**). Obviously, the wider spread in the cross-plots of both pressure and saturation can be confirmed compared to the early time (Figure 2.60). Account for the boundary reflection would provide better matching between the FDSim and FMM-based simulations (Huang et al, 2017).

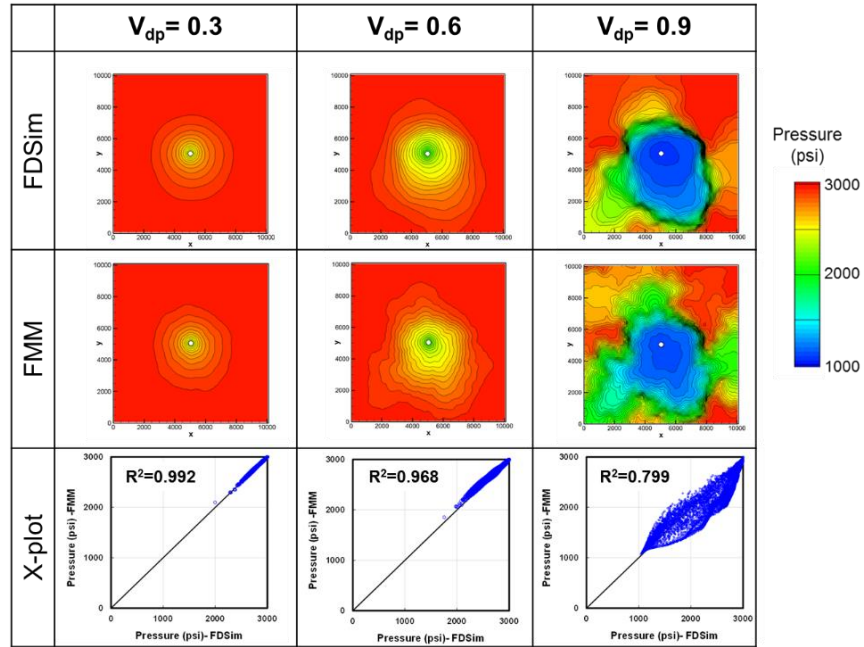


(a) Pressure

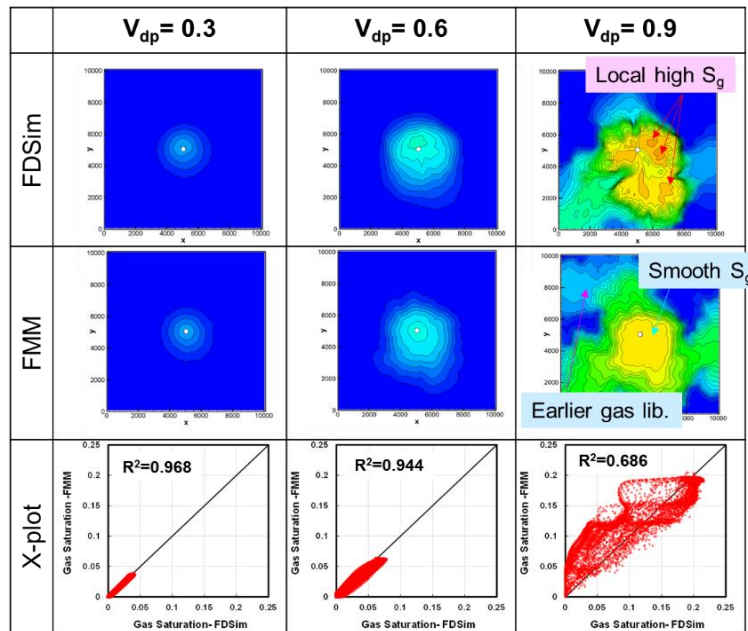


(b) Gas saturation

Figure 2.60 Comparisons of pressure and saturation at 5 days between FDSim and FMM-based simulation for gas liberation case



(a) Pressure



(b) Gas saturation

Figure 2.61 Comparisons of pressure and saturation at 100 days between FDSim and FMM-based simulation for gas liberation case

2.8.1.3 Necessity of Updating DTOF

Finally, we tested if updating the DTOF during the FMM-based simulation improves the matching with the FDSim. **Figure 2.62** illustrates the workflow of the FMM-based simulation incorporating the DTOF update. The map-back of the 1-D solutions from the FMM-based simulation is based on the method detailed in **Appendix C** that honors the mass conservation before and after the map-back.

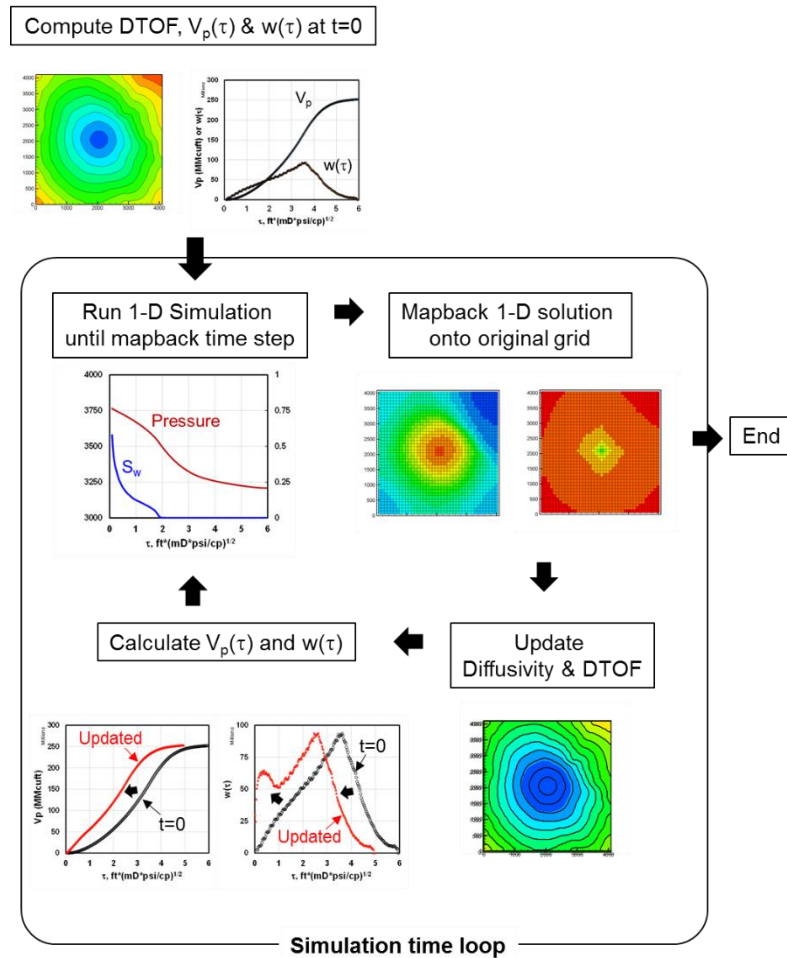
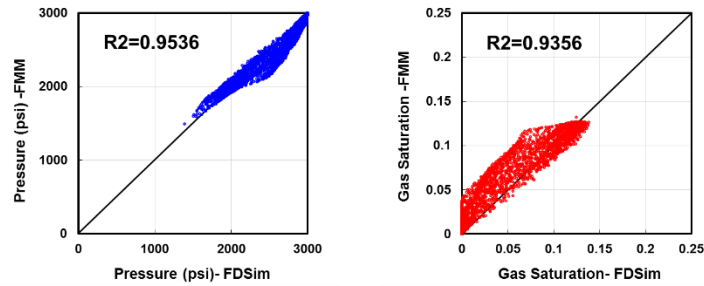
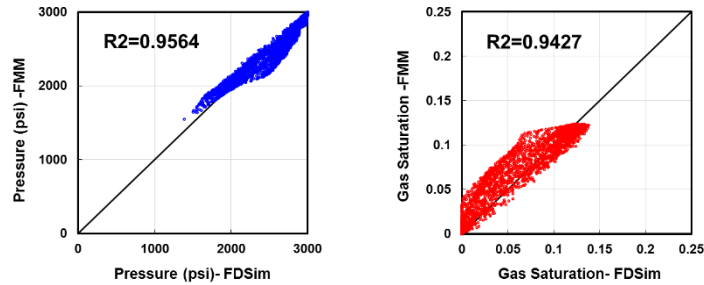


Figure 2.62 Workflow of FMM-based simulation incorporating DTOF update

Figure 2.63a and **b** show the cross-plots of grid block pressures and saturations at 5 days for the high heterogeneity case (V_{dp} of 0.9) between the FDSim and the FMM-based simulations which involve no DTOF update and the DTOF update every day (4 times in total), respectively. It was confirmed that updating DTOF gives little improvement in R^2 values (less than 1%) compared to the case with no update. Better improvement in R^2 values (4-7%) can be seen in **Figure 2.64** that illustrates the cross-plots at 100 day where the DTOF was updated every 5 days (19 times in total) in the FMM-based simulation, however, the improvement seems not to be significant. Thus, we confirmed little necessity to update the DTOF during the simulation in this example.

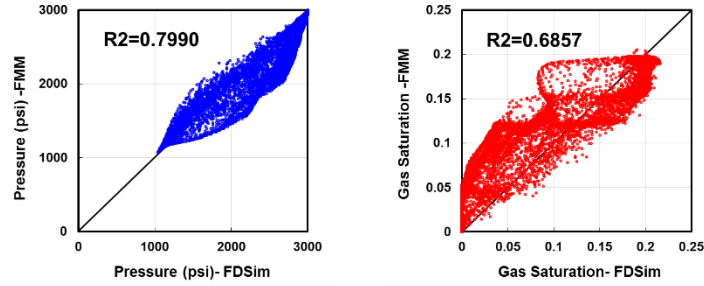


(a) FDSim vs. FMM-based simulation without updating DTOF

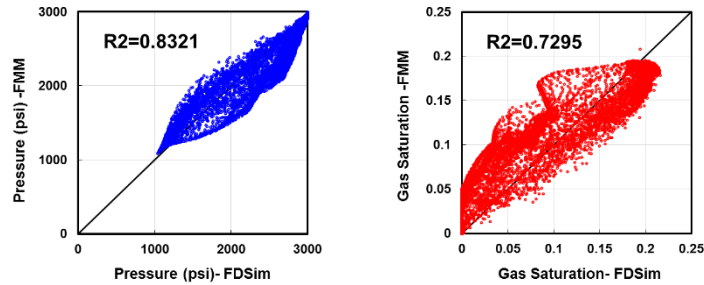


(b) FDSim vs. FMM-based simulation with updating DTOF for 4 times

Figure 2.63 Cross-plots of pressure (blue) and gas saturation (red) at 5 days between FDSim and FMM-based simulation with and without DTOF updates for gas liberation case



(a) FDSim vs. FMM-based simulation without updating DTOF



(b) FDSim vs. FMM-based simulation with updating DTOF for 19 times

Figure 2.64 Cross-plots of pressure (blue) and gas saturation (red) at 100 days between FDSim and FMM-based simulation with and without DTOF updates for gas liberation case

2.8.2 Waterflooding Case

Different from the gas liberation case in the previous section, saturation changes due to waterflood is considered to be less pressure dependent. Furthermore, the saturation profile may be significantly affected by not only the reservoir heterogeneity but also the mobility ratio that is evaluated at the end point (Dake, 1978). In this section, we will validate the FMM-based multi-phase simulation for the waterflood case.

2.8.2.1 Case Setting

We used the same reservoir model as the previous gas liberation case. The water-oil relative permeability used in this case is illustrated in **Figure 2.65**. In addition to the different level of heterogeneity with V_{dp} of 0.3, 0.6 and 0.9, we also tested different mobility ratio ($M = 0.1, 1, 10$ and 100) by assuming the water viscosity of from 0.0152 to 15.2 cp. Changes in total compressibility, total mobility and diffusivity according to the water saturation increase are illustrated in **Figure 2.66** where diffusivity changes are normalized by the reference diffusivity at the initial condition. Waterflooding was simulated for 100 day with an injector located at the center and controlled by the constant rate of 500 stbw/day.

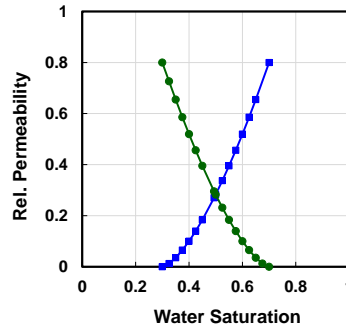


Figure 2.65 Relative permeability for waterflooding case

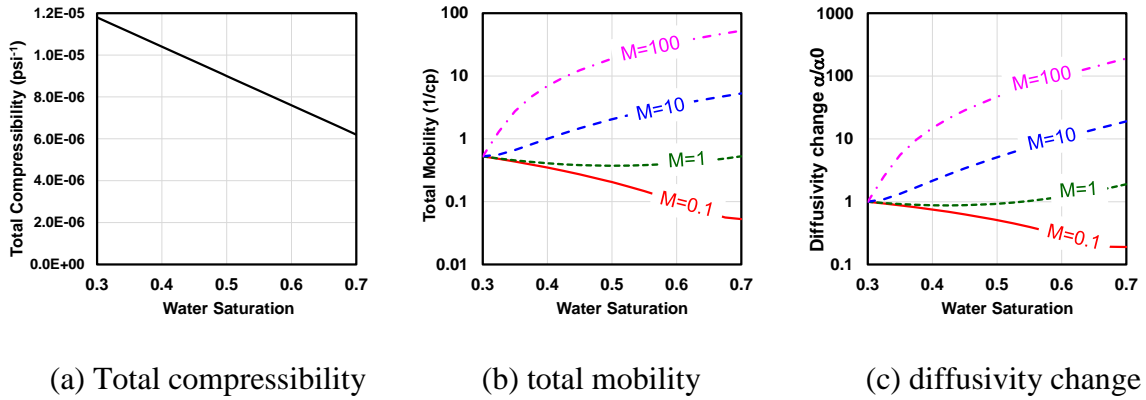


Figure 2.66 Total compressibility, total mobility and diffusivity change versus water saturation for waterflooding case

2.8.2.2 Comparisons of Pressure and Saturation

We first compare pressure and saturation distributions between the FMM-based simulation and the FDSim at 5 days where no boundary effect has appeared. **Figure 2.67** illustrates pressure contours in line and saturation contours in color. The cross-plots of grid block pressures and saturations are also depicted in **Figure 2.68**. For the mobility ratio equal to and higher than 1, the pressure matching is excellent for the low and moderate heterogeneity. For the higher heterogeneity ($V_{dp} = 0.9$), the cross-plot shows wider spread than cases with less heterogeneity, however, the FMM-based simulation well captures the trend of the FDSim. The same trend can be seen in the cross-plots of saturations in Figure 2.68 because saturation changes due to waterflood can be more influenced by the reservoir heterogeneity than pressure changes. Since we use the identical DTOF contours to describe both pressure and saturation changes, it is difficult to distinguish the effects of heterogeneity on pressure and saturation.

Then let us discuss the effect of mobility ratio. For the low mobility ratio ($M = 0.1$), pressure calculation of the FMM-based simulation gets less accurate compared to other cases as seen in the cross-plots in Figure 2.68. This is because of the saturations calculated along the DTOF contours in the FMM-based simulation. The higher mobility ratio facilitates the saturation contours to be more smeared, leading to more uniform saturation within the area where the injected water reached. It results in more uniform saturation within each pressure contour than cases with less mobility ratio. This can be more clearly seen in the contour maps at 100 days in **Figure 2.69**. In addition, because the magnitude of saturation changes is less for higher mobility ratio, the FMM-based can still capture the overall saturation changes of the FDSim. Hence, it is expected that the preferred condition for the FMM-based simulation is less heterogeneity and higher mobility ratio. Although the boundary effects seem to have appeared, the cross-plots of pressures and saturation at 100 days shows the consistent observation as seen in **Figure 2.70**.

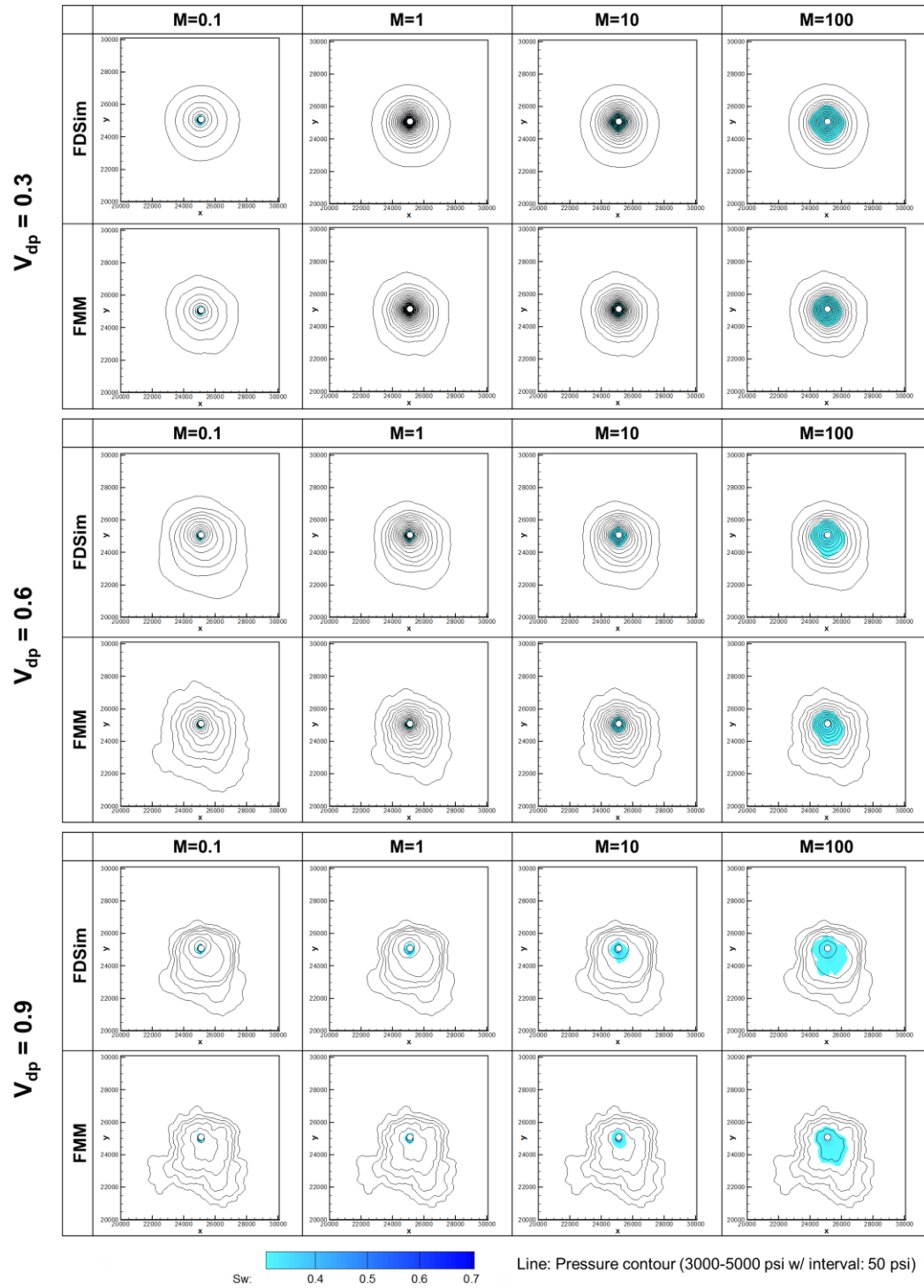
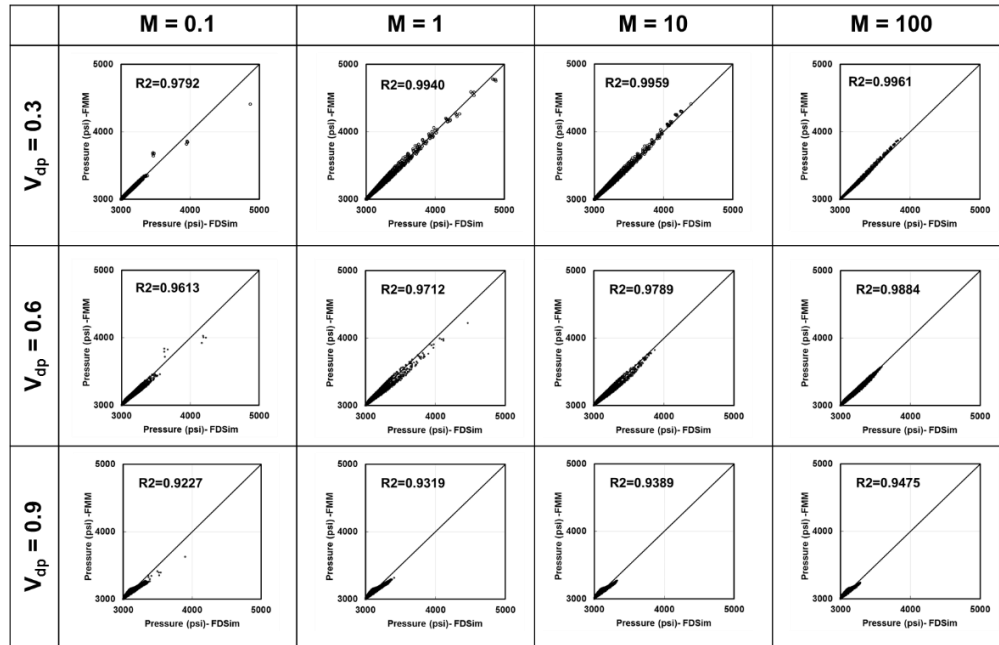
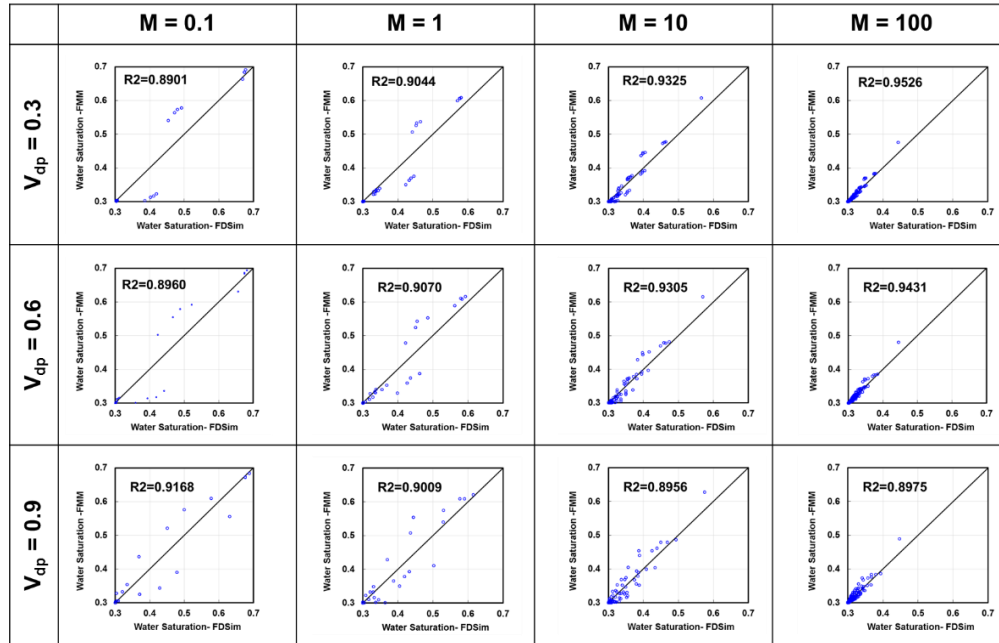


Figure 2.67 Comparison of pressure (line) and saturation contours (color) at 5 days between FMM-based simulation and FDSim for waterflooding case



(a) Pressure



(b) Water saturation

Figure 2.68 Cross-plots of grid block pressure and saturation at 5 days between FMM-based simulation (vertical axis) and FDSim (horizontal axis) for waterflooding case

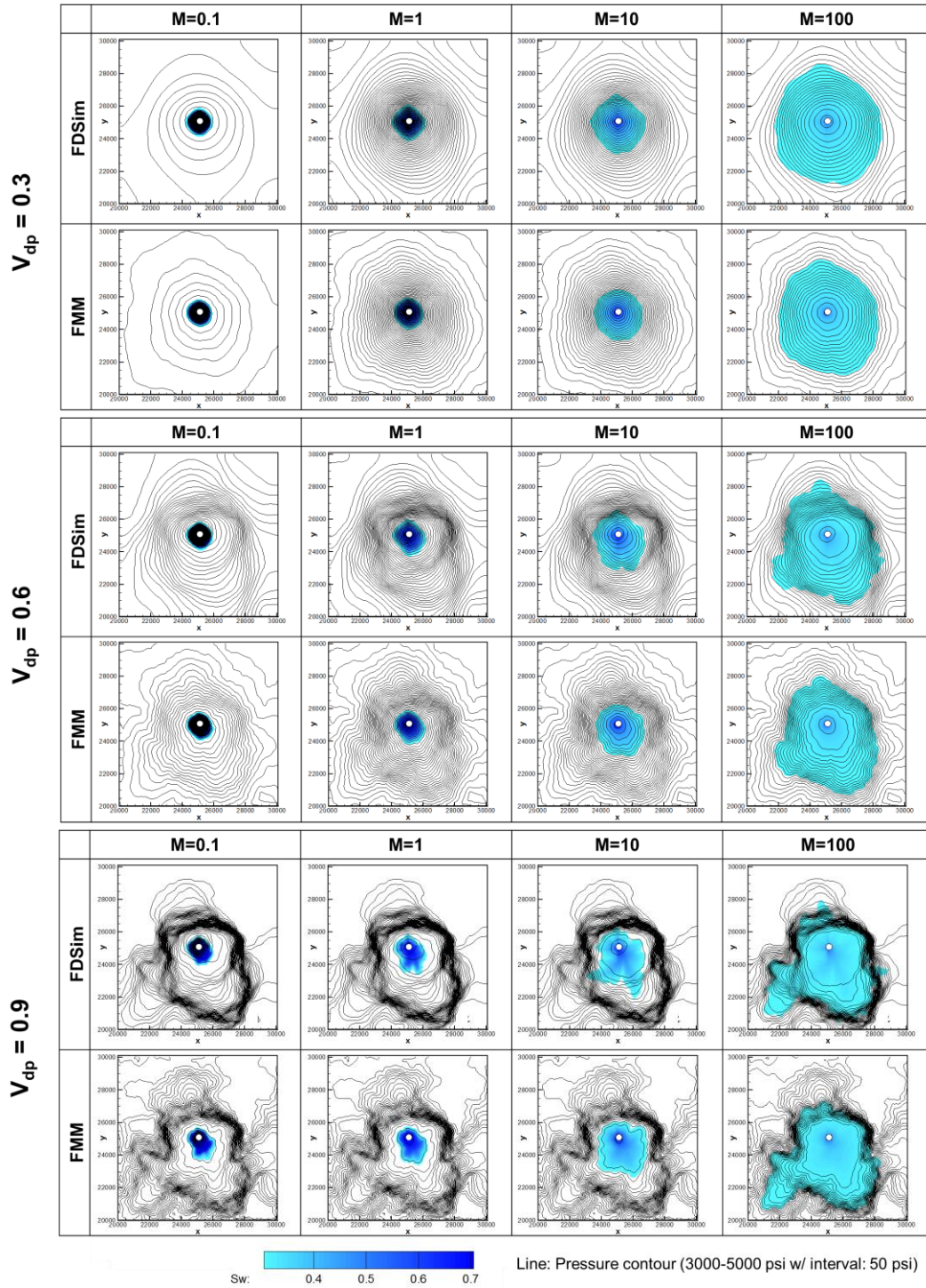
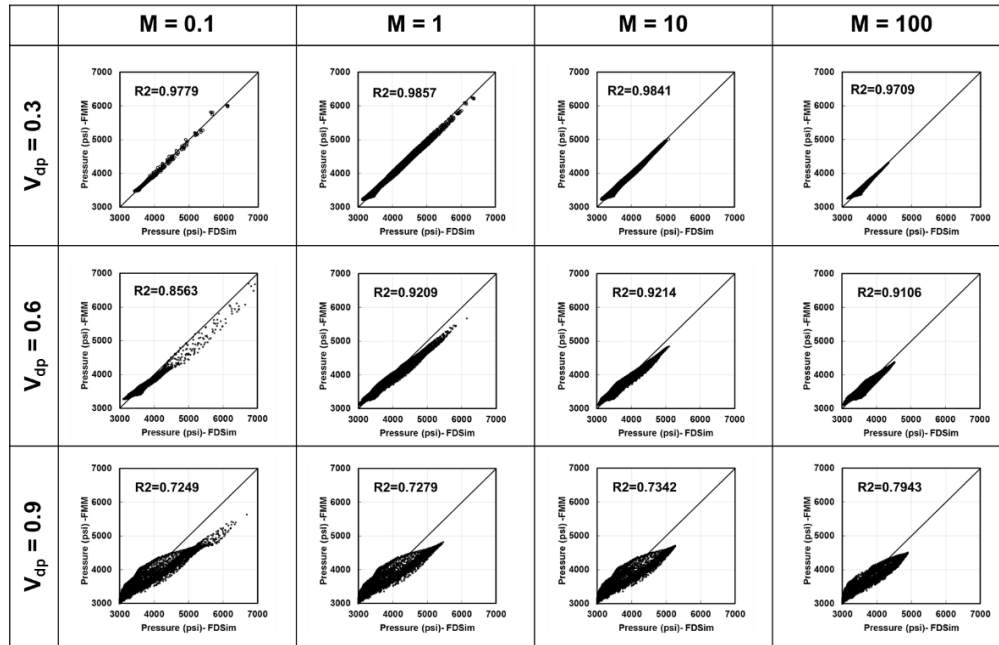
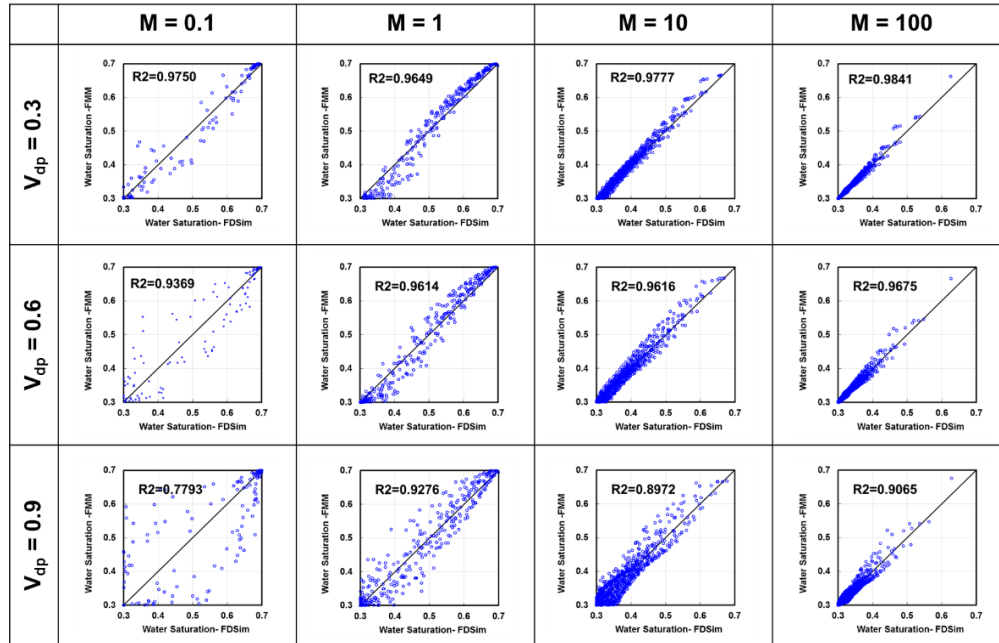


Figure 2.69 Comparison of pressure (line) and saturation contours (color) at 100 days between FMM-based simulation and FDSim for waterflooding case



(a) Pressure



(b) Water saturation

Figure 2.70 Cross plots of grid block pressure and saturation at 100 days between FMM-based simulation and FDSim for waterflooding case

2.8.2.3 Necessity of Updating DTOF

Finally, we tested how the DTOF update influence the results of the FMM-based simulation. We used the case of the high heterogeneity ($V_{dp} = 0.9$) and the low mobility ratio ($M = 0.1$). **Figure 2.71** illustrates the comparison of pressures and saturations at 100 days between different frequencies of the DTOF update.

It can be observed that there is little difference in the pressure contours (line contours in Figure 2.71) among the different frequencies of the DTOF update. In the cross-plots of grid block pressures between the FMM-based simulation and the FDSim, the R^2 values calculated for the cases with the DTOF update ($R^2 = 0.715-0.732$) are not significantly improved from the case with no DTOF update ($R^2 = 0.725$). Thus, in terms of pressure, there is little necessity to update the DTOF during the FMM-based simulation.

On the other hand, the saturation profile is more affected by the DTOF update than pressure. Although the R^2 values in the saturation cross-plots are improved in the cases with the DTOF update compared to the case with no update, the saturation contours clearly shows that increasing the frequency of the DTOF update results in more smeared saturation profile. This is because the DTOF update involves mapping and mapping-back the solutions between the original grid blocks and the 1-D grid blocks, leading to the averaged saturation especially around the displacement front. Thus, updating the DTOF does not always improve the accuracy of the FMM-based simulation.

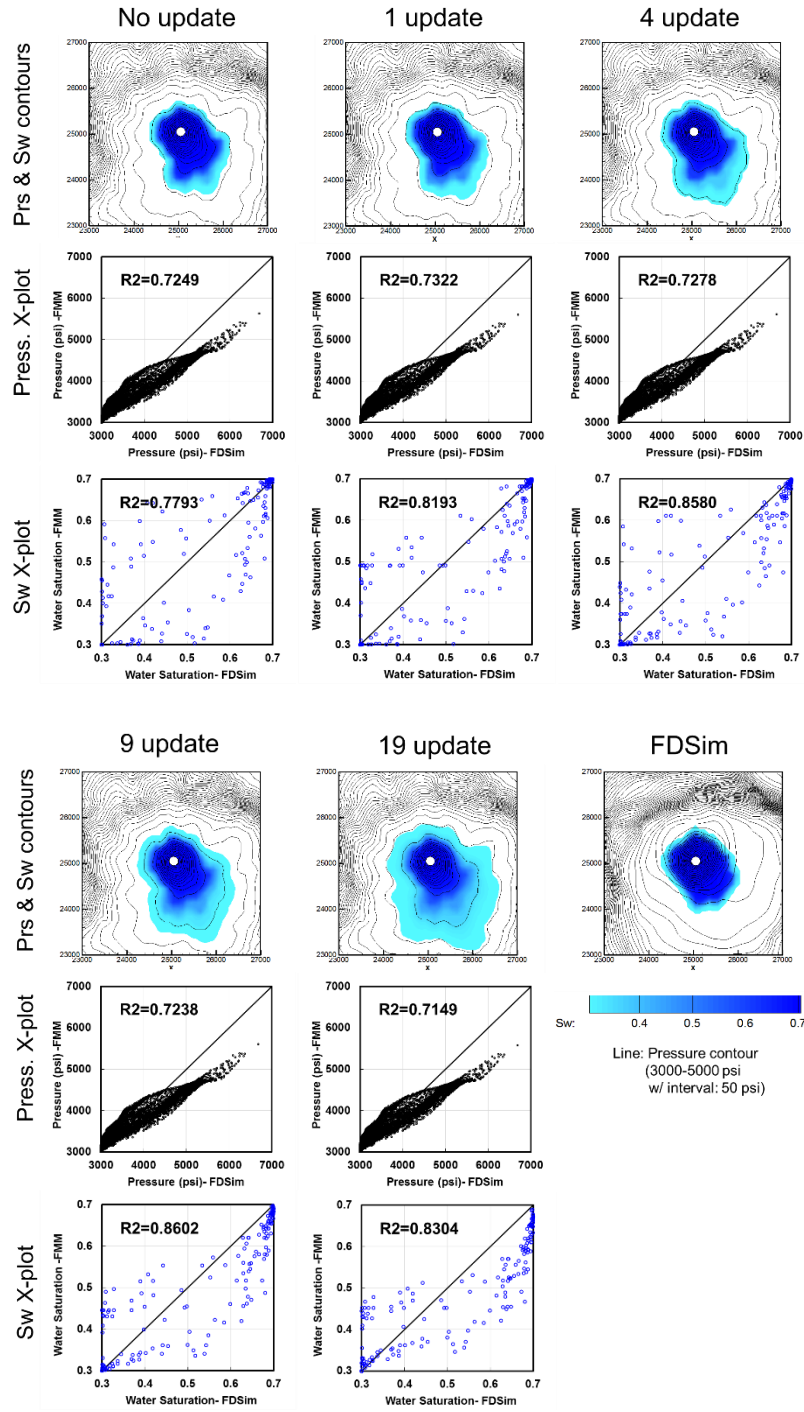


Figure 2.71 Comparisons of pressures and saturations at 100 days between different frequencies of DTOF update for waterflooding case ($V_{dp} = 0.9$ & $M = 1$)

2.9 Conclusions

In this chapter, we have proposed a novel approach that is based on the FMM for rapid multi-phase simulation in unconventional reservoirs. Our proposed approach is a bridge between simplified analytical methods and full 3-D numerical simulation and offers rapid computation that incorporates reservoir heterogeneity, complicated completion geometry, three-phase flow and relevant physics. The conclusions arising from this study are the followings.

- We have developed the mathematical formulation for the FMM-based 1-D simulation that involves three-phase flow and dual-porosity model. The 3-D flow equations were transformed into 1-D equation along the DTOF coordinate where the spatial heterogeneity has been reflected.
- The workflow for multi-phase simulation using the FMM was proposed. We first generate the multi-phase DTOF on the original grid block system. Subsequently, the multi-phase simulation is carried out using the 1-D DTOF grid blocks.
- The proposed approach was validated using synthetic 3-D examples incorporating multi-phase flow. It was confirmed that the FMM-based simulation shows a good accuracy and orders of magnitude faster computation at the field scale, as compared to the commercial finite difference simulator. Additional advantage of the FMM is flow visualization using the DTOF and $w(\tau)$ function, which assists us to easily identify the flow regimes.

- The field application of history matching was studied for a multi-stage hydraulically fractured well in a shale oil field in Texas. It demonstrated that the rapid simulation by the FMM-based approach assists efficient history matching using the population-based technique that requires a large number of simulation runs. Multiple history matched models were generated and used for the assessment of uncertainty ranges in the reservoir properties and remaining recovery.
- We discussed the validity to use the DTOF as a spatial coordinate to describe both saturation and pressure changes. For cases with the low to moderate heterogeneity e.g. V_{dp} less than 0.6, the FMM-based simulation can provide good matching with the finite difference simulation. Even for the case with the severe heterogeneity e.g. V_{dp} of 0.9, the FMM-based simulation can still capture the overall trend of the finite difference simulation. When water or gas flooding is simulated, less mobility ratio results in less matching quality between the FMM-based and the finite difference simulations. Updating the DTOF during the FMM-based simulation does not necessarily improve the accuracy.

CHAPTER III

OPTIMIZING CO₂ AND FIELD GAS INJECTION EOR IN UNCONVENTIONAL RESERVOIRS USING THE FAST MARCHING METHOD[‡]

3.1 Chapter Summary

Recently there has been an increasing interest in Enhanced Oil Recovery (EOR) from shale oil reservoirs, including CO₂ and field gas injection. For the performance assessment and optimization of CO₂ and gas injection processes, compositional simulation is a powerful and versatile tool because of the capability to incorporate reservoir heterogeneity, complex fracture geometry, multi-phase and multi-component effects in nano-porous rocks. However, flow simulation accounting for such complex physics can be computationally expensive. In particular, field scale optimization studies requiring large number of high resolution compositional simulations can be challenging and sometimes computationally prohibitive. In this chapter, we present a rapid and efficient approach for optimization of CO₂ and gas injection EOR in unconventional reservoirs using the Fast Marching Method (FMM)-based flow simulation.

[‡] Material adapted with permission from “Rapid Compositional Simulation and History Matching of Shale Oil Reservoirs Using the Fast Marching Method” by Iino et al. 2017b: Paper URTeC-2693139-MS Presented at the Unconventional Resources Technology Conference held in Austin, Texas, USA, 25-27 July 2017. Copyright 2017, Unconventional Resources Technology Conference. Further reproduction is prohibited without permission.

[‡] Material adapted with permission from “Optimizing CO₂ and Field Gas Injection EOR in Unconventional Reservoirs Using the Fast Marching Method” by Iino and Datta-Gupta 2018: Paper SPE-190304-MS Presented at SPE IOR Conference held in Tulsa, Oklahoma, USA, 14-18 April 2018. Copyright 2018, Society of Petroleum Engineers. Further reproduction is prohibited without permission.

The FMM-based simulation is analogous to streamline simulation and utilizes the concept of ‘Diffusive Time-of-Flight’ (DTOF). The DTOF is a representation of the travel time of pressure ‘front’ propagation and accounts for geological heterogeneity, well architecture and complex fracture geometry. The DTOF can be efficiently obtained by solving the Eikonal equation using the FMM. The 3-D flow equation is then decoupled into equivalent 1-D equation using the DTOF as a spatial coordinate, leading to orders of magnitude faster computation for high-resolution and compositional models as compared to full 3-D simulations. The speed of computation enables the use of robust population-based optimization techniques such as genetic or evolutionary-based algorithm that typically require large number simulation runs to optimize the operational and process parameters.

We demonstrated the efficiency and robustness of our proposed approach using synthetic and field scale examples. We first develop and validate the FMM-based compositional simulation using examples of simple homogeneous model and CO₂ Huff-n-Puff for a synthetic dual-porosity and heterogeneous model with a multi-stage hydraulically fractured well. In the field-scale application, we present an optimization of operating strategies for gas injection EOR for a depleted shale oil reservoir in the Eagle Ford formation. The rapid computation of the FMM-based approach enabled intensive simulation study involving high-resolution geological models with million cells resulting in a comprehensive evaluation of the EOR project including sensitivity studies, parameter importance analysis and optimal operating strategies.

This chapter shows the novelty and efficiency of the systematic optimization workflow incorporating the FMM-based compositional simulation for the field-scale modeling of CO₂ and gas injection in shale oil reservoirs. Not only can it account for relevant physics such as reservoir heterogeneity, fracture geometry and fluid phase behavior but also lead to orders of magnitude saving in computational time over commercial finite difference simulators.

3.2 Background

Unconventional tight oil reservoirs contribute significantly to the oil production in the United States. However, due to ultra-low permeability and rapid production decline, the recovery factor remains low as estimated to be 7% on average that is far short compared to conventional reservoirs (Jacobs, 2015a). It has resulted in increasing interest in the application of Enhanced Oil Recovery (EOR) techniques, especially CO₂ and gas injection EOR (Alfarge et al., 2017b).

In the last decade several projects of pilot IOR/ EOR have been reported in the literature (Alfarge, 2017a; Jacobs, 2015a). Todd and Evans (2016) analyzed seven IOR pilot tests performed in the U.S. Bakken Shale during 2008-2014, which involved continuous injection and Huff-n-Puff using water, CO₂ or natural gas. However, little or no incremental oil was confirmed in all these tests due to early breakthrough and possibly less reservoir sweep than expected. On the other hand, Schmidt and Sekar (2014) reported successful pilot in 2011 where dry natural gas was injected from a horizontal injector perpendicular to the toes and heels of the offset horizontal producers. It resulted in the

increase of oil production rate from 130 to 295 bbl/d, as well as reduction in the decline rate from 20% to 15%. Most recently, there has been a report of a successful gas injection pilot in the Eagle Ford Shale where significant increase in oil production from fifteen (15) wells were confirmed (Jacobs, 2015a). Thus, the industry has been pursuing the best practice for successful EOR for unconventional reservoirs and a lot of research and projects are ongoing for this purpose (Rassenfoss, 2017).

Recent experimental work has shown the feasibility of EOR using CO₂ and hydrocarbon gases for improved oil recovery from unconventional rock samples of ultra-low permeability. Exposure to CO₂ at reservoir condition makes it possible to recover more than 90% of hydrocarbon from the Middle Bakken rock samples (Hawthorne et al., 2013; Jin et al., 2017). Using the CT scanning, Sun et al. (2016) visually confirmed that CO₂ kept invading into cores during the exposition, indicating that molecular diffusion is the main mechanism of mass transfer. It has also been demonstrated that natural gas can be another option that can potentially recover as much oil as CO₂ does (Jin et al., 2017). In addition, much effort has been devoted for simulation studies to investigate the recovery mechanisms and feasibility of CO₂ and gas injection EOR in unconventional reservoirs (Alfarge et al, 2017b). Wan and Sheng (2015) used dual-permeability simulation to study gas injection in fractured shale oil reservoirs and demonstrated that matrix/ fracture and matrix/ matrix diffusion play an important role in the oil recovery process. Chen et al. (2014) investigated the effects of heterogeneity on CO₂ Huff-n-Puff performance using a compositional reservoir simulator. Alfarge et al. (2017b) compared the performances of miscible Huff-n-Puff for the Bakken Shale using lean gas, rich gas and CO₂ solvents. They

found that hydrocarbon gases could be a better option as it required less molecular diffusion effects to increase the recovery compared to CO₂. However, the gap of recovery mechanisms between lab-scale and field-scale needs to be addressed. Alharthy et al. (2016) conducted a comprehensive study of CO₂ EOR from laboratory to field scales. The CO₂ solvent-soaking-experiments using the Bakken cores showed that molecular diffusion significantly contributes to the recovery, whereas the history-matched field scale model showed little effects of molecular diffusion on the incremental recovery.

For such simulation studies, compositional simulation is widely used to account for relevant physics such as fluid phase behavior, complex fracture geometry, reservoir heterogeneity and multi-component effects, etc. However, substantial computational burden makes it challenging to use high-resolution field-scale models and to carry out large number of simulation runs. It sometimes leads to over-simplification of the simulation models that might mask important underlying physics.

In this chapter, we develop and validate a rapid compositional simulator using the FMM and an efficient workflow for optimizing CO₂ and gas Huff-n-Puff in unconventional reservoirs. The use of the rapid FMM-based approach enables us to incorporate compositional simulations using high-resolution reservoir models with population-based optimization algorithms. We first present the mathematical formulation of our FMM-based approach, followed by the validation using synthetic models. Next, we show the field-scale optimization of an Eagle Ford well to demonstrate the efficacy and robustness of our proposed workflow.

3.3 Mathematical Formulation

In the previous chapter, we presented the FMM-based simulation for multi-phase system. We extended the method to multi-component system as discussed by Fujita (2014).

3.3.1 Dual-porosity Compositional Formulation

Based on the dual-porosity assumption, we have the governing equations for fracture as follows:

$$\begin{aligned} \frac{\partial}{\partial t} \left[\phi \left(x_i \rho_o S_o + y_i \rho_g S_g \right) \right]_f &= \nabla \cdot \left[k \left(x_i \rho_o \lambda_o + y_i \rho_g \lambda_g \right) \nabla p \right]_f \\ &+ x_i \rho_o \tilde{q}_o + y_i \rho_g \tilde{q}_g - (x_i \rho_o)_{up} \Gamma_o - (y_i \rho_g)_{up} \Gamma_g, \end{aligned} \quad (3.1)$$

$$\frac{\partial}{\partial t} [\phi \rho_w S_w]_f = \nabla \cdot [k \rho_w \lambda_w \nabla p]_f + \rho_w \tilde{q}_w - (\rho_w)_{up} \Gamma_w, \quad (3.2)$$

$$(F_i^L)_f = (F_i^V)_f. \quad (3.3)$$

The above Eqs. (3.1), (3.2) and (3.3) represent hydrocarbon mole conservation, water mole conservation and hydrocarbon fugacity equilibrium between liquid and vapor phases, respectively. F_i is fugacity of component i (Firoozabadi, 1999), ρ is phase molar density, \tilde{q} is volumetric flow rate per unit bulk volume, x and y are phase mole fraction in oil and gas phase. Subscripts m, f, i and up stand for matrix, fracture, i -th component and upstream that is either matrix or fracture, respectively. The fluid transfer Γ between the fracture and matrix is given by Eq. (2.29). Similar equations can be written for matrix:

$$\frac{\partial}{\partial t} \left[\phi (x_i \rho_o S_o + y_i \rho_g S_g) \right]_m = (x_i \rho_o)_{up} \Gamma_o + (y_i \rho_g)_{up} \Gamma_g, \quad (3.4)$$

$$\frac{\partial}{\partial t} [\phi \rho_w S_w]_m = (\rho_w)_{up} \Gamma_w, \quad (3.5)$$

$$(F_i^L)_m = (F_i^V)_m. \quad (3.6)$$

By assuming that all the pressure, saturation and composition changes are aligned with the DTOF contour, we can apply the coordinate transformation (2.24) to Eqs. (3.1) and (3.2) to obtain 1-D formulation along the DTOF:

$$\begin{aligned} & \frac{\partial}{\partial t} \left[\phi (x_i \rho_o S_o + y_i \rho_g S_g) \right]_f \\ &= \frac{\phi_{f,ref}}{w(\tau)} \frac{\partial}{\partial \tau} \left[w(\tau) \left(\frac{c_t}{\lambda_t} \right)_{ref} (x_i \rho_o \lambda_o + y_i \rho_g \lambda_g) \left(\frac{\partial p}{\partial \tau} \right) \right]_f \\ &+ (x_i \rho_o \tilde{q}_o + y_i \rho_g \tilde{q}_g) \delta(\tau_{wb}) - (x_i \rho_o)_{up} \Gamma_o - (y_i \rho_g)_{up} \Gamma_g, \end{aligned} \quad (3.7)$$

$$\begin{aligned} \frac{\partial}{\partial t} [\phi \rho_w S_w]_f &= \frac{\phi_{f,ref}}{w(\tau)} \frac{\partial}{\partial \tau} \left[w(\tau) \left(\frac{c_t}{\lambda_t} \right)_{ref} \rho_w \lambda_w \left(\frac{\partial p}{\partial \tau} \right) \right] \\ &+ \rho_w \tilde{q}_w \delta(\tau_{wb}) - (\rho_w)_{up} \Gamma_w. \end{aligned} \quad (3.8)$$

3.3.2 Phase Equilibrium Calculation

In this research, we will use Peng-Robinson's cubic equation of state (EoS) in conjunction with Peneloux volume correction (Peng and Robinson, 1976; Robinson and Peng, 1978; Jhaveri and Youngren, 1988):

$$p = \frac{RT}{V-b} - \frac{a(T)}{(V+c)(V+2c+b) + (b+c)(V-b)}, \quad (3.9)$$

where R , V and T and c denote universal gas constant, volume, temperature and volume shift or volume translation parameter, respectively. The parameters a and b are calculated with the following formulations:

$$a(T) = a_c \alpha(T), \quad (3.10)$$

$$a_c = 0.45724 \frac{R^2 T_c^2}{P_c}, \quad (3.11)$$

$$\alpha(T) = \left[1 + m \left(1 - \sqrt{\frac{T}{T_c}} \right) \right]^2, \quad (3.12)$$

$$b = \frac{0.07780 R T_c}{P_c}, \quad (3.13)$$

where subscript c stands for the critical condition. The parameter m can be computed with the following two formulations as per the acentric factor ω :

$$m = \begin{cases} 0.37464 + 1.54226\omega - 0.26992\omega^2 & \text{if } \omega \leq 0.490 \\ 0.379642 + 1.48503\omega - 0.164423\omega^2 + 0.016666\omega^3 & \text{if } \omega > 0.490 \end{cases} \quad (3.14)$$

For N_c -component mixture,

$$a = \sum_i^{N_c} \sum_j^{N_c} z_i z_j a_{ij}, \quad (3.15)$$

$$b = \sum_i^{N_c} z_i b_i, \quad (3.16)$$

$$a_{ij} = \sqrt{a_i a_j} (1 - k_{ij}), \quad (3.17)$$

where z_i and k_{ij} denote the mole fraction of component i and binary interaction coefficient between components i and j . The following cubic equation for the Z-factor can be obtained by equating the Equation of State for real gas $PV = ZRT$ with Eq. (3.9):

$$Z^3 - Z^2 + (A - B + B^2)Z - AB = 0, \quad (3.18)$$

where

$$A = \frac{a(T)p}{R^2 T^2}, \quad (3.19)$$

$$B = \frac{bp}{RT}. \quad (3.20)$$

For the phase equilibrium calculation, fugacity of component i is calculated below:

$$\ln \frac{F_i}{z_i p} = \frac{b_i}{b} (Z - 1) - \ln(Z - B) + \frac{A}{(m_1 - m_2)B} \left[\frac{2 \sum_j^{N_c} a_{ij} z_j}{a} - \frac{b_i}{b} \right] \ln \left(\frac{Z + m_2 B}{Z + m_1 B} \right), \quad (3.21)$$

where constants m_1 and m_2 are $1 + \sqrt{2}$ and $1 - \sqrt{2}$, respectively. Note that parameters a and b must be computed for each liquid and vapor phase by substituting mole fraction in liquid phase x_i or mole fraction y_i into z_i in Eqs. (3.15) and (3.16). Thus, all the resulting parameters A , B and Z and fugacity are different between liquid and vapor phase.

3.3.3 Phase Density, Compressibility and Viscosity

The phase molar density in Eq. (3.1) can be computed based on the phase molar volume \tilde{v} as follows:

$$\tilde{v}_L = \frac{Z_L RT}{p} - \sum_i^{N_c} x_i c_i, \quad (3.22)$$

$$\tilde{v}_V = \frac{Z_V RT}{p} - \sum_i^{N_c} y_i c_i, \quad (3.23)$$

$$\rho_L = 1/\tilde{v}_L, \quad (3.24)$$

$$\rho_V = 1/\tilde{v}_V. \quad (3.25)$$

The phase compressibility to be used in the Eikonal equation (2.17) can be calculated numerically by the derivatives of phase molar density with respect to pressure:

$$c_o = \frac{1}{\rho_L} \frac{\partial \rho_L}{\partial p}, \quad (3.26)$$

$$c_g = \frac{1}{\rho_V} \frac{\partial \rho_V}{\partial p}, \quad (3.27)$$

For viscosity calculation, the Lohrenz-Bray-Clark (LBC) correlation was used (Lohrenz et al., 1964) which can be computed by the following equation:

$$\left[(\mu - \mu_0) \xi + 10^{-4} \right]^{0.25} = \sum_{i=1}^5 d_i \rho_r^{i-1}, \quad (3.28)$$

where d_1 : 0.10230, d_2 : 0.023364, d_3 : 0.058533, d_4 : -0.040758 and d_5 : 0.0093324. μ_0 is the low-pressure gas mixture viscosity, ρ_r is the reduced molar density ρ/ρ_c , ξ is the viscosity-reducing parameter defined as follows:

$$\mu_0 = \frac{\sum_i^{N_c} z_i \mu_{0,i} \sqrt{M_i}}{\sum_i^{N_c} z_i \sqrt{M_i}}, \quad (3.29)$$

$$\mu_{0,i} = \begin{cases} 34 \times 10^{-5} \frac{1}{\xi_i} T_{ri}^{0.94} & \text{for } T_{ri} < 1.5 \\ 17.78 \times 10^{-5} \frac{1}{\xi_i} (4.58 T_{ri} - 1.67)^{5/8} & \text{for } T_{ri} > 1.5 \end{cases}, \quad (3.30)$$

$$\xi = \frac{\left[\sum_i^{N_c} z_i T_{ci} \right]^{1/6}}{\left[\sum_i^{N_c} z_i M_i \right]^{1/2} \left[\sum_i^{N_c} z_i P_{ci} \right]^{2/3}}, \quad (3.31)$$

$$\xi_i = \frac{T_{ci}^{1/6}}{M_i^{1/2} P_{ci}^{2/3}}, \quad (3.32)$$

where M_i and T_{ri} is the molecular weight and reduced temperature of component i .

3.4 Validation using 3-D Homogeneous Case

We validated our approach using 3-D synthetic reservoir models by comparisons with a commercial FDSim. We first present an example of primary depletion using a homogeneous reservoir model. The example demonstrates accuracy and computational efficiency of the FMM-based compositional simulation.

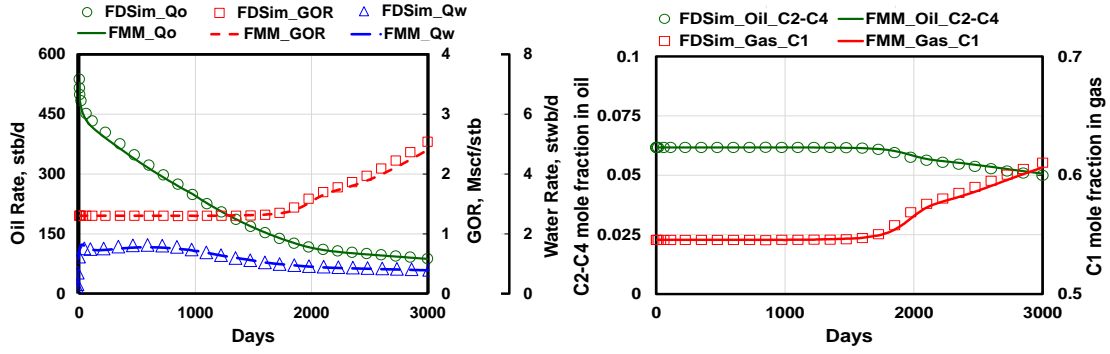
3.4.1 Model Setting

The same model input was used as the example in the last chapter (Table 2.4) except the fluid model. The EoS model was generated based on the Bakken data (Najabaei et al., 2013) that shows a bubble point pressure of 2860 psi at the reservoir temperature of 240 degF. Initial composition is listed in **Table 3.1**. A production well with the constant bottomhole pressure of 2,000 psi was placed at the center and completed vertically in all layers. The number of 1-D grid blocks was set to be 200.

Table 3.1 Initial composition for 3-D homogeneous compositional case (reprinted with permission from Iino et al., 2017b)

	C1	C2	C3	C4	C5-6	C7-12	C13-21	C22-80
Initial Mole fraction	0.367	0.149	0.093	0.058	0.064	0.159	0.073	0.037

Figure 3.1a shows comparisons of gas-oil-ratio (GOR), oil and water rates between the FMM-based simulation and the FDSim. All the three-phase productions are in good agreement. Furthermore, mole fractions of intermediate components (C2-4) in produced oil and methane (C1) in produced gas are also illustrated in **Figure 3.1b**. FMM-based simulation correctly captures changes in mole fraction due to liberation of solution gas in the reservoir.



(a) Oil, gas and water rate

(b) Mole fraction in produced oil and gas

Figure 3.1 Comparisons between FMM-based (lines) and FDSim (symbols) for homogeneous case (reprinted with permission from Iino et al., 2017b)

3.4.2 CPU Time

In order to study the computational efficiency of our approach, additional simulations were run using the same reservoir model with grid refinement. **Figure 3.2** shows comparisons of CPU time between the FMM-based simulator and the FDSim. For all the cases, 200 grid blocks were used for 1-D simulation, which was confirmed to be a sufficient number based on the analysis of $w(\tau)$ convergence discussed in 2.5.1.3. The results demonstrate that two to three orders of magnitude faster computation can be expected by the use of FMM-based simulation, particularly for large scale and high resolution models with millions of grid blocks.

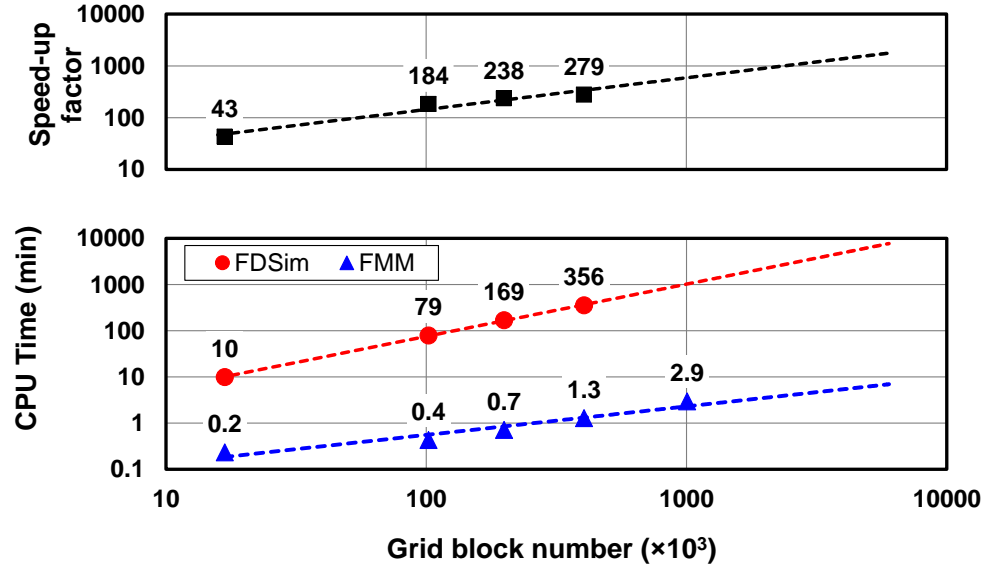


Figure 3.2 CPU Time comparison (bottom) and speed-up factor (top) between FMM-based and FD simulations. Number of 1-D grid blocks and number of time steps are fixed to be 200 and 128, respectively (reprinted with permission from Iino et al., 2017b)

Furthermore, the speed-up factors to the FDSim are compared between blackoil and compositional simulations in **Figure 3.3**. The speed-up is more significant in the compositional simulation by an order-of-magnitude. Since the compositional simulation requires additional $2 \times (N_c - 1) \times N_x \times N_y \times N_z$ primary variables compared to the blackoil simulation, it leads to more significant reduction in the number of primary variables by the 1-D transformation. In addition, flash calculations in the compositional simulation can also be significantly reduced in the FMM-based simulation. For the case of 0.4 million grid blocks ($201 \times 201 \times 10$), flash calculations involved in the FDSim and the FMM-based simulation were 70.3 million and 35 thousands, respectively.

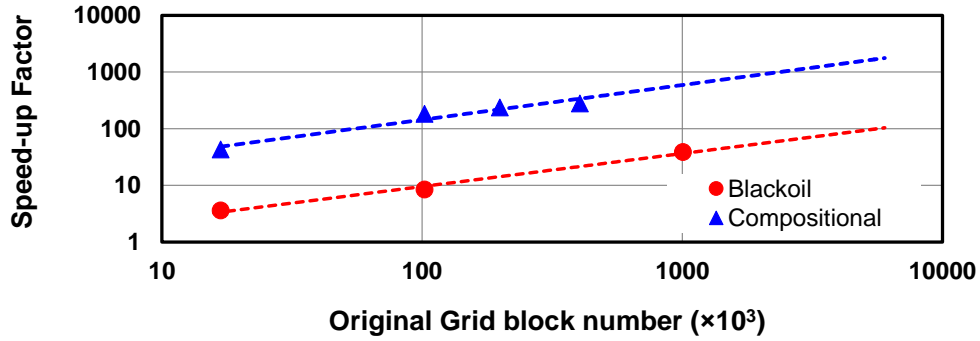


Figure 3.3 Comparison of speed-up factors between blackoil and compositional simulations

3.5 Validation using CO₂ Huff-n-Puff Example in Unconventional Reservoir

We further validated our approach using an example of CO₂ Huff-n-Puff in heterogeneous reservoir completed with multi-stage hydraulically fractured well.

3.5.1 Model Setting

A heterogeneous dual-porosity reservoir model completed with multi-stage hydraulically fractured well was set-up. A reservoir domain of 2000'×6000'×100' was meshed by a tartan grid (200×394×5, 0.4 million cells) and 4-cluster×10-stage hydraulic fractures with the uniform geometry were placed (**Figure 3.4**). The properties of reservoir and hydraulic fractures are summarized in **Table 3.2**. **Figure 3.5** illustrates the distributions of reservoir properties.

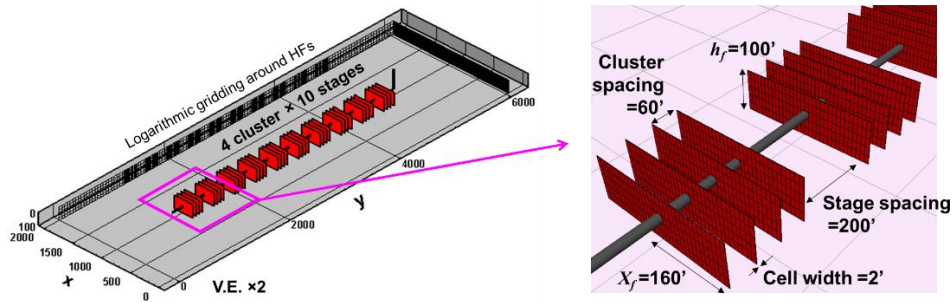


Figure 3.4 Geometry of multi-stage hydraulic fractures for CO₂ Huff-n-Puff case (reprinted with permission from Iino and Datta-Gupta, 2018)

Table 3.2 Reservoir properties and initial condition for CO₂ Huff-n-Puff case (reprinted with permission from Iino and Datta-Gupta, 2018)

	Hydraulic Fracture	Fracture	Matrix
Porosity	0.076	Figure 3.5	0.076
Permeability (mD)	10.0	Figure 3.5	1×10^{-6}
k_v/k_h	0.1	Figure 3.5	0.1
Rock compressibility (psi^{-1})	1.0×10^{-6}	1.0×10^{-6}	1.0×10^{-6}
Initial water saturation	0.8	Figure 3.5	0.4
Pressure-dependent Compaction coeff. b (psi^{-1})	5.9×10^{-5}	5.5×10^{-4}	0
Initial Pressure (psi)		6425	
Reservoir Temperature (degF)		160	

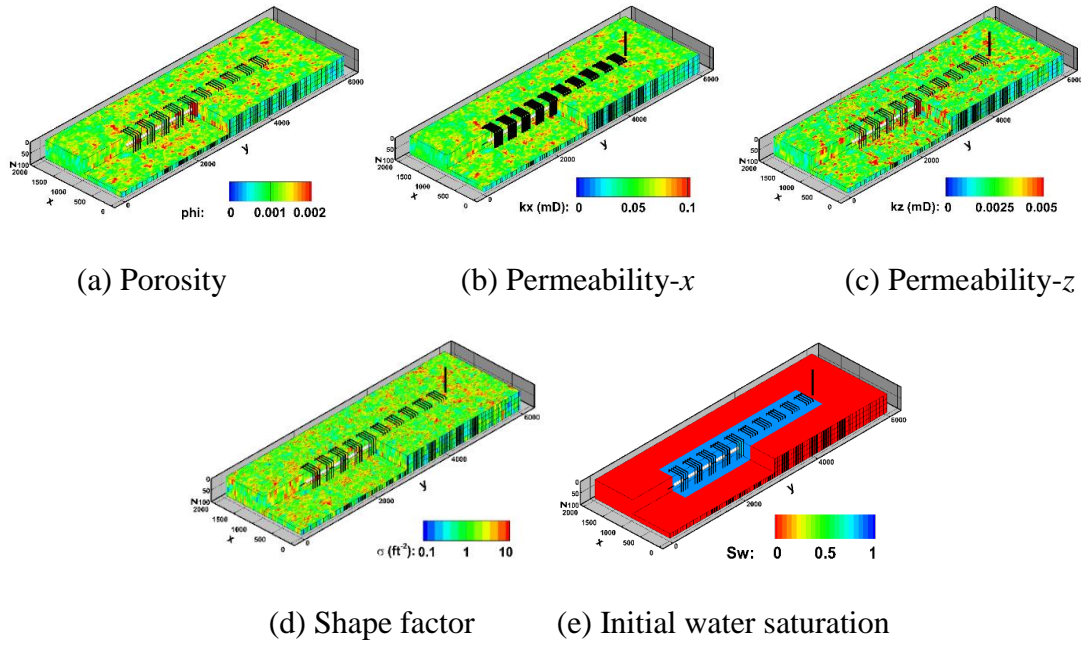
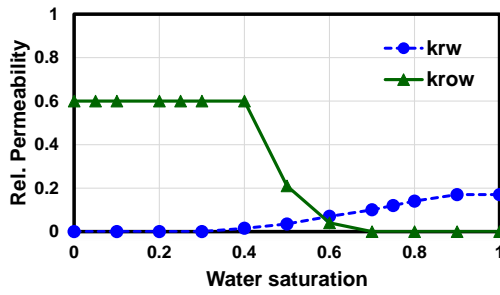
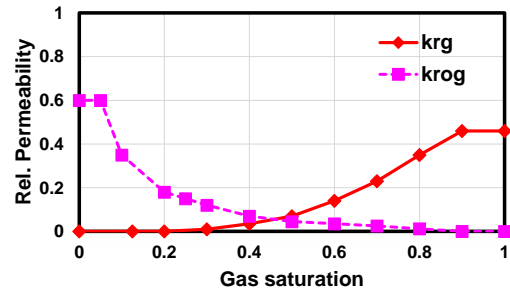


Figure 3.5 Geometry of multi-stage hydraulic fractures for CO₂ Huff-n-Puff case (reprinted with permission from Iino and Datta-Gupta, 2018)

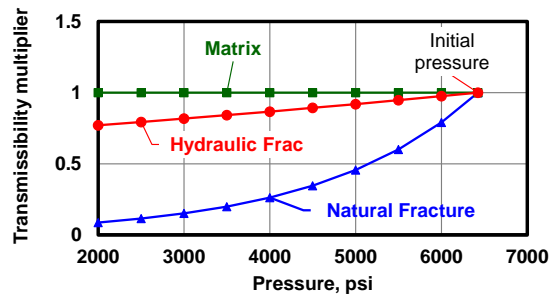
Three-phase relative permeability for the matrix is shown in **Figure 3.6a** and **b** whereas straight lines were used for the fracture system. **Figure 3.6c** illustrates the permeability reduction due to compaction using the relation: $k = k_i \times e^{-b\Delta p}$ where k_i is the initial permeability, Δp is pressure depletion and b is the compaction coefficient (Raghavan and Chin, 2002). The EoS model with seven pseudo-components was adapted from (Wan and Sheng, 2015) and the initial composition is listed in **Table 3.3**. The bubble point pressure is 2,300 psi at the reservoir temperature of 160 degF and Minimum Miscibility Pressure (MMP) with the injection CO₂ is estimated to be 2,200 psi based on the slimtube simulation.



(a) Oil-water relative permeability



(b) Gas-oil relative permeability



(c) Rock compaction table

Figure 3.6 Relative permeability and rock compaction tables for CO₂ Huff-n-Puff case (reprinted with permission from Iino and Datta-Gupta, 2018)

Table 3.3 Initial composition and molecular weight for CO₂ Huff-n-Puff case (reprinted with permission from Iino and Datta-Gupta, 2018)

Component	Initial Mole Fraction.	Mol. Weight (g/mole)
C1	0.50	16
CO ₂	0.00	44.01
C2-3	0.03	44.1
C4-6	0.07	86.2
C7-11	0.20	142.2
C12-15	0.15	206
C16p	0.05	282

3.5.2 Base Case Simulation

We first simulated primary depletion for 1,000 days under constant bottomhole pressure of 2,500 psi. Number of 1-D grid blocks was set to be 800 based on the analysis of $w(\tau)$ convergence discussed in 2.4.1. Both oil and water productions are in good agreement between the FMM-based simulation and the FDSim (**Figure 3.7**).

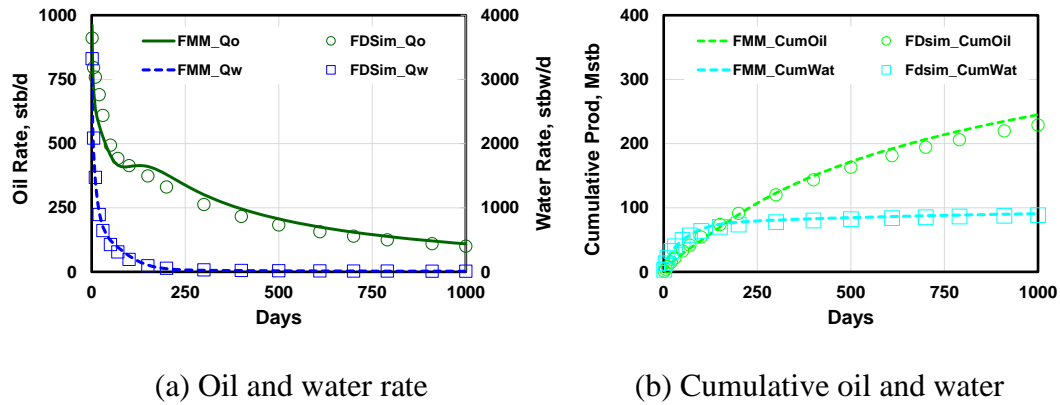


Figure 3.7 Comparison of FMM-based simulation with FDSim in primary depletion before Huff-n-Puff (reprinted with permission from Iino and Datta-Gupta, 2018)

Subsequently, seven cycles of CO₂ Huff-n-Puff were simulated for another 1,000 days where one cycle consists of three periods: (1) CO₂ injection with 5 MMscf/d for 25 days, (2) soaking for 20 days and (3) production with bottomhole pressure of 2,500 psi for 100 days. **Figure 3.8** illustrates the simulated well performance during the Huff-n-Puff. The FMM-based simulation (lines) provides good agreement with the FDSim (symbols). The incremental oil in Figure 3.8 is evaluated from the end of primary depletion at 1,000 days.

For comparison purpose, the incremental oil production of ‘do-nothing’ case (i.e. continued primary depletion) simulated by the FMM-based approach is also plotted (dashed line) in Figure 3.8. Increase in incremental oil recovery was predicted to be 56 Mstb for CO₂ Huff-n-Puff case compared to the do-nothing case.

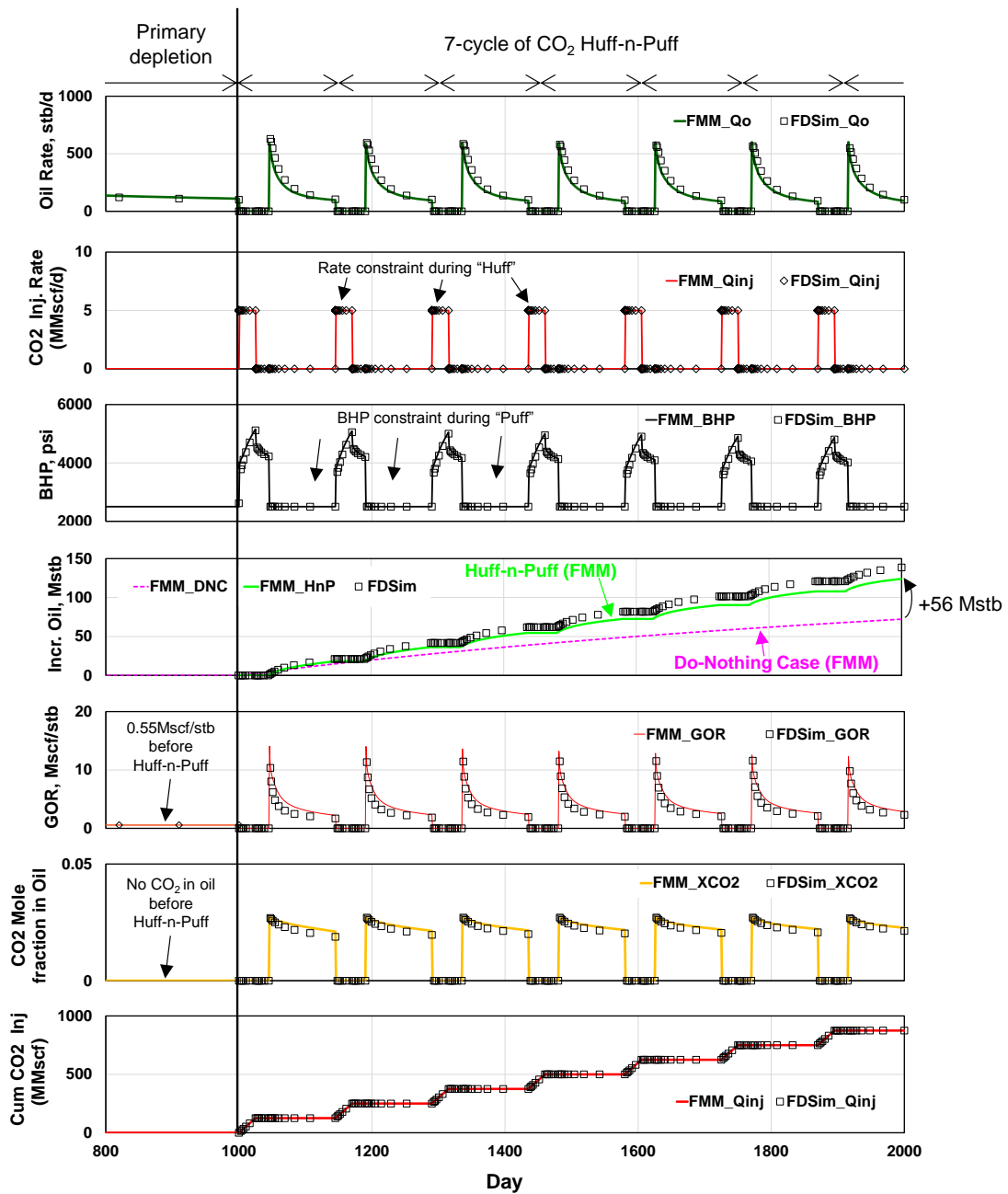


Figure 3.8 Simulated well performance during CO₂ Huff-n-Puff (line: FMM-based simulation, symbol: FDSim) (reprinted with permission from Iino and Datta-Gupta, 2018)

3.5.3 CPU Time

In addition to the good agreement of simulation results with the FDSim, the FMM-based simulation provides significant computational efficiency. **Table 3.4** shows the comparison of computational performances between the FDSim and the FMM-based simulation. The FMM-based approach achieves two-order of magnitude faster computation because of mainly two reasons: it significantly reduces (1) the number of simulation grid blocks by transforming the 3-D to 1-D problem and (2) the number of flash calculations and stability analysis involved in compositional simulation. The breakdown of CPU time for the FMM-based approach is also illustrated in **Figure 3.9**. The FMM can efficiently solve the Eikonal equation within a minute for this example with 0.4 million cells. In the next section, we will present the sensitivity of Huff-n-Puff operational parameters. The 1-D simulation dataset can be used for any well schedules as long as well completion remains the same, which means we can skip the steps of solving the Eikonal equation and calculating $w(\tau)$ and 1-D transmissibilities for such sensitivity runs once the 1-D dataset is generated.

Table 3.4 Computational efficiency of FMM-based compositional simulation for CO₂ Huff-n-Puff simulation

	FDSim	FMM	Scale-up or Speed-up
# of grid blocks	394,000	800	493
# of flash & stability analysis	2,220 millions	3.6 millions	617
CPU Time (min)	2,121	4	530

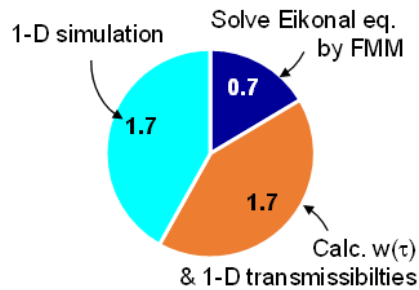


Figure 3.9 Breakdown of CPU time of FMM-based simulation for 1000day primary depletion plus 1000day CO₂ Huff-n-Puff (reprinted with permission from Iino and Datta-Gupta, 2018)

3.5.4 Sensitivity Analysis

Designing a Huff-n-Puff EOR involves the selection of operational parameters such as injection rate, injection time, soaking and production times, etc. Such parameters may significantly influence the incremental recovery during the project life and need to be comprehensively explored for optimizing the Huff-n-Puff. Based on the parameter ranges in **Table 3.5** and the maximum injection pressure limit of 6,425 psi, sensitivity analysis was performed as shown in **Figure 3.10**. The injection rate is the most influential parameter; the higher injection rate improves the oil recovery as it facilitates further propagation of injected CO₂ and more increase in reservoir pressure. The injection time shows similar sensitivity but less impact than the injection rate. The shorter production time has a positive impact on the incremental recovery with the base case parameters. The soaking time shows relatively small impact in this case possibly because we do not model the molecular diffusion.

Table 3.5 Ranges of operational parameters of Huff-n-Puff for 1,000 days (reprinted with permission from Iino and Datta-Gupta, 2018)

Parameter	Low	Base	High
Injection rate (MMscf/day)	1	5	10
Injection time (day)	10	25	50
Soaking time (day)	10	20	40
Production time (day)	25	50	200

* Maximum injection BHP was set as 6425 psi

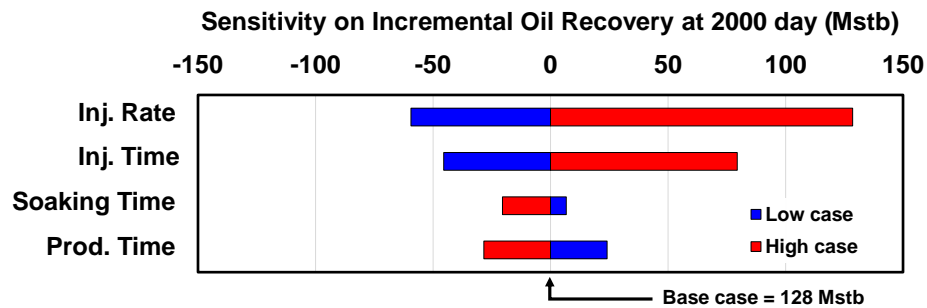


Figure 3.10 Sensitivity of operational parameters for Huff-n-Puff on incremental recovery (reprinted with permission from Iino and Datta-Gupta, 2018)

To further validate our FMM-based approach and see the impact on the incremental recovery, fifty (50) parameter combinations were sampled by Latin Hypercube Sampling (McKay et al., 1979) from the parameter space of Table 3.5. **Figure 3.11a** illustrates the cross-plot of incremental oil production computed from the FMM-based simulation and the FDSim. The FMM-based simulation consistently gives a good matching with the FDSim for all the simulation cases. In addition, computational efficiency of the FMM-

based approach enables us to run large number of cases in a practical timeframe as seen in **Figure 3.11b**. The FMM-based approach required only two hours whereas the FDSim would have required 59 days if simulations were run in sequence using the same computer resources. In the next section, we will present a field-scale optimization of operational parameters of Huff-n-Puff EOR.

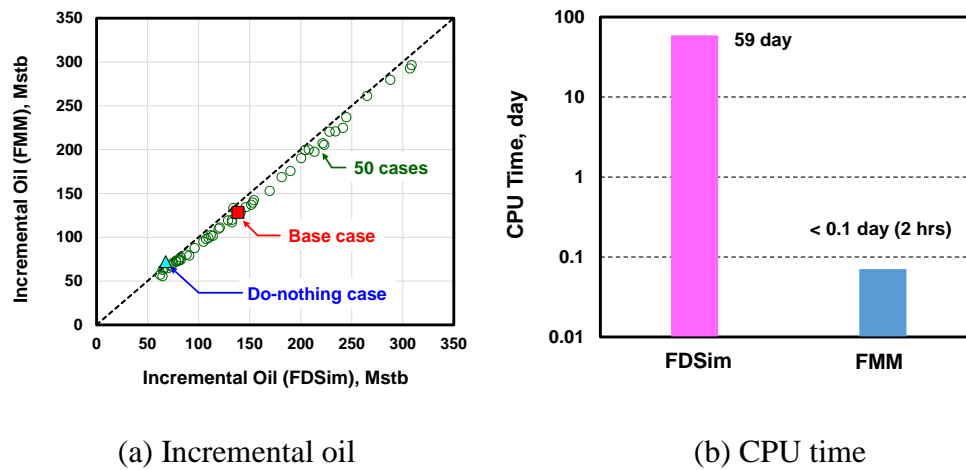


Figure 3.11 Comparisons between FMM-based simulation and FDSim: incremental oil and CPU time for fifty combinations of operational parameters for Huff-n-Puff (reprinted with permission from Iino and Datta-Gupta, 2018)

3.6 Field Scale Application

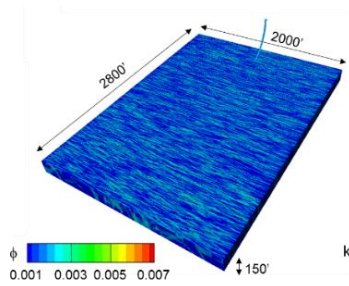
In this section, we present an efficient framework for field-scale optimization of Huff-n-Puff EOR in unconventional reservoirs using Genetic Algorithm and the FMM-based simulation.

3.6.1 Model Setting

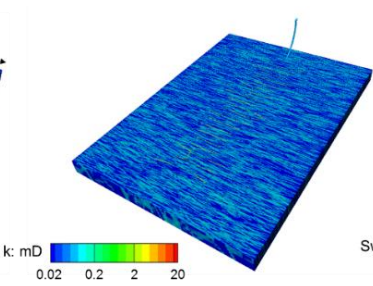
A 3-D dual-porosity reservoir model was built using typical properties for the Eagle Ford Shale (**Table 3.6**). The reservoir domain of 2,000'×2,800'×150' was regularly gridded using Cartesian cells of 400×560×5 (1,120,000). Natural fracture porosity and permeability were upscaled from the stochastically generated discrete fractures (**Figure 3.12a** and **b**). We assumed homogeneous properties and water saturation for the matrix. High water saturation was assigned to the region around hydraulic fractures (**Figure 3.12c**). Four stages of hydraulic fractures were generated as illustrated in **Figure 3.12d** by a commercial software where each stage has five fractures with a spacing of 100 ft (Yang et al., 2017b). The permeability of hydraulic fractures were adjusted to account for the grid block size (5'×5'×30') such that the actual fracture conductivity was replicated. The same EoS model, relative permeability and rock compaction tables were used as the previous example. The DTOF was computed as depicted in **Figure 3.12e**, which indicates that pressure will first propagate within hydraulic fracture planes, followed by the formation linear flow and then compound linear flow.

Table 3.6 Reservoir and hydraulic fracture properties for field-scale example of Huff-n-Puff optimization (reprinted with permission from Iino and Datta-Gupta, 2018)

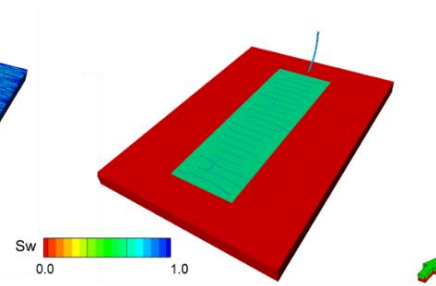
	Hydraulic Fracture	Fracture	Matrix
Porosity	Figure 3.12	Figure 3.12	0.08
Permeability (mD)	Figure 3.12	Figure 3.12	1.5×10^{-4}
k_v/k_h	1.0	0.1	0.1
Rock compressibility (psi^{-1})	1.0×10^{-6}	1.0×10^{-6}	1.0×10^{-6}
Initial water saturation	0.9	Figure 3.12	0.4
Pressure-dependent Compaction coeff. b (psi^{-1})	5.9×10^{-5}	5.5×10^{-4}	0
Initial Pressure (psi)		6425	
Reservoir Temperature (degF)		160	



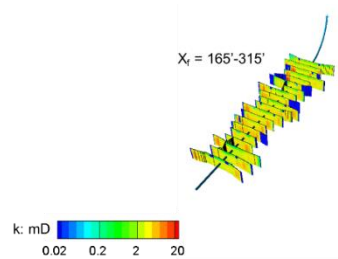
(a) Porosity



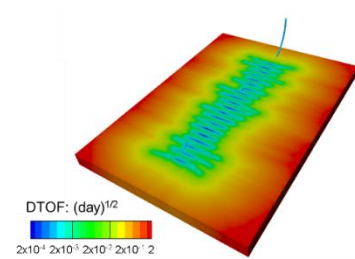
(b) Permeability



(c) Initial water saturation



(d) Hydraulic fracture geometry and permeability



(e) Computed DTOF

Figure 3.12 Fracture properties and computed DTOF for field-scale example of Huff-n-Puff optimization (reprinted with permission from Iino and Datta-Gupta, 2018)

3.6.2 Fluid Composition and Phase Behavior

Fluid Composition and Phase Behavior. In this case study, we will use the hydrocarbon gas as a solvent. The gas composition was generated by an atmospheric flash of the reservoir fluid (**Table 3.7**). The MMP of 4,850 psi was estimated by the slimtube simulation. The swelling test simulation indicates that oil volume increase of 50% will be achieved with the injected gas of 60 mole% and saturation pressure of 4,500 psi (**Figure 3.13**).

Table 3.7 Composition of reservoir fluid and solvent for field-scale example of Huff-n-Puff optimization (reprinted with permission from Iino and Datta-Gupta, 2018)

Component	Reservoir Fluid	HC gas solvent
C1	0.50	93.15
CO2	0.00	0.00
C2-3	0.03	4.97
C4-6	0.07	1.83
C7-11	0.20	0.05
C12-15	0.15	0.00
C16+	0.05	0.00
MMP (psi)		4,850 psi

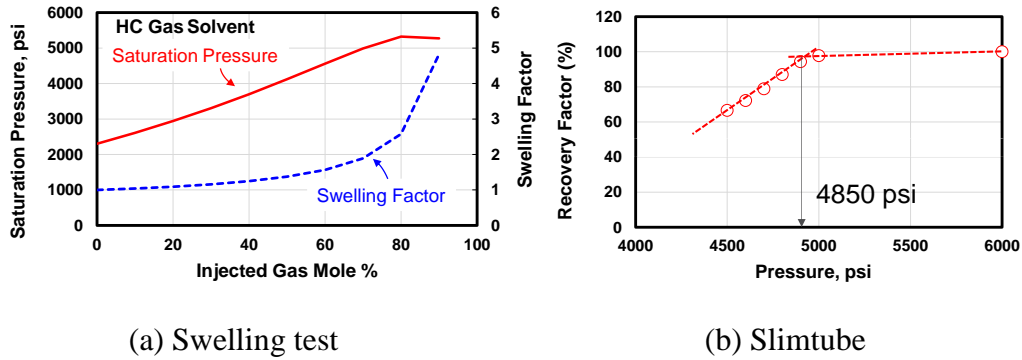
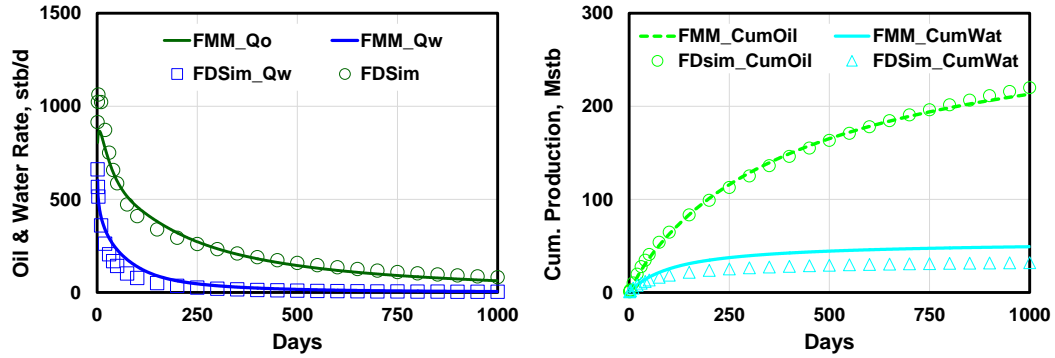


Figure 3.13 Slimtube and swelling test simulation (reprinted with permission from Iino and Datta-Gupta, 2018)

3.6.3 Primary Depletion

We first simulated the primary depletion for 1,000 days under constant bottomhole pressure of 2,500 psi. **Figure 3.14** compares oil and water production between the FMM-based simulation and the FDSim and shows good agreement. The cumulative oil production amounts to 212 Mstb that corresponds to a recovery factor of 4.2%. The CPU times of the FMM-based approach and the FDSim are 0.1 hours and 20.6 hours, respectively. The FMM-based approach shows two-order of magnitude faster computation.



(a) Oil and water rate

(b) Cumulative oil and water production

Figure 3.14 Simulated well performances for primary depletion for for field-scale example of Huff-n-Puff optimization (reprinted with permission from Iino and Datta-Gupta, 2018)

3.6.4 Huff-n-Puff: Base Case Simulation

As we have seen in the previous example, the operational parameters of Huff-n-Puff have significant impact on the incremental recovery and need to be optimized. We defined the objective function as incremental oil recovery for 1,000 days after the primary depletion. Parameters to be tuned are injection rate, injection time, soaking time and production time per cycle. For optimization, we used the Genetic Algorithm (Yin et al., 2011) incorporated with the rapid FMM-based simulation, which enables a large number of simulations in a practical timeframe. We first performed a base case simulation, followed by the sensitivity analysis using the parameters in **Table 3.8**. The production period was constrained by constant BHP of 2,500 psi, whereas the injection period was controlled by the assigned surface rate with the maximum BHP limit of 5,500 psi, which is above the MMP with hydrocarbon gas.

Table 3.8 Parameter ranges, objective function and simulation setting for Huff-n-Puff optimization (reprinted with permission from Iino and Datta-Gupta, 2018)

Parameter	Low	Base	High
Injection rate (MMscf/day)	0.5	5	10
Injection time (day)	10	25	50
Soaking time (day)	5	20	50
Production time (day)	50	100	200
Simulation period (day)	1000 day primary depletion + 1000 day Huff-n-Puff		
Objective function	Incremental oil recovery (Mstb) for 1000-2000 days		
Production constraints	Const. BHP control of 2,500 psi		
Injection constraints	Rate control with max. BHP limit of 5,500 psi		
Solvent	HC gas		

Figure 3.15 shows the simulated well responses of BHP, cumulative and incremental production where the ‘do-nothing case’ i.e. continuation of primary depletion is also depicted for comparison. Huff-n-Puff case shows an incremental recovery of 170 Mstb, which is significantly improved compared to the ‘do-nothing’ case of 36 Mstb. During the injection periods in Huff-n-Puff, injection BHP and well grid pressure reached the MMP but it falls off below the MMP in the soaking period. Hence, the base case simulation cannot maintain the single-phase condition during the production period. However, we still have effects of vaporizing, swelling and viscosity reduction by gas injection, leading to the improved oil recovery. **Figure 3.16**, which is change in methane

mole fraction in matrix oil, illustrates footprints of the injected gas at the end of gas injection in first, third and seventh cycles. We can confirm that the injected gas well propagates into the formation in the base case as the cycle of Huff-n-Puff proceeds. We will further optimize the operational parameters for better design of Huff-n-Puff.

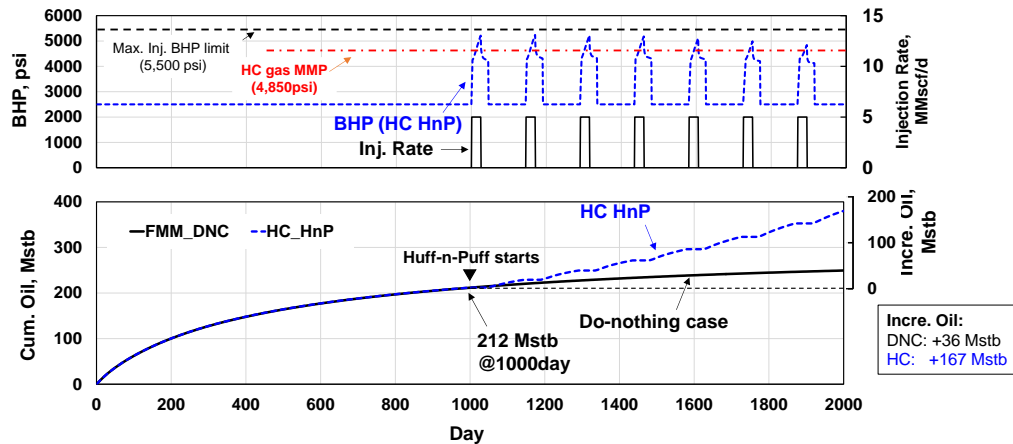


Figure 3.15 Simulated BHP and cumulative oil responses with base case parameters for field scale example of Huff-n-Puff optimization (reprinted with permission from Iino and Datta-Gupta, 2018)

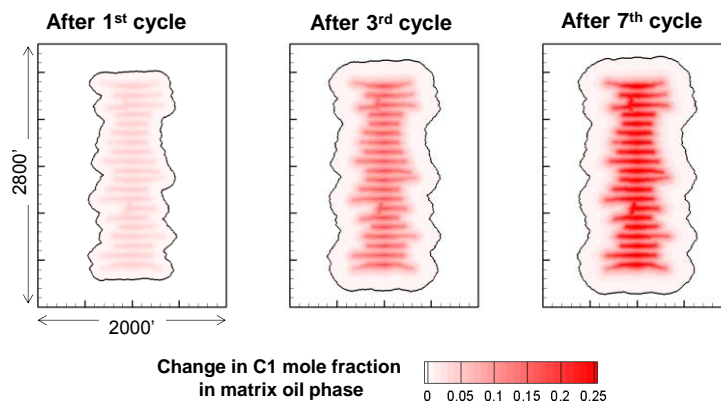


Figure 3.16 Footprint of injected gas at each cycle (Base case)

3.6.5 Huff-n-Puff: Sensitivity Analysis

Subsequently, sensitivity analysis was performed with the parameter ranges in Table 3.8. **Figure 3.17** shows a tornado chart that quantifies the impact of individual parameters. As we have seen in the previous example, injection rate is the most influential parameter on incremental recovery because it affects pressure increase, propagation distance of injected gas and achievement of miscibility. Injection time has similar effect but less impact since the longer injection time leads to reduced number of Huff-n-Puff cycles. The shorter production and soaking times have a positive impact with the base case parameters.

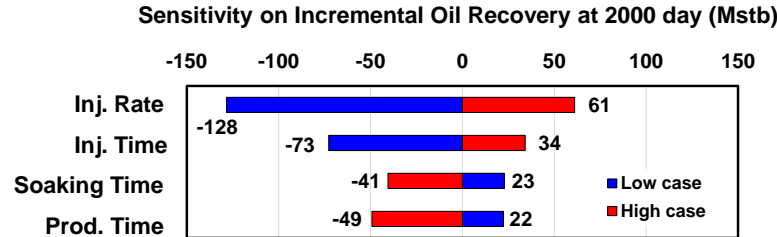


Figure 3.17 Sensitivity analysis on incremental recovery for field-scale example of Huff-n-Puff optimization (reprinted with permission from Iino and Datta-Gupta, 2018)

3.6.6 Optimizing Huff-n-Puff

In the optimization using the Genetic Algorithm, parameters were adjusted to maximize the objective function i.e. incremental recovery. **Figure 3.18** illustrates the

simulated incremental recovery versus generation numbers, which stabilizes after three generations. The required number of simulations was approximately 160 but was finished within 9 hours by use of the rapid FMM-based simulation. This would be computationally prohibitive in a practical timeframe if we used a normal finite difference simulation.

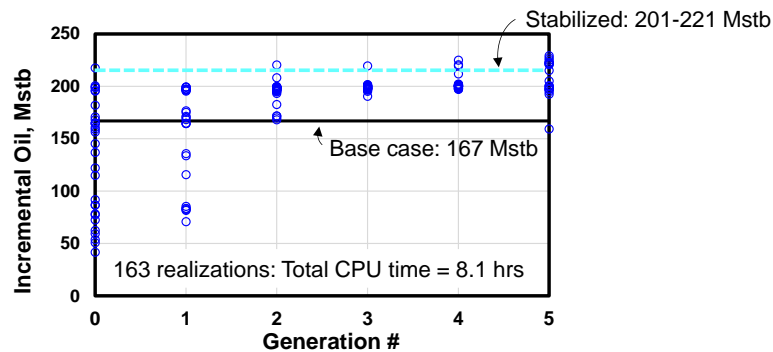
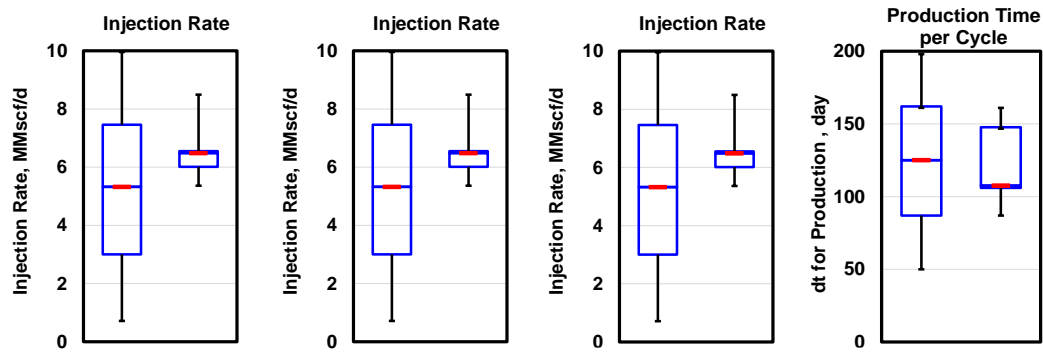


Figure 3.18 Incremental oil recovery vs. generation number during the optimization using Genetic Algorithm (reprinted with permission from Iino and Datta-Gupta, 2018)

The ranges of parameter distributions have been narrowed down through the optimization. By selecting the best thirty (30) realizations from the entire population, we depict the boxplots (**Figure 3.19**) that show the distributions of parameters and incremental recovery before and after optimization, which would assist designing the Huff-n-Puff parameters. For example, 6-7 MMscf/d is sufficiently enough for the injection rate with the injection time of 33-40 days and it is not required to achieve a higher rate such as 10 MMscf/d, which was the upper bound of the range. The soaking time of 25 days in base case seems to be too long and is preferred to be 8-12 days. The production

time should not be too short or too long; 110-150 days would be an appropriate choice to maximize the incremental oil recovery. Consequently, distributions of incremental oil recovery, voidage-replacement ratio (V.R.R.) and solvent usage were obtained as depicted in **Figure 3.20**. The V.R.R. (fraction) and solvent usage (Mscf/STB) are defined as cumulative production divided by cumulative injection in reservoir volumes and cumulative injection (Mscf) divided by incremental oil production (STB) in surface volume, respectively. With optimized parameters, we expect the resulting V.R.R. between 1.38 and 1.46 and the solvent usage between 5.7 and 6.3 Mscf/stb.



(Left: initial population, right: best 30 realization after optimization)

Figure 3.19 Box plots of parameters before/ after Huff-n-Puff optimization
(reprinted with permission from Iino and Datta-Gupta, 2018)

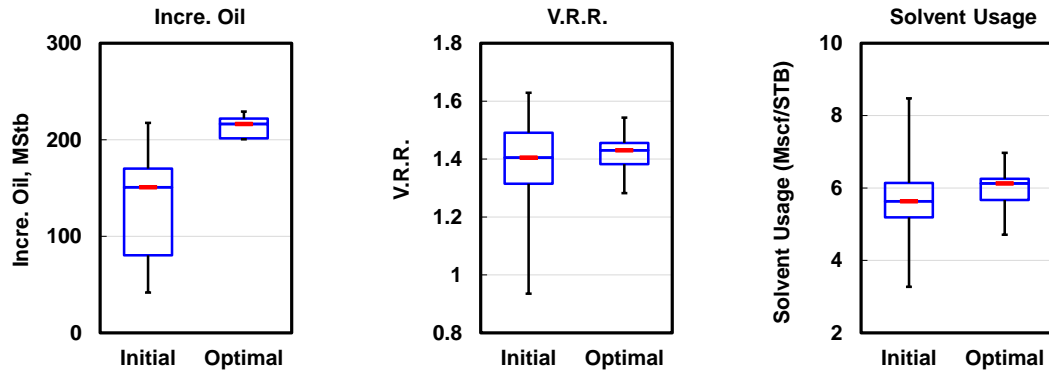


Figure 3.20 Box plots of simulated incremental recovery, V.R.R. and solvent usage before/ after optimization

Finally, we compare the worst, base and best cases to understand how the parameters influence the reservoir performance. **Figure 3.21** shows footprints of the injected gas for three cases along with the parameters and resulting V.R.R. and usage ratio. Because of the low injection rate (0.7 MMscf/d) in the worst case, the injected gas propagates less than the other cases and the field average pressure (**Figure 3.22**) decreases, leading to less improved recovery. On the other hand, the best case shows deeper propagation of the injected gas and the average pressure is maintained at higher level, requiring the larger V.R.R. of 1.4 and solvent usage of 6.0 Mscf/stb.

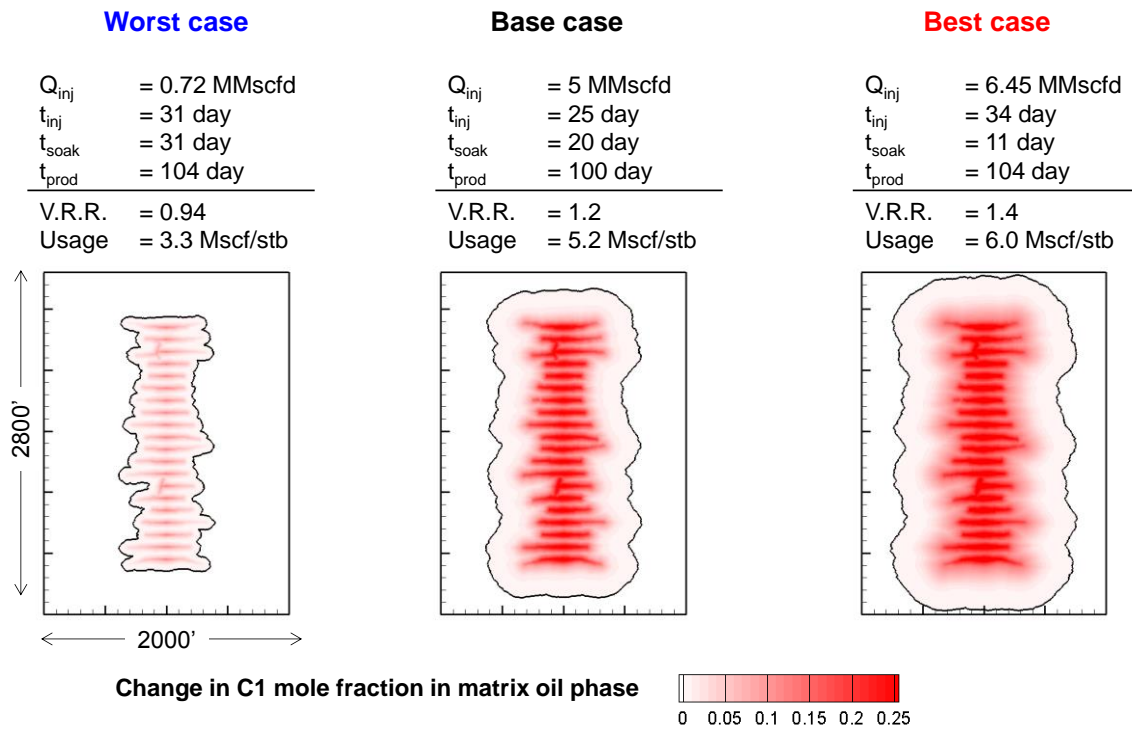


Figure 3.21 Footprint of injected gas at final cycle (worst, base and best cases)

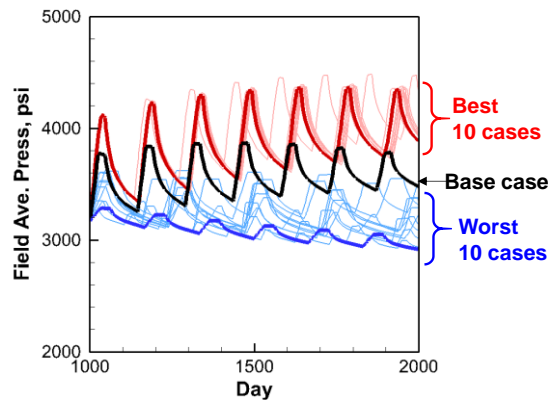


Figure 3.22 Average pressure during Huff-n-Puff (worst, base and best cases)

It should be noted that selection of objective function, parameters and their ranges can be specific to the project of interest. For instance, one might prefer to use Net Present Value (NPV) as the objective function rather than incremental recovery or prefer to include the commencement time of Huff-n-Puff as a parameter to get an idea when EOR should be started, etc. Our workflow using the FMM-based simulation provides a practical framework to improve the Huff-n-Puff design.

3.7 Conclusions

In this chapter, we presented the FMM-based compositional simulation and its application to rapid optimization of Huff-n-Puff EOR in unconventional reservoirs. Conclusions from this chapter are summarized below:

- The Diffusive Time-of-Flight (DTOF) obtained from the Fast Marching Method (FMM) is a representation of travel time of pressure ‘front’ propagation in heterogeneous and fractured reservoirs. The rapid FMM-based simulation utilizes the DTOF as a spatial coordinate to decouple the 3-D flow equations into 1-D flow equations, leading to significant reduction in computation time compared to full 3-D simulation.
- We validated the FMM-based approach by comparing with a commercial finite difference simulator using a CO₂ Huff-n-Puff in a synthetic dual-porosity reservoir with multi-stage hydraulic fractures. The FMM-based approach showed good agreement in simulated well responses and orders of magnitude faster computation as compared to the 3-D finite difference simulation.

- We presented a Huff-n-Puff optimization using the Genetic Algorithm coupled with the FMM-based simulation for a field-scale dual-porosity model with over a million cells and complex fracture geometry. Operational parameters such as injection rate, injection time, soaking and production times were tuned to maximize the incremental recovery.
- In the optimization example, approximately 160 simulation runs were required to achieve convergence but finished within only 9 hours. Use of rapid compositional simulation based on the FMM enables a large number of Huff-n-Puff simulations with a field-scale reservoir model in a practical timeframe.
- We can flexibly select any objective function, parameters and their ranges subject to the purpose and constraints specific to the project of interest. The optimization using a rapid FMM-based simulation can quickly assist designing and evaluating the Huff-n-Puff EOR in unconventional reservoirs.

CHAPTER IV

RAPID FIELD-SCALE WELL SPACING OPTIMIZATION IN TIGHT AND SHALE OIL RESERVOIRS USING THE FAST MARCHING METHOD[§]

4.1 Chapter Summary

An immediate and pressing need in the development of unconventional reservoirs is an innovative workflow that facilitates fast optimization of well placement. The optimal well placement design must ensure minimal interference between wells while maximizing the recovery/NPV. However, due to highly uncertain and poorly understood complex fracture geometries, optimal well spacing designs based on classical analytical techniques can be unreliable. We propose a rapid workflow to optimize well placement in unconventional reservoirs using the Fast Marching Method (FMM).

Our approach is to partition the reservoir model into independent sub-domains associated with individual wells based on the Diffusive Time of Flight (DTOF) computed as solution to the Eikonal equation using the FMM. Multi-phase production rates are then computed for each well by utilizing the DTOF as spatial coordinate to reduce the full 3-D numerical model to 1-D equivalent models resulting in orders of magnitude speed up in computation time. The computational efficiency of our approach enables extensive

[§] Material adapted with permission from “Rapid Field-Scale Well Spacing Optimization in Tight and Shale Oil Reservoirs Using Fast Marching Method” by Iino et al. 2018: Paper URTeC-2901376-MS Presented at the Unconventional Resources Technology Conference held in Houston, Texas, USA, 23-25 July 2018. Copyright 2018, Unconventional Resources Technology Conference. Further reproduction is prohibited without permission.

simulation runs to determine the point of diminishing return for additional well placement to obtain the optimal well spacing.

We illustrate the power and utility of our optimization workflow using synthetic and field-scale examples with multiple multi-stage hydraulically fractured wells. First, we demonstrate the reliability of our technique by confirming good rank correlation between our FMM-based simulation workflow and the 3-D finite difference simulation. Next we apply our optimization strategy to obtain the optimal well spacing while accounting for uncertainties in complex fracture geometries and conductivities. Finally, we show the robustness of our well spacing optimization workflow with an application to a shale oil reservoir in the Eagle Ford.

A unique and distinctive feature of our workflow is the computational efficiency that results from the significant reduction in simulation complexity through the FMM-based 1-D transformation. This enables rapid evaluation of well placement designs for large field models using an exhaustive search method which can be computationally prohibitive using classical numerical simulation techniques.

4.2 Background

Unconventional reservoirs account for significant hydrocarbon reserves in the U.S. (EIA, 2016). In most U.S. unconventional reservoir development, operators often first drill the minimum number of wells (parent wells) to hold their acreage followed by placing infill (child) wells to enhance the recovery generally 1 to 4 years after parent well depletions (Ranjan, 2015; Lindsay et al., 2018). As many operators initiated

unconventional reservoir developments between 2003 and 2010, majority of parent wells have been depleted, leading to increasing number of child wells drilled in recent years (Mason, 2012; Miller et al., 2016). Depletion of parent wells creates pressure sinks and therefore the stress field changes accordingly. Hydraulic fractures from the child well tend to grow towards lower resistance i.e. towards pressure sinks that can cause fracture interference (frac hit), resulting in a negative impact on production performance of both parent and child wells (Rodionov et al., 2017). Thus, careful reservoir management is essential in designing and optimizing the infill well placement.

In an effort to better understand the unconventional reservoirs, analytical and numerical models incorporating relevant physics at varying fidelity levels have been developed. Decline curve analysis (Fetkovich, 1980) and pressure/rate transient analysis (Song and Ehlig-Economides, 2011) are commonly used for fracture characterization and well performance predictions. While these analytical models provide significant benefits in terms of computational efficiency and simplicity, capturing important details such as heterogeneities of reservoir properties remains a considerable challenge.

High-fidelity, full-physics numerical simulators that typically employ finite difference/volume schemes are capable of simulating detailed non-linear descriptions. For fractured media, many approaches including multiple continuum models (e.g., Warrant and Root 1963; Kazemi et al., 1976) and discrete fracture models (Hyman et al., 2015; Monteagudo and Firoozabadi, 2004; Noorishad and Mehran, 1982) have been presented. For unconventional reservoirs, detailed spatial and temporal discretization is required to accurately model multi-phase flow in complex fracture network and high contrast systems

and therefore numerical models tend to be computationally expensive. This challenge has been partly mitigated by state-of-the-art solvers and parallelization, however, it is still too expensive to perform uncertainty assessment or optimizations where hundreds or thousands of simulations are required.

In this chapter, we present a rapid simulation technique based on the Fast Marching Method (FMM) for multiple wells. Recently, Huang et al. (2017) presented extension of the FMM-based approach to multi-well applications by partitioning the reservoir based on the flux and stationary tracer solutions. We demonstrate the robustness and efficacy of the FMM-based simulation for field scale optimization of infill development scenarios.

4.3 Methodology

This section describes the mathematical formulations and simulation methodology for multi-well simulation for a particular scenario where all the wells are controlled by the same bottomhole pressure.

4.3.1 Mathematical Formulation

In this chapter, we assumed the single-porosity and blackoil system. By removing the transfer term between fracture and matrix in Eqs. (2.33) through (2.35), we obtain the following governing equations on 1-D DTOF coordinate:

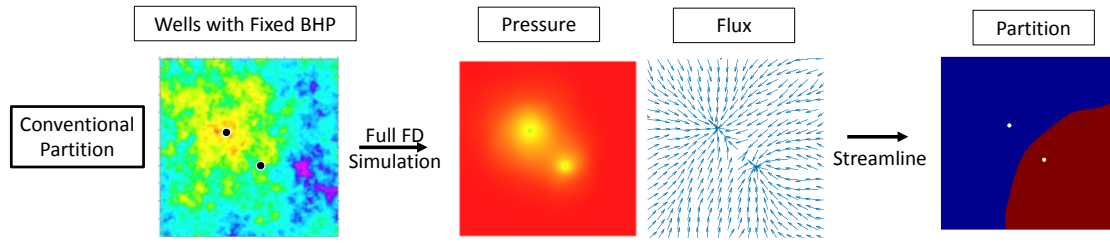
$$\frac{\partial}{\partial t} \left(\phi \frac{S_w}{B_w} \right) = \frac{\phi_{ref}}{w(\tau)} \frac{\partial}{\partial \tau} \left(w(\tau) \left(\frac{c_t}{\lambda_t} \right) \frac{k_{rw}}{B_w \mu_w} \frac{\partial p}{\partial \tau} \right) + \frac{\tilde{q}_w}{B_w} \delta(\tau_{wb}) \text{ (Water)}, \quad (4.1)$$

$$\frac{\partial}{\partial t} \left(\phi \frac{S_o}{B_o} \right) = \frac{\phi_{ref}}{w(\tau)} \frac{\partial}{\partial \tau} \left(w(\tau) \left(\frac{c_t}{\lambda_t} \right)_{ref} \frac{k_{ro}}{B_o \mu_o} \frac{\partial p}{\partial \tau} \right) + \frac{\tilde{q}_o}{B_o} \delta(\tau_{wb}) \text{ (Oil)}, \quad (4.2)$$

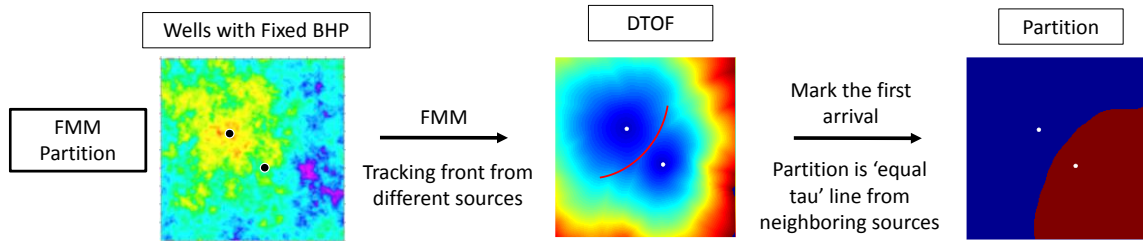
$$\begin{aligned} \frac{\partial}{\partial t} \left[\phi \left(\frac{S_g}{B_g} + R_s \frac{S_o}{B_o} \right) \right] &= \frac{\phi_{ref}}{w(\tau)} \frac{\partial}{\partial \tau} \left[w(\tau) \left(\frac{c_t}{\lambda_t} \right)_{ref} \left(\frac{k_{rg}}{B_g \mu_g} + R_s \frac{k_{ro}}{B_o \mu_o} \right) \frac{\partial p}{\partial \tau} \right] \\ &+ \left(\frac{\tilde{q}_g}{B_g} + R_s \frac{\tilde{q}_o}{B_o} \right) \delta(\tau_{wb}) \text{ (Gas)}. \end{aligned} \quad (4.3)$$

4.3.2 Drainage Volume Partition

To date, the application of the FMM-based approach to nonlinear problems such as multi-phase flow has been limited to the single-well simulation where no well interference effects need to be incorporated. However, for simulations where all the wells are controlled by the same bottomhole pressure, we can directly apply the FMM-based approach without any major corrections. Huang (2017) showed that ‘equal- τ ’ interfaces, at which the pressure front marching from one well encounters the others, physically approximates the no flow boundary between the producers. This is because the τ -contours represent the pressure contours and ‘equal- τ ’ represents the same pressure. **Figure 4.1a** illustrates the flow partition defined by the flux obtained from finite difference simulation (Huang et al., 2017; Shahvali et al., 2012). This agrees with the flow partition defined by the ‘equal- τ ’ depicted in **Figure 4.1b**, indicating that ‘equal- τ ’ interfaces can be an approximation of no flow boundaries.



(a) Well drainage partition (right) defined by flux obtained by finite difference simulation (middle) using heterogeneous permeability (left).



(b) Well drainage partition (right) defined by ‘equal- τ ’ interface based on the DTOF solution (middle) using heterogeneous permeability (left).

Figure 4.1 Comparison of well drainage partition. Circles in the permeability field on the left represent the producers (Huang, 2017)

4.3.3 Simulation Workflow

Once we can define the flow partitions for each well, the extension of the FMM-based technique to multi-well case is fairly straightforward. Our proposed approach is simply to partition the reservoir into independent sub-domains associated with individual wells based on the equal DTOF and perform series of independent 1-D simulation within each domain. **Figure 4.2** illustrates the workflow of the FMM-based multiple-well simulation for fixed BHP constraints, which consists of the following five (5) steps:

1. Solve the Eikonal equation using the FMM assigning $\tau = 0$ at completions of each well and obtain the DTOF map. Keep track on marching fronts from different sources to label which source gets a first arrival at each grid block.
2. Partition the reservoir domain based on the 'equal- τ ' interfaces where the marching front from a well encounters the others.
3. Calculate the drainage pore volume V_p and $w(\tau)$ associated with each individual well as a function of the DTOF from the well.
4. Discretize pore volume V_p and build 1-D simulation grid blocks for each well
5. Run individual 1-D simulations for each well.

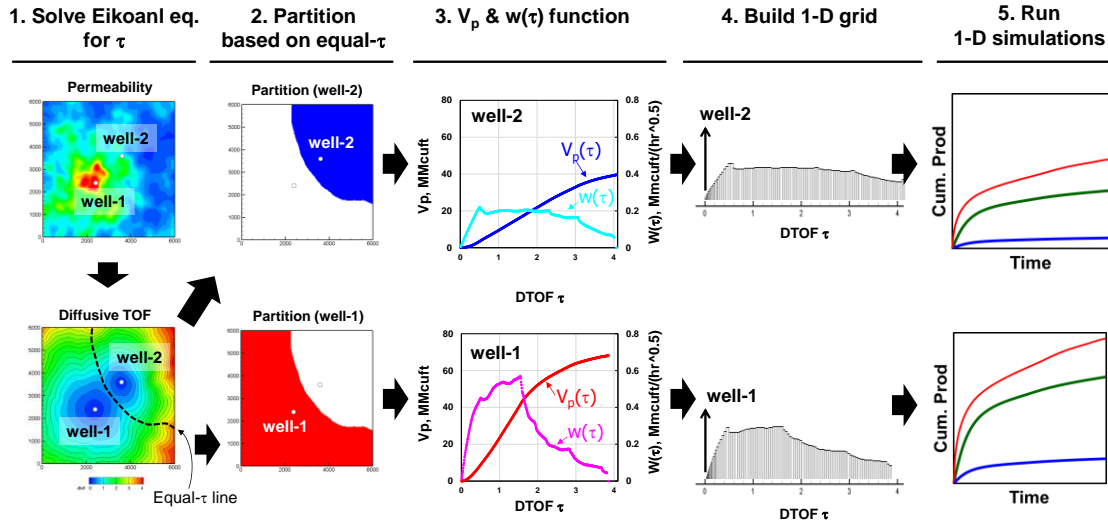


Figure 4.2 An illustration of drainage volume partition and 1-D simulation. Circles in the permeability field on the left represent the producers (reprinted with permission from Iino et al., 2018)

Once we generate the partition at step-2, the remaining steps 3–5 can be carried out in parallel for each individual well. Note that Figure 4.2 illustrates the case where two wells start producing at the same time. If the second well production starts later such as infill wells, we run the FMM-based simulation for the first well only until the time step when the second well starts producing. Subsequently, we map the 1-D solution back onto the original grid blocks and carry out the FMM-based simulation for two wells following the workflow.

4.4 Validation

In this section, we validate our simulation methodology for multi-well simulation based on the FMM by comparisons with a commercial finite difference simulator (FDSim). A 3-D synthetic reservoir model was used to simulate the infill well performances following the depletion by the parent well.

4.4.1 Case Setting

For a validation case, we built the synthetic 3-D reservoir model with reservoir, fluid and rock properties listed in **Table 4.1**. The reservoir domain of 2,600'×2,800'×150' was gridded into 520×560×15 and the total number of grid blocks amounted to 4.4 million. **Figure 4.3a** shows the matrix permeability upscaled from the Discrete Fracture Network. The 'parent well', which is placed at 750' away from the reservoir boundary on the left (**Figure 4.3b**), has four stages of hydraulic fractures generated by a commercial software where each stage has five fractures with a spacing of 100 ft (Yang et al., 2017b). The same

PVT data as Figure 2.15 was used. The three-phase relative permeability is depicted in **Figure 4.4**.

Table 4.1 Reservoir, fluid and rock property for infill validation case (reprinted with permission from Iino et al., 2018)

Item	Value
Model size (ft ³)	2600'×2800'×150'
Grid block dimension	520×560×15 (4,368,000)
Matrix permeability (mD)	Figure 4.3
Hydraulic fracture permeability (mD)	Figure 4.3
Matrix porosity	0.05
Hydraulic fracture porosity	5×10^{-4}
Initial water saturation	0.20
Rock compressibility (psi ⁻¹)	1.0×10^{-6}
Water viscosity (cp)	1.0
Water compressibility (psi ⁻¹)	1.0×10^{-6}
Water formation volume factor (rbbl/stb)	1.0
Initial solution gas-oil ratio (Mscf/stb)	1.12
Bubble point pressure (psi)	2,500
Initial pressure (psi)	6425

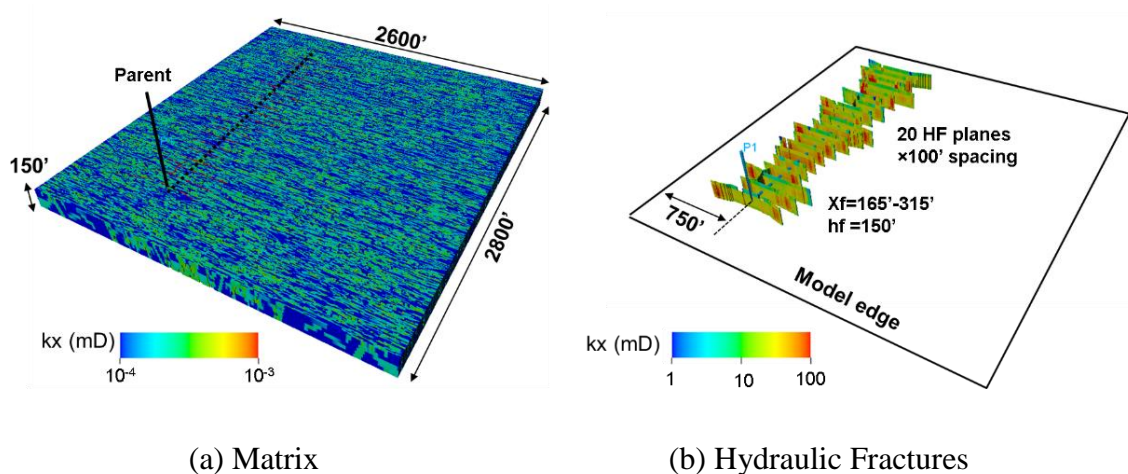


Figure 4.3 Permeability of matrix and hydraulic fractures for infill validation case (reprinted with permission from Iino et al., 2018)

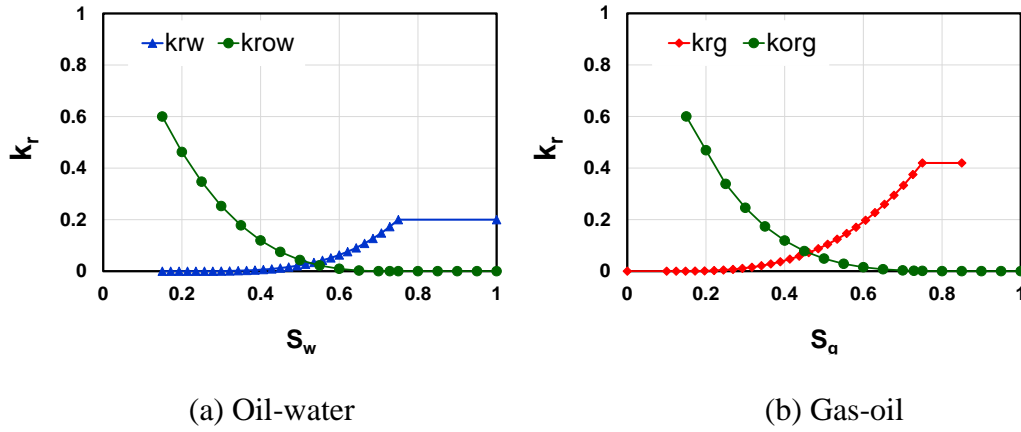
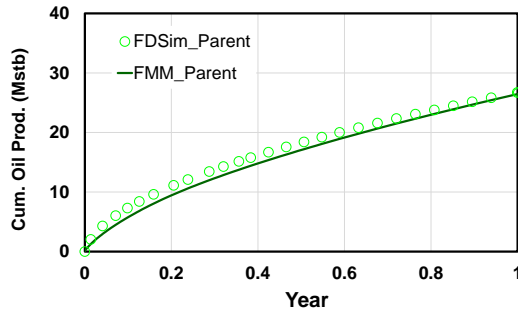


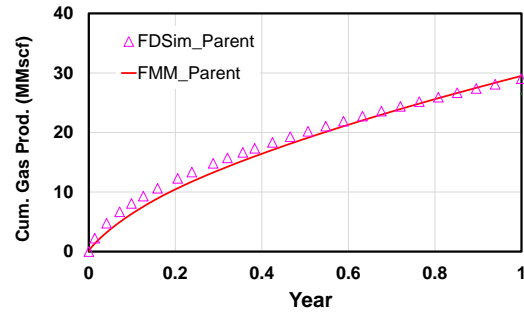
Figure 4.4 Relative permeability for infill validation case (reprinted with permission from Iino et al., 2018)

4.4.2 Depletion by Parent Well Production

We first simulated the pressure depletion for one year by the production of the parent well with constant bottomhole pressure of 2,000 psi. Cumulative production of oil and gas from the FMM-based approach and the FDSim illustrated in **Figure 4.5** show a good agreement. At the end of simulation, the pressure, saturation and solution gas-oil ratio solved on the 1-D DTOF coordinate were mapped back onto the original grid. **Figure 4.6** shows the pressure profile of the middle layer, which also confirms a good consistency between the FMM-based simulation and the FDSim, although the pressure profiles from the FMM-based simulation appear to be more diffused. This is because the 1-D DTOF grid block has less resolution compared to the original 3-D grid block.

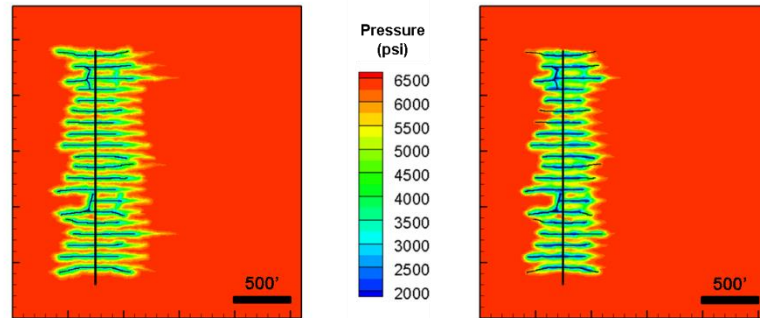


(a) Cumulative oil production



(b) Cumulative gas production

Figure 4.5 Cumulative oil and gas production of parent well– comparison between FMM-based simulation (line) and FDSim (symbol) (reprinted with permission from Iino et al., 2018)



(a) FMM-based simulation

(b) FDSim

Figure 4.6 Pressure profile after 1 year production by parent well– comparison between FMM-based simulation and FDSim (reprinted with permission from Iino et al., 2018)

4.4.3 Performances after Infill Well Placement

Following the one-year depletion by the parent well, we placed an infill (child) well and simulated performances of both wells to validate if the FMM-based approach gives an agreement with the 3-D finite difference simulation. **Table 4.2** summarizes the

simulation setting: we tested five (5) different well spacing to see the trade-off between the incremental oil production and well spacing. In this example, the hydraulic fracture geometry and property of the child well were assumed to be identical to those of the parent well. Thus, effects of pressure depletion on the fracture geometry of the child well were not accounted for in this section because we focus on the validation of simulation methodology. We will discuss the spacing optimization of infill wells accounting for effects of pressure depletion on the child well's fractures in the next section.

Table 4.2 Simulation setting for additional depletion by parent and child wells (reprinted with permission from Iino et al., 2018)

Item	Value
Infill well spacing (ft)	200, 300, 400, 500, 800
Timing child well placed	After 1yr depletion by parent well
Prediction period (yr)	1
Well constraints	2000 psi (const. BHP) for both parent and child wells
# of 1-D DTOF grid blocks	1,000

Figure 4.7 illustrates the child well location and drainage volume partition based on the 'equal- τ ' interfaces for different spacing. The 200'-spacing shows severe overlaps (frac hits) of hydraulic fractures between parent and child wells, whereas there is no overlap in the 800'-spacing. **Figure 4.8a** shows the comparison of cumulative oil production from the FMM-based simulation and the FDSim, which confirms a good agreement. The cumulative production increases as we take the larger spacing. However,

increase in the cumulative oil production starts converging around spacing of 500'— the plot of incremental oil recovery after the infill well was placed versus well spacing (**Figure 4.8b**) clearly tells that there is an inflection point around 500', indicating the trade-off between minimizing the spacing and maximizing the recovery. The pressure maps (**Figure 4.9**) at the simulation end show that two wells severely interfere for 200'-spacing case and non-depleted zone exists between two wells for 800'-spacing, while 500'-spacing case seems to efficiently drain without significant interference.

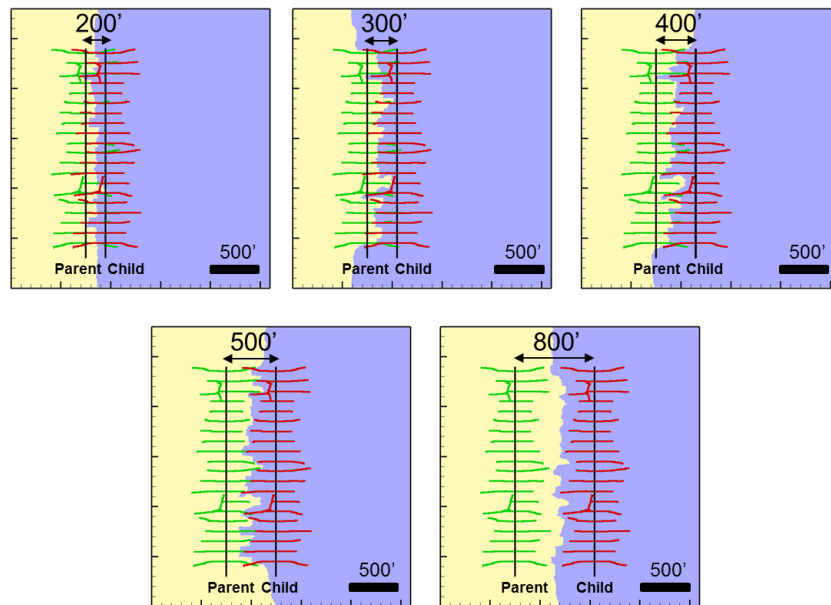
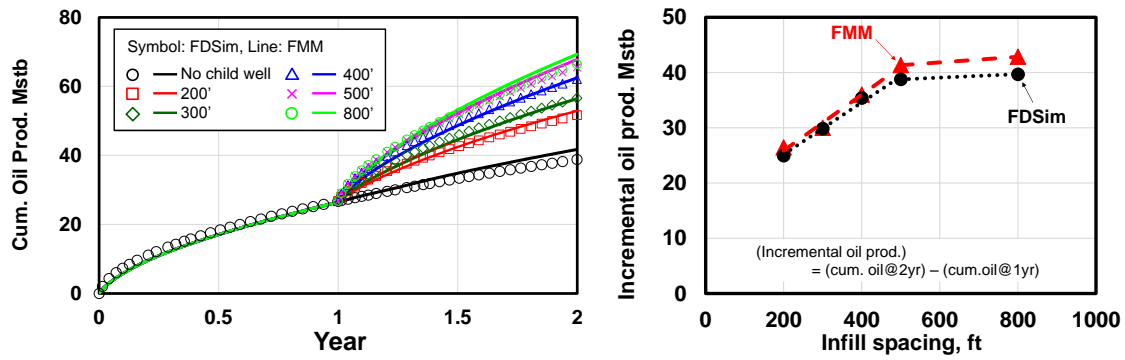


Figure 4.7 Child well locations and drainage volume partition on the middle layer based on the 'equal-tau' for difference well spacing (reprinted with permission from Iino et al., 2018)



(a) Cumulative oil production

(b) Incremental oil after placing child well

Figure 4.8 Comparison of cumulative oil production between FMM-based simulation and finite difference simulation (reprinted with permission from Iino et al., 2018)

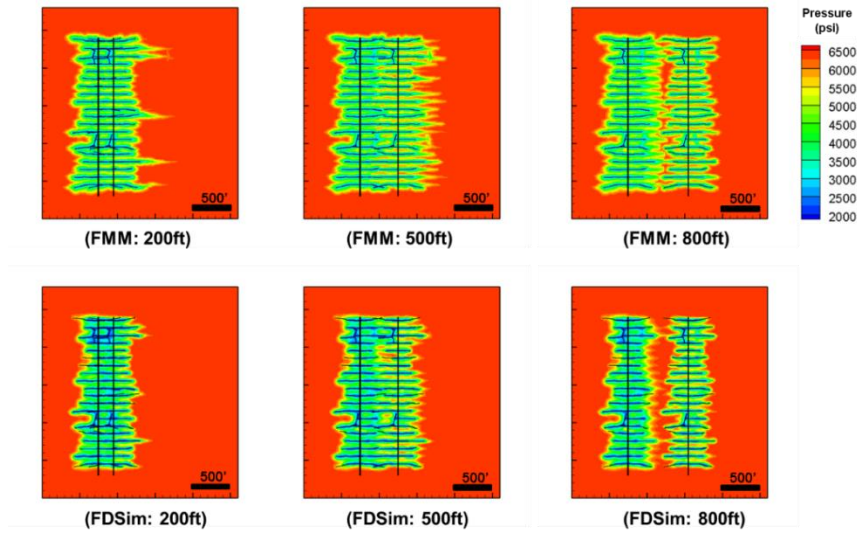


Figure 4.9 Pressure profile after 1 year since the infill well was placed: FMM-based simulation (upper row) and FDSim (lower row) (reprinted with permission from Iino et al., 2018)

4.4.4 CPU Time

In addition to the good accuracy discussed above, the most important feature and advantage of the FMM-based simulation is its computational efficiency. **Table 4.3** highlights the CPU time for a 2-year simulation of the 500' spacing case. The finite difference simulation required 19 hours whereas the FMM-based simulation spent only 0.5 hours. Thus, the orders of magnitude faster computation can be achieved by use of the FMM, which offers robust and quick assessment of infill well planning.

Table 4.3 Comparison of grid block number and CPU time between FDSim and FMM-based simulation

Item	FDSim	FMM	Scale-up/ Speed-up factor
# of grid blocks	4,368,000	2,000	2,184
CPU time (hrs)	18.9	0.5	37

4.5 Field-scale Application

In this section, we present a field-scale application of the FMM-based approach to a realistic example with complicated fracture geometry due to the existence of natural fractures and changes in pressure/ stress field by the parent well depletion. The fracture propagation was simulated by a commercial software. Our focus in this example is to show the applicability of the FMM-based approach to the optimization workflow of infill spacing by demonstrating the consistency of the simulated well and reservoir performances with a commercial finite difference simulator.

4.5.1 Generating Fracture Geometry

We carried out the field scale infill development study based on a case representative of the Eagle Ford reservoir properties and completion/stimulation practices using the integrated workflow (Marongiu-Procu et al., 2016) illustrated in **Figure 4.10**. The hydraulic fractures along a 4,800 ft lateral of the parent well was generated in a sector model of $6,200 \times 4,200 \times 350$ ft³ using the treatment schedule presented in Marongiu-Porce et al. (2016) where each of 16 treatment stages contains 5 perforation clusters (6 shots per foot) with 50 ft spacing. The 20/40 proppant with cross-linked gel was used for the hydraulic fracturing treatment and the pumping schedule begins with slick water, followed by the gel and proppant with gradually increasing concentration (**Table 4.4**). We generated the discrete fracture network (DFN) of natural fractures based on the statistical properties listed in **Table 4.5**. Note that spatial variability of natural fractures such as intensity and orientations are typically characterized based on 3-D seismic attributes and image logs (Offenberger et al., 2013); however, these were not considered in this study.

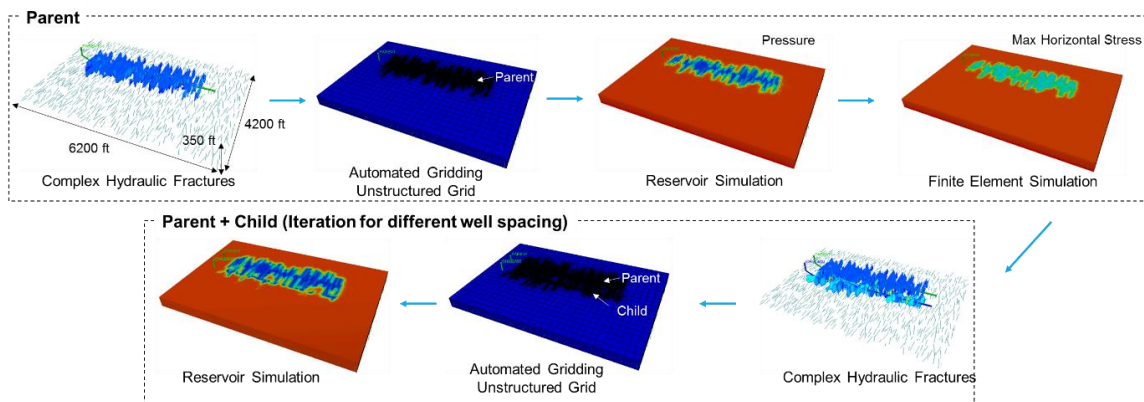


Figure 4.10 Complex fracture modeling workflow for infill development (reprinted with permission from Iino et al., 2018)

Table 4.4 Pumping schedule for fracturing simulation (reprinted with permission from Iino et al., 2018)

Fluid Type	Pump Rate (bpm)	Fluid Vol. (gal)	Proppant	Proppant Conc. (PPA)	Prop. Mass (lb)
Slick water	10	11000	-	-	-
Slick water	50	25000	-	-	-
30# X-linked gel	50	40000	-	-	-
30# X-linked gel	50	12600	20/40 sand	0.50	6300
30# X-linked gel	50	12600	20/40 sand	0.75	9450
30# X-linked gel	50	12600	20/40 sand	1.00	12600
30# X-linked gel	50	12600	20/40 sand	1.50	18900
30# X-linked gel	50	12600	20/40 sand	2.00	25200
30# X-linked gel	50	12600	20/40 sand	2.50	31500
30# X-linked gel	50	12600	20/40 sand	3.00	37800
30# X-linked gel	50	12600	20/40 sand	3.50	44100
30# X-linked gel	50	12600	20/40 sand	4.00	50400
30# X-linked gel	50	12600	20/40 sand	4.50	56700
Flush	50	String Volume	-	-	-

Table 4.5 Statistical parameters used to generate discrete natural fractures (reprinted with permission from Iino et al., 2018)

Item	Average	Standard Deviation
Length (ft)	250.0	7.0
Orientation (deg)	0.0	10.0
Spacing (ft)	90.0	20.0

Hydraulic fracture propagation was then simulated using a commercial software Mangrove[®]. Based on the DFN including natural and hydraulic fractures, an unstructured grid was generated by the automated gridding algorithm (Cipolla et al., 2011) whereby cell widths of fracture and matrix were assigned to be 5 ft and 200 ft, respectively, after Marongiu-Porce et al. (2015). The parent well depletion was then simulated for one year using a commercial reservoir simulator with reservoir properties and well constraints shown in **Table 4.6**. The same PVT and relative permeability data in the previous section was used here. Subsequently, the simulated pressure distribution and the DFN were fed to a finite element geomechanical simulator VISAGE[®] in order to update the in-situ stress field (top right in Figure 4.10). Bottom part of Figure 4.10 illustrates the subsequent procedures for a child well. Here, we repeated the same procedure as the parent well for the child well but considered the existing fractures of the parent well and the updated pressure and stress field. We examined four scenarios of different child well spacing: 300, 600, 900, and 1,200 ft, which are in a range of common practice in the Eagle Ford infill developments. The same set of input from the parent well are used to simulate fracture propagation of the child well. We converted the unstructured grid from the commercial simulator into an equivalent structured grid system for the FMM-based simulation of the parent and child wells. Note that, although the number of grid blocks of the structured grid system after the conversion from the unstructured grid became large (~3.3 millions) to accurately describe hydraulic fractures and it can result in substantial rise in CPU time, it is not a significant concern with the FMM-based simulation framework because of its computational efficiency. The permeability of hydraulic fractures for reservoir simulation

are illustrated in **Figure 4.11**, showing severe frac hits in 300 ft spacing case, whereas little hits in 1,200 ft spacing case.

Table 4.6 Reservoir, fluid and rock properties for field-scale application of infill spacing optimization (reprinted with permission from Iino et al., 2018)

Item	Value
Model size (ft ³)	6300'×4200'×350'
Grid block dimension	840×560×7 (3,292,800)
Matrix permeability (mD)	5×10 ⁻⁴
Matrix porosity	0.06
Hydraulic fracture porosity	6×10 ⁻⁴
Initial water saturation	0.15
Rock compressibility (psi ⁻¹)	1.0×10 ⁻⁶
Water viscosity (cp)	0.404
Water compressibility (psi ⁻¹)	3.0×10 ⁻⁶
Water formation volume factor (rbbl/stb)	1.02
Initial solution gas-oil ratio (Mscf/stb)	0.55
Bubble point pressure (psi)	2,302
Initial pressure (psi)	6,425
Production period	1 year with parent well, followed by another 1 year by parent and child wells
Well control	Const. BHP of 2,000 psi
# of 1-D DTOF grid blocks	2,000

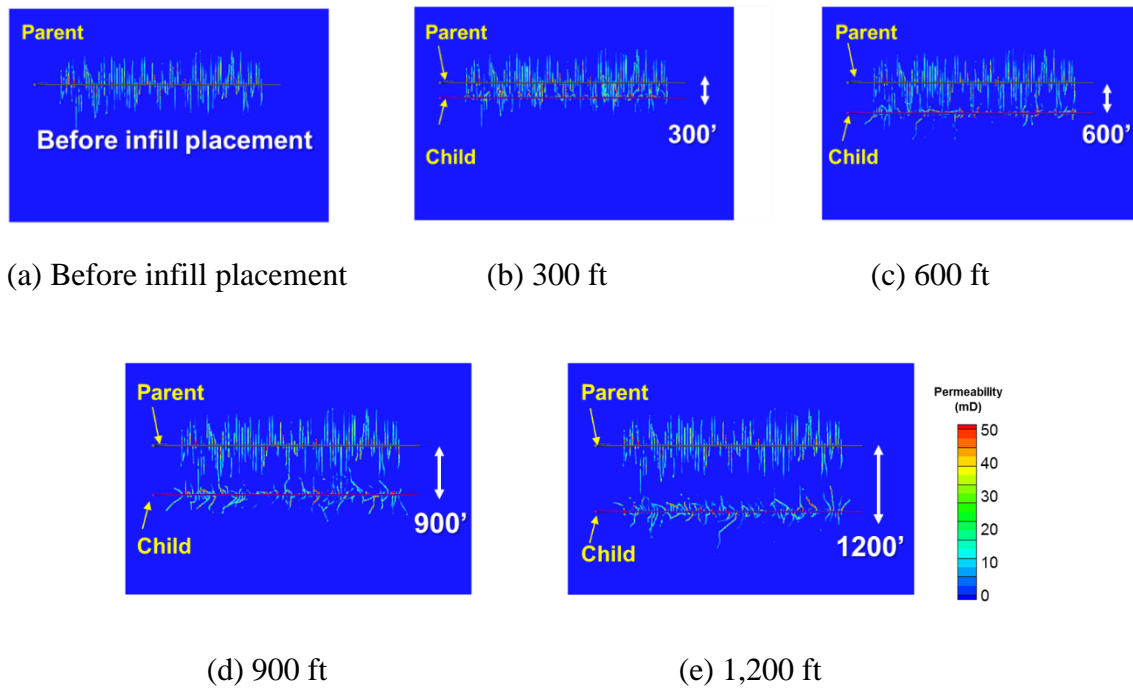
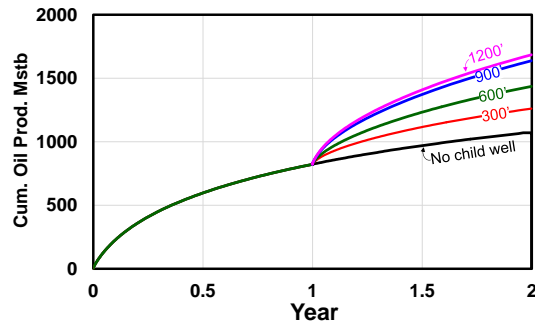


Figure 4.11 Permeability of field-scale example for reservoir simulation with different infill well spacing (top view of middle layer) (reprinted with permission from Iino et al., 2018)

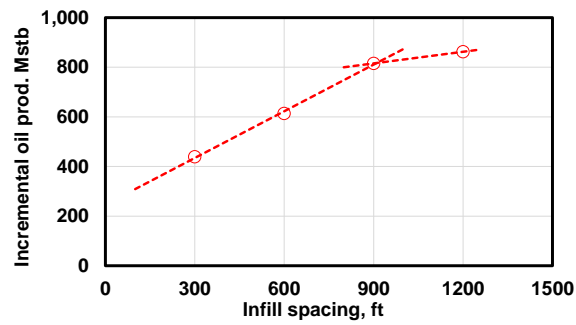
4.5.2 Optimal Well Spacing

We simulated well performances of parent and child wells for each spacing using the FMM-based approach. **Figure 4.12a** shows the cumulative oil production from both parent and child wells. The profile of cumulative production converges, which indicates less interference effects with larger spacing. The incremental oil after the child well placement (**Figure 4.12b**) clearly shows that the spacing larger than 900ft does not give significant additional gain. This is consistent with the pressure maps at the simulation end in **Figure 4.13** where the parent and child wells significantly interferes with each other up

to 600' spacing, while the 900' spacing shows very limited child well interfere with the parent well.



(a) Cumulative oil production from parent and child wells



(b) Incremental oil production after child well placement

Figure 4.12 Cumulative oil production and incremental recovery for field-scale example (reprinted with permission from Iino et al., 2018)

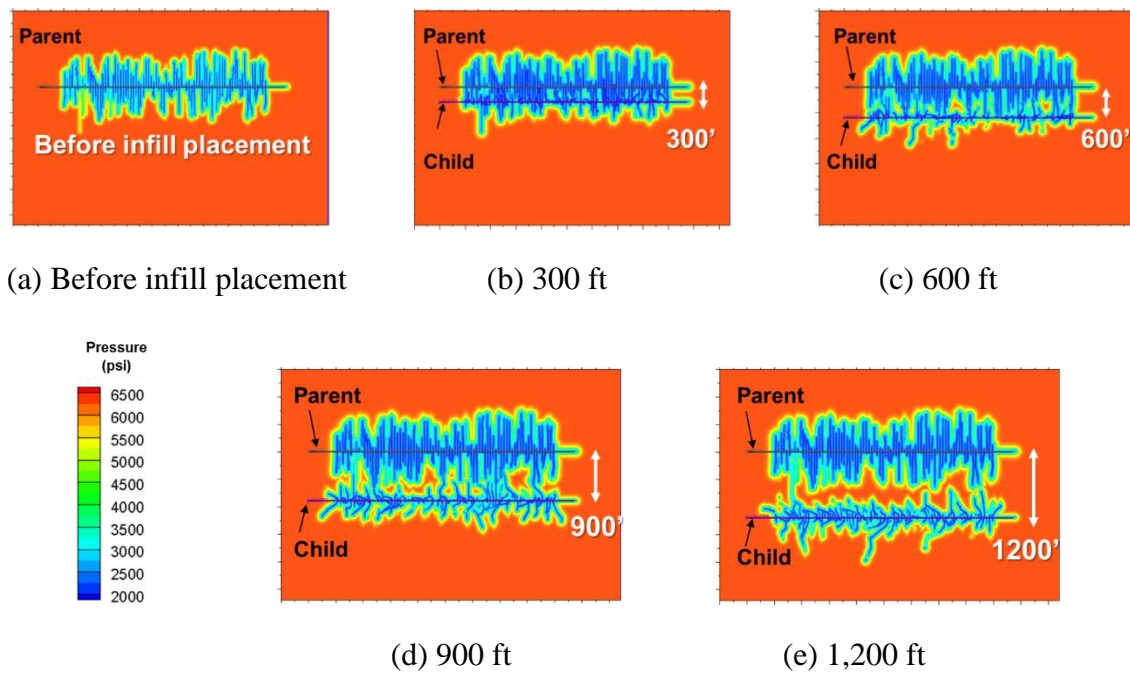


Figure 4.13 Pressure maps of the middle layer: (a) just before the child well placement at 1 year and (b)-(e) at the end of simulation at 2 years (reprinted with permission from Iino et al., 2018)

Finally, we compared the CPU time for the 300' spacing case between the FMM-based approach and the FDSim (Table 4.7). The FMM-based approach required 0.6 hours for reservoir simulation of two years, whereas the FDSim required 14 hours for the same. The FMM-based approach can quickly provide quantitative assessment of infill well spacing that would help efficient design and optimization of development planning of unconventional reservoirs.

Table 4.7 Comparison of grid block number and CPU time between FDSim and FMM for field-scale application

Item	FDSim	FMM	Scale-up/ Speed-up factor
# of grid blocks	3,292,800	2,000	1,646
CPU time (hrs)	14.0	0.6	23

4.6 Conclusions

The Fast Marching Method (FMM) based rapid flow simulation technique has shown great promise in modeling and performance assessment of unconventional reservoirs (Zhang et al., 2016; Fujita et al., 2016; Iino et al., 2017a and 2017b). However, to-date the application of the FMM simulation has been mostly limited to single well studies. In this chapter, we have extended the Fast Marching Method (FMM) to multiple-well problem in unconventional reservoirs with an application to optimization of well spacing. Conclusions from this study are summarized below:

- When multiple wells are constrained at the same bottomhole pressure, the extension of the FMM-based technique to multi-well case is fairly straightforward. This is because under such conditions, 'equal- τ ' contours from different wells represent the same pressure. Hence, the 'equal- τ ' interface, at which the marching front of pressure propagation from a well encounters that of the others', approximates a no flow boundary. Our proposed approach is simply to partition the reservoir into independent sub-domains associated with individual wells based

on the equal DTOF and perform independent 1-D simulation within each domain.

This requires one FMM-based 1-D simulation per well.

- We validated our proposed FMM-based multi-well simulation approach by comparing the results with a commercial finite difference simulator using a synthetic reservoir model with infill-well scenario. We confirmed that the FMM-based simulation shows good agreement with finite difference simulation with orders of magnitude faster computation. Although the incremental recovery from the FMM results shows close agreement, the pressure distribution from the FMM solution shows smeared features compared to the finite difference simulation results. This is because the 1-D DTOF grid block has less resolution as compared to the original 3-D grid blocks.
- For field-scale application, we presented a comprehensive workflow for assessing and optimizing the infill well spacing that incorporates the fracture propagation simulation accounting for the parent well depletion. We demonstrated that the use of FMM-based approach can quickly provide quantitative assessment of potential frac hits and help efficient design and optimization of infill well planning in unconventional reservoirs

CHAPTER V

EXTENTION OF FMM-BASED MULTI-WELL SIMULATION TO CONSTANT RATE PRODUCTION SCENARIO

5.1 Chapter Summary

In development planning or actual field operations, we often have situations where production wells are controlled by the constant rates because of the limitation of sand-face drawdown, surface facility limits and variable sales demand, etc. In such situations, the degree of pressure depletion may have a contrast among drainage areas according to the production rate of each well, leading to the dynamic migration of the drainage volume partition over time. In this chapter, we newly proposed two different methods of the FMM-based multi-well simulation that can account for the dynamic changes in the drainage volume partition.

The first method utilizes the flux fields, which can be efficiently calculated by the asymptotic approximation, to define the drainage volume partition. The unique feature is that it also involves the dynamic updates of the flux-based partition during the FMM-based simulation in order to capture the effects of the drainage volume changes. The second method, which still uses the fixed partition based on the ‘equal- τ ’ interface, introduces a novel inter-partition transmissibility that allows the flux-in and flux-out across the partitions.

We demonstrate the efficacy and utility of our proposed approaches using synthetic reservoir models. We first validated our methodologies using a 2-D

homogeneous model by confirming good agreement in the simulated bottomhole pressures with the commercial finite difference simulator. Next, we applied our methodologies to a 3-D million-cell model with four hydraulically fractured wells. We confirmed that the FMM-based simulation can show faster computation than the commercial finite difference simulator, however, the extra calculation for the inter-partition transmissibility requires expensive computational costs. In addition, we also found that the velocity calculation using the asymptotic approximation needs to be further improved in order to obtain a robust drainage volume partition.

This study demonstrated the feasibility of the rapid FMM-based multi-well simulation for the scenario of constant rate productions. As future work, we need to mitigate the remaining challenges identified in this study for further improvement of the proposed methods.

5.2 Background

In Chapter IV, we proposed the FMM-based multi-well simulation for the fixed BHP scenario using the equal- τ interface as a drainage volume partition. However, Huang (2017) showed that equal- τ no longer represents the drainage volume partition in the situation where wells are controlled by different constant rates. This is because difference in the withdrawal rates creates different degree of depletion in each partition, resulting in the dynamic shift in the drainage volume partition over time.

Let us first illustrate the dynamic change in the drainage volume partition using the 2-D homogeneous example. The reservoir domain of $10,100 \times 10,100 \times 50$ ft³ was

uniformly gridded by $101 \times 101 \times 1$ grid blocks. Porosity, permeability and rock compressibility are 30%, 1 mD and $1 \times 10^{-5} \text{ psi}^{-1}$, respectively. Single-phase oil is assumed with viscosity of 0.49 cp, initial formation volume factor of 1.93 rbbl/stb and compressibility of $5 \times 10^{-5} \text{ psi}^{-1}$. Three (3) producers are placed at grid blocks (21, 21), (41, 81) and (81, 21) and operated with the constant rate of 25, 50 and 100 stb/d, respectively. **Figure 5.1** shows pressure maps from the FDSim and corresponding streamlines at four different time steps of 100, 500, 2000 and 5000 day. The streamlines are generated based on the flux from the FDSim using the Pollock's method (Pollock, 1988). In the early time (100 day), the flow partition does not reach the equal- τ interface, indicating the independent transient flow for each well. Flow regimes at 500 days show transitions to the pseudo-steady state, and the flow partition starts deviating from the equal- τ partition. Once it becomes the pseudo-steady flow (2000 and 5000 days), the flow partition keeps changing over time. The drainage area of the well P1 with the smallest rate is shrinking whereas that of the well P3 with the largest rate is expanding. Finally, the drainage volume will be allocated proportional to the production rate of each well (Matthews and Russel, 1967).

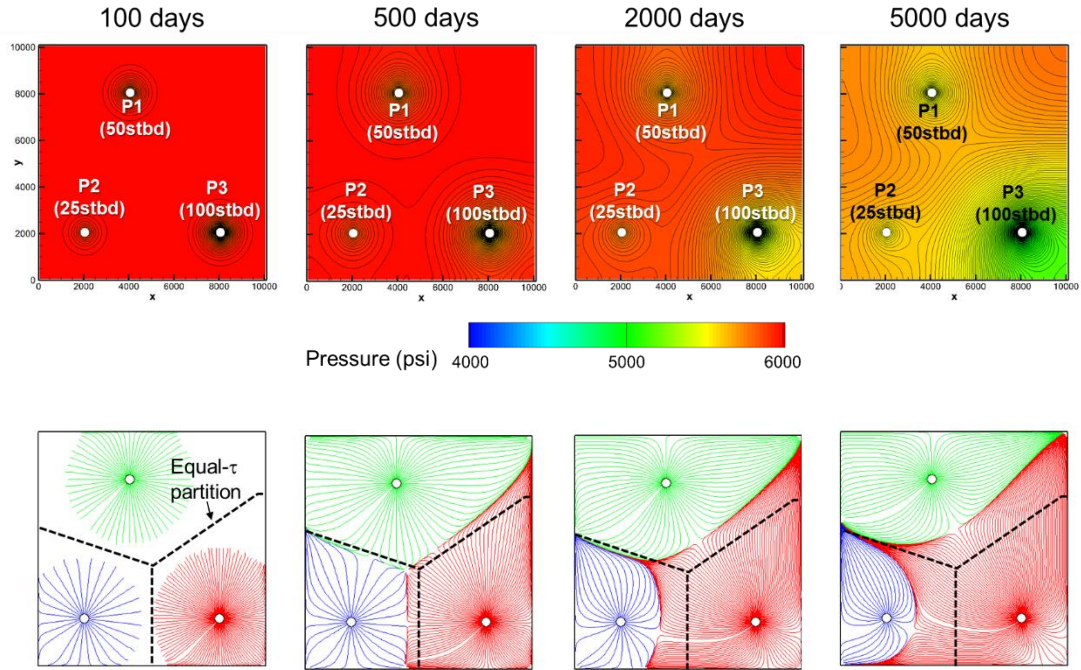
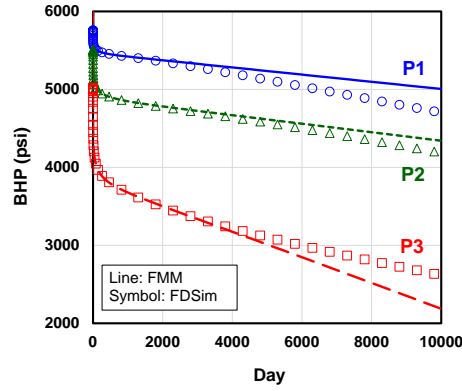
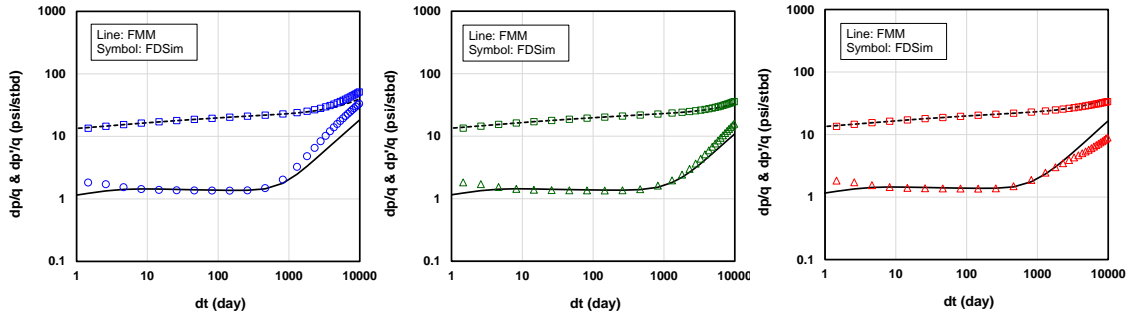


Figure 5.1 Dynamic change in pressure (top) and drainage volume partition based on streamlines (bottom) by depletion from three wells controlled by constant rates of 25, 50 and 100 stb/day

In such situations, the FMM-based simulation with equal- τ partition does not provide consistent bottomhole pressure with the FDSim as shown in **Figure 5.2a**. The log-log diagnostic plots (**Figure 5.2b**) clearly shows that the FMM-based simulation does not replicate the pressure performances after the infinite acting period is over. Thus, key challenge for the FMM-based multi-well simulation is to appropriately model the dynamic changes in the drainage volume partition.



(a) Linear plot



(b) Log-log diagnostic plot (left: P1, middle: P2 and right: P3)

Figure 5.2 Comparisons of simulated bottomhole pressures between FDSim (symbol) and FMM-based simulation (line) for three wells producing at different constant rates

5.3 Methodology and Validation

In this section, we tested and compared the following four approaches for multi-well simulations using the FMM:

1. Equal- τ partition (presented in Chapter IV)
2. Flux-based partition (Huang 2017; Huang et al., 2017)
3. Flux-based partition with dynamic update (newly proposed approach)

4. Inter-partition transmissibility (newly proposed approach)

5.3.1 FMM-based Flux Partition

Huang et al. (2017) proposed the method to define the drainage volume partition based on the flux field, which can be efficiently calculated using the FMM-based asymptotic approximation of pressure gradient along the DTOF coordinate (King et al., 2016). Their approach consists of three decoupled steps: (1) generating flux fields associated with each well and superimposing them to get a flux map, (2) solving the steady-state tracer equation to define the interfaces between drainage volume partitions and (3) running the FMM-based 1-D simulations for each well. Although the drainage volume partition keeps changing over time, they assumed that we can approximate such dynamic partition by selecting one representative snapshot of the drainage volume partition. Thus, this method requires the appropriate selection of the time step to generate the flux field at step (1), as discussed later. In addition, we need to assume single-phase flow in order to adopt the asymptotic approximation for pressure gradient calculation along the DTOF coordinate.

5.3.1.1 Methodology

For slightly compressible fluid flow, King et al. (2016) derived the following approximation for the Darcy flux across the τ -contours:

$$q(\tau, t) \approx c_t w(\tau) \frac{\partial p}{\partial \tau}, \quad (5.1)$$

where the flux q is a function of location τ and time t . Rearranging Eq.(5.1) yields the pressure gradient along the DTOF:

$$\frac{\partial p}{\partial \tau} \approx \frac{q(\tau, t)}{c_t w(\tau)}. \quad (5.2)$$

The approximated flux is given by:

$$q(\tau, t) = \frac{q_{sf}}{V_0(t)} \int_{\tau'=\tau}^{\infty} dV_p(\tau') e^{-\tau'^2/4t}, \quad (5.3)$$

where subscript sf stands for a sand-face and $V_p(\tau)$ will be numerically computed from the FMM solution. $V_0(t)$ is defined as:

$$V_0(t) = \int_{\tau=0}^{\infty} dV_p(\tau) e^{-\tau^2/4t}. \quad (5.4)$$

Thus, the pressure gradient at location τ and time t can be semi-analytically computed by the following formulation:

$$\frac{\partial p(\tau, t)}{\partial \tau} \approx \frac{q_{sf}}{c_t w(\tau)} \frac{1}{V_0(t)} \int_{\tau'=\tau}^{\infty} dV_p(\tau') e^{-\tau'^2/4t}, \quad (5.5)$$

Velocity on the Cartesian grid system, $\mathbf{u}(\mathbf{x})$, can be translated from the pressure gradient along the DTOF:

$$\mathbf{u}(\mathbf{x}, t) \approx -\frac{\mathbf{k}}{\mu} \frac{\partial p(\tau, t)}{\partial \tau} \nabla \tau, \quad (5.6)$$

Note that we have discussed the pressure gradient associated with individual well thus far. Huang et al. (2017) generated the flux map in the reservoir model with multiple wells by the superposition of the velocity fields associated with individual wells as follows:

$$\mathbf{U}(\mathbf{x}, t) = \sum_{iw}^{N_w} [\mathbf{u}(\mathbf{x}, t)]_{iw}, \quad (5.7)$$

where N_w is the well counts and subscript iw is the index of wells. Finally, the drainage volume partition associated with each individual well is determined by solving the steady-state tracer equation for the concentration c (Shahvali et al., 2012):

$$\nabla \cdot [\mathbf{U}(\mathbf{x}, t) c_{iw}] = \hat{q} c_{iw} \delta(\mathbf{x} - \mathbf{x}_{iw}). \quad (5.8)$$

As boundary conditions, any concentration c_{iw} to label wells will be assigned with the flow rate per unit bulk volume at each well location \mathbf{x}_{iw} such that the solution c identifies the well to which each grid block belongs. The steady-state assumption reduces Eq. (5.8) as follows:

$$\mathbf{U}(\mathbf{x}, t) \cdot \nabla c = \hat{q} c_{iw} \delta(\mathbf{x} - \mathbf{x}_{iw}), \quad (5.9)$$

because the divergence of velocity vanishes. The gradient of tracer concentration is evaluated from the inflow directions:

$$\mathbf{U} \cdot \nabla c \approx \sum_j^{face} U_j \frac{(c_i - c_j)}{\Delta L_j} \text{ (if flow direction is } j \rightarrow i), \quad (5.10)$$

where i : grid block index, j : directions of adjacent cells and ΔL : grid block length.

Integrating Eq. (5.10) over the grid block volume yields the following expression:

$$\sum_j^{face} \int_{V_i} U_j \frac{c_i - c_j}{\Delta L_j} dV_i \approx \sum_j^{face} Q_j (c_i - c_j) = q c_{iw} \delta(\mathbf{x} - \mathbf{x}_{iw}). \quad (5.11)$$

Thus, the drainage volume partition can be determined only with the volumetric flux. Note that Eq. (5.11) defines the tracer concentration associated with the single well i_w . Therefore, we need to solve Eq. (5.11) as many times as the number of wells with different boundary conditions by the finite difference scheme. Subsequently, we compare the concentration maps associated with each well in order to assign the well label to each grid block based on the highest concentration.

5.3.1.2 Results and Discussion

For the same 2-D homogeneous example as the last section, we generated the drainage volume partition using the FMM-based flux partition (**Figure 5.3**). It is observed that the FMM-based flux partition shows reasonable agreement with those from the FDSim.

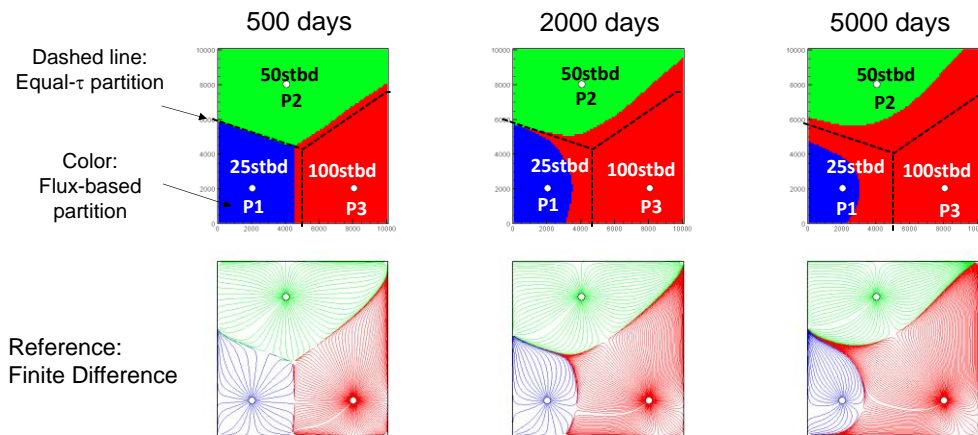
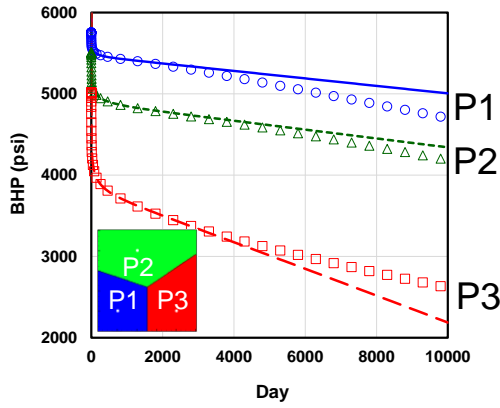
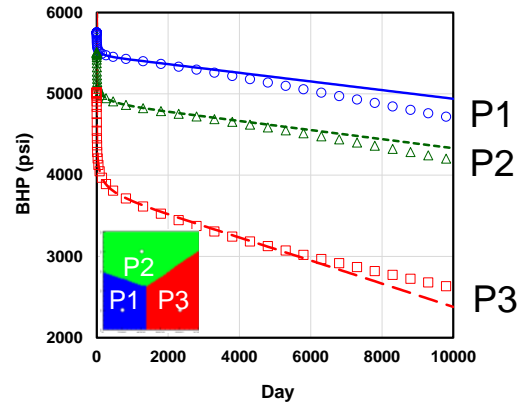


Figure 5.3 Drainage volume partition at each time step from FMM-based flux calculation (top) and FDSim (bottom). Production rate = 25, 50 and 100 stb/day.

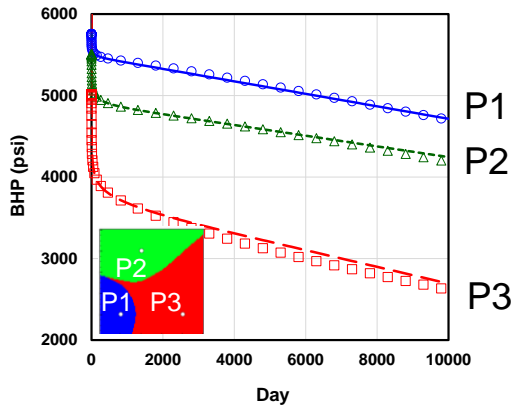
Subsequently, we run the FMM-based 1-D simulations using drainage volume partitions at different time steps. **Figure 5.4** illustrates the comparison of bottomhole pressure between the FDSim and the FMM-based simulation. For comparison purpose, the FMM-based simulation with equal- τ partition is also compared with the FDSim (Figure 5.4a), which indicates significant deviation in the late time where the pseudo-steady state has been reached. On the other hand, the FMM-based simulation with the flux-based partition gives better matching with the FDSim compared to the equal- τ . Obviously, the simulation results of the FMM-based approach depends on the selection of the time step to generate the drainage volume partition. If we select 500 days or 5000 days for the time step to generate the drainage volume partition, the bottomhole pressure from the FMM-based simulation shows significant deviation from the FDSim (Figure 5.4b and Figure 5.4d). It seems that selecting 2,000 days for the drainage volume partition provides the excellent agreement between both simulations, however, we need a guideline for the optimal time step selection. In this study, rather than pursuing the optimal time step selection for the fixed drainage volume partition, we propose a new methodology that dynamically updates the drainage volume partition during the FMM-based simulation in the next section.



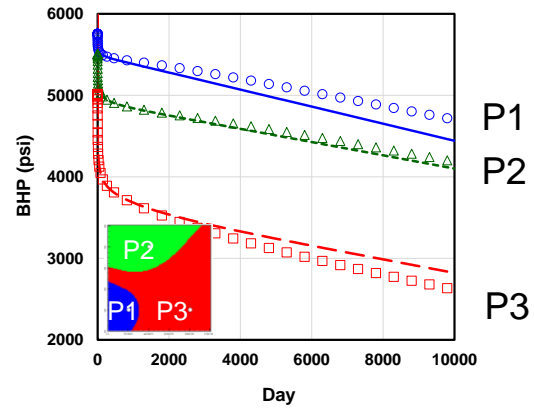
(a) FMM with equal- τ partition



(b) FMM with partition at 500 days



(c) FMM with partition at 2,000 days



(d) FMM with partition at 5,000 days

Figure 5.4 Comparison of simulated bottomhole pressure between FDSim (symbol) and FMM-based simulation (line) using flux-based drainage volume partition at different time steps

5.3.2 FMM-based Flux Partition with Dynamic Update

In the previous section, we pointed out that the selection of the time step to generate the drainage volume partition is critical. Although investigating the optimum time step selection is one option to tackle this issue, we will study another option that

involves the dynamic update of the drainage volume partition during the FMM-based simulation.

5.3.2.1 Methodology

This method can be easily implemented with minor corrections to the workflow of the previous method as illustrated in **Figure 5.5**:

1. Generate the DTOF from each well for the entire reservoir domain.
2. Generate the FMM-based flux partition for all the time steps to update the drainage volume partition.
3. Run the FMM-based simulation using the initial drainage volume partition until it reaches the time step to update the drainage volume partition.
4. Map-back the 1-D solutions onto the original grid blocks. Update the drainage volume partition.
5. Go back to step-3 until the simulation terminates.

At step-1, we need to define the time steps for updating the drainage volume partition. Here, we will study the sensitivity of the update frequency, and leave the optimal frequency selection as future work.

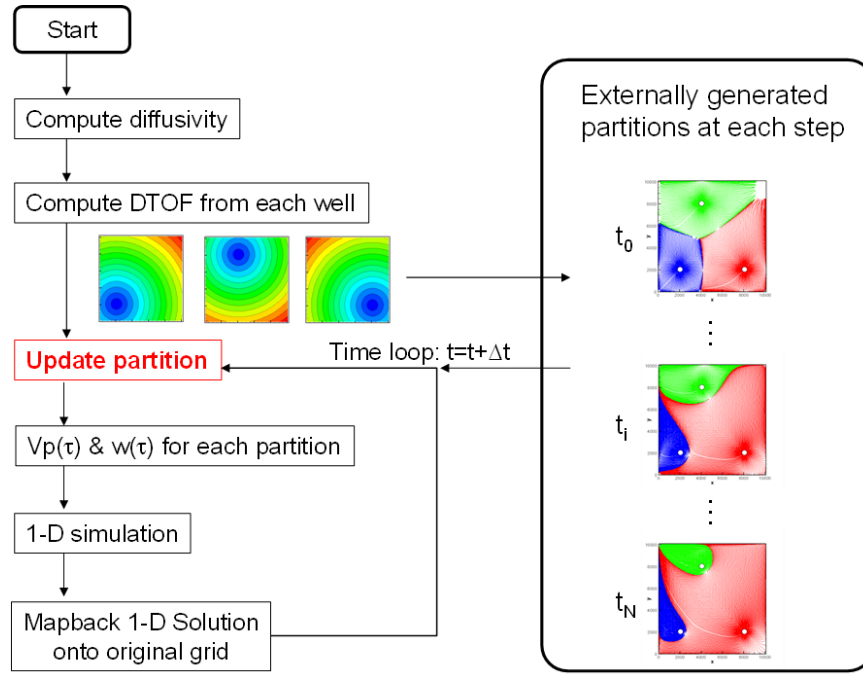


Figure 5.5 Flowchart of FMM-based multi-well simulation using flux-based drainage volume partition with dynamic update

5.3.2.2 Results and Discussion

Using the same 2-D homogenous model with three wells producing 25, 50 and 100 stb/day, respectively, we compared the bottomhole pressure between the FDSim and the FMM-based simulation with dynamically updating the drainage volume partition. **Figure 5.6** illustrates comparisons with (a) the fixed equal- τ partition, (b) the flux-based partition with three times updates, (c) 9 times updates and (d) 19 times updates. Obviously, the dynamic update of flux-based partition yields better matching with the FDSim compared to the equal- τ partition. In addition, there is no significant difference in the simulated well performances between the update frequencies, indicating that only a few update can be

sufficient. **Figure 5.7** shows percentages of the drainage volume partition associated with each well. After 6,000 days, drainage volumes are almost stabilized according to the ratio of the production rates of each well (Matthews and Russell, 1967). Thus, we may not need to update the drainage volume partition once the partition is stabilized. In addition, we need not update the drainage volume partition until the time when interference starts, which can be inferred based on the DTOF. The optimal selection of the update frequency and time steps will be left as future work.

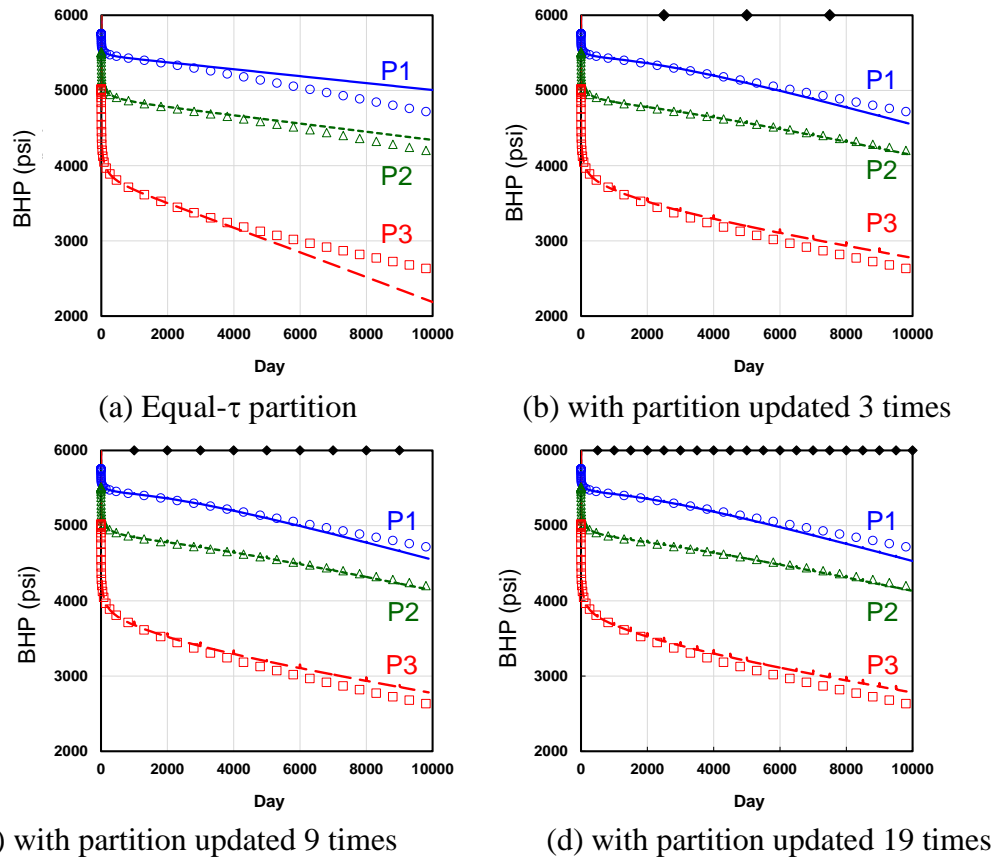


Figure 5.6 Comparison of bottomhole pressure between FDSim (symbol) and FMM-based simulation (line) with dynamic update of drainage volume. Drainage volume partition was updated with different frequency denoted by black diamonds

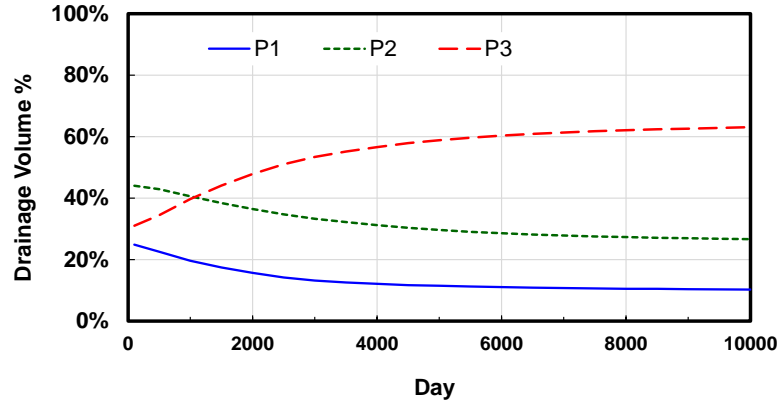


Figure 5.7 Percentage of drainage volume associated with each well from FMM-based flux partition

5.3.3 Inter-partition Transmissibility

As we have discussed thus far, the idea of the FMM-based multi-well simulation using the flux-based partition is to define the drainage volume partition prior to the flow simulation. Limitation is that such partitions are scenario dependent and we need to generate the partitions for different well schedules. In addition, the flux calculation needs to be based on single-phase assumption in terms of the velocity superposition and the asymptotic flux approximation.

Here, we propose a new methodology that introduces the inter-partition transmissibility to model the dynamic flow-in and flow-out across the partitions. The advantage of the inter-partition transmissibility is that there is no scenario dependency because it is determined purely based on the static properties. Furthermore, the method is not limited to the single-phase system, but is valid for multi-phase flow.

5.3.3.1 Methodology

Figure 5.8 illustrates the FMM-based simulation workflow that incorporates the inter-partition transmissibility, consisting of four (4) steps:

1. Generate the equal- τ partition
2. Calculate $V_p(\tau)$ and $w(\tau)$ for each well
3. Calculate the inter-partition transmissibility
4. Run the 1-D simulation using a series of the 1-D grid blocks where the inter-partition transmissibility is assigned to allow the flow-in and flow-out across the partitions

Hence, step-3 is an extra computation required for this method where the inter-partition transmissibility is calculated for each τ -contours of each well pair. Thus, the 1-D simulations are no longer run independently as we need to account for the dynamic communication between partitions. Rather, the flow simulation in this approach is close to the 2-D simulation where 1-D grid block systems for each well are connected via the non-neighbor connections.

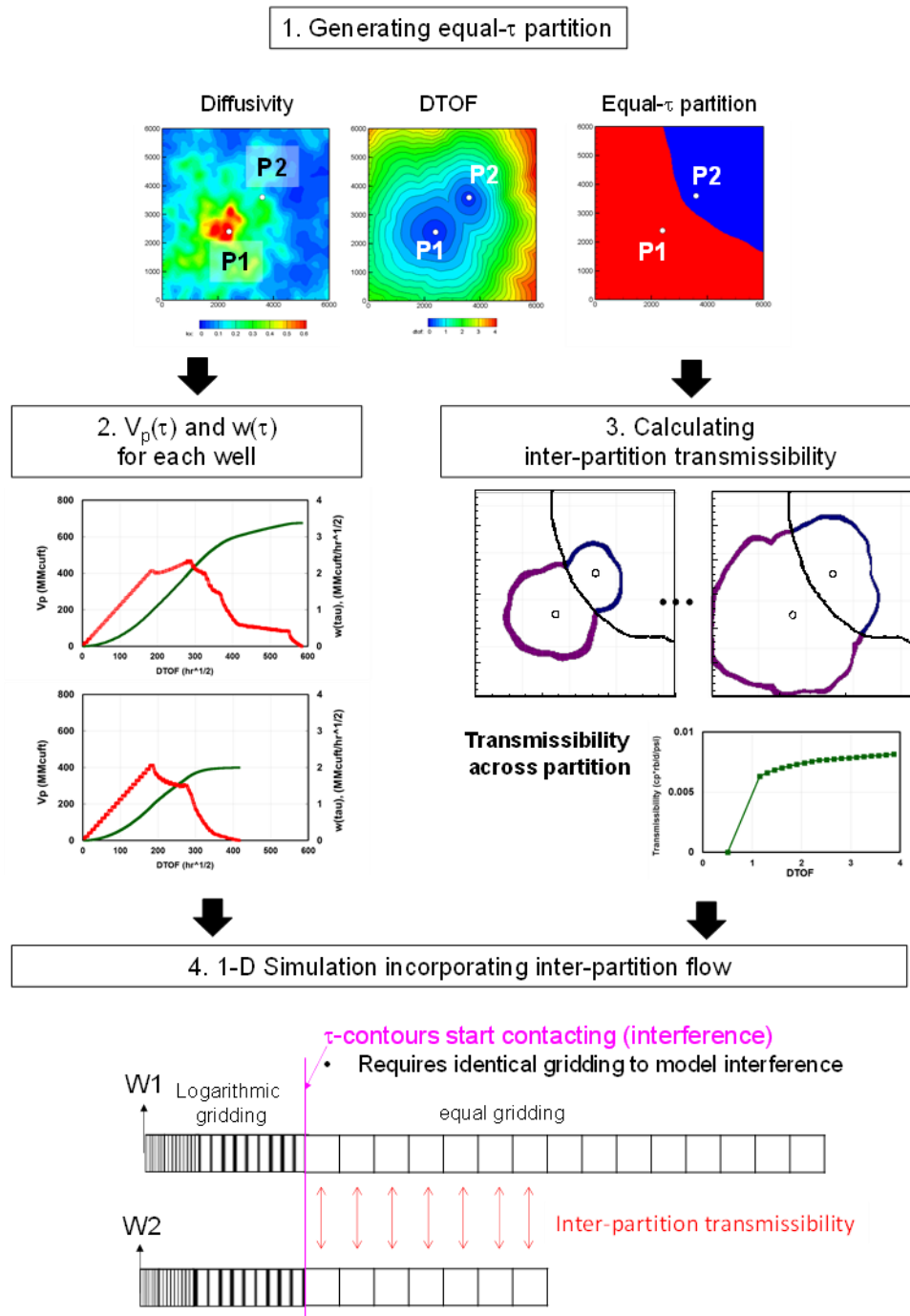


Figure 5.8 FMM-based multi-well simulation workflow incorporating inter-partition transmissibility

5.3.3.2 Computation of Inter-partition Transmissibility

The critical step of this method is to calculate the inter-partition transmissibility. As depicted in **Figure 5.9**, we need to visit every τ -contour and regard the blue grid blocks lying in the τ -contour of interest as a single grid block, as well as purple grid blocks. The inter-partition transmissibility is defined as the transmissibility between the blue and purple regions.

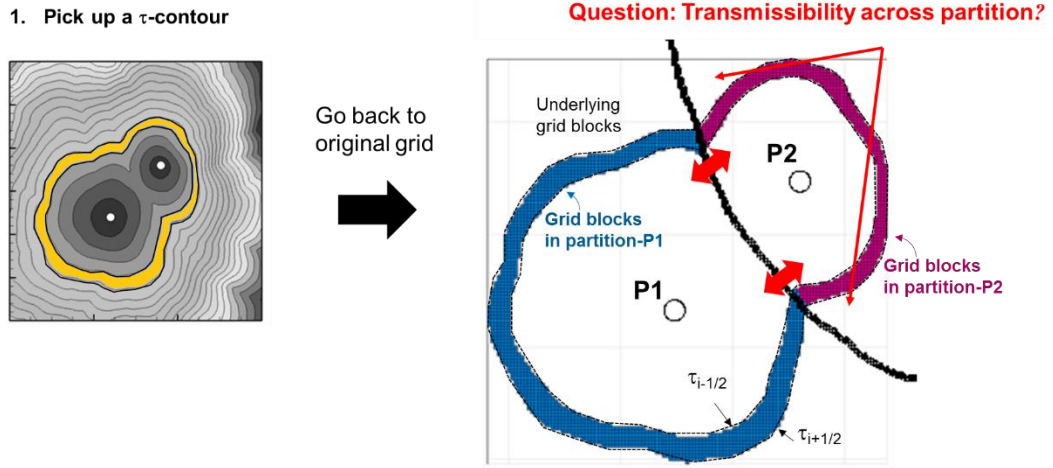


Figure 5.9 Illustration of DTOF-contour where inter-partition transmissibility is computed

Due to the complex geometry of τ -contours, it is difficult to apply analytical methods to calculate the transmissibility between partitions. In addition, flow-based transmissibility calculation is not preferred as it may require substantial computation time. Therefore, we use the analytical pressure calculation based on the DTOF to evaluate the inter-partition transmissibility.

Figure 5.10 illustrates the procedure to calculate the inter-partition transmissibility. We first pick up the underlying grid blocks lying in the τ -contour of interest (step-1). We then place source points along the partition interface and run the FMM to get the DTOF within the contour (steps-2 and 3). When we run the FMM, all the other cells than the contour of interest are set to be inactive. Subsequently, we separately count the pore volumes for each partition and calculate $w(\tau)$ functions (steps-4 and 5). Assuming the steady-state with the unit flux across the partition interface, pressure profiles in each partition will be calculated along the DTOF based on the Darcy's law (step-6):

$$q = -\frac{w(\tau)(c_t\mu)_{ref}}{\mu} \frac{\partial p}{\partial \tau} \approx -\frac{w(\tau_{i+1/2})(c_t\mu)_{ref}}{\mu} \frac{p_i - p_{i-1}}{\Delta \tau_i}, \quad (5.12)$$

where we need to impose any arbitrary value for the boundary pressure $p_{i=0}$ at $\tau=0$ (e.g. 3,000 psi in this example). The steady-state transmissibility can be determined based on the pressures at maximum τ in each partition (step-7). The same steps will be repeated for every τ -contour and the inter-partition transmissibility will be accumulated as a function of the DTOF (step-8). The number of τ -contours for the transmissibility calculation can be different from the number of τ -contours for the 1-D simulation because we can interpolate the transmissibility from the cumulative transmissibility obtained at step-8. See further detail in **Appendix D** that illustrates a step-by-step explanation and validation using a 2-D homogeneous example with two producers.

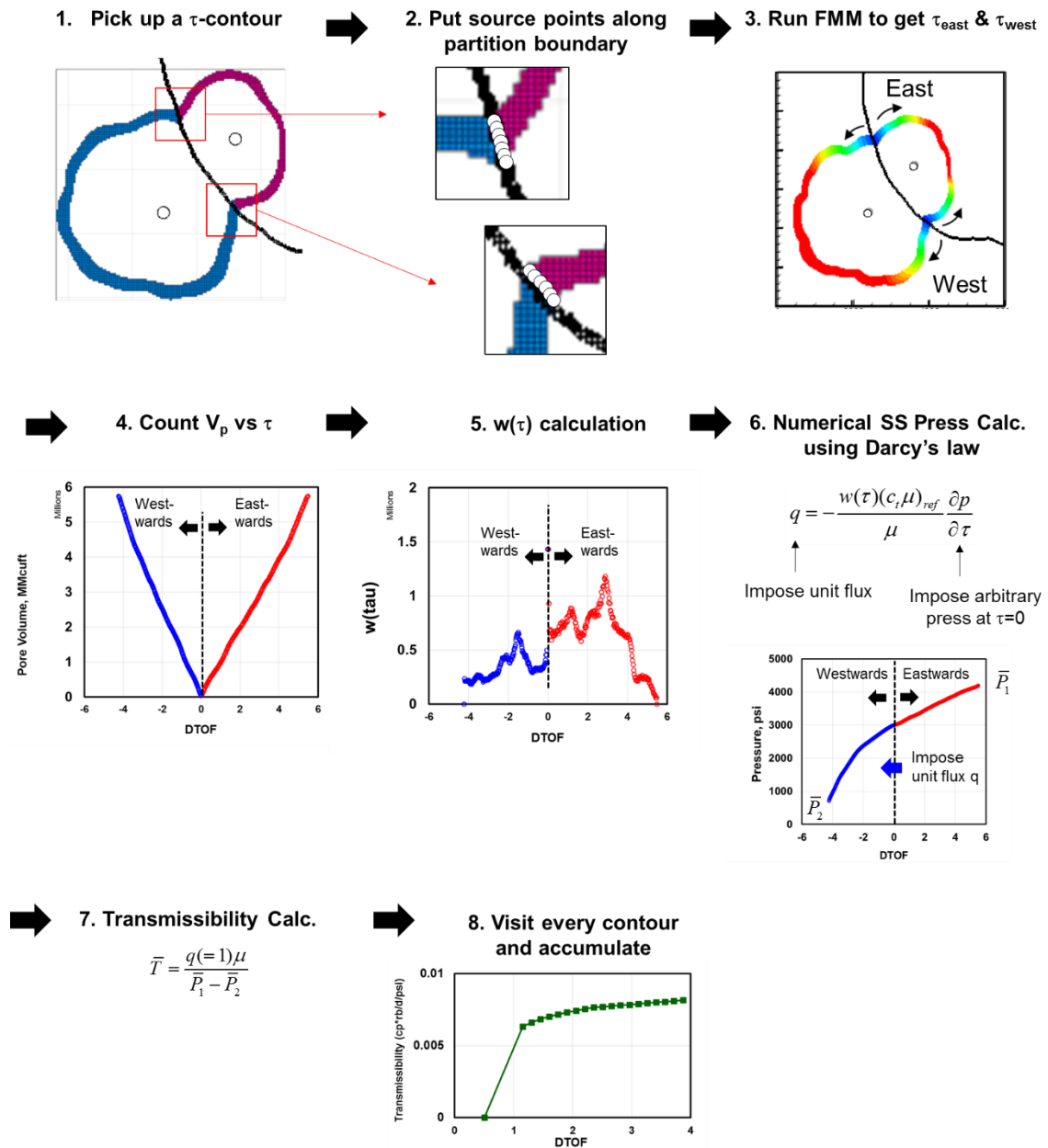


Figure 5.10 Workflow to calculate inter-partition transmissibility using the FMM

For the 2-D homogeneous example with three wells in section 5.3.1, the inter-partition transmissibility was calculated as shown in **Figure 5.11** where different numbers of τ -contours (N) for transmissibility calculation were examined. Although it does not perfectly converge as increasing the number of τ -contours, it shows stable results.

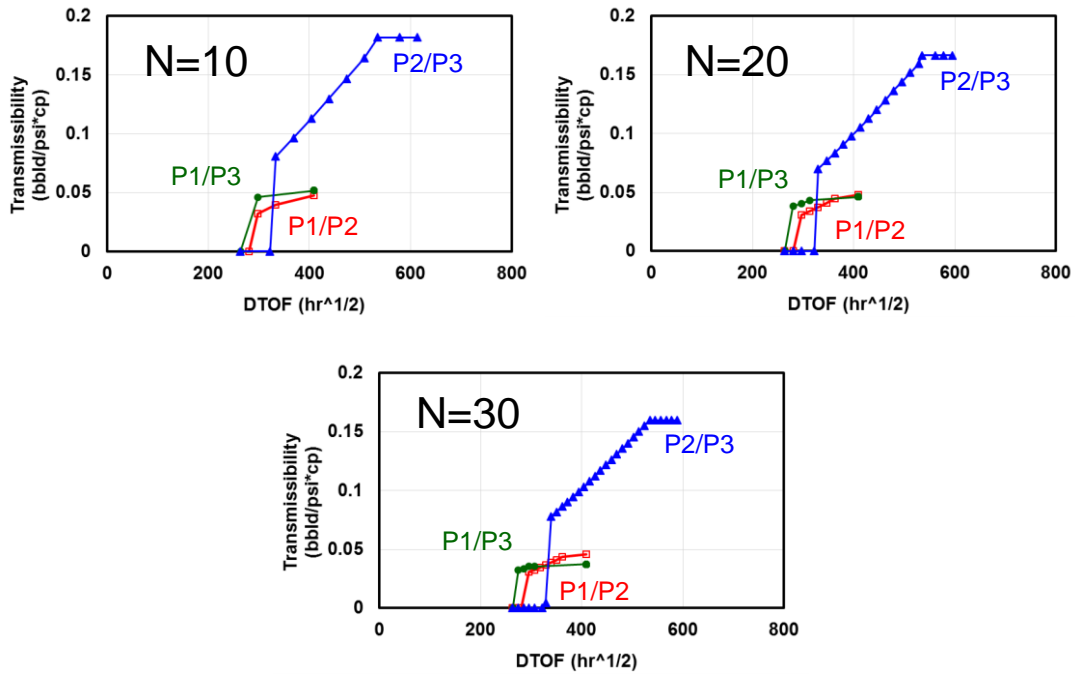


Figure 5.11 Inter-partition transmissibility for 2-D homogeneous example with three wells. Different numbers of DTOF-contours are examined

5.3.3.3 Building 1-D Simulation Grid Blocks

Since this method allows the interaction between the drainage volume partitions, the 1-D simulation grid blocks associated with individual wells should be consistently set up each other. Let us consider the case with three wells. **Figure 5.12** depicts an example

of simulation grid blocks for the FMM-based multi-well simulation using the inter-partition transmissibility. The pink dotted line indicates the first τ -contour of the partition interface. Between the well location and the first partition interface, gridding can be different for each well. On and after the first partition interface, the 1-D grid blocks need to be aligned with the same gridding in order to model the interference. For each well pair, the inter-partition transmissibility will be assigned via the non-neighbor connection.

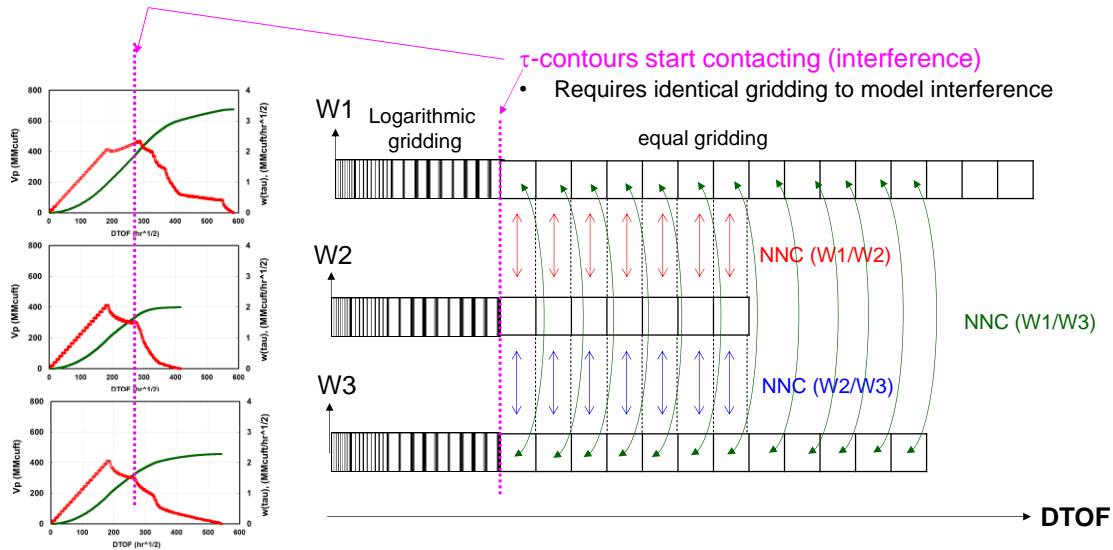


Figure 5.12 Example of grid block set-up for FMM-based simulation incorporating inter-partition transmissibility

5.3.3.4 Results and Discussion

By assigning the calculated inter-partition transmissibility (Figure 5.11) to the 1-D grid systems, the bottomhole pressure of three wells were simulated. **Figure 5.13** shows comparisons between the FDSim and the FMM-based simulation with the inter-partition

transmissibility. Compared to the equal- τ partition, the bottomhole pressure matching was significantly improved by introducing the inter-partition transmissibility, indicating that the flux-in and flux-out across the partitions can be reasonably modeled via the inter-partition transmissibility. We also tested three different numbers of DTOF contours for calculating the inter-partition transmissibility (Figure 5.11) and confirmed that the simulated bottomhole pressures were almost identical. Thus, we should further investigate the optimum selection of the number of the DTOF contours for computing the inter-partition transmissibility, which has been left as future work. **Figure 5.14** illustrates comparisons of the log-log diagnostic plot where the FMM-based simulation with the inter-partition transmissibility better captures the trends of pressure derivatives from the FDSim, compared to the equal- τ partition. The computation time required for the inter-partition transmissibility calculation will be discussed in the next section using a field-scale model.

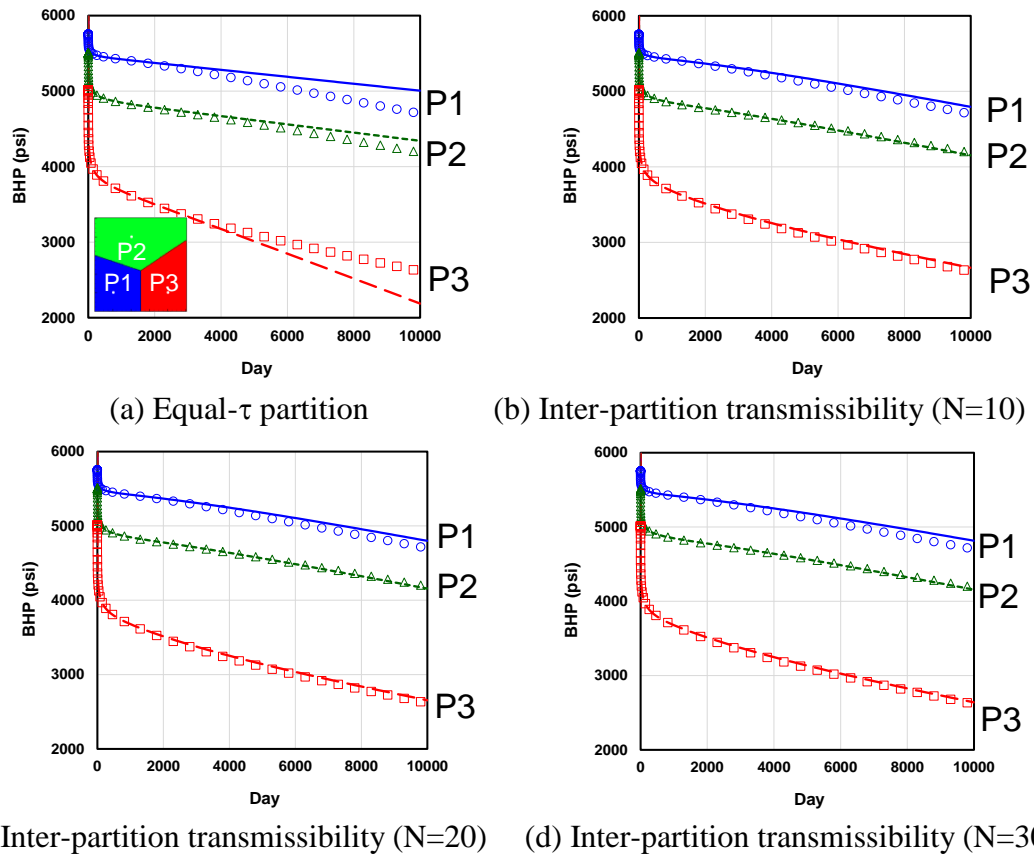


Figure 5.13 Comparison of bottomhole pressure between FDSim (symbol) and FMM-based simulation using inter-partition transmissibility (line)

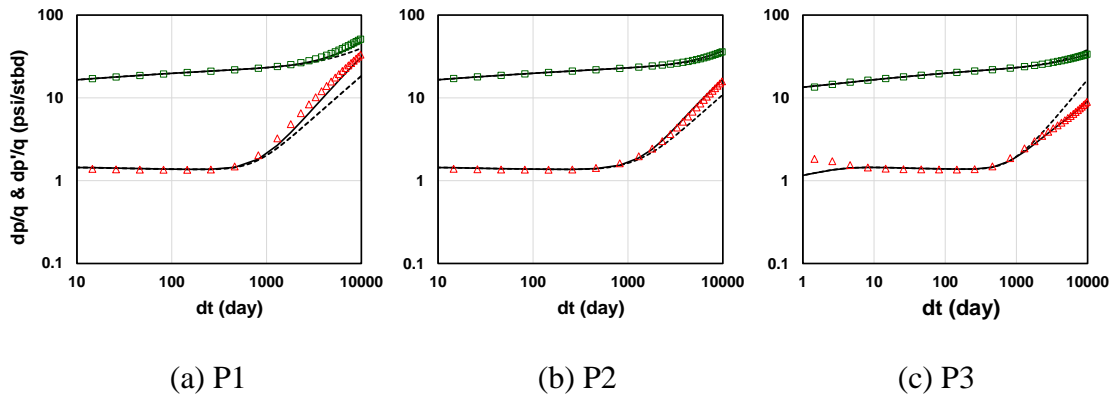


Figure 5.14 Comparisons of log-log diagnostic plot (symbol: FDSim, dashed line: FMM with equal-tau, solid line: FMM with inter-partition transmissibility)

5.4 Extreme Rate Contrast

We further tested a case with the extreme contrast in production rates where the constant rates of 10, 10 and 100 stb/day were assigned for P1, P2 and P3, respectively. **Figure 5.15** shows the comparison of the simulated BHP between the FDSim and the FMM-based simulations. In this particular example, the fixed flux-based partition does not give a reasonable matching with the FDSim (Figure 5.15b), indicating that there is no one representative partition that can approximate the whole simulation period. The flux-based partition with the dynamic update shows better matching than the fixed partition, but it overestimates the drainage volumes of P2 and P3 (Figure 5.15c). The inter-partition transmissibility shows excellent matching in P2 and P3, however, it cannot replicate the BHP of P1. Although the more contrast in the production rates seems to result in less accuracy, both FMM-based simulations, with the dynamic update of the flux-based partition and with the inter-partition transmissibility, can still captures the overall trend of the FDSim.

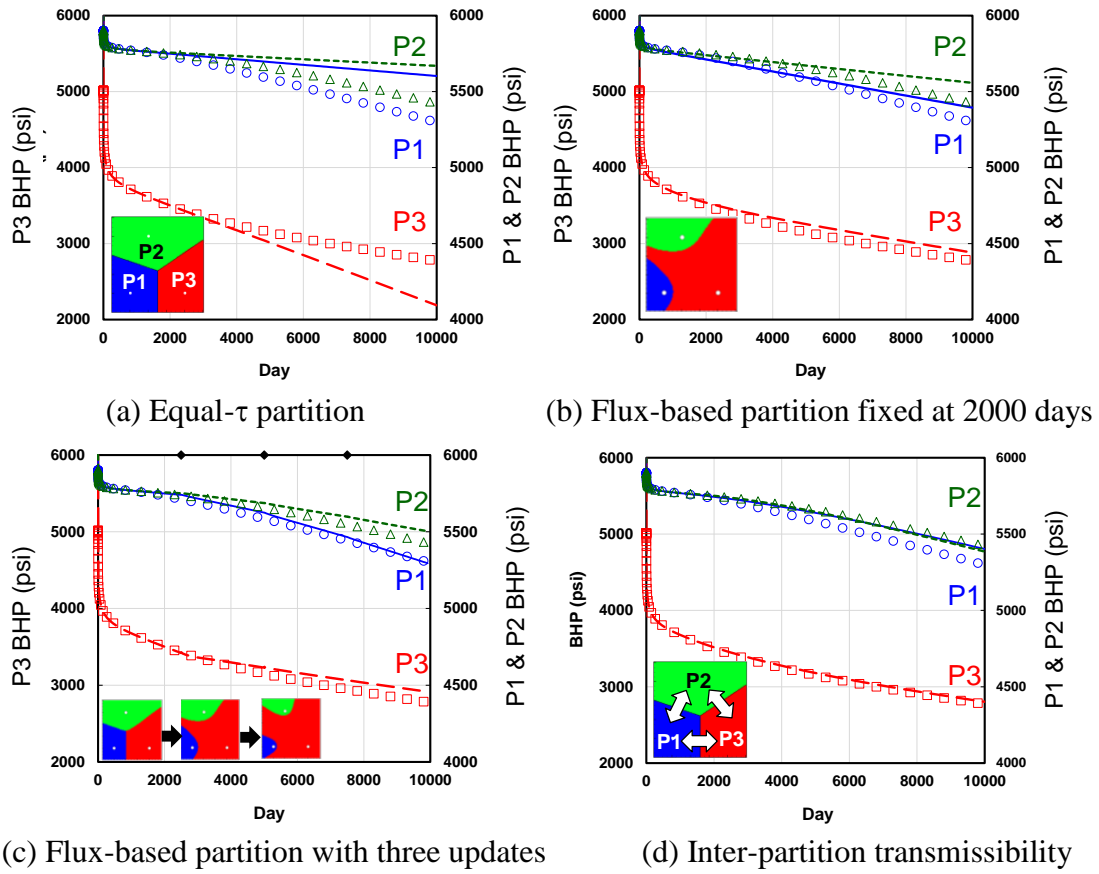


Figure 5.15 Comparison of simulated BHP between FDSim (symbol) and FMM-based simulation (line) with four different methods. Production rate = 10, 10 and 100 stb/day

5.5 Application to Million-cell Model with Fractured Wells

Finally, we present the example of a million-cell model with four (4) fractured wells to illustrate the applicability of the methods to unconventional reservoirs and computational efficiency.

5.5.1 Model Setting

We set up the 3-D Tartan grid dimensioned by $765 \times 300 \times 5$ (1.1 million cells) to model the reservoir section of $8,000 \times 3,000 \times 150$ ft³ and four (4) hydraulically fractured wells (**Figure 5.16**). Each well has 20 stages and 4 clusters per stage with the spacing of 100 ft and 40 ft, respectively. The uniform half length of 170 ft was assumed for all fractures where there is no frac hit for the well spacing of 400 ft apart. The uniform fracture permeability was assumed; 1,000 mD for wells P1 and P3 and 100 mD for wells P2 and P4, respectively.

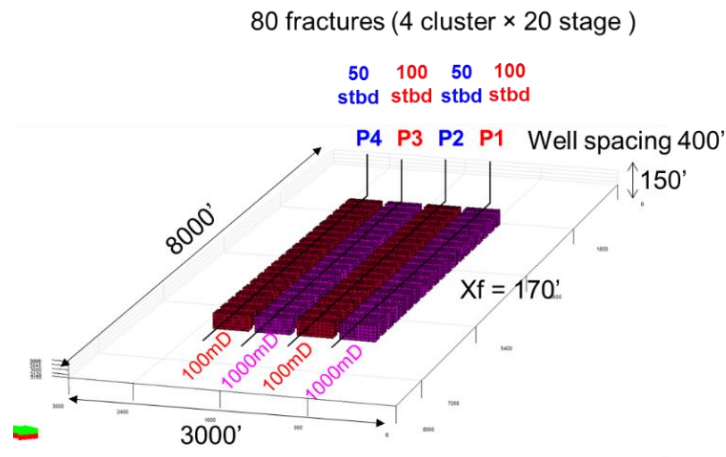
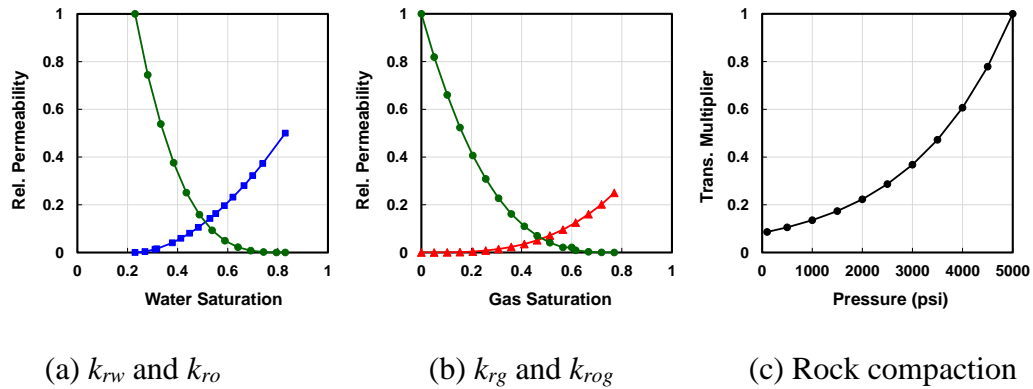


Figure 5.16 Geometry of hydraulic fractures for four fractured wells case

Other input data is summarized in **Table 5.1**. The same PVT properties was used shown in Figure 2.15. The relative permeability and rock compaction tables are depicted in **Figure 5.17** where rock compaction was applied only for the hydraulic fractures.

Table 5.1 Input data for four fractured wells case

Item	Value
Model size (ft ³)	8000'×3000'×150'
Grid block dimension	765×300×5 (1,147,500)
Matrix permeability (mD)	1×10 ⁻³
Hydraulic fracture permeability (mD)	100 or 1000
Matrix porosity	0.05
Hydraulic fracture porosity	5×10 ⁻⁴
Initial water saturation	0.23
Rock compressibility (psi ⁻¹)	1.0×10 ⁻⁶
Water viscosity (cp)	1.0
Water compressibility (psi ⁻¹)	1.0×10 ⁻⁶
Water formation volume factor (rbbl/stb)	1.0
Initial solution gas-oil ratio (Mscf/stb)	1.34
Bubble point pressure (psi)	2,860
Initial pressure (psi)	5,000

**Figure 5.17 Relative permeability and rock compaction for four fractured wells case**

5.5.2 Comparison of Simulation Results

We run the simulation for 3,000 days with the constant rate controls of 50, 100, 50, 100 stb/day for wells P1, P2, P3 and P4, respectively. **Figure 5.18** shows the

comparison of the BHP responses from the FDSim (symbol), the FMM-based simulation with equal- τ partition (black dashed line), the fixed flux-based partition (blue solid line; flux field was generated at 100 day) and the inter-partition transmissibility (red solid line). As discussed later, solutions of the flux-based partition collapsed after 200 days and therefore we cannot obtain the simulation results from the flux-based partition with the dynamic update. For wells P2 and P4, the FMM-based simulation with the flux-based partition shows better matching with the FDSim compared to the equal- τ partition, whereas the FMM-based simulation with the inter-partition transmissibility shows excellent matching. However, the FMM-based simulation shows the significant deviation from the FDSim for well P3.

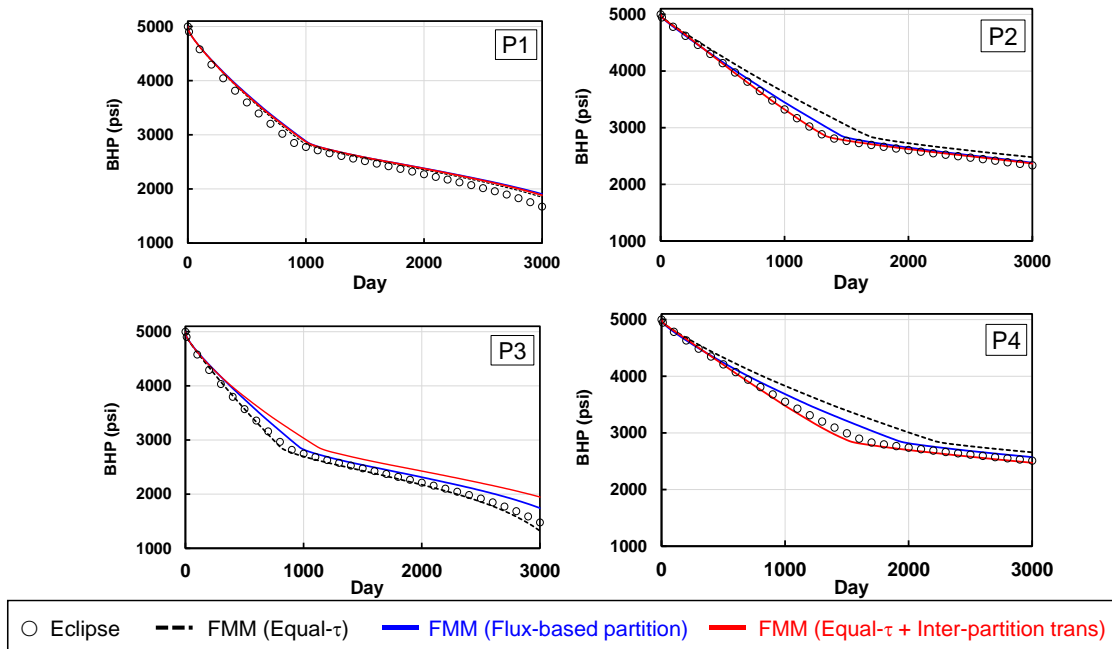


Figure 5.18 Comparison of BHP responses for four fractured wells case

In this example, the flux-based partition was fixed at 100 day because we have seen the solution collapse for the drainage volume partition at 200 days and after as illustrated in **Figure 5.19**. We have confirmed that we did not see this issue as long as we use the velocity field from the FDSim. Therefore, the flux field calculated from the superposition of Eq. (5.2) may have some issues, and this has been left as future work. The dynamic update would improve the matching between the FDSim and the FMM-based simulation with the flux-based partition.

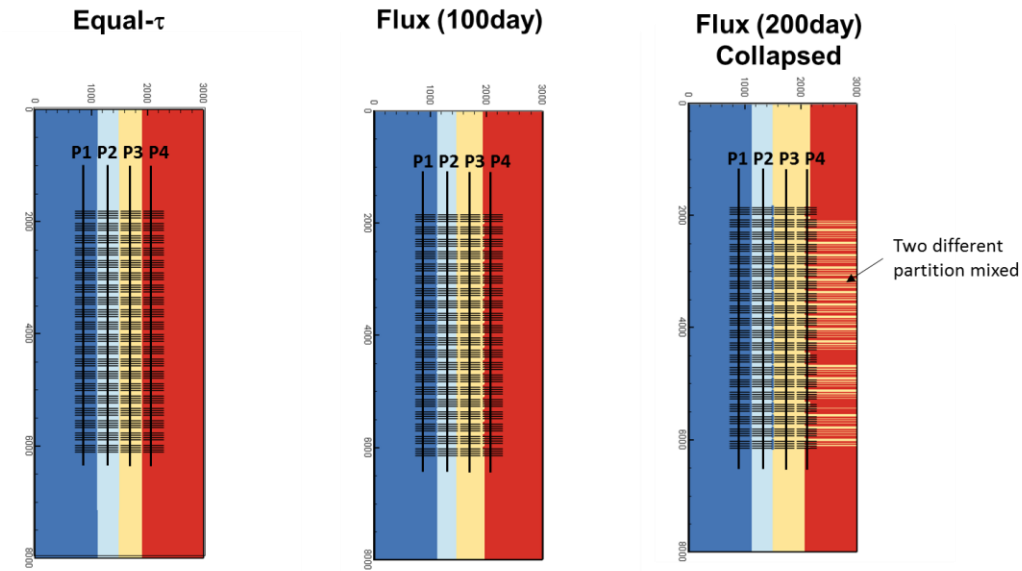


Figure 5.19 Equal-tau and flux-based partition for four fractured wells case

On the other hand, we also identified the challenge for the FMM-based simulation with the inter-partition transmissibility. **Figure 5.20** shows the inter-partition transmissibility

calculated with different numbers of τ -contours, indicating that the transmissibility calculation is unstable. This might be because of the less accurate calculation of $w(\tau)$ from the cell-center Eikonal solution and the smoothing technique, rather than the 27-pt stencil Eikonal solver. The reason we used the cell-center approach is to save computational time required for the inter-partition transmissibility calculation. Thus, one potential mitigation is to implement the 27-pt stencil Eikonal solver for the inter-partition transmissibility calculation although it requires extra the computation time.

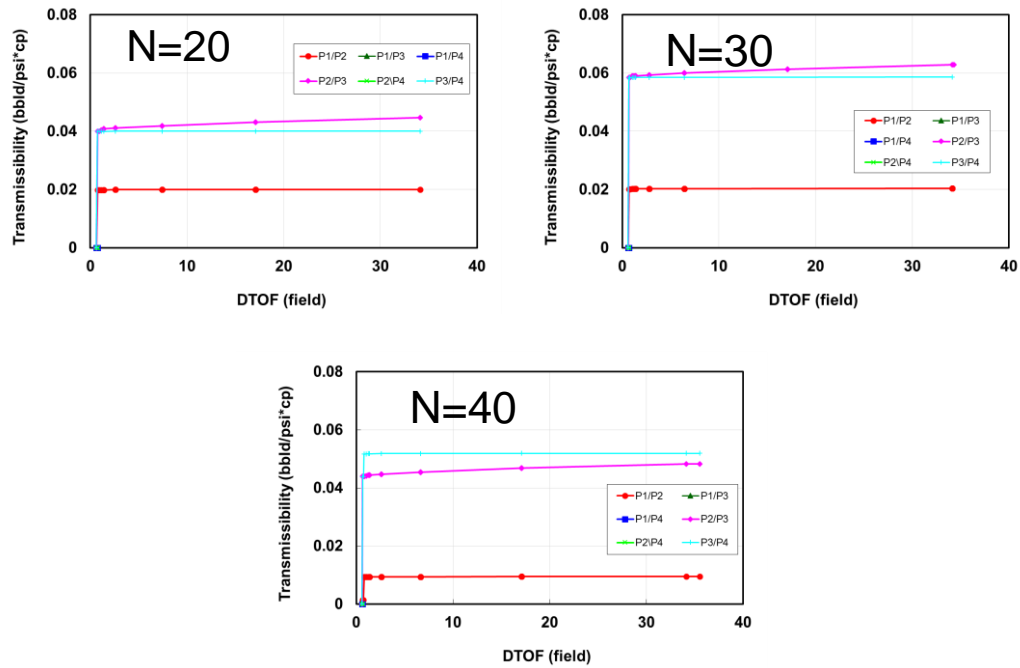


Figure 5.20 Inter-partition transmissibility for four fractured wells case. Different numbers of DTOF-contours are examined

5.6 Summary

In this chapter, we studied the FMM-based simulation for multiple wells. We revisited the flux-based partition which was previously proposed by Huang et al. (2017), and we also newly proposed two methods that incorporate (1) the dynamic update of the flux-based partition and (2) the inter-partition transmissibility to model the flux-in and flux-out across the partitions, respectively. Conclusions from this study are summarized below for each methodology:

FMM-based simulation with flux-based partition

- The FMM-based simulation proposed by Huang et al. (2017) used the velocity field to define the drainage volume partition. The velocity field can be efficiently calculated by the FMM-based asymptotic approximation of pressure gradient along the DTOF coordinate (King et al., 2016). The drainage volume partition, which is obtained assuming one particular time step, will be fixed during the FMM-based simulation. Thus, the assumption is that we can approximate the dynamically changing partition by a single snapshot of the partition maps.
- For cases with multiple wells constrained by the different constant rates, the FMM-based simulation with the flux-based partition shows better matching with the FDSim compared to the FMM-based simulation with equal- τ partition presented in Chapter IV.
- The simulation results from this method are sensitive to the time step selected for generating the flux field. The possible two options to mitigate this challenge are

(1) investigating the optimal time step selection or (2) dynamically updating the drainage volume partition during the FMM-based simulation.

FMM-based simulation with flux-based partition with dynamic update

- Rather than selecting one representative time step to model the drainage volume partition over time, we proposed a new approach that dynamically updates the drainage volume partition during the simulation.
- It was confirmed that only a few update of the drainage volume partition improved matching between the FMM-based simulation and the FDSim compared to the fixed flux-based partition. The optimal frequency of updating the drainage volume partition should be further studied.
- Extra computations for the 1-D pore volume and the 1-D transmissibility are required when the partition is updated. However, it should be only a small portion of total CPU.
- Solutions of the drainage volume partition from the tracer equation can collapsed due to the flux field generated from the FMM-based asymptotic approximation. A robust flux calculation should be investigated.

FMM-based simulation with inter-partition transmissibility

- The FMM-based simulation introducing the inter-partition transmissibility was newly proposed. This method first defines the drainage volume partition using the equal- τ interface, followed by the calculation of the transmissibility across the

partitions. The 1-D simulations for each well are no longer independent because the communication across the partitions is enabled via the inter-partition transmissibility. The inter-partition transmissibility can be determined purely based on the static properties and there is no rate and time dependency.

- The simulation results from this method showed better matching with the FDSim than the FMM-based simulation with the equal- τ partition. Similar or better matching quality was confirmed compared to the FMM-based simulation with the dynamic update of the flux-based partition.
- Two remaining issues were identified: (1) calculation of the inter-partition transmissibility is sensitive to the number of the DTOF contours especially for the fractured well case and (2) calculation of the inter-partition transmissibility is computationally expensive. Results indicate that the 27pt-stencil FMM is required for accurate calculations of $w(\tau)$ functions and inter-partition transmissibility.

CPU Time

- For a million cell example with four fractured wells, all the FMM-based approaches, including the flux-based partition and the inter-partition transmissibility, achieved faster computation than the FDSim. Due to the extra computation of the inter-partition transmissibility, the FMM-based simulation with the inter-partition transmissibility required almost double CPU time than the FMM-based simulation with the equal- τ partition. On the other hand, the additional time required for the flux-based partition is not significant.

CHAPTER VI

CONCLUSIONS AND RECOMMENDATIONS

6.1 Conclusions

In this study, we developed and validated an efficient simulation approach for multi-phase and multi-component flow in unconventional reservoirs using the Fast Marching Method (FMM). The high frequency asymptotic solution of the diffusivity equation leads to the Eikonal equation, which is a generalized form of the depth of investigation in heterogeneous and fractured reservoirs with arbitrary well completions. The Eikonal equation can be efficiently solved by the FMM for the Diffusive Time-of-Flight (DTOF) that governs the geometry and the travel time of pressure ‘front’ propagation. The key concept of the proposed FMM-based simulation is to utilize the DTOF as a 1-D spatial coordinate embedding reservoir heterogeneity to transform an original 3-D reservoir model into an equivalent 1-D model, leading to orders-of-magnitude faster computation compared to the normal finite difference simulation (FDSim).

We applied the FMM-based simulation to field history matching, optimization of gas injection EOR, and design of infill well placement for unconventional reservoirs. The rapid simulation of the FMM-based approach enables us to use high resolution models to describe geological heterogeneity and complex fracture geometry. Furthermore, robust population-based algorithms for history matching and optimization can be incorporated even if large numbers of simulations are required. Thus, the FMM-based simulation

provides wide applicability for quick and comprehensive assessment of unconventional reservoirs. Conclusions from this research are summarized as follows:

- We developed and validated the FMM-based simulation for multi-phase flow in dual-porosity single-permeability (DPSP) models. We also confirmed that the FMM-based simulation can provide orders-of-magnitude faster computation for million-cell models compared to the FDSim. The field application of history matching demonstrated that the rapid FMM-based simulation assists efficient history matching using the population-based technique that requires a large number of simulation runs. Multiple history matched models were generated and used for uncertainty assessment in reservoir properties as well as the remaining recovery.
- We further extended the FMM-based simulation to multi-component flow in DPSP model. The speed-up compared to the FDSim was more significant than blackoil simulations because of the reduction in the total number of primary variables, as well as in the number of flash calculations and stability analysis involved in the compositional simulation. Use of the rapid compositional simulation based on the FMM provides not only quick assist to optimize operational parameters for field-scale application, but also physical assessment of displacement/ recovery processes.
- We proposed a FMM-based multi-well simulation approach for a scenario where all the wells are constrained by the same and constant bottomhole pressures. In this scenario, 'equal- τ ', the interface at which the marching front of pressure

propagation from a well encounters that of the others', approximates no flow boundary. Our proposed approach partitions the reservoir model into independent sub-domains associated with individual wells based on the equal- τ followed by independent 1-D simulations within each domain. Coupling with the FMM-based multi-well simulation, we proposed a comprehensive workflow for assessing and optimizing the infill well spacing that incorporates the fracture propagation simulation accounting for the parent well depletion. We demonstrated that the use of the FMM-based approach can quickly provide quantitative assessment of potential frac hits and help efficient design and optimization of infill well planning in unconventional reservoirs.

- We newly proposed and validated two methods of the FMM-based multi-well simulation for the constant rate production scenario where drainage volume partition dynamically changes over time. The first method involves the dynamic update of drainage volume partition during the FMM-based simulation, using the flux fields obtained from the asymptotic approximation. We found that only a few updates seems enough to capture the migration of drainage volume, but the optimal frequency of the dynamic update needs to be further investigated. In addition, a robust calculation of flux fields should also be studied since we identified a case where physically reasonable solutions for the drainage volume partition could not be obtained. The other method introduces the inter-partition transmissibility that allows flux-in and flux-out across the partition. The identified challenge is to

reduce the computational time that is required for calculating the inter-partition transmissibility.

6.2 Recommendations and Future Work

In order to extend and improve the current work, the followings are recommended as future work:

- A methodology to incorporate gravity in the FMM-based simulation needs to be developed. Phase segregation due to gravity in hydraulic fractures may significantly affect the simulated well performances. One possible option is a multi-domain modeling that uses original multi-dimensional grid blocks for hydraulic fractures and the 1-D DTOF grid blocks for the rest of the regions.
- Molecular diffusion, which is considered important physics for modeling gas injection in unconventional reservoirs, should also be incorporated in the FMM-based simulation.
- A robust and efficient Eikonal solver needs to be developed. Although the 27pt-stencil FMM provides accurate and stable $w(\tau)$ function, the challenge is expensive computational costs since it requires more numbers of solution nodes for the DTOF than the cell-center FMM. A hybrid approach might be one option that applies the 27pt-stencil FMM for near-well regions and the cell-center for the remaining regions.
- We identified several remaining challenges for the FMM-based multi-well simulation. For the flux-based partition with dynamic update, a robust calculation

of flux fields as well as the optimal frequency of updating the drainage volume partition needs to be further investigated. For the inter-partition transmissibility, we should address: (1) further validation of the inter-partition transmissibility calculation based on the FMM, especially for fractured well case and (2) improvement of computational efficiency of the inter-partition transmissibility calculation to reduce the CPU time.

NOMENCLATURE

a	Parameter in Equation-of-State for molecular interaction
b	Coefficient for exponential transmissibility reduction model or parameter in Equation-of-State for molecular volume
B	Formation volume factor
BHP	Bottomhole pressure
c	Compressibility
CDF	Cumulative distribution function
DTOF	Diffusive Time-of-Flight
DPSP	Dual-porosity Single-permeability
EOR	Enhanced oil recovery
EoS	Equation-of-State
F	Fugacity
FMM	Fast Marching Method
FDSim	Finite Difference Simulation
GA	Genetic Algorithm
GOR	Gas-oil ratio
h	Thickness
HC	Hydro Carbon
HF	Hydraulic fractures
Huff-n-Puff	Huff and Puff

k	Permeability
\mathbf{k}	Permeability tensor
k_{ij}	Binary interaction coefficient between components i and j
k_r	Relative permeability
l	length of matrix blocks in dual-porosity model
L	Liquid phase
L_w	Effective well length of horizontal well
M	Mobility ratio
MMP	Minimum Miscibility Pressure
p	Pressure
PVT	Pressure-volume-temperature
q	Flow rate
r_w	Well radius
R	Universal gas constant
R_s	Solution gas-oil ratio
RMS	Root-mean-squared error
S	Saturation
scf	Standard cubic foot
SRV	Stimulated reservoir volume
stb	Stock tank barrel
t	Time
\mathbf{u}	Velocity

V	Volume or vapor phase
V_{dp}	Dykstra-Parson's coefficient
V.R.R.	Voidage-replacement ratio
w	Weight
$w(\tau)$	Function defined as derivative of drainage pore volume w.r.t τ
WC	Water cut
WHP	Wellhead pressure
WI	Well Index
x_i	Mole fraction of component- i in liquid phase
\mathbf{x}	Location vector
X_f	Fracture half length
y_i	Mole fraction of component- i in vapor phase
z_i	Global mole fraction of component- i
z_w	Distance from reservoir top to horizontal well
α	Diffusivity
δ	Dirac Delta
ϕ	Porosity
Γ	Transfer rate between fracture and matrix or surface area
λ	Mobility or inter-porosity coefficient
μ	Viscosity
θ	Phase function

ρ	Mass or mole density
σ	Shape factor
τ	Diffusive Time-of-Flight
ω	Frequency or storativity ratio
Ω	Domain

Subscript

b	Bulk
h	Horizontal
j	Phase
g	Gas
mp	Multi-phase
o	Oil
p	Pore
ref	Reference condition
sc	Standard condition
t	Total
v	Vertical
w	Water

Superscript

n	Time step
-----	-----------

up

Upstream

REFERENCES

- Alexander, T, J. Baihly, and C. Boyer. 2011. "Shale Gas Revolution." *Oilfield Review* 23 (3): 40-55.
- Alfarge, D., M. Wei, and B. Bai. 2017a. "IOR Methods in Unconventional Reservoirs of North America: Comprehensive Review." *SPE Western Regional Meeting*. Apr. 24-27, Bakersfield, CA. SPE-185640-MS. doi:<https://doi.org/10.2118/185640-MS>.
- Alfarge, D., M. Wei, and B. Bai. 2017b. "Comparative Study for CO₂-EOR and Natural Gases Injection-Techniques for Improving Oil Recovery in Unconventional Oil Reservoirs." *Carbon Management Technology Conference*. Jul. 17-20, Houston, TX. CMTC-485175-MS. doi:<https://doi.org/10.7122/485175-MS>.
- Alharthy, N. S., T. W. W. Teklu, T. N. Nguyen et al. 2016. "Nanopore Compositional Modeling in Unconventional Shale Reservoirs." *SPE Res. Eval & Eng.* 19 (3): 415-428. doi:<http://dx.doi.org/10.2118/166306-PA>.
- Arps, J. J. 1945. "Analysis of Decline Curves." *Trans. AIME* 160 (1): 228-247. doi:<https://doi.org/10.2118/945228-G>.
- Bragg, L. R. and J. W. Dettman. 1968. "Related Problems in Partial Differential Equations." *Bulletin of the American Mathematical Society* 74 (2): 375-378. doi:<https://doi.org/10.1090/S0002-9904-1968-11959-7>.
- Cerveny, V., I. A. Molotkov and I. Psensik. 1978. *The Ray Method in Seismology*. Prague: Charles Univ. Press.
- Chapman, J. S., J. MH. Lawry and J. R. Ockendon. 1999. "Ray Theory for High-Peclet-Number Convection-Diffusion." *SIAM Journal of Applied Mathematics* 60 (1): 121-135. doi:<https://doi.org/10.1137/S0036139998344088>.
- Chen, C., M. T. Balhoff and K. K. Mohanty. 2014. "Effect of Reservoir Heterogeneity on Primary Recovery and CO₂ Huff 'n' Puff Recovery in Shale-Oil Reservoirs." *SPE Res. Eval & Eng.* 17 (3): 404-413. doi:<https://doi.org/10.2118/164553-PA>.
- Cheng, H., K. Dehghani and T. C. Billiter. 2008. "A Structured Approach for Probabilistic-Assisted History Matching Using Evolutionary Algorithms: Tengiz Field Applications." *SPE Annual Technical Conference and Exhibition*. Sep. 21-24, Denver, CO. SPE-116212-MS. doi:<https://doi.org/10.2118/116212-MS>.

- Cho, Y., O. G. Apaydin and E. Ozkan. 2013. "Pressure-Dependent Natural-Fracture Permeability in Shale and Its Effect on Shale-Gas Well Production." *SPE Res. Eval & Eng.* 216-228. doi:<http://dx.doi.org/10.2118/159801-PA>.
- Cipolla, C. L., M. J. Williams, X. Weng et al. 2010a. "Hydraulic Fracture Monitoring to Reservoir Simulation: Maximizing Value." *SPE Annual Technical Conference and Exhibition*. Sep. 19-22, Florence, Italy. SPE-133877-MS. doi:<https://doi.org/10.2118/133877-MS>.
- Cipolla, C. L., E. P. Lolon, J. C. Erdle et al. 2010b. "Reservoir Modeling in Shale-Gas Reservoirs." *SPE Res. Eval & Eng.* 13 (4): 638-653. doi:<http://dx.doi.org/10.2118/125530-PA>.
- Cipolla, C. L., T. Fitzpatrick, M. J. Williams et al. 2011. "Seismic-to-Simulation for Unconventional Reservoir Development." *SPE Reservoir Characterisation and Simulation Conference and Exhibition*. Oct. 9-11, Abu Dhabi, UAE. SPE-146876-MS. doi:<http://dx.doi.org/10.2118/146876-MS>.
- Clarkson, C. R. and F. Qanbari. 2015. "An Approximate Semianalytical Multiphase Forecasting Method for Multifractured Tight Light-Oil Wells with Complex Fracture Geometry." *Journal of Canadian Petroleum Technology* 54 (6): 489-508. doi:<http://dx.doi.org/10.2118/178665-PA>.
- Courant, R. and D. Hilbert. 1953. *Methods of Mathematical Physics*. New York: Interscience Publishers. ISBN 978-0470179529.
- Cui, J., C. Yang, D. Zhu et al. 2016. "Fracture Diagnosis in Multiple-Stage-Stimulated Horizontal Well by Temperature Measurements with Fast Marching Method." *SPE Journal*. 21 (6): 2289-2300. doi:[doi:10.2118/174880-PA](http://dx.doi.org/10.2118/174880-PA).
- Dake, L. P. 1978. *Fundamentals of Reservoir Engineering*, No. 8. Amsterdam: Developments in Petroleum Science. ISBN 978-0444418302.
- Datta-Gupta, A. and M. J. King. 2007. *Streamline Simulation: Theory and Practice*. SPE Textbook Series Vol. 11. Richardson, TX: Society of Petroleum Engineers. ISBN: 978-1555631116
- Datta-Gupta, A., J. Xie, N. Gupta et al. 2011. "Radius of Investigation and Its Generalization to Unconventional Reservoirs." *Journal of Petroleum Technology* 63 (7): 52-55. doi:<http://dx.doi.org/10.2118/0711-0052-JPT>.
- Diaz de Souza, O. C., A. J. Sharp, R. C. Martinez et al. 2012. "Integrated Unconventional Shale Gas Reservoir Modeling: A Worked Example From the Haynesville Shale, De Soto Parish, North Louisiana." *SPE Americas Unconventional Resources*

- Conference. Jun. 5-7, Pittsburgh, Pennsylvania. SPE-154692-MS. doi:<http://dx.doi.org/10.2118/154692-MS>.
- Dijkstra, E. W. 1959. "A Note on Two Problems in Connexion with Graphs." *Numerische Mathematik*. 1: 269–271. doi:<https://doi.org/10.1007/BF01386390>
- Du, C., X. Zhang., B. Melton et al. 2009. "A Workflow for Integrated Barnett Shale Gas Reservoir Modeling and Simulation." *SPE Latin American and Caribbean Petroleum Engineering Conference*. May. 31 –Jun. 3, Caragena, Colombia. SPE-122934-MS. doi:<http://dx.doi.org/10.2118/122934-MS>.
- Duong, A. N. 2011. "Rate-Decline Analysis for Fracture-Dominated Shale Reservoirs." *SPE Res. Eval & Eng.* 14 (3): 377-387. doi:<http://dx.doi.org/10.2118/137748-PA>.
- EIA. 2016. "Annual Energy Outlook 2016 with Projections to 2040." August. <http://www.eia.gov/forecasts/aeo>. Accessed on Decembter 20, 2016.
- Fetkovich, M. J. 1980. "Decline Curve Analysis Using Type Curves." *Journal of Petroleum Technology* 32 (6): 1-065. doi:<https://doi.org/10.2118/13169-PA>.
- Firoozabadi, A. 1999. *Thermodynamics of Hydrocarbon Reservoirs*. New York: McGraw-Hill Education. ISBN 978-0070220713.
- Fujita, Y. 2014. *Fast Marching Method with Multiphase Flow and Compositional Effects*. Master Thesis. Texas A&M University. College Station, TX.
- Fujita, Y., A. Datta-Gupta and M. J. King. 2016. "A Comprehensive Reservoir Simulator for Unconventional Reservoirs That Is Based on the Fast-Marching Method and Diffusive Time of Flight." *SPE Journal* 21 (6): 2276-2288. doi:<http://dx.doi.org/10.2118/173269-PA>.
- Gilman, J. R. and H. Kazemi. 1983. "Improvements in Simulation of Naturally Fractured Reservoirs." *SPE Journal* 23 (4): 695-707. doi:<http://dx.doi.org/10.2118/10511-PA>.
- Hassouna, M. S. and A. A. Frag. 2007. "Multistencils Fast Marching Methods: A Highly Accurate Solution to the Eikonal Equation on Cartesian Domains." *IEEE Transactions of Pattern Analysis and Machine Intelligence* 29 (9): 1-12. doi:<https://doi.org/10.1109/TPAMI.2007.1154>.
- Hawthorne, S. B., C. D. Gorecki, J. A. Sorensen et al. 2016. "Hydrocarbon Mobilization Mechanisms from Upper, Middle, and Lower Bakken Reservoir Rocks Exposed to CO₂." *SPE Unconventional Resources Conference*. Nov. 5-7, Calgary, Canada. SPE-167200-MS. doi:<https://doi.org/10.2118/167200-MS>.

- He, Z., H. Parikh, A. Datta-Gupta et al. 2004. "Identifying Reservoir Compartmentalization and Flow Barriers From Primary Production Using Streamline Diffusive Time of Flight." *SPE Res. Eval. & Eng.* 7 (3): 238-247. doi:<https://doi.org/10.2118/88802-PA>.
- Horne, R. N. 1995. *Modern Well Test Analysis: A Computer-Aided Approach*. 2nd edition. Palo Alto, California: Petroway. ISBN 978-0962699214.
- Huang, J. 2017. *Analysis of Hydraulic Fracture Propagation and Well Performances using Geomechanical Models and Fast Marching*. College Station: Ph.D Dissertation. Texas A&M University.
- Huang, J., F. Olalotiti-Lawal, M. J. King et al. 2017. "Modeling Well Interference and Optimal Well Spacing in Unconventional Reservoirs Using the Fast Marching Method." *SPE/AAPG/SEG Unconventional Resources Technology Conference*. Jul. 24-26, Austin, TX. URTEC-2688841-MS. doi:<https://doi.org/10.2118/180148-MS>.
- Hyman, J. D., S. Karra, N. Makedonska et al. 2015. "dfnWorks: A Discrete Fracture Network Framework for Modeling Subsurface Flow and Transport." *Computers & Geosciences* 84: 10-19. doi:<https://doi.org/10.1016/j.cageo.2015.08.001>.
- Iino, A., A. Vyas, J. Huang et al. 2017a. "Efficient Modeling and History Matching of Shale Oil Reservoirs Using the Fast Marching Method: Field Application and Validation." *SPE Western Regional Meeting*. Apr. 24-27, Bakersfield, CA. SPE-185719-MS. doi:<https://doi.org/10.2118/185719-MS>.
- Iino, A., A. Vyas, J. Huang et al. 2017b. "Rapid Compositional Simulation and History Matching of Shale Oil Reservoirs Using the Fast Marching Method." *SPE/AAPG/SEG Unconventional Resources Technology Conference*. Jul. 24-26, Austin, TX. URTEC-2693139-MS. doi:<https://doi.org/10.15530/URTEC-2017-2693139>.
- Iino, A. and A. Datta-Gupta, 2018. "Optimizing CO₂ and Field Gas Injection EOR in Unconventional Reservoirs Using the Fast Marching Method." *SPE Improved Oil Recovery Conference*. Apr. 14-18, Tulsa, OK. SPE-190304-MS. doi:<https://doi.org/10.2118/190304-MS>.
- Iino, A., T. Onishi, F. Olalotiti-Lawal et al. 2018. "Rapid Field-Scale Well Spacing Optimization in Tight and Shale Oil Reservoirs Using Fast Marching Method." *SPE/AAPG/SEG Unconventional Resources Technology Conference*. Jul. 23-25, Houston, TX. URTEC-2901376-MS. doi:<https://doi.org/10.15530/URTEC-2018-2901376>.

- Ilk, D., J. A. Rushing, A. D. Perego et al. 2008. "Exponential vs. Hyperbolic Decline in Tight Gas Sands — Understanding the Origin and Implications for Reserve Estimates Using Arps' Decline Curves." *SPE Annual Technical Conference and Exhibition*. Sep. 21-24, Denver, Colorado. SPE-116731-MS. doi:<http://dx.doi.org/10.2118/116731-MS>.
- Jacobs, T. 2015a. "Unconventional Resources Will Require Unconventional EOR." *Journal of Petroleum Technology* 67 (09): 68-70. doi:<https://doi.org/10.2118/0915-0068-JPT>.
- Jacobs, T. 2015b. "Changing the Equation: Refracturing Shale Oil Wells." *Journal of Petroleum Technology* 67 (4): 44-49. doi:<https://doi.org/10.2118/0415-0044-JPT>.
- Jhaveri, B. S. and G. K. Youngren. 1988. "Three-parameter Modification of the Peng-Robinson Equation of State to Improve Volumetric Predictions." *SPE Reservoir Engineering* 3 (03): 1-033. doi:<https://doi.org/10.2118/13118-PA>.
- Jin, L., J. A. Sorensen, S. B. Hawthorne et al. 2013. "Improving Oil Recovery by Use of Carbon Dioxide in the Bakken Unconventional System: A Laboratory Investigation." *SPE Res. Eval & Eng.* 20 (3): 602-612. doi:<https://doi.org/10.2118/178948-PA>.
- Kam, P., M. Nadeemm, A. Novlesky et al. 2015. "Reservoir Characterization and History Matching of the Horn River Shale: An Integrated Geoscience and Reservoir-Simulation Approach." *Journal of Canadian Petroleum Technology* 54 (6): 475-488. doi:<http://dx.doi.org/10.2118/171611-PA>.
- Kazemi, H., L. S. Merrill Jr., K. L. Porterfield et al. 1976. "Numerical Simulation of Water-Oil Flow in Naturally Fractured Reservoirs." *SPE Journal* 16 (6): 317-326. doi:<https://doi.org/10.2118/5719-PA>.
- King, G. E. 2010. "Thirty Years of Gas Shale Fracturing: What Have We Learned?" *SPE Annual Technical Conference and Exhibition*. Sep. 19-22, Florence, Italy. SPE-133456-MS. doi:<http://dx.doi.org/10.2118/133456-MS>.
- King, M. J., Z. Wang and A. Datta-Gupta. 2016. "Asymptotic Solutions of the Diffusivity Equation and Their Applications." *SPE Europec featured at 78th EAGE Conference and Exhibition*. 30 May-2 June, Vienna, Austria. SPE-180149-MS. doi:<https://doi.org/10.2118/180149-MS>.
- Kline, M. and I. W. Kay. 1965. *Electromagnetic Theory and Geometrical Optics*. New York: John Wiley. ISBN 978-0882757391.

- Kuchuk, F. J. and T. Habashy. 1992. "Pressure Behavior of Laterally Composite Reservoirs." *SPE Formation Evaluation* 12 (1): 47-56. doi:<https://doi.org/10.2118/24678-PA>.
- Kulkarni, K. N., A. Datta-Gupta and D. W. Vasco. 2001. "A Streamline Approach for Integrating Transient Pressure Data into High Resolution Reservoir Models." *SPE Journal* 6 (3): 273-282. doi:<https://doi.org/10.2118/74135-PA>.
- Lee, J. W. 1982. *Well Testing*. SPE Textbook Series Vol. 1. Richardson: Society of Petroleum Engineers. ISBN 978-0895203175.
- Lee, J. W., J. B. Rollins, and J. P. Spivey. 2003. *Pressure Transient Testing*. SPE Textbook Series Vol. 9. Richardson: Society of Petroleum Engineers. ISBN 978-1555630997.
- Li, C. 2018. *Application of the Fast Marching Method to Reservoir Characterization and Pressure Transient Analysis in Structured and Corner Point Grid Geometries*. Ph.D Dissertation, College Station, Texas: Texas A&M University.
- Lindsay, G., G. Miller, T. Xu et al. 2018. "Production Performance of Infill Horizontal Wells vs. Pre-Existing Wells in the Major US Unconventional Basins." *SPE Hydraulic Fracturing Technology Conference and Exhibition*. Jan. 23-25, The Woodlands, TX. SPE-189875-MS. doi:<https://doi.org/10.2118/189875-MS>.
- Lohrenz, J., B. G. Bray and C. R. Clark. 1964. "Calculating Viscosities of Reservoir Fluids from Their Compositions." *Journal of Petroleum Technology* 16 (10): 1-171. doi:<https://doi.org/10.2118/915-PA>.
- Marongiu-Porcu, M., D. Lee, D. Shan et al. 2016. "Advanced Modeling of Interwell Fracturing Interference: An Eagle Ford Shale Oil Study." *SPE Journal*. 21 (5). doi:<https://doi.org/10.2118/174902-PA>.
- Mason, J. 2012. "Oil Production Potential of the North Dakota Bakken." *Oil & Gas Journal* 110 (4).
- Matthews, C. S. and D. G. Russell. 1967. *Pressure Buildup and Flow Tests in Wells*. Vol. 1. Dallas, TX: Society of Petroleum Engineers of AIME. ISBN 978-0895202000.
- McKay, M. D., R. J. Beckman and W. J. Conover. 1979. "Comparison of Three Methods for Selecting Values of Input Variables in the Analysis of Output from a Computer Code." *Technometrics* 21 (2): 239-245. doi:<https://doi.org/10.1080/00401706.1979.10489755>.

- Miller, G., G. Lindsay, J. Baihly et al. 2016. "Parent Well Refracturing: Economic Safety Nets in an Uneconomic Market." *SPE Low Perm Symposium*. May 5-6. Denver, CO. SPE-180200-MS. doi:<https://doi.org/10.2118/180200-MS>.
- Monteagudo, J. E. and A. Firoozabadi. 2004. "Control-volume Method for Numerical Simulation of Two-phase Immiscible Flow in Two-and Three-dimensional Discrete-fractured Media." *Water Resources Research* 40 (7). doi:<https://doi.org/10.1029/2003WR002996>.
- Najabaei, B., R. T. Johns and L. Chu. 2013. "Effect of Capillary Pressure on Phase Behavior in Tight Rocks and Shales." *SPE Res. Eval & Eng.* 16 (3): August, 281-289. doi:<http://dx.doi.org/10.2118/159258-PA>.
- Noorishad, J. and M. Mehran. 1982. "An Upstream Finite Element Method for Solution of Transient Transport Equation in Fractured Porous Media." *Water Resources Research* 18 (3): 588-596. doi:<https://doi.org/10.1029/WR018i003p00588>.
- Novlesky, A., A. Kumar and S. Merkle. 2011. "Shale Gas Modeling Workflow: From Microseismic to Simulation – A Horn River Case Study." *Canadian Unconventional Resources Conference*. Nov. 15-17, Calgary, Alberta, Canada. SPE-148710-MS. doi:<http://dx.doi.org/10.2118/148710-MS>.
- Offenberger, R., N. Ball, K. Kousic et al. 2013. "Integration of Natural and Hydraulic Fracture Network Modeling with Reservoir Simulation for an Eagle Ford Well." *Unconventional Resources Technology Conference*. Aug. 12-14, Denver, CO. URTEC-1563066-MS.
- Oliver, D. 1994. "Application of a Wave Transform to Pressure Transient Testing in Porous Media." *Transport in Porous Media* 16 (3): 209-236. doi:<https://doi.org/10.1007/BF00617148>.
- Peng, D. and D. B. Robinson. 1976. "A New Two-constant Equation of State." *Industrial & Engineering Chemistry Fundamentals* 15 (1): 59-64.
- Pierce, A. 1986. "Wave Methods for an Inverse Problem in Diffusion." *Inverse Problems* 2: 205-217. doi: <https://doi.org/10.1088/0266-5611/2/2/011>.
- Pollock, D. W. 1988. "Semianalytical Computation of Path Lines for Finite-difference Models." *Groundwater* 26 (6): 743-750. doi:<https://doi.org/10.1111/j.1745-6584.1988.tb00425.x>.
- Rafiee, M. and T. Grover. 2017. "Well Spacing Optimization in Eagle Ford Shale: An Operator's Experience." *Unconventional Resources Technology Conference*. Jul. 24-26, Austin, TX. URTEC-2695433-MS. doi:<https://doi.org/10.15530/URTEC-2017-2695433>.

- Raghavan, R. and L. Y. Chin. 2002. "Productivity Changes in Reservoirs With Stress-Dependent Permeability." *SPE Annual Technical Conference and Exhibition*. Sep. 29- Oct. 2, San Antonio, TX. SPE-77535-MS. doi:<https://doi.org/10.2118/77535-MS>.
- Ranjan, P. 2015. "Harvesting Reserves with a Balanced Portfolio can Reduce Breakeven Points of Unconventional Assets." *Second Unconventional Revolution, white paper from Halliburton*.
- Rassenfoss, S. 2017. "Shale EOR Works, But Will It Make a Difference?" *Journal of Petroleum Technology* 69 (10): 34-40. doi:<https://doi.org/10.2118/1017-0034-JPT>.
- Robinson, D. B. and D. Peng. 1978. *The Characterization of the Heptanes and Heavier Fractions for the GPA Peng-Robinson Programs*. Denver: Gas processors association.
- Rodionov, Y., C. Defeu, K. Gakhar et al. 2017. "Optimization of Infill Well Development Using a Novel Far-Field Diversion Technique in the Eagle Ford Shale." *SPE/AAPG/SEG Unconventional Resources Technology Conference*. Jul. 24-26, Austin, TX. URTEC-2670497-MS. doi:<https://doi.org/10.15530/URTEC-2017-2670497>.
- Schmidt, M. and B. K. Sekar. 2014. "Innovative Unconventional EOR-A Light EOR an Unconventional Tertiary Recovery Approach to an Unconventional Bakken Reservoir in Southeast Saskatchewan." *21st World Petroleum Congress*. Jun. 15-19, Moscow, Russia. WPC-21-1921.
- Schneider, W. A. 1995. "Robust and Efficient Upwind Finite-Difference Traveltime Calculations in Three Dimensions." *Geophysics* 60 (4): 1108-1117. doi:<https://doi.org/10.1190/1.1443839>.
- Sethian, J. A. 1996. "A Fast Marching Level Set Method for Monotonically Advancing Front." *Proc. Natl. Acad. Sci. USA* 93 (4): 1591-1595. doi:<https://doi.org/10.1073/pnas.93.4.1591>.
- Sethian, J. A. 1999. "Fast Marching Methods." *SIAM Rev* 41 (2): 199-235. doi:<http://dx.doi.org/10.1137/S0036144598347059>.
- Sethian, J. A. 2002. "Fast Algorithms for Optimal Control, Anisotropic Front Propagation and Multiple Arrivals." *International Congress Mathematicians*, Aug. 20-28, Beijing, China.

- Sethian, J. A. and A. M. Popovici. 1999. "3-D Traveltime Computation Using the Fast Marching Method." *Geophysics* 64 (2): 516-523. doi: <https://doi.org/10.1190/1.1444558>.
- Shahvali, M., B. Mallison, K. Wei et al. 2012. "An Alternative to Streamlines for Flow Diagnostics on Structured and Unstructured Grids." *SPE Journal*. 17 (3): 768-778. doi:<https://doi.org/10.2118/146446-PA>.
- Smith, R. 1981. "The Early Stages of Contaminant Dispersion in Shear Flows." *Journal of Fluid Mechanics* 111: 107-122. Doi:<https://doi.org/10.1017/S0022112081002310>.
- Song, B. and A. C. Ehlig-Economides. 2011. "Rate-normalized Pressure Analysis for Determination of Shale Gas Well Performance." *North American Unconventional Gas Conference and Exhibition*. Jun. 14-16, The Woodland, TX. SPE-144031-MS. doi:<https://doi.org/10.2118/144031-MS>.
- Sun, J., A. Zou and D. Schechter. 2016. "Experimental and Numerical Studies of CO₂ EOR in Unconventional Liquid Reservoirs with Complex Fracture Networks." *SPE Improved Oil Recovery Conference*. Apr. 11-13, Tulsa, OK. SPE-179634-MS. doi:<https://doi.org/10.2118/179634-MS>.
- Tabatabaie, S. H. and M. Pooladi-Darvish. 2016. "Multiphase Linear Flow in Tight Oil Reservoirs." *SPE Res. Eval. & Eng.* 20 (1): 1-13. Doi:<http://dx.doi.org/10.2118/180932-PA>.
- Todd, H. B. and J. G. Evans. 2016. "Improved Oil Recovery IOR Pilot Projects in the Bakken Formation." *SPE Low Perm Symposium*. May. 5-6, Denver, CO. SPE-180270-MS. doi:<https://doi.org/10.2118/180270-MS>.
- Um, J. and C. Thurber. 1987. "A Fast Algorithm for Two-point Seismic Ray Tracing." *Bulletin of the Seismological Society of America* 77 (3): 972-986.
- Valko, P. P. 2009. "Assigning Value to Stimulation in the Barnett Shale: a Simultaneous Analysis of 7000 plus Production Histories and Well Completion Records." *SPE Hydraulic Fracturing Technology Conference*. Jan. 19-21, The Woodlands, TX. SPE 119369. doi:<http://dx.doi.org/10.2118/119369-MS>.
- Van Trier, J. and W. W. Symes. 1991. "Upwind Finite-Difference Calculation of Traveltimes." *Geophysics* 56 (6): 812-821. doi:<https://doi.org/10.1190/1.1443099>.
- Vasco, D. W. 2008. "Modelling Quasi-static Poroelastic Propagation Using an Asymptotic Approach." *Geophys. J. Int.* 173 (3): 1119-1135. doi:<https://doi.org/10.1111/j.1365-246X.2008.03758.x>.

- Vasco, D. W. 2009. "Modelling Broad-band Poroelastic Propagation Using an Asymptotic Approach." *Geophys. J. Int.* 179: 299-318. doi:<https://doi.org/10.1111/j.1365-246X.2009.04263.x>.
- Vasco, D. W. 2011. "On the Propagation of a Coupled Saturation and Pressure Front." *Water Resources Research* 47 (3). doi:<https://doi.org/10.1029/2010WR009740>.
- Vasco, D. W. and A. Datta-Gupta. 1999. "Asymptotic Solutions for Solute Transport: A Formalism for Tracer Tomography." *Water Resources Research* 35 (1): 1-16. doi:<https://doi.org/10.1029/98WR02742>.
- Vasco, D. W. and A. Datta-Gupta. 2001. "Asymptotics, Saturation Fronts, and High Resolution Reservoir Characterization." *Transport in Porous Media* 42 (3): 315-350. doi:<https://doi.org/10.1023/A:1006788413831>.
- Vasco, D. W. and A. Datta-Gupta. 2016. *Subsurface Fluid Flow and Imaging: Application for Hydrology, Reservoir Engineering and Geophysics*. Cambridge: Cambridge University Press. ISBN 978-0521516334.
- Vasco, D. W. and S. Finsterle. 2004. "Numerical Trajectory Calculations for the Efficient Inversion of Transient Flow and Tracer Observations." *Water Resources Research* 40 (1). doi:<https://doi.org/10.1029/2003WR002362>.
- Vasco, D. W., H. Keers and K. Karasaki. 2000. "Estimation of Reservoir Properties Using Transient Pressure Data: An Asymptotic Approach." *Water Resources Research* 36 (12): 344-3465. doi:<https://doi.org/10.1029/2000WR900179>.
- Vidale, J. 1988. "Finite-Difference Calculation of Travel Times." *Bulletin of the Seismological Society of America* 78 (6): 2062-2076.
- Vidale, J. 1990. "Finite-Difference Calculation of Traveltimes in Three Dimensions." *Geophysics* 55 (5): 521-526. doi:<https://doi.org/10.1190/1.1442863>.
- Vincent, M. C. 2012. "The Next Opportunity To Improve Hydraulic-Fracture Stimulation." *JPT* 64 (3): 118-127. doi:<https://doi.org/10.2118/144702-JPT>.
- Virieux, J., C. Flores-Luna and D. Gibert. 1994. "Asymptotic Theory For Diffusive Electromagnetic Imaging." *Geophysical Journal International* 119 (3): 857-868. doi:<https://doi.org/10.1111/j.1365-246X.1994.tb04022.x>.
- Wan, T. and J. Sheng. 2015. "Compositional Modelling of the Diffusion Effect on EOR Process in Fractured Shale-Oil Reservoirs by Gasflooding." *Journal of Canadian Petroleum Technology* 54 (2): 107-115. doi:<https://doi.org/10.2118/2014-1891403-PA>.

- Wang, H. Y. 2017. "What Factors Control Shale-Gas Production and Production-Decline Trend in Fractured Systems: A Comprehensive Analysis and Investigation." *SPE Journal* 22 (2): 562-581. doi:<https://doi.org/10.2118/179967-PA>.
- Wang, L., A. Torres, L. Xiang et al. 2015. "A Technical Review on Shale Gas Production and Unconventional Reservoirs Modeling." *Natural Resources* 6 (3): 141-151. doi:<https://doi.org/10.4236/nr.2015.63013>.
- Wang, Z. 2018. *Asymptotic Solutions to the Diffusivity Equation: Validation and Field Applications*. College Station. Ph.D Dissertation, College Station, Texas: Texas A&M University.
- Warren, J. E. and P. J. Root. 1963. "The Behavior of Naturally Fractured Reservoirs." *SPE Journal* 3 (03): 245-255. doi:<https://doi.org/10.2118/426-PA>.
- Wilson, W. J. 1983. "An Inverse Scattering Approach to the Pressure Transient Analysis of Petroleum Reservoirs." In *Conference on Inverse Scattering: Theory and Application*, by J. B. Bednar, R. Redner, E. Robinson and A. Weglein, 170-180. Philadelphia: Soc. Indust. Appl. Math.
- Xie, J., C. Yang, N. Gupta et al. 2015a. "Integration of Shale-Gas-Production Data and Microseismic for Fracture and Reservoir Properties With the Fast Marching Method." *SPE Journal* 20 (2): 347-359. doi:<https://doi.org/10.2118/161357-PA>.
- Xie, J., C. Yang, N. Gupta et al. 2015b. "Depth of Investigation and Depletion in Unconventional Reservoirs With Fast-Marching Methods." *SPE Journal* 20 (4): 831-841. doi:<http://dx.doi.org/10.2118/154532-PA>.
- Xue, X., C. Yang, V. K. Sharma et al. 2016. "Reservoir and Fracture Flow Characterization Using a Novel $w(\tau)$ Formulation." *Unconventional Resources Technology Conference*. Aug. 1-3, San Antonio, TX. URTEC-2440083-MS. doi:<https://doi.org/10.15530/URTEC-2016-2440083>.
- Yang, C., V. K. Sharma, M. J. King et al. 2015. "A Novel Approach for Production Transient Analysis of Shale Gas/Oil Reservoirs." *Unconventional Resources Technology Conference*. Jul. 20-22, San Antonio, TX. URTEC-2176280-MS. doi:<https://doi.org/10.15530/URTEC-2015-2176280>.
- Yang, C., X. Xue, J. Huang et al. 2016. "Rapid Refracturing Candidate Selection in Shale Reservoirs Using Drainage Volume and Instantaneous Recovery Ratio." *Unconventional Resources Technology Conference*. Aug. 1-3, San Antonio, TX. URTEC-2459368-MS. doi:<https://doi.org/10.15530/URTEC-2016-2459368>.
- Yang, C., M. J. King, and A. Datta-Gupta. 2017a. "Rapid Simulation of Naturally Fractured Unconventional Reservoirs with Unstructured Grids Using the Fast

- Marching Method." *SPE Reservoir Simulation Conference*. Feb. 20-22, Montgomery, TX. SPE-182612-MS. doi:<https://doi.org/10.2118/182612-MS>.
- Yang, C., M. J. King, and A. Datta-Gupta. 2017b. "Flow Simulation of Complex Fracture Systems With Unstructured Grids Using the Fast Marching Method." *SPE/AAPG/SEG Unconventional Resources Technology Conference*. Jul. 24-26, Austin, TX. URTEC-2691393-MS. doi:<https://doi.org/10.15530/URTEC-2017-2691393>.
- Yin, J., J. Xie, A. Datta-Gupta et al. 2011. "Improved Characterization and Performance Assessment of Shale Gas Wells by Integrating Stimulated Reservoir Volume and Production Data." *SPE Eastern Regional Meeting*. Columbus, Ohio. August 17-19. SPE-148969-MS. doi:<http://dx.doi.org/10.2118/148969-MS>.
- Zhang, S. and D. Zhu. 2017. "Inversion of Downhole Temperature Measurements in Multistage Fracture Stimulation in Horizontal Wells." *SPE Annual Technical Conference and Exhibition*. Oct. 9-11. San Antonio, TX. SPE-187322-MS. doi:<https://doi.org/10.2118/187322-MS>.
- Zhang, Y., N. Bansal, Y. Fujita et al. 2016. "From Streamlines to Fast Marching: Rapid Simulation and Performance Assessment of Shale-Gas Reservoirs by Use of Diffusivity Time of Flight as a Spatial Coordinate." *SPE Journal* 21 (5): 1-16. doi:<http://dx.doi.org/10.2118/168997-PA>. doi:<https://doi.org/10.2118/168997-PA>.
- Zhang, Y., C. Yang, M. J. King et al. 2013. "Fast-Marching Methods for Complex Grids and Anisotropic Permeabilities: Application to Unconventional Reservoirs." *SPE Reservoir Simulation Symposium*. Feb. 18-20, The Woodlands, TX: SPE. SPE-163637-MS. doi:<https://doi.org/10.2118/163637-MS>.

APPENDIX A

COUPLING FMM-BASED SIMULATION WITH EXISTING RESERVOIR SIMULATOR

One of the advantage of FMM-based simulation is that it can be coupled with any existing reservoir simulators. This is because the 1-D mass/ mole conservation equations along the DTOF coordinate are basically the same as those of 1-D Cartesian coordinate, while the pore volume, transmissibility and pore volume need to be specific to the DTOF coordinate. In addition, any heterogeneity within the same τ -contour have to be averaged as shown in Table 2.2. Then, once we calculate and feed all the relevant properties defined on the 1-D DTOF coordinate to the existing reservoir simulator, the 1-D simulation can be readily performed. In this appendix, we summarize the keywords which should be specific to the 1-D FMM-based simulation in **Table A.1** through **Table A.5**. Eclipse® is assumed as a reservoir simulator to be used.

Table A.1 RUNSPEC Keywords required for FMM-based 1-D simulation

Item	Value
DIMENS	NX should be number of 1-D grid blocks. NY and NZ should be 1.

Table A.2 GRID Keywords required for FMM-based 1-D simulation

Item	Value
DX, DY, DZ	Arbitrary values can be entered. DX, DY and DZ will be unused since pore volume and transmissibility will be explicitly specified in EDIT section
PERMX, PERMY, PERMZ	Arbitrary values can be entered for fractures because PERMX, PERMY and PERZ will be unused since transmissibility and well index will be explicitly specified in EDIT and SCHEDULE sections. PERMX for matrix should be the permeability calculated by Eq. (2.64) for each 1-D grid. PERMY and PERMZ for matrix will be unused.
PORO	PORO for fracture can be arbitrary. PORO for matrix should be the averaged matrix porosity for each 1-D grid block as it will be used for bulk volume calculation that is a part of fracture/ matrix transmissibility
SIGMAV	SIGMAV should be the shape factor calculated by Eq. (2.64) for each 1-D grid.
TOPS	TOPS can be arbitrary but should be (reference depth of the well in WELSPECS) – (DZ/2)

Table A.3 EDIT Keywords required for FMM-based 1-D simulation

Item	Value
TRANX	TRANX for fracture should be calculated by (2.40). TRANX for matrix needs to be zero.
PORV	PORV should be calculated based on either (2.52) or (2.56)

Table A.4 REGIONS Keywords required for FMM-based 1-D simulation

Item	Value
SATNUM	Should be averaged value by majority vote within each τ -contours.
ROCKNUM	Should be averaged value by majority vote within each τ -contours.
PVTNUM	Should be averaged value by majority vote within each τ -contours.
EOSNUM	Should be averaged value by majority vote within each τ -contours.

Table A.5 SCHEDULE Keywords required for FMM-based 1-D simulation

Item	Value
WELSPECS	Well head location should be the first cell of 1-D grid. BHP reference depth needs to be consistent with the original data.
COMPDAT	Completion location should be the first cell of 1-D grid. Well connection factor (well index) should be calculated by Eq. (2.51). Well diameter can be arbitrary as it will be unused due to explicitly assigned well connection factor.

APPENDIX B

FMM-BASED SIMULATION FOR RESERVOIRS WITH MULTIPLE ROCK TYPES ACROSS DTOF CONTOURS

In Chapter II, we discussed limitations of the FMM-based multi-phase simulation using the cases of gas liberation and waterflooding. In this appendix, we further present special cases involving multiple rock types with extremely different relative permeability or rock compaction. The first case is an example that is beyond the capability of the FMM-based simulation, and the second case requires the frequent DTOF updates.

B.1 Waterflooding in Reservoirs with Multiple Rock Types

When pressures and saturations are mapped back from the 1-D to the original 3-D grid blocks, we accordingly update the compressibility, viscosity, relative permeability and compaction (pressure-dependent pore volume and transmissibility) on grid-by-grid basis. If there exist multiple rock types of which distributions are not aligned with the initial DTOF contours, diffusivity changes will have spatial variation, leading to changes in the DTOF geometry. In this section, we present a waterflooding example in reservoirs with multiple rock types to illustrate how the FMM-based simulation works in such cases.

B.1.1 Case Setting

We set up the 2-D reservoir model as summarized in **Table B.1**. Two rock types that have extremely different water relative permeability are defined as illustrated in

Figure B.1. The rock type #1 (blue) allows little water movement and diffusivity remains almost constant until water saturation reaches approximately 0.45. On the other hand, water phase can easily move in the rock type #2 (red) and diffusivity (mobility) significantly increases as water saturation increase. However, the initial DTOF (depicted by white lines on the center) only reflects the spatial heterogeneity of absolute permeability and is not affected by rock types since the initial water saturation is homogeneous and equal to immobile saturation (0.3). Once we start water injection from the center, it is expected that the injected water preferably goes through the rock type #1 as it increases mobility, leading to change in the DTOF geometry.

Table B.1 Input data for waterflooding example with multiple rock types

Item	Value
Model size (ft ³)	30,000'×30,000'×10'
Grid block dimension	155×155×1 (24025)
Size of Area of Interest (Aoi) (ft ³)	10,100'×10,100'×10'
Grid block dimension of Aoi	101×101×1
Permeability (mD)	50 (rock type #1) & 100 (rock type #2)
Porosity	0.046
Initial water saturation (immobile)	0.30
Rock compressibility (psi ⁻¹)	1.0×10 ⁻⁶
Water compressibility (psi ⁻¹)	1.0×10 ⁻⁶
Water viscosity	0.152
Initial oil compressibility (psi ⁻¹)	1.5×10 ⁻⁵
Initial oil viscosity (cp)	1.52
Initial pressure (psi)	3,000
Water injection rate (stbw/d)	500

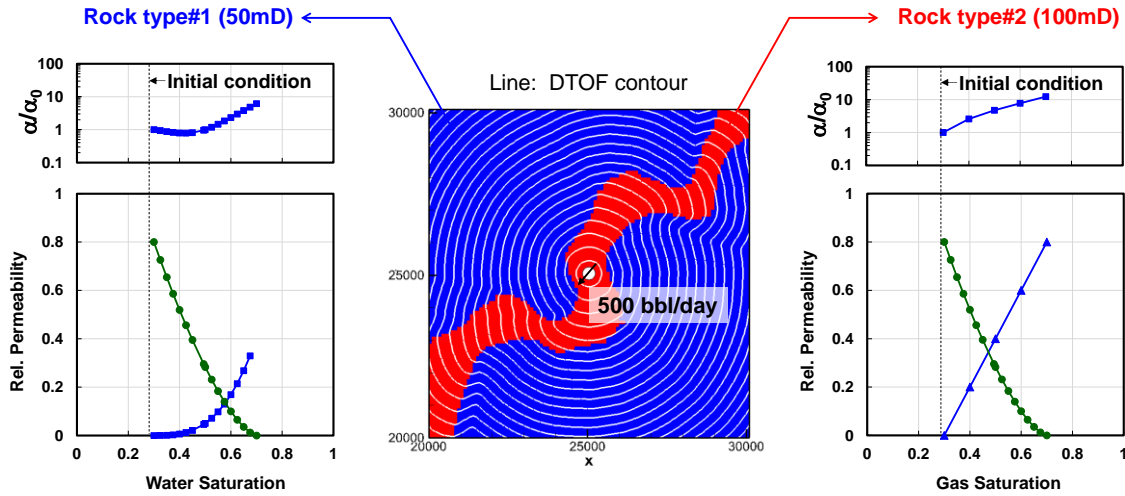


Figure B.1 Rock type distribution (center), DTOF contour (lines on the center plot) and associated relative permeabilities and diffusivity (left and right)

B.1.2 Pressure, Saturation and Diffusivity from Finite Difference Simulation

We first run the FDSim to see how pressure and saturation evolve in such reservoirs with multiple rock types. **Figure B.2** shows frontal arrival times of pressure and saturation from the FDSim (Vasco, 2011). Obviously, the early arrival of the saturation front is observed along the rock type #2 (Figure B.2b) due to the contrast in the mobility increase between two rock types, whereas the pressure arrival is less sensitive to it. The cross-plot of arrival times of pressure and saturation (Figure B.2c) shows two distinct trends between two rock types. It indicates that there will be significant variation in saturation within each DTOF contour.

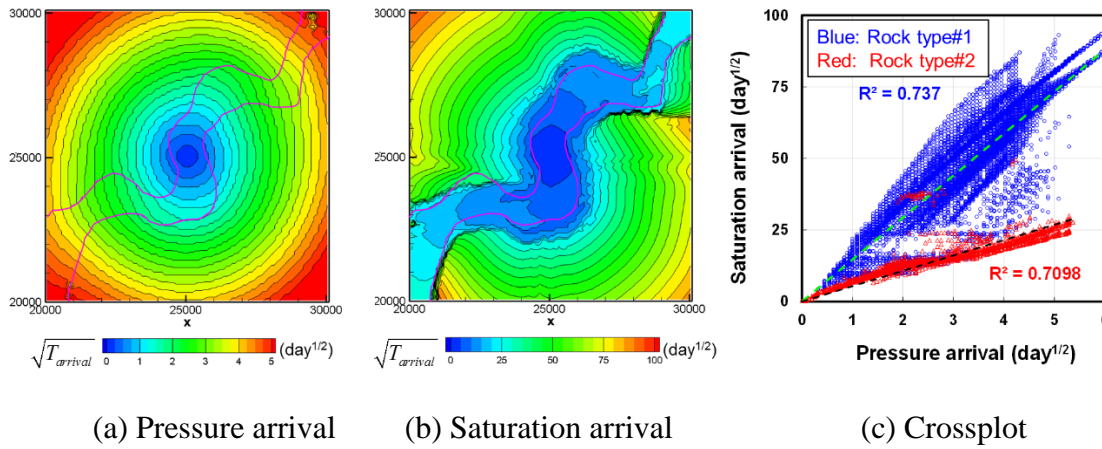
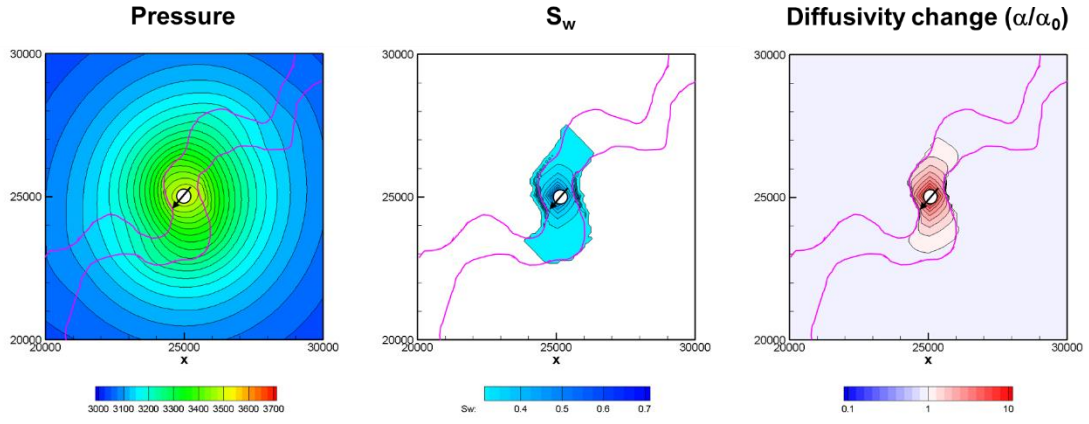
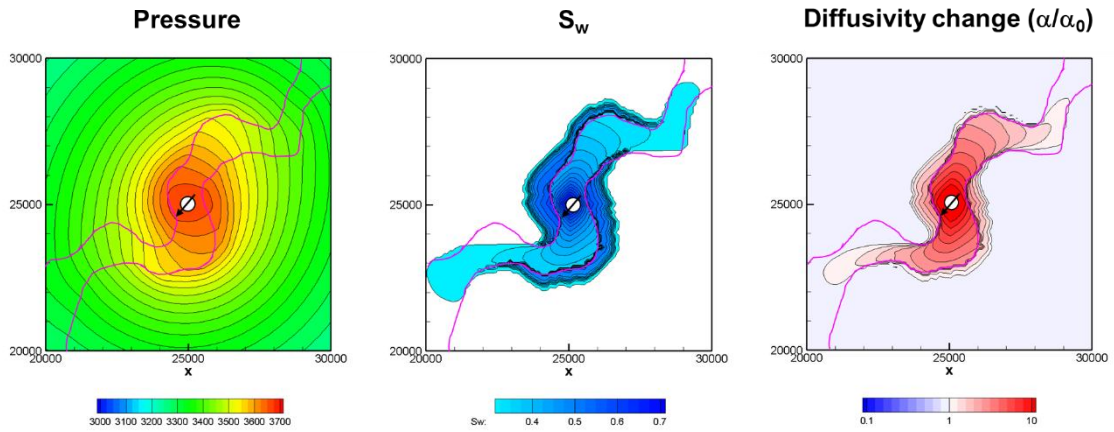


Figure B.2 Front arrival of pressure and saturation in 2-D reservoir with multiplerock types

Figure B.3 shows the maps of pressure, saturation and diffusivity change from the FDSim at 40 and 400 days. It is observed that evolution of water saturation and changes in diffusivity take place selectively along the rock type #2. On the other hand, changes in the geometry of pressure contours are less sensitive to the underlying rock type as we can see little or slight changes between Figure B.3a and 3b. Thus, saturation contours are not well aligned with pressure contours in this case, indicating that this can be beyond the assumption of the FMM-based multi-phase simulation.



(a) 40 days



(b) 400 days

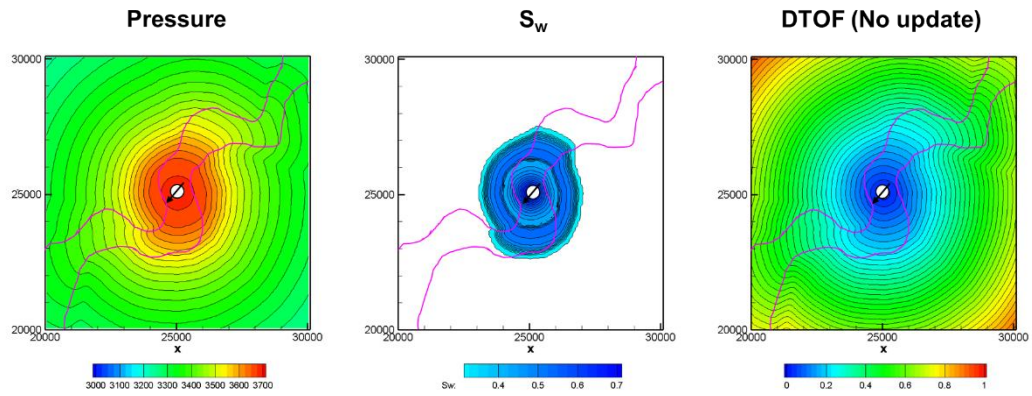
Figure B.3 Pressure, saturation and diffusivity change from FDSim in 2-D reservoir with multiple rock types

B.1.3 FMM-based Simulation

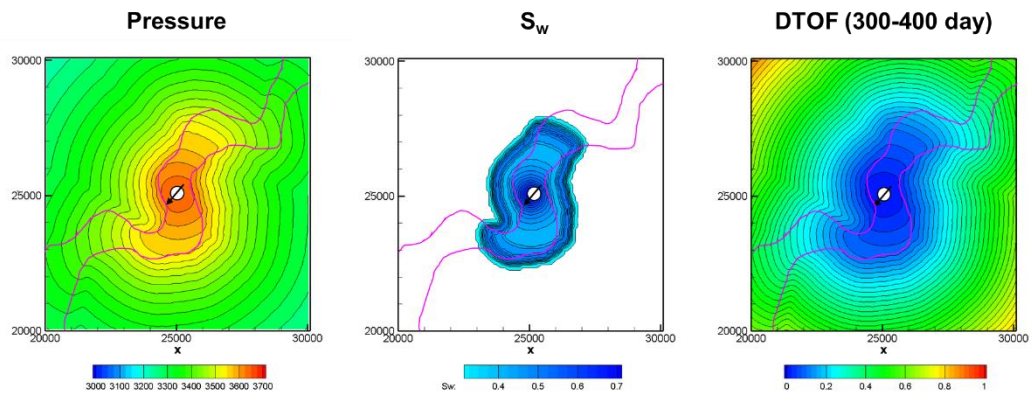
Based on the above observation, it is obvious that the initial DTOF contour, which is independent from diffusivity changes expected in the simulation, cannot represent

saturation contours in this case. Therefore, we tested updating the DTOF during the FMM-based simulation to honor the diffusivity changes.

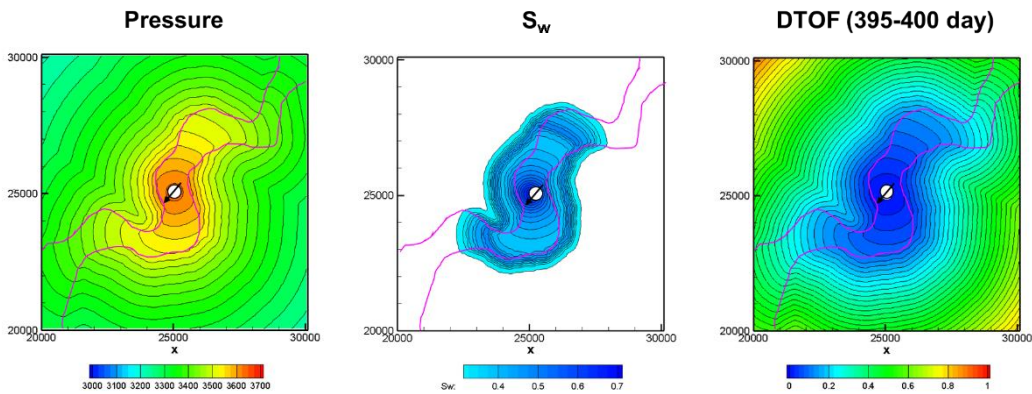
For simulating water injection for 400 days, three different frequencies of the DTOF update were examined: (a) no update, (b) update every 100 days and (c) update every 5 days. **Figure B.4** illustrates the maps of pressure, saturation and DTOF at 400 days from the FMM-based simulations. Compared to the ones from the FDSim (Figure B.3b), no update case shows good matching in pressure but not in saturation (Figure B.4a). On the other hand, updating the DTOF every 100 days changes the geometry of the DTOF contour from the initial map, resulting in the pressure and saturation contours to elongate along the rock type #2 (Figure B.4b). The more frequent update yields more elongation of the DTOF contour as seen in Figure B.4c. Thus, in this particular example, updating the DTOF leads to the improved matching in terms of saturation, but it also results in deviation in pressure compared to the FDSim. Although the FMM-based simulation might be able to capture some sort of averaged trends of both pressure and saturation by updating the DTOF, there is a trade-off between the pressure matching and saturation matching. Thus, it may be beyond the capability of the FMM-based approach if multiple rock types with extremely different relative permeability are lying across the DTOF contours.



(a) No DTOF update



(b) DTOF update every 100 day



(c) DTOF update every 5 days

Figure B.4 Pressure, saturation and diffusivity change at 400 days from FMM-based simulation in 2-D reservoir with multiple rock types

B.2 Injection into Stress-sensitive Layer

In the above example, we discussed the multiple rock types across the DOF contour in terms of extremely different relative permeability. The transmissibility reduction due to the compaction i.e. pressure-dependent permeability is another example that may require the DTOF update during the FMM-based simulation.

It should be noted that we presented a case with different compaction tables defined for hydraulic and natural fractures in Chapters II and III, indicating little or no necessity to update the DTOF. This is because the rock type distribution i.e. hydraulic fractures and natural fractures was aligned with the DTOF contours in those examples. In other words, original grid blocks lying within each DTOF contour had almost uniform rock types. Therefore, it did not significantly change the geometry of DTOF contours during the FMM-based simulation.

Here, we will discuss the case where rock types with different compaction tables are distributed across the initial DTOF contour. The stress-sensitive layer is one example of such cases.

B.2.1 Case Setting

We set up a 2-D cross-sectional reservoir model as summarized in **Table B.2**. Two rock types are defined as illustrated in **Figure B.5**: the middle zone have extreme increase in transmissibility as per pressure increase and the others have no pressure dependency in transmissibility. A vertical injector is completed for the whole thickness of the middle zone and constrained with the constant rate of 50 stb/day. At the initial condition,

permeability is uniform, and the resulting DTOF contour is illustrated in the bottom of Figure B.5. Once the water injection is started, we expect that the permeability increases selectively in the middle zone, and the DTOF contour will keep elongating along the middle zone.

Table B.2 Input data for water injection example with multiple compaction tables

Item	Value
Model size (ft ³)	4,100'×100'×820'
Grid block dimension	41×41×1 (1681)
Permeability (mD)	0.01
Porosity	0.30
Initial water saturation (immobile)	0.0
Rock compressibility (psi ⁻¹)	1.0×10 ⁻⁵
Oil compressibility (psi ⁻¹)	1.0×10 ⁻⁵
Water compressibility (psi ⁻¹)	1.0×10 ⁻⁶
Water viscosity	0.5
Oil viscosity (cp)	0.5
Initial pressure (psi)	3,000
Water injection rate (stbw/d)	100

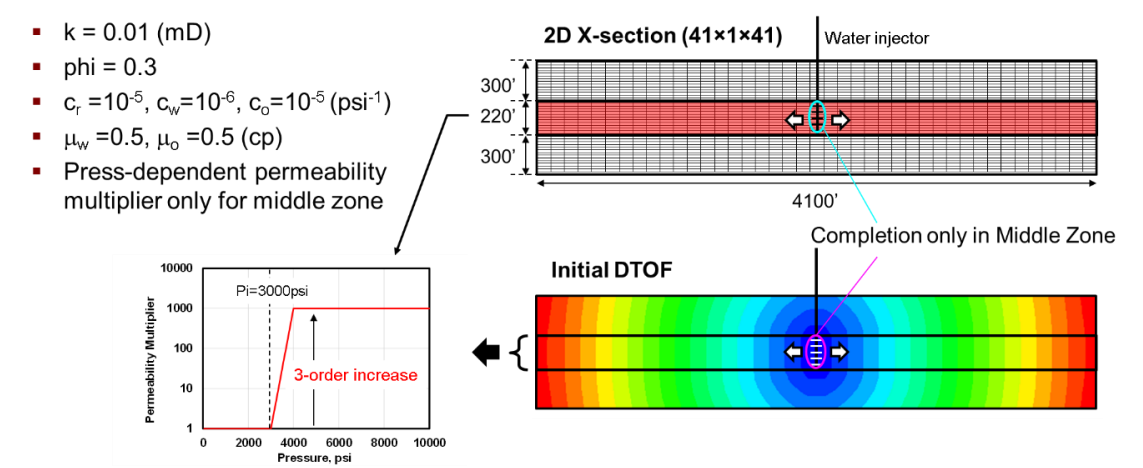


Figure B.5 Illustration of 2-D cross-sectional model for water injection into stress-sensitive layer

B.2.2 Simulation Results

We compared simulation results for 2,000 days injection between FDSim and FMM-based simulation where we tested three different frequency of updating the DTOF: (1) no update, (2) every 250 days and (3) every 100 days. **Figure B.6** and **Figure B.7** show comparisons of the simulated bottomhole pressure and the maps of pressure and saturation, respectively. Obviously, the FMM-based simulation with no DTOF update shows significant deviation from the FDSim because the permeability increase is limited only around the well. On the other hand, updating the DTOF shows excellent agreement in the bottomhole pressure with the FDSim. Pressure and saturation contours in Figure B.7 shows that the higher frequency of DTOF update yields the closer matching with the FDSim.

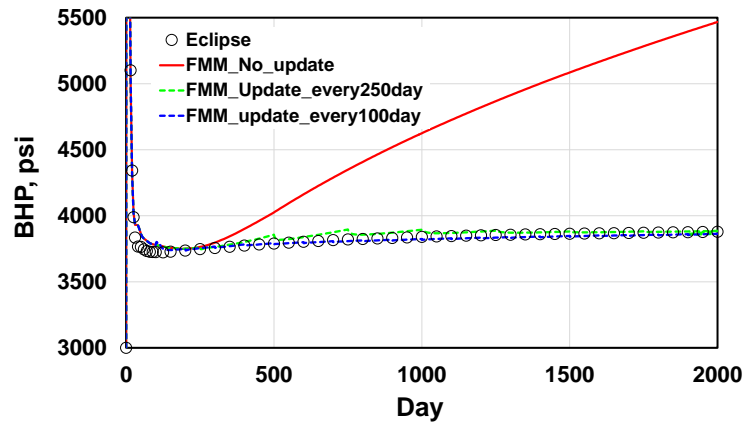
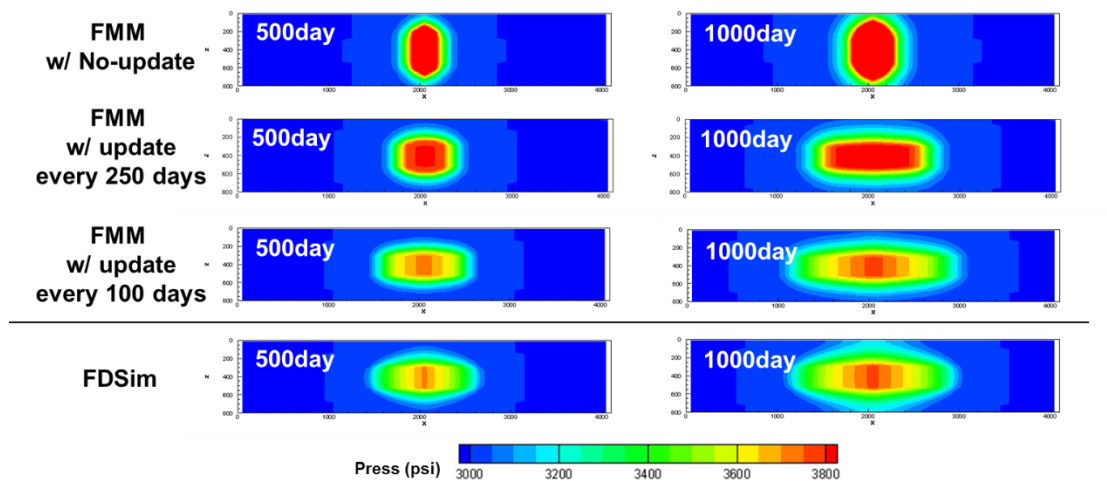
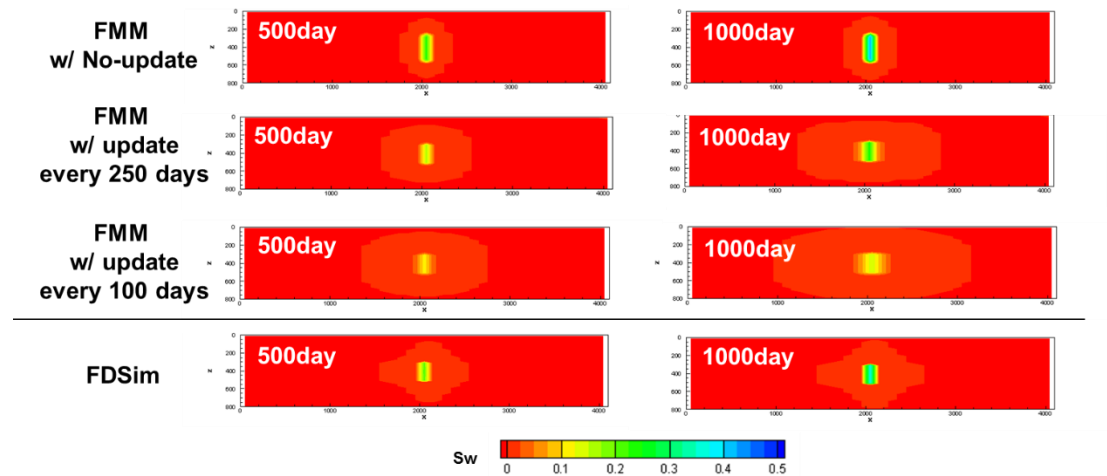


Figure B.6 Simulated injection pressure for water injection into stress-sensitive layer



(a) Pressure



(b) Saturation

Figure B.7 Pressure and saturation maps at 500 and 1000 days for water injection into stress-sensitive layer

Thus, it is effective to update the DTOF to better capture pressure and saturation profiles in the reservoir with multiple compaction tables lying across the DTOF contour. The difference from the previous example, multiple relative permeability tables, is that

diffusivity changes in this case are dominantly associated with pressure changes rather than saturation changes. Since the DTOF is a representation of the pressure wave propagation, the FMM-based simulation can provide reasonable approximation for such cases where the pressure change is a dominant process for fluid flow and reservoir dynamics.

B.3 Summary

In this appendix, we discussed the validity to use the DTOF as a spatial coordinate for special cases that have multiple rock types across the DTOF contour:

- If multiple rock types with extremely different relative permeability lie across the DTOF contour, saturation contours can be significantly different from pressure contours, which may violate the assumption of the FMM-based simulation. Updating the DTOF indeed helps better capture the evolution of saturation, however, it results in less accuracy in pressure calculation.
- Multiple rock types with extremely different compaction tables lying across the DTOF contour can be reasonably modeled in the FMM-based simulation by updating the DTOF. It indicates that the DTOF can still be a valid spatial coordinate in cases where the diffusivity changes are mainly associated with the pressure changes, which is different from the cases with multiple relative permeability tables.

APPENDIX C

MAP-BACK 1-D SOLUTIONS ONTO ORIGINAL GRID BASED ON MASS CONSERVATION

The FMM-based simulation solves pressure, saturation and composition on the 1-D DTOF coordinate. As we have seen thus far, there are several situations that require mapping back the 1-D solution onto the original grid block system:

- Visualizing pressure, saturation and composition changes in the physical space
- Updating the DTOF contours because of the dynamic diffusivity changes
- Updating the DTOF contours to simulate infill wells

We will discuss two different methods to map back the 1-D solutions onto the original grid block system:

1. Interpolation map-back based on the grid block DTOF
2. Material balance-based map-back

C.1 Interpolation map-back

This method is fairly simple and straight forward. Prior to the 1-D simulation, the DTOF values have been assigned onto every grid block as solutions of the Eikonal equation. On the other hand, the FMM-based 1-D simulation provides us with pressure, saturation and composition solutions as functions of the DTOF. Thus, we can approximate the pressure, saturation and composition on the original grid blocks by interpolating the

1-D solutions based on the DTOF value assigned to the original grid blocks (**Figure C.1**). However, this method does not guarantee the mass conservation before and after the map-back.

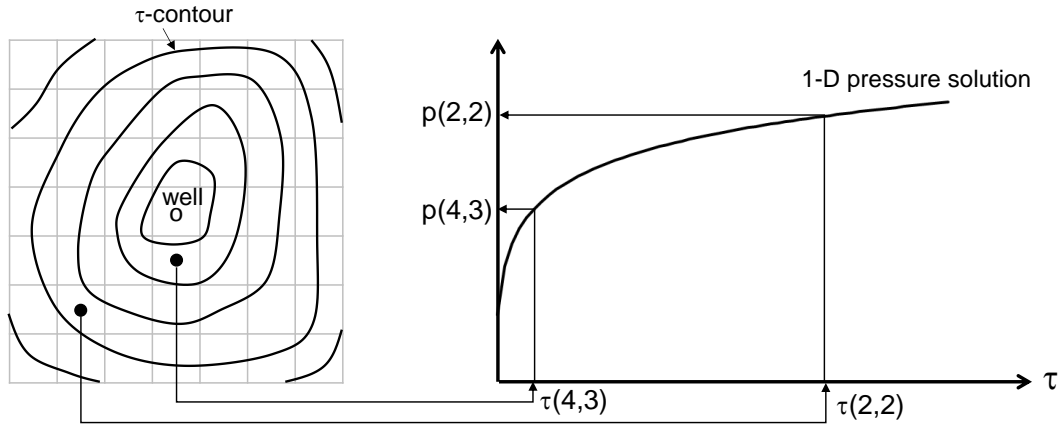


Figure C.1 Illustration of the interpolation map-back

C.2 Material Balance-based Map-back

The alternative approach is to honor the material balance but requires extra computation. Let us consider the three-phase blackoil simulation where the solutions to be mapped back are p , S_w , S_g and R_s .

The key idea of this method is to reallocate the pressure and fluid volumes in the 1-D grids onto original grid blocks. **Figure C.2** illustrates the τ -contours and underlying original grid blocks, indicating that the pore volume of each τ -contour consists of contributions of multiple grid blocks in the original grid system. Conversely, one original grid block can lie across the multiple τ -contours.

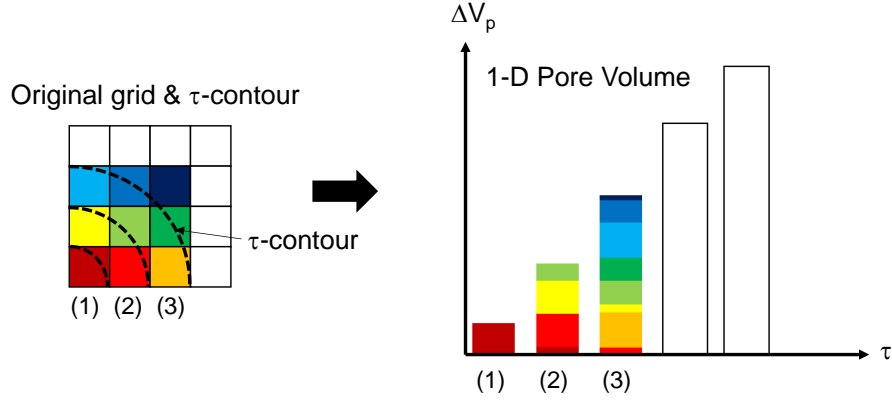


Figure C.2 Illustration of pore volumes of original grid blocks lying in each t-contour

Fortunately, we can record how much percentages of the pore volume of each grid lie in each τ -contour when we compute $V_p(\tau)$ by Eq. (2.56) where the 27pt-stencil FMM is incorporated. Thus, we will use the pore volume as a weight for the reallocation in order to honor the material balance. We can write down the relationship between pore volumes of 1-D grids and original grids by introducing the weight matrix \mathbf{w} :

$$\begin{bmatrix} \Delta V_{p,1} \\ \Delta V_{p,2} \\ \vdots \\ \Delta V_{p,N} \end{bmatrix} = \begin{bmatrix} w_{1,1} & w_{1,2} & \cdots & w_{1,n\tau} \\ w_{2,1} & w_{2,2} & & w_{2,n\tau} \\ \vdots & & \ddots & \vdots \\ w_{N,1} & w_{N,2} & \cdots & w_{N,n\tau} \end{bmatrix} \begin{bmatrix} \Delta V_p(\tau_1) \\ \Delta V_p(\tau_2) \\ \vdots \\ \Delta V_p(\tau_{n\tau}) \end{bmatrix}, \quad (\text{C.1})$$

where n_τ and N are number of grid blocks of the 1-D DTOF grid and the original grid, respectively. The weight $w_{i,j}$ represents the fraction of pore volume of grid block i which is included in j^{th} τ -contour subject to:

$$\sum_j^{n_\tau} w_{i,j} = 1 \text{ for } i=1,\dots,N, \quad (\text{C.2})$$

The pore volume weighted pressure (psi×rbbl), water volume (rbbl) and gas volume (rbbl) on original grid blocks can be computed with the 1-D solutions using following formulations:

$$\begin{bmatrix} \Delta V_{p,1} p_1 \\ \Delta V_{p,2} p_2 \\ \vdots \\ \Delta V_{p,N} p_N \end{bmatrix} = \begin{bmatrix} w_{1,1} & w_{1,2} & \dots & w_{1,n_\tau} \\ w_{2,1} & w_{2,2} & & w_{2,n_\tau} \\ \vdots & & \ddots & \vdots \\ w_{N,1} & w_{N,2} & \dots & w_{N,n_\tau} \end{bmatrix} \begin{bmatrix} \Delta V_p(\tau_1) p(\tau_1) \\ \Delta V_p(\tau_2) p(\tau_2) \\ \vdots \\ \Delta V_p(\tau_{n_\tau}) p(\tau_{n_\tau}) \end{bmatrix}, \quad (\text{C.3})$$

$$\begin{bmatrix} \Delta V_{w,1} \\ \Delta V_{w,2} \\ \vdots \\ \Delta V_{w,N} \end{bmatrix} = \begin{bmatrix} w_{1,1} & w_{1,2} & \dots & w_{1,n_\tau} \\ w_{2,1} & w_{2,2} & & w_{2,n_\tau} \\ \vdots & & \ddots & \vdots \\ w_{N,1} & w_{N,2} & \dots & w_{N,n_\tau} \end{bmatrix} \begin{bmatrix} \Delta V_p(\tau_1) S_w(\tau_1) \\ \Delta V_p(\tau_2) S_w(\tau_2) \\ \vdots \\ \Delta V_p(\tau_{n_\tau}) S_w(\tau_{n_\tau}) \end{bmatrix}, \quad (\text{C.4})$$

$$\begin{bmatrix} \Delta V_{g,1} \\ \Delta V_{g,2} \\ \vdots \\ \Delta V_{g,N} \end{bmatrix} = \begin{bmatrix} w_{1,1} & w_{1,2} & \cdots & w_{1,n\tau} \\ w_{2,1} & w_{2,2} & & w_{2,n\tau} \\ \vdots & & \ddots & \vdots \\ w_{N,1} & w_{N,2} & \cdots & w_{N,n\tau} \end{bmatrix} \begin{bmatrix} \Delta V_p(\tau_1) S_g(\tau_1) \\ \Delta V_p(\tau_2) S_g(\tau_2) \\ \vdots \\ \Delta V_p(\tau_{n\tau}) S_g(\tau_{n\tau}) \end{bmatrix}, \quad (C.5)$$

Dividing these quantities by pore volume of each grid block yields pressure, water and gas saturation mapped back onto the original grid blocks:

$$p_{ijk} = \frac{\sum_l^{n\tau} w_{ijk,l} \Delta V_{p,l} p_l}{\sum_l^{n\tau} w_{ijk,l} \Delta V_{p,l}}, \quad (C.6)$$

$$S_{j,ijk} = \frac{\sum_l^{n\tau} w_{ijk,l} \Delta V_{p,l} S_{j,l}}{\sum_l^{n\tau} w_{ijk,l} \Delta V_{p,l}}, \quad (C.7)$$

The next step is to determine the solution gas-oil ratio. We first need to map back the oil volume (stb) and solution gas volume (Mscf) both at the surface condition:

$$\begin{bmatrix} \Delta V_{o,1}^{sc} \\ \Delta V_{o,2}^{sc} \\ \vdots \\ \Delta V_{o,N}^{sc} \end{bmatrix} = \begin{bmatrix} w_{1,1} & w_{1,2} & \cdots & w_{1,n\tau} \\ w_{2,1} & w_{2,2} & & w_{2,n\tau} \\ \vdots & & \ddots & \vdots \\ w_{N,1} & w_{N,2} & \cdots & w_{N,n\tau} \end{bmatrix} \begin{bmatrix} \Delta V_p(\tau_1) \frac{S_o(\tau_1)}{B_o(\tau_1)} \\ \Delta V_p(\tau_2) \frac{S_o(\tau_2)}{B_o(\tau_2)} \\ \vdots \\ \Delta V_p(\tau_{n\tau}) \frac{S_o(\tau_{n\tau})}{B_o(\tau_{n\tau})} \end{bmatrix}, \quad (C.8)$$

$$\begin{bmatrix} \Delta V_{g1}^{sol} \\ \Delta V_{g2}^{sol} \\ \vdots \\ \Delta V_{gN}^{sol} \end{bmatrix} = \begin{bmatrix} w_{1,1} & w_{1,2} & \dots & w_{1,n\tau} \\ w_{2,1} & w_{2,2} & & w_{2,n\tau} \\ \vdots & & \ddots & \vdots \\ w_{N,1} & w_{N,2} & \dots & w_{N,n\tau} \end{bmatrix} \begin{bmatrix} \Delta V_p(\tau_1) \frac{S_o(\tau_1)R_s(\tau_1)}{B_o(\tau_1)} \\ \Delta V_p(\tau_2) \frac{S_o(\tau_2)R_s(\tau_2)}{B_o(\tau_2)} \\ \vdots \\ \Delta V_p(\tau_{n\tau}) \frac{S_o(\tau_{n\tau})R_s(\tau_{n\tau})}{B_o(\tau_{n\tau})} \end{bmatrix}. \quad (C.9)$$

The solution gas-oil ratio can be determined by dividing the solution gas volume by the surface oil volume:

$$R_{s,ijk} = \frac{\sum_l^{n\tau} w_{ijk,l} \Delta V_{p,l} \frac{R_{s,l} S_{o,l}}{B_{o,l}} \text{ (sol. gas vol. in Mscf)}}{\sum_l^{n\tau} w_{ijk,l} \Delta V_{p,l} \frac{S_{o,l}}{B_{o,l}} \text{ (oil vol. in STB)}}, \quad (C.10)$$

Strictly speaking, in order to perfectly conserve the mass balance, iterative calculations should be required because the oil volume is a function of pressure and solution GOR. However, we do not see any necessity for the iterative calculation based on the examples presented in the next section. Another challenge is a huge memory required for the weight matrix \mathbf{w} ($N \times n\tau$), especially for high resolution models.

C.3 Comparison of Map-back Methods

We compared the interpolation-based and material balance-based map-back schemes in terms of the material balance error, the simulated well performances and the computation time. The gas liberation case with the heterogeneity of $V_{dp} = 0.9$ in 2.8.1 is

used. For the simulation period of 100 days, two different map-back frequencies were tested: every 2 days and 10 days which correspond to 50 times and 10 times map-back, respectively. The material balance error is defined as follows:

$$e_o = \frac{\text{OIIP} - \left(\text{OCIP}_i + \sum_i^N q_{o,i} \Delta t_i \right)}{\text{OIIP}} \times 100, \quad (\text{C.11})$$

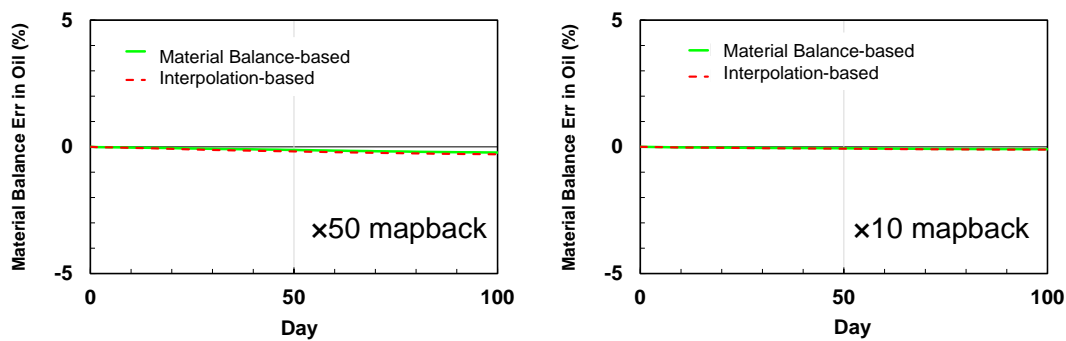
$$e_g = \frac{\text{GIIP} - \left(\text{GCIP}_i + \sum_i^N q_{g,i} \Delta t_i \right)}{\text{GIIP}} \times 100. \quad (\text{C.12})$$

where terminologies IIP and CIP denote the initial-in-place and the current-in-place, respectively. All the oil and gas volumes in Eqs. (C.11) and (C.12) are evaluated at the surface condition, and the gas includes both solution and free gases.

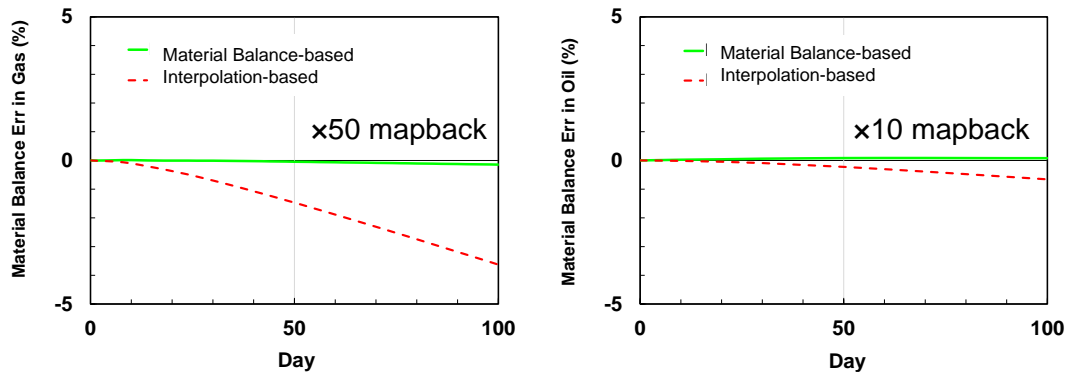
C.3.1 Material Balance Error

Figure C.3 shows the comparison of material balance errors between the map-back schemes with two different map-back frequencies. For oil volume, both map-back schemes yield material balance errors less than 1%. On the other hand, significant difference can be observed in the material balance error in gas volume that is magnified by larger compressibility compared to the oil phase. In the case of 50 times map-back, the material balance error from the interpolation map-back amounts up to 5% whereas the material balance-based scheme shows less than 1%. It seems that the material balance error from the interpolation map-back increases with increasing number of map-back

performed. In the case of 10 times map-back, the interpolation map-back yields enough small material balance error in gas volume less than 1%. Thus, the interpolation map-back can still be a reasonable approach if only the map-back is required only a few or several times such as the example presented in Chapter-IV where only one map-back was performed for modeling a child well.



(a) Oil volume



(b) Gas volume

Figure C.3 Comparisons of material balance errors between material balance-based map-back (green solid line) and interpolation-based map-back (red dashed line) with two different map-back frequencies

C.3.2 Well Performances

Next, we compared the simulated well performances between the two map-back schemes and two different map-back frequencies, including the case with no map-back (**Figure C.4**). For the oil rate, all the cases show almost identical profile. On the other hand in the GOR plot, the material balance-based method (green solid lines) shows ‘zigzag’ profile at map-back time steps, which is not observed in the interpolation-based method (red dashed lines). This is because pressure, saturation and solution GOR of the well cell on original grid block system will be computed by averaging those of the well grid and adjacent several 1-D grid blocks, leading to the different conditions in the 1-D well grid blocks before and after map-back.

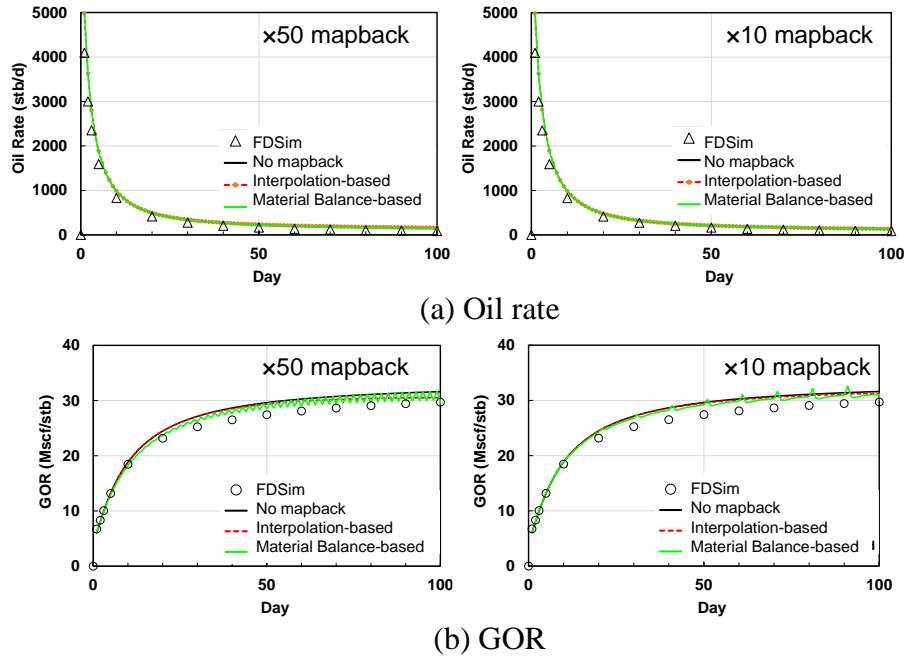


Figure C.4 Comparisons of well performances between material balance-based map-back (green solid line) and interpolation-based map-back (red dashed line) with two different map-back frequencies

C.3.3 Computation Time

Finally, we compared the computation time required for the two map-back schemes. The interpolation-based method requires a table-lookup as many times as the number of original grid blocks whereas the material balance-based method involves multiplication of the weight matrix ($N \times n_\tau$) and the 1-D solution vector ($n_\tau \times 1$). **Figure C.5** illustrates comparison of the CPU time required to map-back the 1-D solutions for different numbers of original grid blocks. It shows that there is no significant difference between the two map-back methods. However, the weight matrix in the material balance-based method involves extra memory to store the weight matrix, which can be huge for high resolution models.

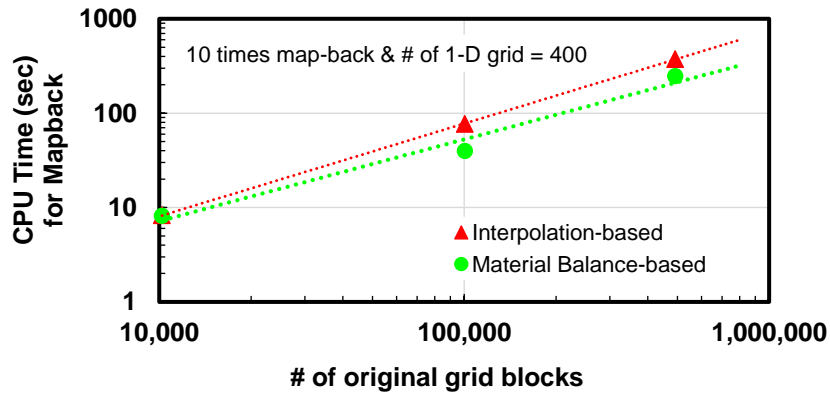


Figure C.5 Comparisons of CPU time required to map-back 1-D solutions with respect to number of original grid blocks (numbers of map-back and 1-D grid blocks are 10 and 400, respectively)

C.4 Summary

In this appendix, we presented and compared two methods for mapping back the 1-D solutions onto the original grid blocks. The following is summary and recommendation:

- The interpolation-based map-back is a simple table lookup. Based on the DTOF value on original grid blocks, pressure, saturations and solution GOR on the original grid blocks are determined by directly interpolating 1-D solutions on the DTOF coordinate.
- The material balance-based map-back is a volumetric reallocation where pore volume-weighted pressure and volumes of water, oil and gas are mapped back then saturations and solution GOR are determined. The weight matrix, which represents how much pore volumes of each original grid are allocated to each 1-D grid, is constructed and used for reallocation.
- No significant difference in the simulated well performances and the CPU time was confirmed between the two map-back schemes. However, the interpolation-based method may result in significant material balance error if a large number of map-back is performed, whereas the material balance-based method shows little error.
- It is recommended that the material balance-based method should be used to honor the material balance for cases where a large number of map-back will be performed. Otherwise, either the interpolation or material balance-based method can be used.

APPENDIX D

CALCULATING INTER-PARTITION TRANSMISSIBILITY: STEP-BY-STEP
ILLUSTRATION

In Chapter V, we described a workflow for the FMM-based multi-well simulation incorporating the inter-partition transmissibility. In this appendix, we provide more detailed explanation on each step in the simulation workflow.

D.1 Model Set-up

Here, we will use a simple 2-D homogeneous model to illustrate the workflow. Two wells are symmetrically placed 3,231ft apart in the reservoir domain of $10,200 \times 10,100 \times 50$ ft³. Porosity and permeability are set to be 0.3 and 1 mD, respectively. Single-phase oil is assumed with the compressibility of 1.486×10^{-5} psi⁻¹ and the viscosity of 0.49 cp. The corresponding $\sqrt{\alpha}$ is 677 (mD \times psi \times cp⁻¹)^{0.5}. **Figure D.1** shows the well locations and the DTOF contours. The equal- τ interface lies across the center of the model. In the following section, we present procedures to compute the inter-partition transmissibility.

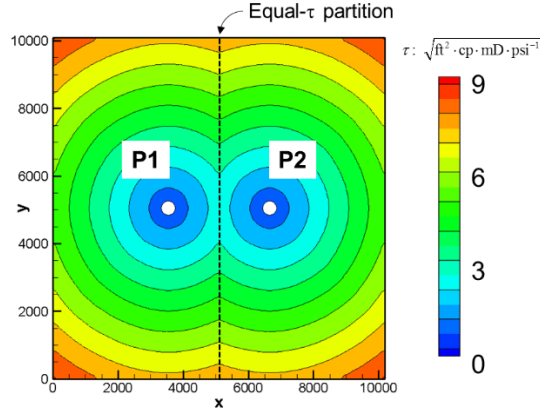


Figure D.1 Well locations and DTOF contour for two-well case in 2-D homogeneous reservoir

D.2 Illustration of the Method

In this research, computation of inter-partition transmissibility was implemented by the following four steps.

- 1) Identify the maximum τ where two contours have no contact

We first identify the maximum DTOF where the DTOF contours associated with each well have no contact with the others. In this case, no contact can be found for $\tau < 2.39$, as illustrated in **Figure D.2**. Thus, we will assign zero to the inter-partition transmissibility for the 1-D DTOF grid blocks within this threshold (τ_{th}). Here, suppose we set the number of τ -contours (N) for the inter-partition transmissibility calculation to be 9. We adopt equal-spacing to discretize the contours, giving the step size $\Delta\tau = (\tau_{max} -$

$\tau_{th})/9 = (9.05-2.39) = 0.74$ where τ_{max} is the maximum DTOF value in the domain. We could also use the logarithmic discretization.

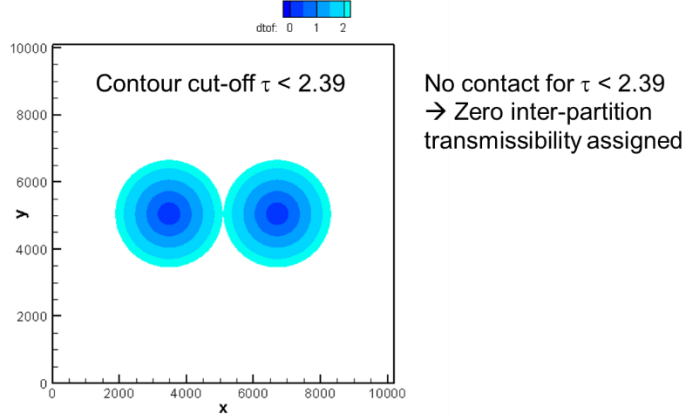


Figure D.2 DTOF contours that have no contact for the DTOF less than threshold

2) Calculate the transmissibility between τ -grids of the first contact

The first τ -grid is defined between 0 and $\tau_{th} + \Delta\tau (=3.11)$ as illustrated in **Figure D.3**. It should be noted that we need to include the grid blocks not only between τ_{th} and $\tau_{th} + \Delta\tau$ but also in $\tau < \tau_{th}$, which resulting in ‘eyeglass-like’ grid blocks. This special treatment is because of the fact that reservoir fluids in the DTOF contours less than the threshold can flow in and out through the contour of the first contact. Then we place the imaginary sources on all the grid blocks along the partition interface and run the FMM to get the DTOF. This DTOF (top-middle in Figure D.3), which is different from the DTOF that we first generated in Figure D.1, will be used for calculating pressure profiles within two τ -grid blocks where we compute the inter-partition transmissibility. The pressure profile is simply calculated on the 1-D coordinate assuming the unit flux and unit viscosity

under the steady-state flow condition. Finally, we get the inter-partition transmissibility for the τ -grids that have the first contact.

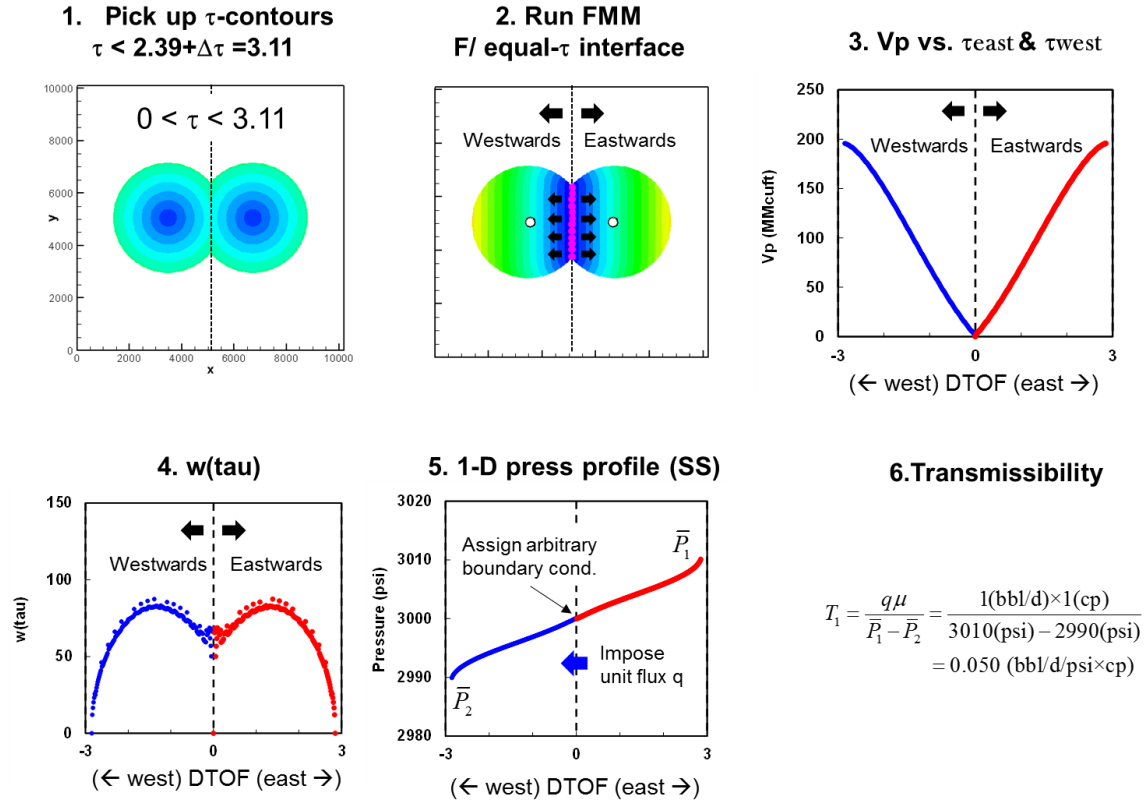


Figure D.3 Illustration of procedure to compute inter-partition transmissibility between DTOF-grids that have first contact

3) Calculate the transmissibility between τ -grids of the second contact

We visit the next τ -grids defined between τ of 3.11 and 3.86 (**Figure D.4**). For second grid and after, we work on the ‘two rings’ grid blocks. We will repeat the same calculation as step 2) to obtain the inter-partition transmissibility.

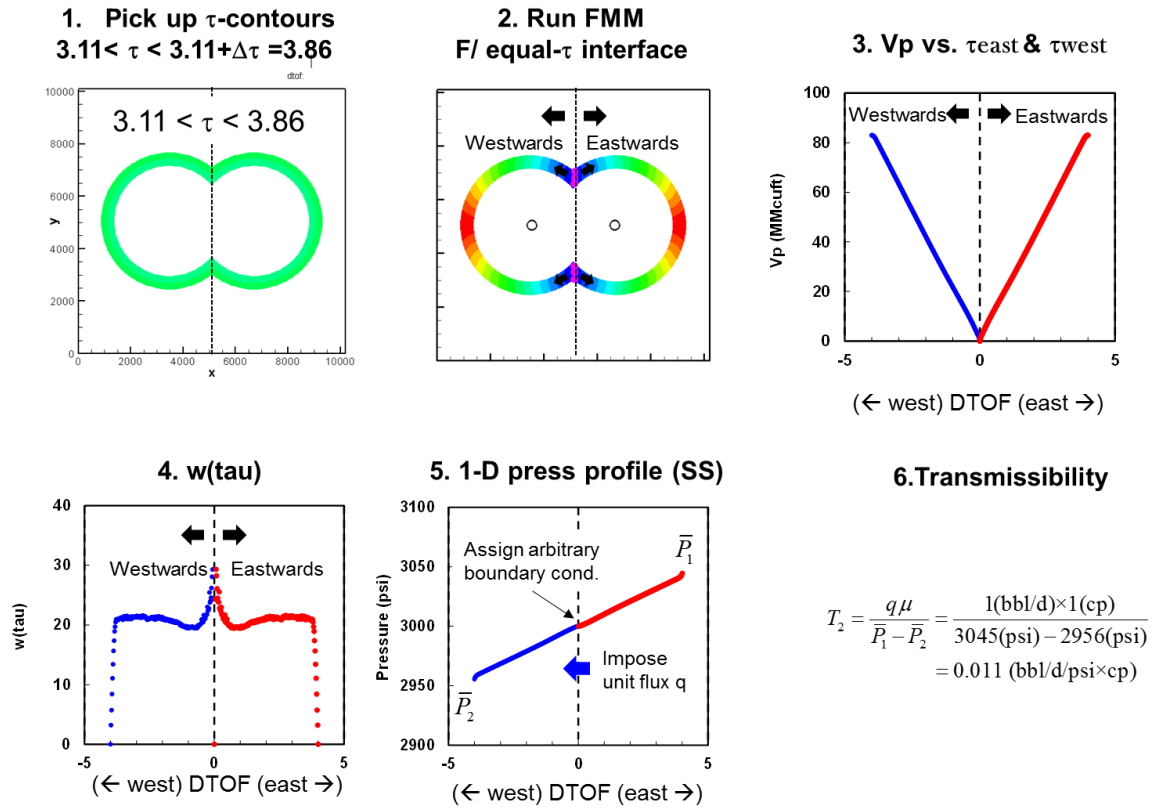


Figure D.4 Illustration of procedure to compute inter-partition transmissibility between DTOf-grids that have second contact and after

4) Visit every τ -grid and accumulate the inter-partition transmissibility

We repeat the step 3) for every τ -grid and accumulate the inter-partition transmissibility to construct a correlation between the cumulative transmissibility and the DTOf (**Figure D.5**). Note that the last two τ -grids have no apparent contact and therefore they were aggregated with 7th τ -grid.

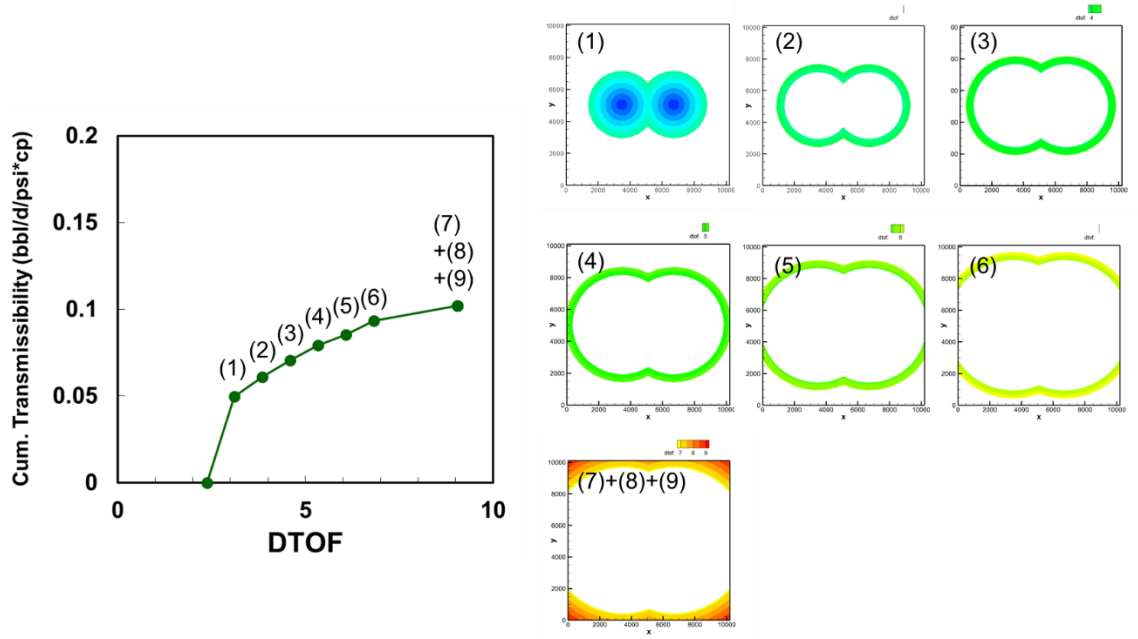
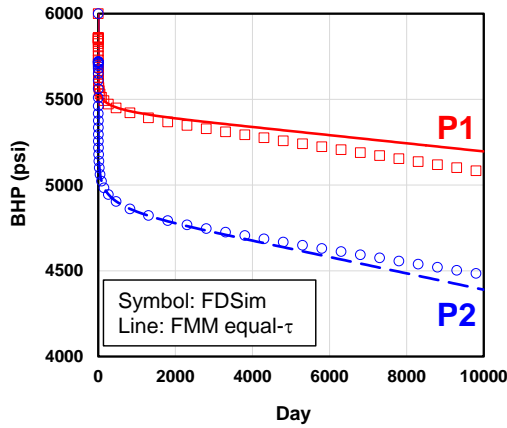


Figure D.5 Inter-partition transmissibility for each DTOF grid

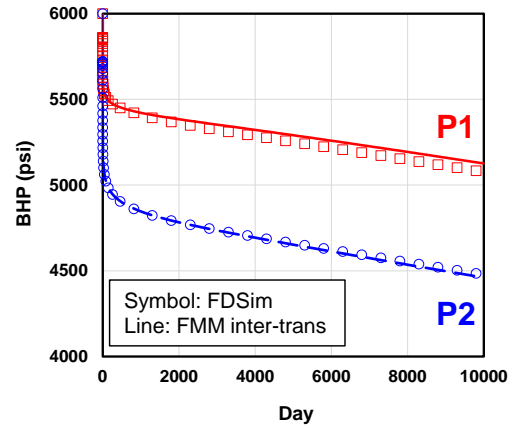
D.3 Comparison of Simulated BHP

Subsequently, we compared the bottomhole pressure from the FMM-based simulation and the FDSim. The production rates were set to be 25 stb/day and 50 stb/day for P1 and P2, respectively. In **Figure D.6a**, we partition the reservoir model using the equal- τ and no inter-partition transmissibility was incorporated, resulting in deviation from the FDSim in the mid-late time. On the other hand, **Figure D.6b** shows the case using the inter-partition transmissibility where good agreement can be confirmed with the FDSim. The log-log diagnostic plot in **Figure D.7** gives us the better idea on how the inter-partition transmissibility improved the simulated BHP. Incorporating the inter-

partition transmissibility yields the better matching with the FDSim during the transition from the infinite-acting to the pseudo-steady state flow periods and afterwards.



(a) Equal- τ partition



(b) Inter-partition transmissibility

Figure D.6 Comparison of bottomhole pressure between FDSim and FMM-based simulation using (a) equal-tau partition and (b) inter-partition transmissibility

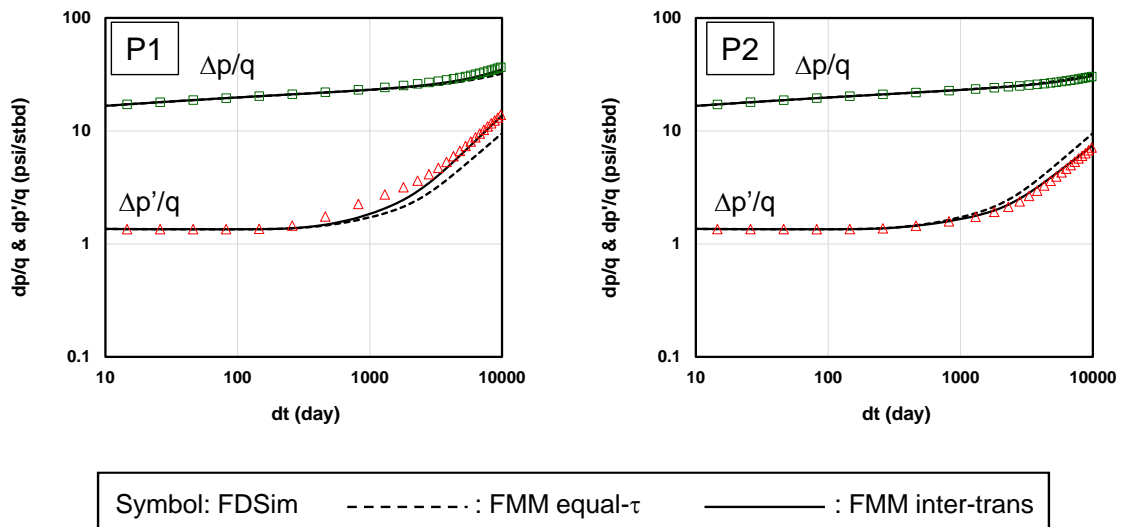


Figure D.7 Comparison of log-log diagnostic plot between FDSim and FMM-based simulation using (a) equal-tau partition and (b) inter-partition transmissibility

D.4 Comparison with Flow-based Transmissibility using FDSim

Finally, we performed the flow-based transmissibility calculation using the FDSim in order to make comparison with the calculated inter-partition transmissibility in Figure D.5. For every τ -grid depicted in Figure D.5, we imposed the different initial pressures to each partition and run the flow simulation. In the process of pressure equalization, we obtained average pressures and fluxes across the partition to get the effective transmissibility. **Figure D.8** compares the inter-partition transmissibility between the proposed FMM-based method and the flow-based approach using the FDSim. The inter-partition transmissibility from the FMM-based approach well captures the trend of that from the FDSim although matching in the magnitude is not perfect. In order to see the impact of the difference in the calculated transmissibility on the simulated BHP, we run the FMM-based simulation using the flow-based transmissibility instead of the inter-partition transmissibility. The bottomhole pressures from the FMM-based simulations using the inter-partition and flow-based transmissibility were compared in **Figure D.9** where almost identical results were confirmed.

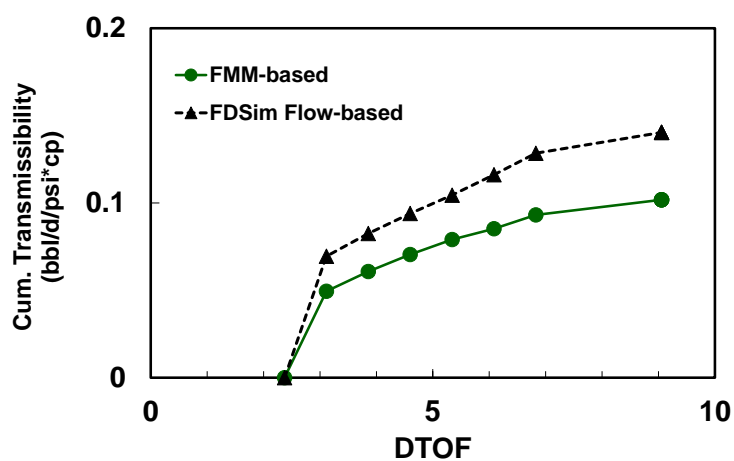
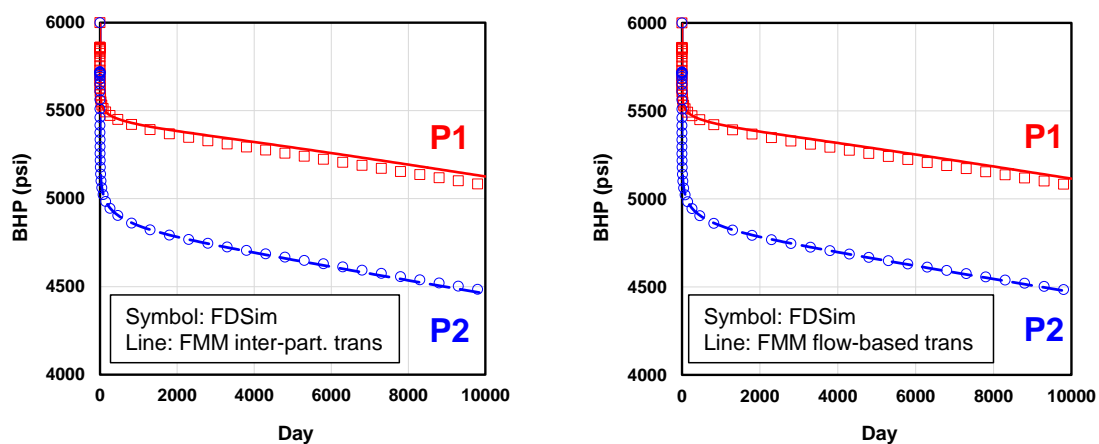


Figure D.8 Comparison of inter-partition transmissibility between FMM-based and FDSim-based approaches



(a) Inter-partition transmissibility

(b) Flow-based transmissibility

Figure D.9 Comparison of bottomhole pressures from FMM-based simulation using two different transmissibilities